

UNIVERSITÀ DELLA CALABRIA



Dipartimento di FISICA

UNIVERSITÀ DELLA CALABRIA

DEPARTMENT OF PHYSICS  
ASTRONOMIA & ASTROFISICA FIS/05

DOCTORATE SCHOOL "SCIENCE AND TECHNIQUE B. TELESIO"  
CURRICULUM IN PHYSICS OF COMPLEX SYSTEMS  
CYCLE XXIV

# NON-ADIABATIC PARTICLE TRANSPORT IN NUMERICAL MODELS OF TURBULENCE

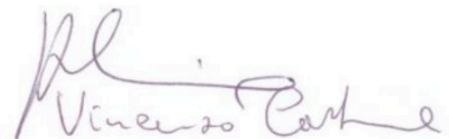
Prof. ROBERTO BARTOLINO, Chair of the School

Prof. VINCENZO CARBONE, Course Coordinator

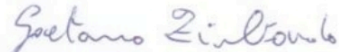
Prof. GAETANO ZIMBARDO, Candidate's Supervisor

Dr. ANTONELLA GRECO, Candidate's Supervisor

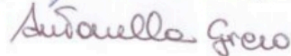
Prof. WILLIAM H. MATTHAEUS, Candidate's Co-Supervisor



Vincenzo Carbone



Gaetano Zimbardo



Antonella Greco

Ph.D. Candidate: SERENA DALENA

---

December, 2011

UNIVERSITÀ DELLA CALABRIA



Dipartimento di FISICA

UNIVERSITÀ DELLA CALABRIA

—  
DEPARTMENT OF PHYSICS  
ASTRONOMIA & ASTROFISICA FIS/05

—  
DOCTORATE SCHOOL "SCIENCE AND TECHNIQUE B. TELESIO"  
CURRICULUM IN PHYSICS OF COMPLEX SYSTEMS  
CYCLE XXIV

# NON-ADIABATIC PARTICLE TRANSPORT IN NUMERICAL MODELS OF TURBULENCE

Prof. ROBERTO BARTOLINO, Chair of the School

Prof. VINCENZO CARBONE, Course Coordinator

Prof. GAETANO ZIMBARDO, Candidate's Supervisor

Dr. ANTONELLA GRECO, Candidate's Supervisor

Prof. WILLIAM H. MATTHAEUS, Candidate's Co-Supervisor

Ph.D. Candidate: SERENA DALENA

---

December, 2011



“Love alters not with his brief hours and weeks  
But bears it out even to the edge of doom.  
If this be error and upon me proved,  
I never writ, nor no man ever love.”  
(W. Shakespeare)

*To all the people I love*



# Contents

|  |           |
|--|-----------|
| <b>Introduction</b>  | <b>1</b>  |
| <b>1 Non-adiabatic motion in the near-Earth magnetotail</b>                          | <b>5</b>  |
| 1.1 Introduction: Oxygen ions and bifurcated current sheets . . . . .                | 5         |
| 1.2 Overview of oxygen observations . . . . .  | 8         |
| 1.3 Magnetic field model . . . . .   | 11        |
| 1.4 Test particle simulations . . . . .  | 15        |
| 1.5 Numerical Results . . . . .  | 17        |
| 1.6 Discussion and Conclusions . . . . .   | 23        |
| <b>2 Theoretical background</b>  | <b>27</b> |
| 2.1 Introduction . . . . .   | 27        |
| 2.2 General theory for magnetic moment conservation . . . . .                        | 29        |
| 2.2.1 Demonstration of $\mu$ conservation . . . . .                                  | 30        |
| 2.2.2 Cosequences of $\mu$ invariance . . . . .                                      | 32        |
| 2.2.3 Poincaré invariant and adiabatic invariant . . . . .                           | 33        |
| 2.3 From the guiding center approximation to the quasilinear theory . . . . .        | 34        |
| 2.4 Overview on wave-particle interaction . . . . .                                  | 35        |
| 2.4.1 Landau Resonance . . . . .   | 37        |
| 2.4.2 The cyclotron interaction . . . . .  | 39        |
| 2.5 What is Diffusion? . . . . .   | 40        |
| 2.5.1 Historical remarks . . . . .   | 41        |
| 2.5.2 Random walk . . . . .  | 42        |
| 2.5.3 Modeling Diffusion with Fick's Law . . . . .                                   | 44        |
| 2.5.4 The Fokker-Planck Equation . . . . .   | 45        |
| 2.5.5 Anomalous diffusion . . . . .  | 45        |
| 2.6 Quasilinear Theory and Diffusion Coefficients . . . . .                          | 46        |
| 2.6.1 Description of particle motion in a random magnetic field . . . . .            | 47        |
| 2.6.2 The diffusion limit . . . . .  | 52        |
| 2.7 Trapping width and resonance overlapping . . . . .                               | 53        |
| <b>3 Model and Basic Equations</b>   | <b>57</b> |
| 3.1 The slab model . . . . .   | 60        |
| 3.1.1 The magnetostatic assumption . . . . .   | 61        |
| 3.1.2 Correlation function and power spectrum . . . . .                              | 63        |
| 3.2 Slab magnetostatic turbulent fields generation . . . . .                         | 65        |
| 3.2.1 Importance of scale separation . . . . .                                       | 66        |
| 3.3 Velocity space diffusion coefficient $D_{\alpha\alpha}$ for slab model . . . . . | 68        |

---

|   |            |
|---|------------|
| <b>4 Analytical and numerical results for magnetic moment conservation</b>              | <b>71</b>  |
| 4.1 Interaction between particles and a single wave . . . . .                           | 71         |
| 4.1.1 Expected behavior at resonance . . . . .  | 71         |
| 4.1.2 Trapping width derivation for a single circularly polarized wave                  | 72         |
| 4.1.3 Resonant vs non resonant particles . . . . .                                      | 75         |
| 4.1.4 Resonance overlap . . . . .   | 82         |
| 4.2 Interaction with the slab spectrum . . . . .  | 85         |
| <b>Conclusions</b>  | <b>99</b>  |
| <b>Acknowledgements</b>   | <b>103</b> |
| <b>A Details of the model used in Chapter 1</b>   | <b>105</b> |
| A.1 Parity of Magnetic Perturbations . . . . .  | 105        |
| A.2 Velocity Space Injection . . . . .  | 106        |
| <b>B Details of the model for <math>\mu</math> conservation and additional results.</b> | <b>109</b> |
| B.1 About test particle simulations & <b>Streamline</b> code . . . . .                  | 109        |
| B.2 Test of Accuracy of Streamline Code . . . . .                                       | 112        |
| B.3 Particles moving in two circularly polarized waves field . . . . .                  | 117        |
| B.3.1 Results from numerical simulations . . . . .                                      | 118        |
| B.4 Diffusion in velocity space . . . . .   | 125        |
| B.4.1 Finite wavenumber spacing $\Delta k$ . . . . .                                    | 126        |
| B.4.2 Numerical results . . . . .   | 126        |
| <b>Bibliography</b>   | <b>137</b> |

---

## **Non-adiabatic particle transport in numerical models of turbulence**

### **Keywords:**

magnetic moment, diffusion, plasmas, turbulence, bifurcated current sheet, near-Earth's magnetotail, solar wind.

---





# List of Figures

|      |  |     |
|------|--|-----|
| 1.1  | Current sheet structures . . . . .   | 7   |
| 1.2  | Sketch of large gyroradius particles motion in a thin current sheet. . . . .                 | 8   |
| 1.3  | An observation of a bifurcated current structure on 1 October 2001 . . . . .                 | 9   |
| 1.4  | Data from Cluster S/C 4 on 1 October 2001 . . . . .  | 10  |
| 1.5  | Projection of the magnetic field structure on the $xz$ plane . . . . .                       | 12  |
| 1.6  | Sample $x$ and $z$ profiles of the three magnetic field components . . . . .                 | 14  |
| 1.7  | Projection on the plane of four sample trajectories of $O^+$ & $H^+$ . . . . .               | 18  |
| 1.8  | Blow up of $O^+$ ions and protons trajectories . . . . .                                     | 19  |
| 1.9  | Vertical profiles for $O^+$ ions temperature and current density . . . . .                   | 20  |
| 1.10 | Vertical profiles for $H^+$ ion temperature and current density . . . . .                    | 21  |
| 1.11 | Total current density profiles . . . . .   | 22  |
| 1.12 | Projection on the plane of a sample trajectory of $O^+$ ions . . . . .                       | 24  |
| 2.1  | Motion of a positively charged particle in a uniform magnetic field $\mathbf{B}_0$ . . . . . | 29  |
| 2.2  | Motion of a charged particle in a converging lines of magnetic force. . . . .                | 31  |
| 2.3  | Random walk representation . . . . .   | 42  |
| 2.4  | Random walk in dynamical systems: normal & anomalous diffusion . . . . .                     | 45  |
| 3.1  | Wave polarizations and their interaction with ion and $e^-$ . . . . .                        | 57  |
| 3.2  | Illustration of the slab model . . . . .   | 61  |
| 3.3  | Correlation function, $R_{xx}^{slab}$ , and correlation length, $\lambda_c$ . . . . .        | 64  |
| 3.4  | Power spectrum of the turbulent magnetic field . . . . .                                     | 67  |
| 4.1  | Gyroresonant interaction particle and wave . . . . .   | 77  |
| 4.2  | An example of resonant particle . . . . .  | 78  |
| 4.3  | Resonant vs non resonant behavior . . . . .  | 80  |
| 4.4  | Resonant vs non-resonant behavior in $f(\alpha)$ and $f(\mu)$ . . . . .                      | 81  |
| 4.5  | Transition from non-overlapping to overlapping resonances . . . . .                          | 83  |
| 4.6  | Distribution function in resonance overlap experiment . . . . .                              | 84  |
| 4.7  | Slab spectrum in physical units . . . . .  | 86  |
| 4.8  | $f(\alpha)$ , $f(\mu)$ and $f(\delta z)$ for $v_p = 10v_A$ . . . . .                         | 88  |
| 4.9  | Statistics for $v_p = 10v_A$ . . . . .   | 89  |
| 4.10 | Statistics for $v_p = 1v_A$ . . . . .  | 92  |
| 4.11 | Statistics for $v_p = 100v_A$ . . . . .  | 93  |
| 4.12 | $\alpha$ and $\mu$ variance for different $v_p$ . . . . .                                    | 94  |
| 4.13 | Standard deviations, $\sigma_\alpha$ and $\sigma_\mu/\mu_{in}$ , vs $\delta b$ . . . . .     | 95  |
| 4.14 | Correlation functions $C_{\alpha\alpha}$ and $C_{\mu\mu}$ vs $t$ . . . . .                   | 96  |
| 4.15 | Correlation times, $\tau_c^\alpha$ and $\tau_c^\mu$ vs $\delta b$ . . . . .                  | 97  |
| A.1  | $z$ dependence of the turbulent magnetic field at a position $x, y$ . . . . .                | 106 |

---

|      |  |     |
|------|--|-----|
| B.1  | Accuracy in a uniform magnetic and electric field at various $racc$ .            | 114 |
| B.2  | Accuracy in a uniform magnetic field for $racc = 10^{-9}$ at different $\beta$ . | 115 |
| B.3  | Accuracy in a circularly polarized electromagnetic wave                          | 116 |
| B.4  | Particle velocities and magnetic field in the two waves experiment               | 119 |
| B.5  | Same of Figure(B.4) but for $\delta b = 0.1$                                     | 120 |
| B.6  | $\alpha$ , $\mu$ and $E_{\parallel}$ in the two waves experiment                 | 122 |
| B.7  | Same of the previous figure, but for different waves orientations                | 123 |
| B.8  | Particle orbits in $v_{\parallel} - v_{\perp}$ space                             | 124 |
| B.9  | Example of pitch angle diffusion coefficient                                     | 127 |
| B.10 | Temporal evolution of $\langle(\Delta\mu)^2\rangle$ varying the box length       | 129 |
| B.11 | Periodicity effects on $D_{\mu\mu}$  | 130 |
| B.12 | Energy consevation varying the box length  | 132 |
| B.13 | $D_{\mu\mu}$ violating the QL assumption   | 133 |
| B.14 | $D_{\mu\mu}$ varying the number of grid points, $N$                              | 134 |

# List of Tables

|     |  |     |
|-----|--|-----|
| 1.1 | Normalization quantities for O <sup>+</sup> test particle simulation . . . . .                         | 16  |
| 3.1 | Normalization quantities used for the study of $\mu$ conservation . . . . .                            | 59  |
| 3.2 | Characteristic scales in the spectrum. . . . .   | 66  |
| 4.1 | Wave polarization and resonance contribution to trapping width. . . . .                                | 73  |
| 4.2 | $\alpha$ and $\mu$ trapping width values . . . . .   | 79  |
| 4.3 | Values of $\Delta v_{\parallel}$ in the resonance overlap experiment . . . . .                         | 83  |
| 4.4 | Typical values used in the simulations. . . . .  | 87  |
| 4.5 | Statistic for particles with $v_p = 10v_A$ and $\alpha = 0.125$ . . . . .                              | 89  |
| 4.6 | Statistic for particles with $v_p = 1v_A$ and $\alpha = 0.125$ . . . . .                               | 91  |
| 4.7 | Statistic for particles with $v_p = 100v_A$ and $\alpha = 0.125$ . . . . .                             | 94  |
| B.1 | $v_{\parallel}$ values at resonances for different $\theta$ values for $l = \pm 1$ resonances. . . . . | 121 |



# Introduction

A fundamental assumption of the adiabatic theory is that magnetic field variations are negligible within a particle gyroperiod. This is generally not the case in the presence of a sharp field reversal, like for the most part of the Earth's magnetotail or near reconnection sites (*Speiser, 1968; Sonnerup, 1971; Gray & Lee, 1982; Delcourt et al., 1994*). The condition for violation of the adiabatic invariant is that particle sees either temporal field variations on the time scale of its gyroperiod or spatial field variations on the order of its gyroradius. In the Earth's magnetotail, the field line curvature may be so strong that the Larmor radii of thermal ions ( $\approx 1 - 10$  keV) exceed the curvature radius many times. Ions, as well as other particles, are not magnetized anymore and this can lead to interesting behaviors.

Motivated by the many observations of ionospheric oxygen,  $O^+$ , in the Earth's magnetotail (*Sauvaud et al., 2004; Wilber et al., 2004; Kistler et al., 2005; Cai et al., 2008; Echer et al., 2008*), we have considered the dynamics of protons and oxygen ions in the magnetotail current sheet, both in the presence and in the absence of magnetic turbulence. Cluster observations in the near-Earth's magnetotail have shown that sometimes the current sheet is bifurcated, i.e., it is divided in two layers (*Sergeev et al., 1993; Runov et al., 2003b*). In order to reproduce this bifurcation, observed in the current profiles, the ion motion has been studied by test particle simulations, where particles are injected in a magnetic quasi-neutral sheet with superimposed magnetic fluctuations. Indeed, the magnetotail current sheet is modeled as a magnetic field reversal with a normal magnetic field component,  $B_n$ , plus a three-dimensional spectrum of magnetic fluctuations,  $\delta\mathbf{B}$ , which represents the observed magnetic turbulence. The dawn-dusk electric field,  $E_y$ , is also included. Test particle simulations are performed using different values of  $\delta\mathbf{B}$  and  $E_y$  for the two different species of particles injected,  $O^+$  ions and protons. Several runs have been made in order to understand the differences between the proton and the oxygen behavior, with emphasis of the possibility to obtain a bifurcated current sheet. When protons are injected in the simulation box, a clear bifurcation of the current profile is obtained for turbulence levels  $\delta B/B_0 \geq 0.3$  (*Greco et al., 2002*), where  $B_0$  is the constant magnetic field in the magnetospheric lobes. Conversely, one of the most intriguing results concerning the oxygen behavior is the appearance of a double hump in the current profile both for the case of no magnetic turbulence,  $\delta B/B_0 = 0.0$ , and for relatively high levels of magnetic fluctuations,  $\delta B/B_0 \geq 0.4$ . We showed that this effect is essentially related to the non-adiabatic motion of oxygen ions during their interaction with the current sheet (*Dalena et al., 2010*). Indeed we found that, in absence of magnetic fluctuations,  $\delta B/B_0 = 0.0$ , the distance between the two peaks in the current profiles is of the same order of the typical excursion in  $z$  observed in the oxygen ions trajectories.

In a more general context, we further investigated the conservation of charged particle magnetic moment,  $\mu$ , in presence of turbulent magnetic fields. From the

particle orbit theory, for slow temporal and spatial magnetic field variations (i.e. if their characteristic length and time scales are greater than the particle orbit diameter and the time spent by a particle to execute one orbit, respectively), the magnetic moment, defined as  $\mu = v_{\perp}^2/B$ , averaged over the particle gyroperiod, is an adiabatic invariant and remains constant during particle motion. But in the presence of well developed magnetic turbulence,  $\mu$  might undergo rapid variations and in any case can no longer be expected to be constant. Of course, this fact could influence particle acceleration and could have a considerable implications in many astrophysical problems, such as coronal heating, cosmic ray transport or temperature anisotropies in the solar wind.

In order to reproduce and to extend some of the result obtained by [Karimabadi et al. \(1992\)](#), we started to study the resonant interaction between ions and a single parallel propagating electromagnetic wave, to understand in this very simple case the limit for magnetic moment conservation. During the interaction with a single finite amplitude fluctuation, a resonant particle undergoes a finite amplitude nonlinear oscillation, given by half peak-to-peak difference in the particle parallel velocity component, the so-called trapping width,  $\Delta v_{\parallel}$ . The period of this oscillation is the so-called bounce time,  $\tau_b = 1/\omega_b$ , where  $\omega_b$  is the bounce or trapped frequency. We specialized the expressions for  $\Delta v_{\parallel}$  and  $\omega_b$ , given by [Karimabadi et al. \(1992\)](#), in the case of a single circularly polarized wave and we wrote a similar expression for the magnetic moment trapping width,  $\Delta\mu$  ([Dalena et al 1.](#), in prep.). Finally, we studied the behavior of many particles interacting with a broad band slab spectrum. For this case we analyzed the diffusion coefficients and the distribution function,  $f$ , of particles pitch angle,  $\alpha$ , magnetic moment,  $\mu$ , and parallel position,  $z$ . We found that the behavior of magnetic moment is strictly related to pitch angle behavior for a low level of magnetic fluctuation, i.e.,  $\delta B/B_0 = 0.001, 0.01$  (where, in this case,  $B_0$  is the steady, uniform, background magnetic field). It undergoes the same finite amplitude nonlinear oscillation during the interaction with a single finite amplitude fluctuation and its distribution half-width is directly related to pitch angle distribution. When stochasticity arises (as a consequence of overlapping resonances in the interaction with a single wave or as an effect of the perturbation due to the neighboring uncorrelated waves in the case of a turbulent spectrum), its effect on pitch angle is the isotropization of the distribution function. This is a transient regime during which magnetic moment exhibits a one-sided long-tail distribution and starts to be influenced by the onset of spatial parallel diffusion. When  $f(\alpha)$  completely isotropizes, spatial diffusion sets in and  $f(\mu)$  behavior is closely related to the sampling of varying magnetic field strength associated with that spatial diffusion ([Dalena et al 1.](#), in prep.).

In addition, using the analytical result for the trapping width in velocity space and for the bounce frequency, it is shown how the quasilinear diffusion coefficient can be written in a physically illuminating form ([Mace et al.](#), in prep.). The concept of an effective trapping width in velocity space for the turbulence modified resonance structure is introduced. It is shown how this effective resonance width implies a condition on the density of wavemodes in Fourier space, in the vicinity of

the resonant wavenumber. The implications of this condition for simulations incorporating discrete fields is discussed in detail and examples of simulations violating this condition are presented.

This thesis is organized according to the research line followed during the three PhD years:

- In Chapter 1 we study oxygen and proton motion in a Harris-like current sheet in the Earth's magnetotail, paying attention to the non-adiabaticity contribution in the formation of bifurcated current sheet (*Dalena et al., 2010*).
- Chapter 2 is a brief review of the basic theories associated with the conservation of magnetic moment, such as single particle motion in varying magnetic field, wave-particle interaction, general view about diffusion, chaotic behavior in quasi-linear approximation and resonance overlapping.
- In Chapter 3 the magnetic field model and the basic equation used to study the magnetic moment conservation, with direct application to the solar wind case, are described.
- In Chapter 4 the results concerning magnetic moment conservation during the interaction between particles and one circularly polarized electromagnetic wave, as well as a broad band slab turbulent spectrum, are shown (*Dalena et al 1., in prep.*).
- In Chapter 4.2, the main conclusion are given.
- Appendix A is related with the work about oxygen ions motion and their contribution in the formation of bifurcated current sheet. It contains a description of the spectrum and the velocity injection used in the study.
- Appendix B is related with the second part of the thesis. It contains the accuracy test of the new code used during the research, some of the results obtains in the study of the particle interaction with two waves and a slab spectrum, valid as additional test of the code (*Dalena et al 2., in prep.*), and, finally, some discussions about velocity space diffusion and the discretization of the field (*Mace et al., in prep.*).





# Non-adiabatic motion in the near-Earth magnetotail

---

## 1.1 Introduction: Oxygen ions and bifurcated current sheets

The magnetotail current sheet, which separates the northern from the southern lobe, is one of the key regions of magnetospheric physics. In the simplest 1-D approximation, it may be described by the Harris solution, an equilibrium solution of the Vlasov equation, in which the current density maximum is near the center of the sheet,  $z = 0$ , where the magnetic field is equal to zero. Although spacecraft observations confirmed the Harris model as a zero-order description of the current sheet, later studies and observations by spacecraft revealed a more complex structure. The observed current sheets can be divided into three different classes, as shown in Figure 1.1: central sheets (type A), with a single peak localized at the center of the sheet, asymmetric off-center current sheets (type B), with the current density maximum shifted from the equatorial plane, bifurcated current sheets (type C), with two off-equatorial maxima of the current density and local minimum of the current density between them. Previously, current density profiles with a double peak were observed in the near-Earth's tail by ISEE 1 and 2 (*Sergeev et al., 1993*) and were deduced by a statistical analysis of Geotail data in the distant tail (*Hoshino et al., 1996*). More recently, bifurcated current sheets have been reported with Cluster data at  $20 R_E$  downtail (*Nakamura et al., 2002; Runov et al., 2003b*). In some of the analyzed events, the formation of the current double layer was associated with magnetic reconnection, as shown by *Runov et al. (2003a)* and *Asano et al. (2004)*. Observations of 29 August 2001 and 26 September 2001, analyzed respectively by *Runov et al. (2004)* and *Sergeev et al. (2003)*, reported on a bifurcated current sheet during apparent flapping motion of the plasma sheet, that lasted for 15 min. The authors concluded that the bifurcation was not associated with reconnection process but was the result of an aging process of a thin current sheet, in which non-adiabatic motion of ions results in a weaker current in the central plasma sheet, as demonstrated theoretically by *Zelenyi et al. (2002)*. However, the physical origin of bifurcated current sheets remain controversial.

Contemporary to the observations, many theoretical models have been proposed. *Zelenyi et al. (2002, 2003)* considered the structure of a thin current sheet in presence of non-adiabatic particles, which reduces the current at the center of the current sheet and the bifurcation has scale size of an ion gyroradius (hundreds of kilometers

in the magnetotail). *Sitnov et al. (2003)* obtained bifurcated current sheets in the case of ion temperature anisotropy,  $T_{\perp} > T_{\parallel}$ , (where  $T_{\perp}(T_{\parallel})$  is the ion temperature perpendicular (parallel) to the magnetic field), together with relatively flat current density profiles. *Ricci et al. (2004)* developed a kinetic simulation of a Harris current sheet, in which the lower-hybrid drift instability causes the current sheet to bifurcate. *Delcourt et al. (2004)* examined the behavior of charged particles when the adiabaticity parameter,  $\kappa$ , is equal to unity in a simple current sheet model and found that nonlinear dynamics lead to bifurcated current sheets on the scale of ion gyroradius. The adiabaticity (or curvature) parameter,  $k$ , was introduced for the first time by *Büchner & Zelenyi (1989)*:

$$k = \sqrt{\frac{R_{min}}{\rho_{max}}}, \quad (1.1)$$

where  $R_{min}$  is the minimum curvature radius of the field, reached at the reversal plane and  $\rho_{max}$  is the maximum particle gyroradius. In a field reversal, these quantities occurs at the equatorial plane,  $z = 0$ , where a particle rotating with its total velocity,  $v_0$ , directed perpendicular to the minimum field,  $B_{min} = B_n \hat{e}_z$ , has the maximum Larmor radius equal to:

$$\rho_{max} = \rho_n = v_0 \Omega_n^{-1} = \frac{mv_0}{eB_n} = \frac{\rho_0}{(B_n/B_0)},$$

in which  $\Omega_n = eB_n/m$  is the Larmor frequency in the field  $B = B_n \hat{e}_z$  and  $\rho_0 = v_0/\Omega_0$ , with  $\Omega_0 = eB_0/m$ . The curvature radius at the reversal plane equals

$$R_{min} = \left\{ \left( \frac{d^2 X}{dZ^2} \right)^{-1} \left[ 1 + \left( \frac{dX}{dZ} \right) \right]^{-3/2} \right\} |_{z=0} = B_n \frac{\lambda}{B_0},$$

where  $X(Z)$  represents the equation of a field line of the magnetotail-like field reversal. The  $k \gg 1$  case corresponds to the usual adiabatic case, for which particle magnetic moment,  $\mu$ , is a first-order invariant of motion. As  $k$  decreases toward unity, particle motion becomes stochastic, due to deterministic chaos (*Lichtenberg & Lieberman, 1983*) caused by non-linear resonances overlapping between the bounce-motion and the gyro-motion. For  $k \simeq 1$ , particle behavior becomes strongly chaotic. For a sharply curved field reversal,  $k \ll 1$ , particle motion is *quasi-adiabatic*, i.e., the jumps of the adiabatic invariant are smaller than the value of the invariant itself. Both a new kind of adiabaticity, characterized by ring-type particle orbits, and a partially adiabatic but weakly chaotic type of motion, in which particles follow cucumber-like orbits, appear. Both types of orbits are closely related with fast oscillations perpendicular to the reversal plane. However, particles trajectories are adiabatic only if they permanently remain crossing the reversal plane. Instead, the result of the slower process of the weak but finite jumps of the adiabatic invariant is a gradual particle trapping in the current sheet. Quasi-trapped particles, that perform cucumber-like orbits, are related with the transient regime due to non-adiabatic scattering. Usually, for realistic ion parameters in the magnetotail,  $k$  is less than unity.

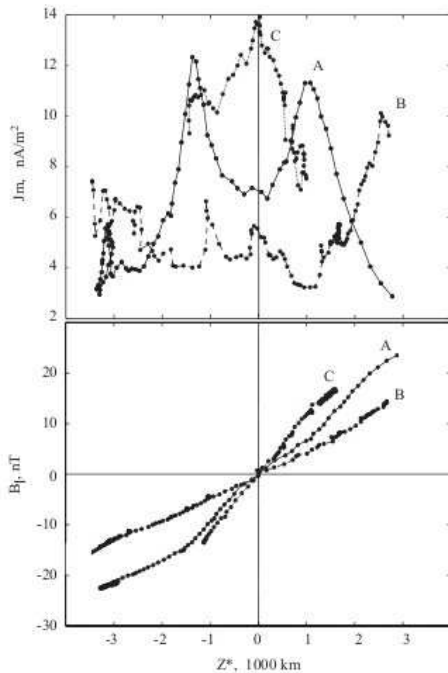


**Figure 1.1:** From *Runov et al. (2005)*. Three different types of current sheet structure observed in the near-Earth magnetotail: central sheet (type A), asymmetric current sheet (type B) and bifurcated sheets (type C)

sequently, *Greco et al. (2002)* and *Zimbaro et al. (2003)*, analyzing the near-Earth's magnetotail, where the average  $B_n$  is not zero and northward oriented, found that the normal magnetic field component,  $B_n$ , and magnetic fluctuations,  $\delta B/B_0$ , have opposite effects on the current structure and on the proton heating. Indeed, a large value of  $B_n$  inhibits the  $y$ -motion in the quasi-neutral sheet, while magnetic fluctuations favor the  $y$  motion at some distance from the center; the strong magnetic turbulence in the center of the current sheet slows down the proton motion and causes the double humped profiles of the current and ion velocity. More recently, *Greco et al. (2007)* have studied the equilibrium of the Earth's magnetotail, injecting protons and electrons. A stationary three-dimensional kinetic-fluid code, with protons represented by particles and electrons by a massless fluid, was developed. For a specific set of magnetotail parameters, the electron finite Larmor radius and the electron drift term are responsible for the formation of a double peak in the total current density, even in those case where the proton current density does not display any bifurcated structure and without turbulence.

A number of experimental studies show that in many cases the electrons are the main current carriers (*Kistler et al., 2005; Runov et al., 2006; Israelevich et al., 2008*). However, some Geotail observations show that in some periods the ion current prevails, while, in other periods, the electron current prevails (*Asano et al., 2003*). Keeping in mind that under different magnetotail conditions the main current car-

In most previous studies, the presence of magnetic turbulence in the near and distant magnetotail was not considered. Although magnetic turbulence is stronger during active geomagnetic periods, it is non-negligible even during quiet times. Usually, the turbulence level is stronger in the center of the plasma sheet (*Bauer et al., 1995; Hoshino et al., 1996*), while a more ordered magnetic configuration is found in the vicinity of the magnetospheric lobes. *Veltri et al. (1998)* investigated the effect of turbulent magnetic fields on the proton dynamics for the distant magnetotail, where the normal component of the unperturbed magnetic field,  $B_{0z} = B_n$ , is statistically negligible (in the GSM coordinate system). By a test particle simulation, they found that magnetic fluctuations play the role of effective scattering mechanism and the current sheet splits in two layers for perturbation levels  $\delta B/B_0 > 0.2$ . Subse-

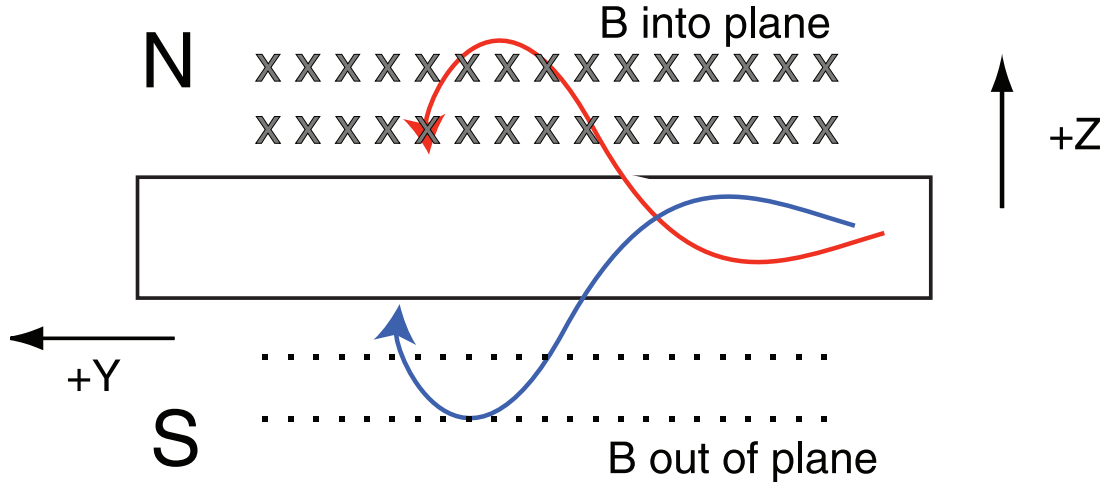


**Figure 1.2:** From *Kistler et al. (2005)*. Sketch of executed motion of large gyroradius particles in a thin current sheet.

riers can be either ions or electrons, here we try to assess the relative contribution to the cross tail current of different ions species, like protons and oxygen ions. The principal motivation to study  $O^+$  ions dynamics is the observation of rather energetic population of such ions, that shows a drift motion from dawn to dusk in the magnetic tail. The same observations (*Wilber et al. , 2004; Kistler et al., 2005; Cai et al., 2008*) have shown that the  $O^+$  behavior is very different from that of the protons  $H^+$ , analyzed till now, because of the different Larmor radius ( $\rho_{O^+} = 4\rho_{H^+}$ , considering same initial energies), so that non-gyrotropic effects become more important for heavy ions. Out of the neutral sheet,  $O^+$  ions and protons perform circular orbits around the magnetic field lines. Nevertheless, since their Larmor radius is greater than the half thickness of the current sheet,  $O^+$  ions can reenter in the neutral sheet, performing meandering orbits, as shown in Figure 1.2. An interesting situation arises where there is a thin current sheet and the plasma sheet is dominated by ionospheric oxygen, for example during magnetospheric active periods: these are the most likely cases to find the plasma sheet dynamics dominated by non-adiabatic ions, that may also carry a large fraction of the current. In this previous work, we investigate the dynamics of ionospheric  $O^+$  ions in the near-Earth's magnetotail in the presence and in the absence of magnetic turbulence. We find that  $O^+$  ions can support the formation of double peaked current sheets even in the absence of magnetic fluctuations, as well as for relatively large values.

## 1.2 Overview of oxygen observations

Measurements have confirmed the presence of out-flowing  $O^+$ ,  $H^+$ ,  $He^+$  and other ions in every magnetospheric region; these ions have low energy in the ionosphere

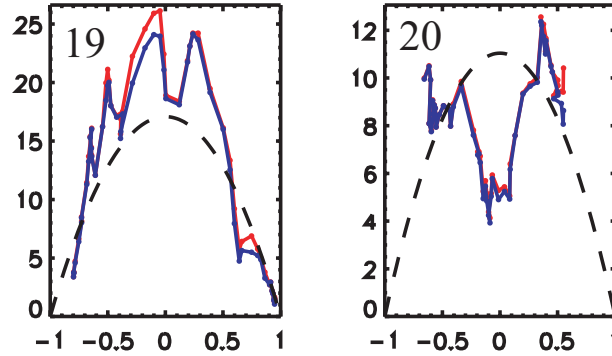


**Figure 1.3:** From [Runov et al. \(2006\)](#). Bifurcation in the current density profiles at 09:48UT and at 09:50UT on 1 October 2001.

and high energy in the magnetosphere, thanks to several acceleration mechanisms. It is known that the outflow of heavy ions from the ionosphere is strongly dependent on geomagnetic and substorms activity ([Yau et al., 1985](#); [Wilson et al., 2004](#)). In particular  $O^+$  ions are not just significant in the inner magnetosphere, but actually the dominant ion species during magnetic storms ([Daglis, 1991](#); [Kistler et al., 2005](#)): they are observed to stream from dawn to dusk across the tail, carrying about (5 – 10)% of the cross-tail current. Indeed, during storm times,  $O^+$  can dominate both the pressure and the density in the plasma sheet, that is already oxygen-rich because of the contribution from ion-outflow.

Inspection of Cluster data shows that often the formation of the double current sheet is in association to the increase of the oxygen amount in the near magnetotail, for example during the events on 1 October 2001 ([Runov et al., 2003a](#); [Wilber et al., 2004](#); [Wygant et al., 2005](#); [Kistler et al., 2005](#)), 17 August 2001 ([Sawvaud et al., 2004](#); [Echer et al., 2008](#)) and 15 September 2001 ([Cai et al., 2008](#)). Generally, these layers are very thin, with typical thickness ranging between 2000 km and 5000 km.

On 1 October 2001 at (0947-0951)UT, during a storm-time substorm, Cluster was located at  $[-16.5; 8.0; 0.5] R_E$  (GSM coordinates). During this interval the Cluster barycenter crossed the neutral sheet 11 times; at 09:48UT and at 09:50UT the current density exhibited a bifurcated structure ([Runov et al., 2003a](#)), as shown in Figure 1.3. At the same time a declining trend in proton density from 0.3 to 0.02  $cm^{-3}$  is observed, that results in  $O^+$  dominance ( $n_{O^+} \simeq 0.07 cm^{-3}$ ) ([Wygant et al., 2005](#); [Wilber et al., 2004](#)). As evident in Figure 1.4, a very thin current sheet was observed, with an half thickness of about 2500 km;  $O^+$  dominates the pressure and density in the plasma sheet and its contribution to the current was as high as 10%. This situation is rather common: [Korth et al. \(2002\)](#) have shown that the  $O^+/H^+$  energy density ratio of storm-time substorms exceeds 100%; for non-storm substorms the ratio is less and amounts to (15 – 65)%. The magnetic field in the magnetospheric lobes,  $B_0$ , and the normal component in the equatorial plane,  $B_n$ , measure approximately 20 nT and 5 nT, respectively. We have also estimated a

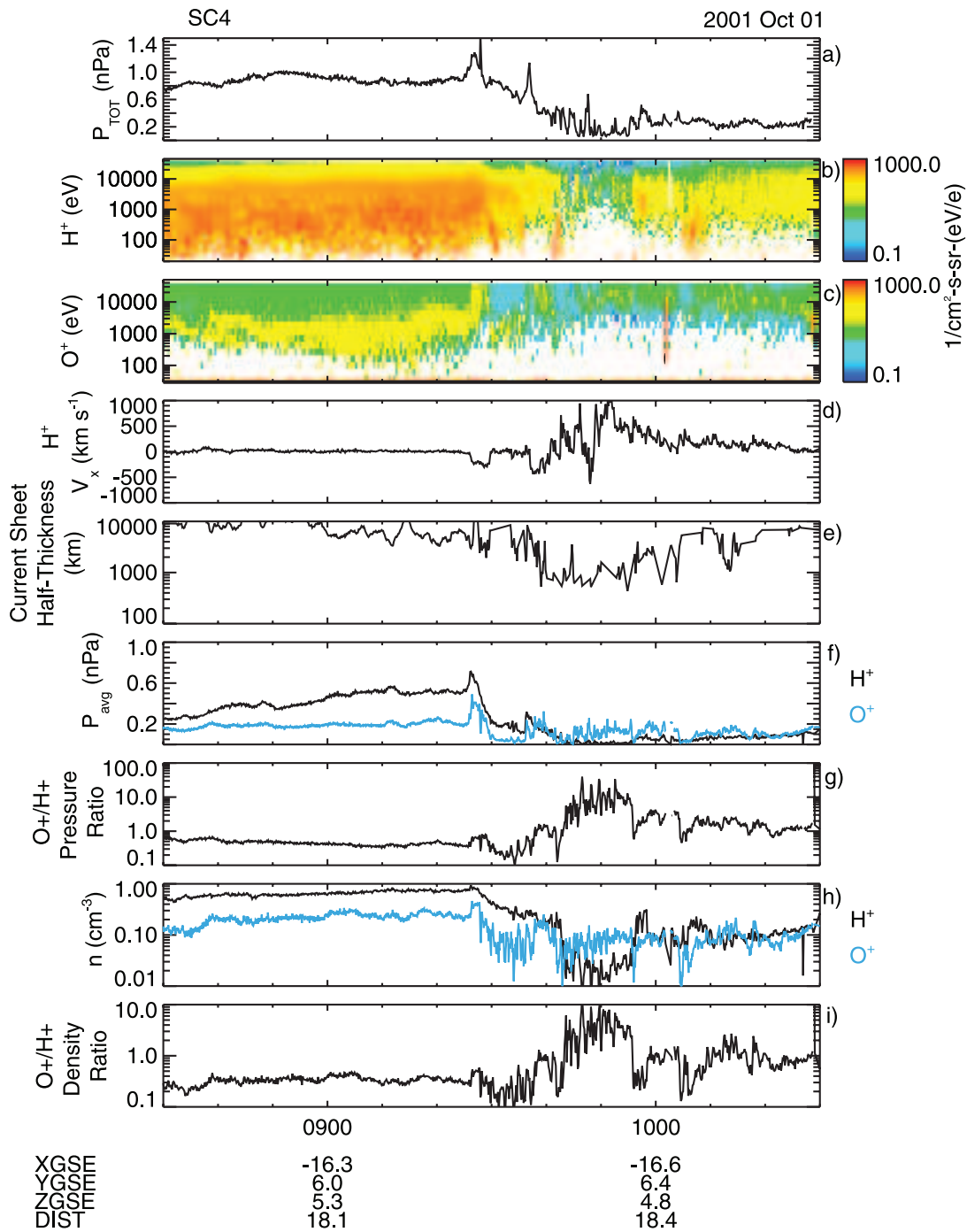


**Figure 1.4:** From *Kistler et al. (2005)*. Data from Cluster S/C 4 on 1 October 2001 from 8:30 to 10:30. (a) Total pressure (plasma plus magnetic field), (b)  $H^+$  differential flux versus energy and time, (c)  $O^+$  differential flux versus energy and time, (d)  $H^+$  velocity in  $X_{gse}$ , (e) current sheet thickness, (f)  $H^+$  (black) and  $O^+$  (blue) pressure, (g)  $O^+/H^+$  pressure ratio, (h)  $H^+$  (black) and  $O^+$  (blue) density, and (i)  $O^+/H^+$  density ratio.

magnetic fluctuations level,  $\delta\mathbf{B}$ , of around 10 nT. The current sheet half-thickness measures approximately 2500 km (*Kistler et al., 2005*).

The event of 17 August 2001 is another example in which the Cluster spacecraft were in the plasma sheet during a geomagnetic storm and observed the  $\text{O}^+$  outflow from the ionosphere into the tail (*Sauvaud et al., 2004; Echer et al., 2008*). In addition, during the storm main-phase, a substorm occurred. Oxygen beams were present in both the lobe and plasma sheet prior to this substorm, so this is an event where the plasma sheet is oxygen rich prior the substorm onset. After the substorm onset at 16:00 UT, the  $\text{H}^+$  density and pressure decreased significantly, while  $\text{O}^+$  pressure remained high. From 16:36 to 16:46 UT,  $\text{O}^+$  was the dominant ion species in the plasma sheet and showed a duskward motion.

During the Cluster spacecraft crossing on 15 September 2001, both an embedded proton (that manifests a pressure anisotropy mainly with  $p_{\parallel} > p_{\perp}$ ) and a bifurcated oxygen ion thin current sheet (that exhibits a pressure anisotropy mainly with  $p_{\parallel} < p_{\perp}$  and nongyrotropy) were observed (*Cai et al., 2008*). Indeed, in the time interval (04:57:45-05:00:25)UT, a localized self-consistent current sheet equilibrium of oxygen ions was observed by C1 and C4, although in this very thin sheet the current contribution from oxygen ions is minor. Magnetic field value in the magnetospheric lobes and normal component of magnetic field are approximately 25 nT and 3 nT. The estimation of the oxygen thin current sheet thickness is about 2500 km.

### 1.3 Magnetic field model

The considered magnetic field model consists of three terms,

$$\mathbf{B} = \mathbf{B}_{0x}(z) + \mathbf{B}_n + \delta\mathbf{B}(\mathbf{r}),$$

where  $\mathbf{B}_{0x}(z)$  is an unperturbed, sign reversing component, directed along the Earth-Sun axis,  $B_n$  is the unperturbed, constant, magnetic field component perpendicular to the current sheet and  $\delta\mathbf{B}(\mathbf{r})$  represents the 3D stationary magnetic fluctuations, having a power law spectrum. The coordinate system used in the description is the *Geocentric Solar Magnetospheric system*, GSM, that is Earth centered. In this system the  $x$ -axis points from the Earth towards the Sun; the  $y$ -axis is defined to be perpendicular to the Earth's magnetic dipole, so that the  $xz$ -plane contains the dipole axis. The positive  $z$ -axis is chosen to be in the same sense as the northern magnetic pole. This system is useful for displaying magnetopause and shock boundary positions, magnetosheath and magnetotail magnetic fields and magnetosheath solar wind velocities because the orientation of the magnetic dipole axis alters the otherwise cylindrical symmetry of the solar wind flow. It is also used in models of magnetopause currents. It reduces the three dimensional motion of the Earth's dipole in other coordinate systems, i.e., GEI (Geocentric Equatorial Inertial), GSE (Geocentric Solar Ecliptic), etc., to motion in a plane (the  $xz$ -plane). In the GSM system, the reversing magnetic field component,  $\mathbf{B}_{0z}$ , is positive in the upper part



(northern) lobe of the tail and negative in the lower (southern) lobe. In a first approximation, this field component could be represented by the magnetic field of the Harris current sheet model, given by Eq. 1.2 (Harris, 1962):

$$\mathbf{B}_0(z) = B_{0x}(z)\mathbf{e}_x = B_0 \tanh \frac{z}{\lambda} \mathbf{e}_x. \quad (1.2)$$

However, because the Harris equilibrium may be not effectively achieved, instead of Eq. 1.2 we use the expression of a modified Harris magnetic field reversal, Eq. 1.3, setting it in such a way that the asymptotic value  $B_0$  is reached smoothly at the edges of the simulation box,  $z = \pm 0.5L$ , where also the derivative of the field with respect to  $z$  becomes zero (Veltri et al., 1998):

$$B_{0x} = B_0 \frac{\tanh\left(\frac{z}{\lambda}\right) - \left(\frac{z}{\lambda}\right) \cosh^{-2}\left(\frac{L}{2\lambda}\right)}{\tanh\left(\frac{L}{2\lambda}\right) - \left(\frac{L}{2\lambda}\right) \cosh^{-2}\left(\frac{L}{2\lambda}\right)} \quad (1.3)$$

where  $B_0$  is the constant magnetic field in the magnetospheric lobes,  $\lambda = 0.25L$  is the current sheet half thickness and  $L$  is the thickness of the considered magnetic field configuration (i.e. of the simulation box). We emphasize that the above magnetic field model is adopted as a reasonable, smooth, magnetic field profile, having the main features of a magnetic field reversal, but we do not assume that the Harris equilibrium actually holds (see also Veltri et al., 1998). Indeed, the main results of our study are unchanged if a different magnetic field reversal is assumed. Note that our study will be performed in a local simulation box in the magnetotail, which does not take into account the magnetotail large scale variations, for instance in  $x$  and  $y$ .

The unperturbed components describes the parabolic field line geometry, which is found in the Earth's tail from approximately 10 to 60  $R_E$  down-tail, and is shown for  $B_n = 0.1B_0$  in the top panel of Figure 1.5. Since usually  $B_n \ll B_0$  (where  $B_0$  is the (normalization) magnetic field observed in the magnetospheric lobes), this configuration is referred to as quasi-neutral

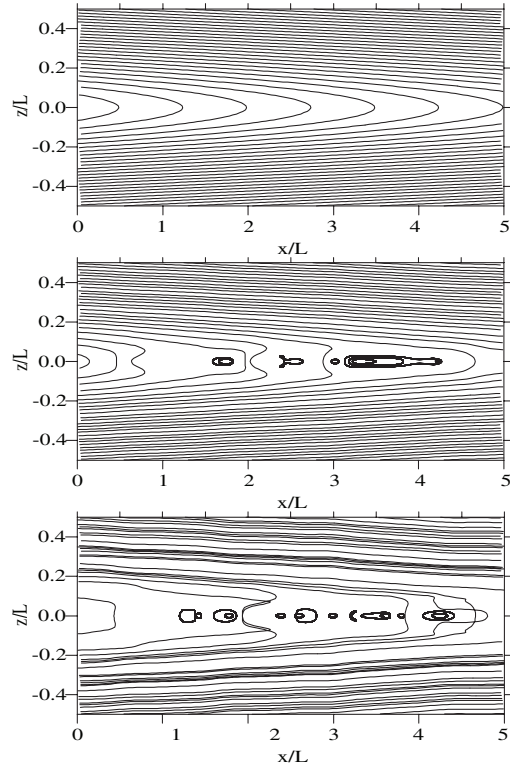


**Figure 1.5:** Projection of the magnetic field structure on the  $xz$  plane, for  $B_n = 0.1B_0$  and (a)  $\delta b = 0$ , (b)  $\delta b = 0.1$ , and (c)  $\delta b = 0.3$ . Magnetic islands are obtained even for  $\delta b = 0.1$ , since the magnetic perturbation can be, locally, larger than the RMS value. Also note that some field lines cross each other: this is because the perturbations are three-dimensional ( $\delta B_y \neq 0$ ).

current sheet. This normal component goes to zero in the distant magnetotail ( $x_{GSM} < -100R_T$ ).

The power law spectrum of the magnetic fluctuations, regularly observed by the Geotail (*Hoshino et al., 1994*), AMPTE/IRM (*Bauer et al., 1995*), ISEE 2 (*Borovsky et al., 1997*) and Interball (*Zelenyi et al., 1998*) satellites in this region of the magnetotail, has well-defined, "reproducible" features, like the spectral shape, the frequency range, and the fluctuation level for given geomagnetic activity levels. This suggests that magnetic turbulence is in a steady state, in statistical sense. In our model the observed magnetic fluctuations are represented as the sum of static magnetic perturbations (*Zimbardo et al., 1995; Veltri et al., 1998*):

$$\delta\mathbf{B}(\mathbf{r}) = \sum_{k,\sigma} \delta\mathbf{B}(\mathbf{k})\mathbf{e}_\sigma(\mathbf{k}) \exp [i(\mathbf{k} \cdot \mathbf{r} + \phi_{\mathbf{k}}^\sigma)],$$

where  $\delta B_\sigma(\mathbf{k})$  represents the amplitude associated with the wavevector  $\mathbf{k}$ ,  $\mathbf{e}_\sigma(\mathbf{k})$  are the polarization unit vectors and  $\phi_{\mathbf{k}}^\sigma$  are random phases fixed in a way to concentrate the magnetic fluctuations in the quasi-neutral sheet, in agreement with the observations. The condition  $\nabla \cdot \mathbf{B} = 0$  implies that  $\mathbf{k} \cdot \mathbf{e}_\sigma(\mathbf{k}) = 0$ , so the unit vectors are given respectively by:

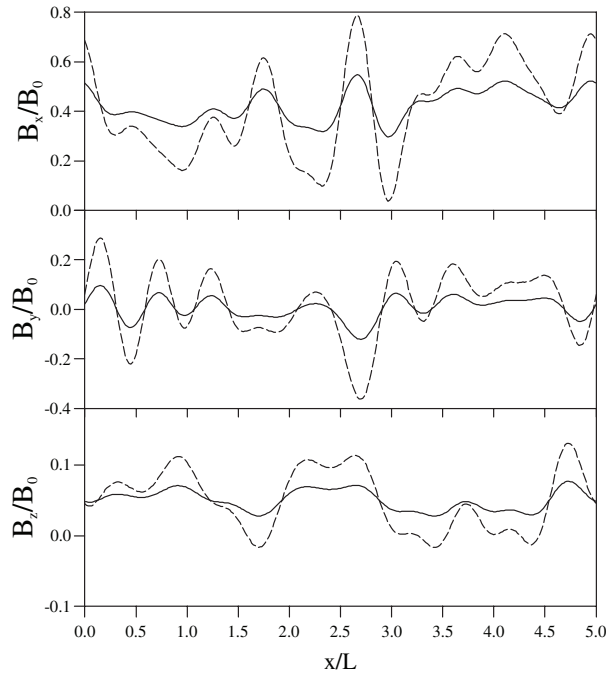
$$\begin{aligned} \mathbf{e}_1(\mathbf{k}) &= i \frac{\mathbf{k} \times \mathbf{B}_0}{|\mathbf{k} \times \mathbf{B}_0|} \\ \mathbf{e}_2(\mathbf{k}) &= -i \frac{\mathbf{k}}{|\mathbf{k}|} \times \mathbf{e}_1(\mathbf{k}) \end{aligned}$$

and the amplitude of magnetic fluctuations depends on the wavevector,  $\mathbf{k}$ , according to a power law:

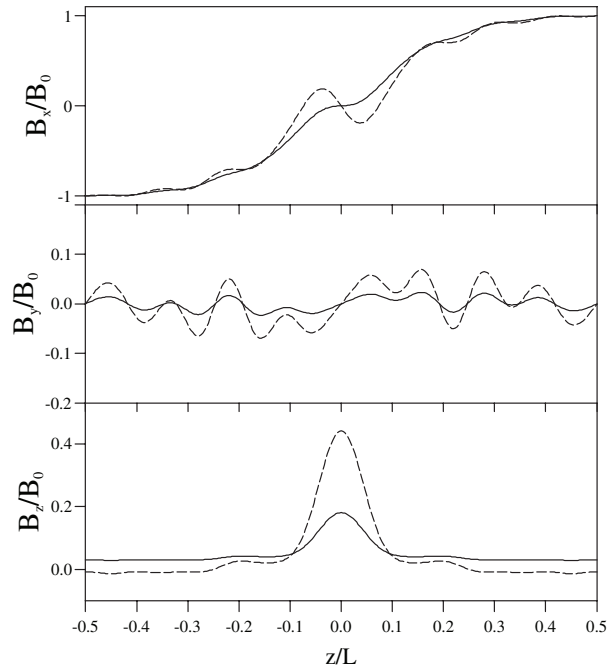
$$\delta B_\sigma(\mathbf{k}) = \frac{C}{(k_x^2 l_x^2 + k_y^2 l_y^2 + k_z^2 l_z^2 + 1)^{\alpha/4+1/2}},$$

where  $C$  is a normalization constant and  $l_x$ ,  $l_y$  and  $l_z$  are the turbulence correlation lengths in the  $x$ ,  $y$  and  $z$  directions, respectively. The spectral index  $\alpha$  for the near-Earth's magnetotail is chosen as  $\alpha = 2.3$  (e.g. *Zimbardo et al., 2010*). The correlation lengths are fixed in terms of the thickness of simulation box and, as  $l_x = l_y = 0.25L$  and  $l_z = 0.05L$ , in order to mimic the geometry of the magnetotail (i.e.  $l_z \ll l_x, l_y$  and  $l_x \sim l_y$ ).

In some cases the magnetic fluctuations can be interpreted as tearing mode turbulence. Streaming instabilities, like the kink-drift instability, have recently received considerable attention, too. For the present study, the fluctuating field components have the tearing and sausage mode parity with respect to the  $z$  direction, that is  $\delta B_z$  is even in  $z$ , i.e.,  $\delta B_z(x, y, z) = \delta B_z(x, y, -z)$ , and  $\delta B_x$  and  $\delta B_y$  are odd in  $z$ , e.g.,  $\delta B_x(x, y, z) = -\delta B_x(x, y, -z)$ . This corresponds to the formation of magnetic islands during the growth of reconnection instabilities in the current sheet (details of how the parity rules determine some specific relations between the random phases are given in Appendix A.1). This parity also corresponds to that of the oblique modes recently considered by *Lapenta et al. (2000)*. The ion dynamics in the presence of magnetic turbulence with kink-drift mode parity will be considered in a



(a) For  $x$ -profiles  $0 < x < 5L$ ,  $y = 0$ , and  $z = 0.1L$  (if  $z = 0$ ,  $B_x$  and  $B_y$  would be null).



(b) For  $z$ -profiles  $x = 0$ ,  $y = 0$ , and  $-0.5 < z/l < 0.5$ .

**Figure 1.6:** Sample  $x$ -profiles, Fig 1.6(a), and  $z$ -profiles, Fig 1.6(b), of the three magnetic field components, for  $b_n = 0.05$ , and  $\delta b = 0.1$  (solid line) and  $\delta b = 0.3$  (dashed line).

future work. For the runs presented here, the wave vector components are chosen on a grid such that  $k_i = 2\pi n_i/l_i$ ,  $i = x, y, z$ , where  $n_i$  are integers number identifying the wave modes, satisfying  $(n_x^2 + n_y^2 + n_z^2) < 144$ , and  $(n_x^2 + n_y^2) > 6$ . While the high wave number cutoff is dictated by computer memory requirements, the low wave number cutoff is introduced in order to have a well discretized representation of turbulence (e.g. [Pommois et al., 2007](#)).

Figure 1.5 shows the magnetic field structure in the quasi-neutral sheet for increasing values of the fluctuations level,  $\delta B/B_0$ . Hereinafter,  $\delta B = \sqrt{\langle \delta \mathbf{B} \cdot \delta \mathbf{B} \rangle}$ , with the average made over the simulation box. We also introduce  $\delta b = \delta B/B_0$  and  $b_n = B_n/B_0$ . We note that the elegant method of plotting the contours of the magnetic flux function to obtain the magnetic structure is not viable in the case of a 3D configuration. In the present case, field lines are traced integrating the field line equations, starting both at  $z = \pm 0.5 L$ , to have the "parabolic" field lines, and at  $z = 0$ , to have the magnetic islands. The middle and bottom panels of Figure 1.5 show magnetic islands formation when  $\delta B \neq 0$ . Note, however, that the magnetic topology at the boundaries of the simulation box is determined by  $B_n$ , that is the flux tubes, which are parabolic when  $\delta b = 0$ , are distorted but still closed when  $\delta b \neq 0$ .

Figure 1.6(a) and Figure 1.6(b) show the horizontal and the vertical profiles, respectively, of the various magnetic field components for  $\delta b = 0.1 - 0.3$  and  $b_n = 0.05$ . Such "cuts" of the model magnetic field mimic the signal which would be observed by a spacecraft crossing the current sheet in the corresponding directions. Of course, much finer structures are found in the data because the actual turbulence has a much longer spectrum than that which can be represented numerically. The relevant parity in  $z$  is clearly seen in Figure 1.6(b). In particular, the fluctuating component  $\delta B_x$  has the same parity of  $B_{0x}$ , which also contributes to the plot of  $B_x$ . In the lower panel, it can be seen that  $B_z$  is positive for  $z \sim 0$  and negative (positive but less than  $B_n$ ) for  $z \sim \pm 0.5L$  for  $\delta b = 0.3$  ( $\delta b = 0.1$ ). In both cases  $B_n = 0.05B_0$  is present. Of course, the details of Figure 1.6(a) and Figure 1.6(b) would be modified by changing the position of the line along which the fields are evaluated.

## 1.4 Test particle simulations

In addition to the above magnetic field configuration, we consider a constant cross tail electric field in the dawn to dusk direction,  $\mathbf{E}_y = E_y \mathbf{e}_y$ , that cannot be removed by transforming to the de Hoffman-Teller frame for the presence of three-dimensional magnetic fluctuations. Since we are considering static magnetic perturbations, the fluctuating electric field is not included in the present runs. We may show that the fluctuating electric field, produced by realistic magnetic perturbations, has a minor impact on particle dynamics, because the ratio  $v_A/v_{th} \ll 1$ . Indeed, as was demonstrated by [Veltri et al. \(1998\)](#), the ratio of the electric component of the Lorentz force over the magnetic one can be estimated as  $v_\phi/v$ , where  $v$  is the particle

| Physical quantity | Normalization           | Typic value            |
|-------------------|-------------------------|------------------------|
| Length            | $L$                     | 4000 km                |
| Time              | $\Omega_{0i}^{-1}$      | 2 s                    |
| Electric field    | $E_0$                   | 0.2 mV/m               |
| Magnetic field    | $B_0$                   | 20 nT                  |
| Current density   | $B_0/\mu_0 L$           | 4000 nA/m <sup>2</sup> |
| Velocity          | $V_E = cE_0/B_0$        | 10 km/s                |
| Temperature       | $m_p V_E^2/k_B$         | $1.2 \times 10^4$ K    |
| Ion density       | $n^* = cB_0/4\pi eLV_E$ | $0.5 \text{ cm}^{-3}$  |

**Table 1.1:** Normalization quantities.

velocity and  $v_\phi$  is the phase velocity of magnetic oscillations. Very few studies have been done to date for the identification of the eigenmode velocity in the neutral sheet, so it is reasonable to assume that  $v_\phi$  is close to the Alfvén velocity,  $v_A$ , in the center of the current sheet given by  $v_{An} \simeq B_n/\sqrt{4\pi\rho_m}$ , where  $\rho_m$  is the mass density. This yields  $v_\phi \sim 20 - 30$  km/s for  $B_n = 1 - 2$  nT, which is considerably less than the ion thermal velocity. However, even for the "slow" particles with  $v \leq 30$  km/s the overall effect on acceleration of the constant dawn-dusk electric field,  $E_y$ , will be more pronounced than the average, diffusive-type acceleration due to the fluctuating electric fields,  $\delta E$ , which have a random distribution of phases. Of course, in the case of monochromatic wave packets, such waves could provide strong acceleration to a small group of resonant particles with  $v \simeq v_\phi$ , see for example [Vainshtein et al. \(1999\)](#), but this case is now beyond our consideration. A study of time dependent fluctuations and the associated energization has been carried out by [Greco et al. \(2009\)](#); [Perri et al. \(2009\)](#). Instead, in this work we are interested in studying the particles dynamic and its role in the formation of the double current layer, rather than the acceleration mechanism to which these particles could be subject.

The equations of motion for ions is:

$$m_i \frac{d\mathbf{v}}{dt} = e \left( \mathbf{E} + \mathbf{v} \times \frac{\mathbf{B}}{c} \right); \quad (1.4)$$

this can be written in a dimensionless form by normalizing all length scales to the unit length  $L$ , velocities to electric drift velocity  $V_E = cE_y/B_0$ , magnetic and electric fields to  $B_0$  and  $E_y$ , respectively, and time to ion gyrofrequency  $\Omega_{0i} = eB_0/m_i c$ . In [Table 3.1](#), normalizations and typical values of the physical quantities, inferred from observations ([Runov et al., 2006](#); [Wygant et al., 2005](#); [Kistler et al., 2005](#)), are shown. For brevity, we introduce  $\delta b_j = \delta B_j/B_0$  and  $b_{0x} = B_{0x}/B_0$ . The

dimensionless equations of motion for particles now are:

$$\frac{dv_x}{dt} = v_y(b_n + \delta b_z) - v_z \delta b_y \quad (1.5)$$

$$\frac{dv_y}{dt} = -v_x(b_n + \delta b_z) + v_z(b_{0x} + \delta b_x) + 1 \quad (1.6)$$

$$\frac{dv_z}{dt} = v_x \delta b_y - v_y(b_{0x} + \delta b_x) \quad (1.7)$$

$$(1.8)$$

We consider that the source of the particles, that are entering the current sheet from the lobes at  $z = \pm 0.5L$ , is located somewhere in the magnetospheric mantle. The relatively cold ion distribution in the mantle magnetic field can be described as a shifted Maxwellian (e.g., [Ashour-Abdalla et al., 1994](#)):

$$f(v_{\parallel}, v_{\perp}) = \left(\sqrt{2\pi}v_{th}^3\right)^{-1} \exp\left(-\frac{(v_{\parallel} - u)^2 + v_{\perp}^2}{2v_{th}^2}\right), \quad (1.9)$$

where  $u$  is the streaming velocity along the unperturbed magnetic field and  $v_{th}$  is the thermal velocity. In the present simulation we assume  $b_n = 0.1$  for the normal magnetic field. Typically, 500000 particles are injected for each run with temperature  $T_i = 0.5$  keV, in agreement with the values observed in the magnetospheric lobes. The corresponding ion injection velocities are  $v_{th}(O^+) = 56$  km/s and  $v_{th}(H^+) = 224$  km/s ([Vaisberg et al., 1996](#)). Besides, we assume  $u = v_{th}$  for both species. We require that particles are injected with random velocity components in such a way to reproduce a distribution function given by Eq. 1.9. Consequently, the flux of particles crossing the simulation box through the surfaces at  $z = \pm 0.5L$  has to be proportional to  $F(v_x, v_y, v_z) \propto v_z f(v_{\parallel}, v_{\perp})$ . The details of the injection scheme in velocity space are given in Appendix A.2. Note that, because of the  $\mathbf{E} \times \mathbf{B}$  drift, the injected particles will reach the neutral sheet even in the case  $B_n = 0$  ([Alfvén, 1968](#); [Veltri et al., 1998](#)).

## 1.5 Numerical Results

In Figure 1.7, we show the projection on the  $yz$  plane of four sample trajectories of  $H^+$  and  $O^+$  ions, for different values of magnetic fluctuations,  $\delta b$ . The corresponding values of the adiabaticity parameter  $k$  ([Büchner & Zelenyi, 1989](#)), see Eq. 1.1, are  $k_p \simeq 0.09$  and  $k_{O^+} \simeq 0.04$ , so that ion motion in the quasi-neutral sheet is in the quasi-adiabatic regime characterized by  $k \ll 1$ , as expected for ions in the magnetotail thin current sheet (see also the proton trajectory, red line, in Figure 1.8). Once entered in the simulation box, in total absence of magnetic fluctuations (panel (A)), both types of particles move toward the central region,  $z = 0$ , following the magnetic field lines, while being subjected to the  $(\mathbf{E} \times \mathbf{B})$  drift. Inside of the quasi-neutral sheet, particles begin to perform the typical meandering orbits, under the action of the unperturbed magnetic field, while being accelerated by the electric

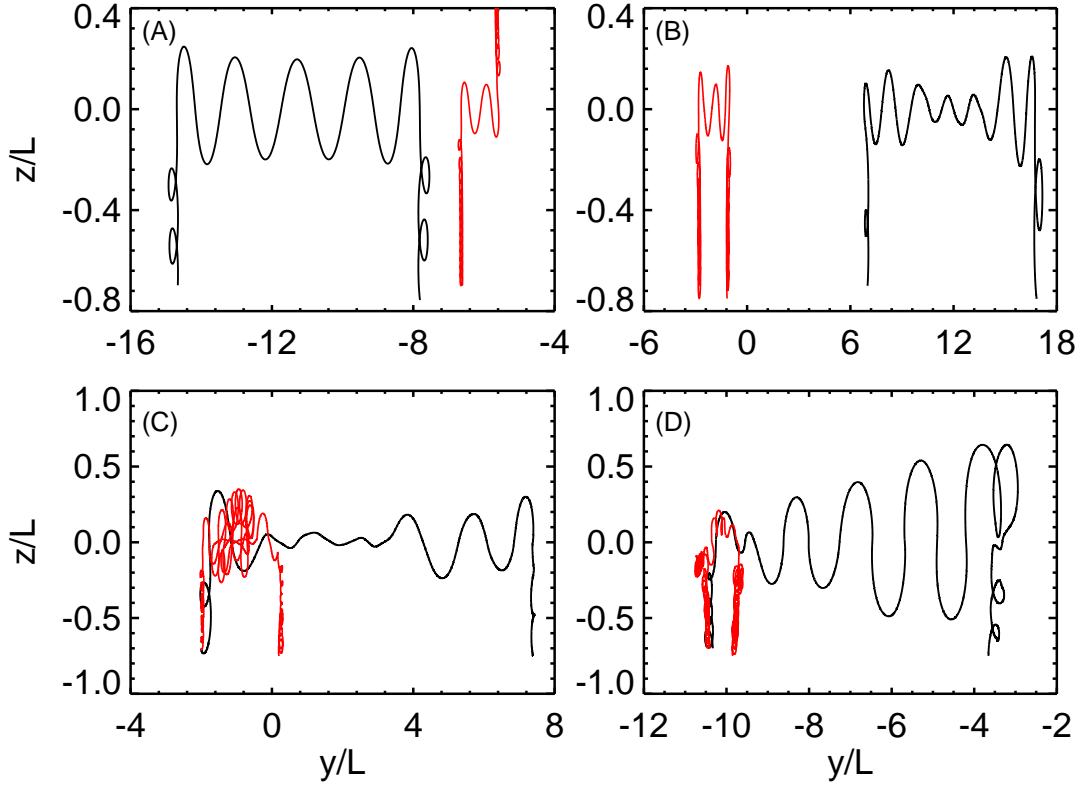


**Figure 1.7:** Projection on the plane of four sample trajectories of  $O^+$  ions (black line) and protons (red line) for  $b_n = 0.1$ ,  $E_y = 1E_0$  and  $\delta b = 0$  (panel (A)),  $\delta b = 0.1$  (panel (B)),  $\delta b = 0.2$  (panel (C)),  $\delta b = 0.6$  (panel (D)).

field,  $E_y$ . It is clear that  $O^+$  has larger Larmor radius than protons of the same energy and they can carry a large fraction of the current away from the center,  $z = 0$ . The non-zero  $B_n$  plays the role of a guiding channel for particles and causes them to exit the quasi-neutral sheet in the  $z$  direction (*Speiser, 1965*). Typically particles, after traversing variable distances in  $y$ , stop meandering and travel towards the lobes with larger Larmor radius, since they gained energy being accelerated by  $E_y$  (this effect is more apparent in the panels B-D). Increasing the values of magnetic fluctuations,  $\delta b$ , (panels (B), (C) and (D)), the performed orbits are perturbed and the trajectories become more intricate, especially for  $H^+$  ions (see the blow up in Figure 1.8). In the regions of meandering motion, different deflections are observed, which slow down the motion along  $y$  and make the trajectory more tangled, although this effect is more evident for protons. Starting from the same initial conditions, the  $O^+$  ions interact less with the magnetic turbulence than the protons  $H^+$ , because of their greater Larmor radius: for  $T = 0.5$  keV and for  $B = 0.1B_0$  (e.g. in the neutral plane),  $\rho(H^+) \simeq 1130$  km and  $\rho(O^+) \simeq 4600$  km. The turbulence characteristic lengths are  $\lambda_{max} = L/k_{min} = 4000$  km and  $\lambda_{min} = L/k_{max} = 333$  km, where  $k_{max} = 12$  and  $k_{min} = 1$  are the maximum and minimum wave number in each

direction, respectively. The  $O^+$  ions are not influenced by the magnetic turbulence so much as protons; besides oxygen ions are able to transport current out of the neutral sheet, because of the performed orbits amplitude. A similar difference in the proton and oxygen interaction with magnetic turbulence was reported by *Taktakishvili et al. (2007)*, with regard to plasma transport across the magnetopause current sheet.

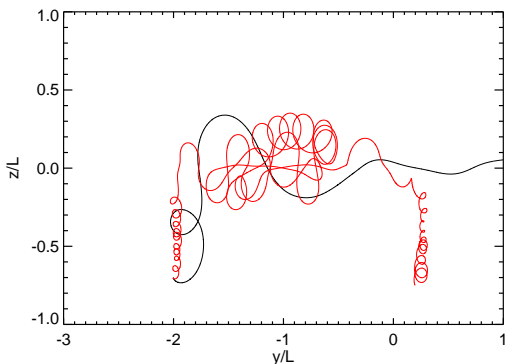
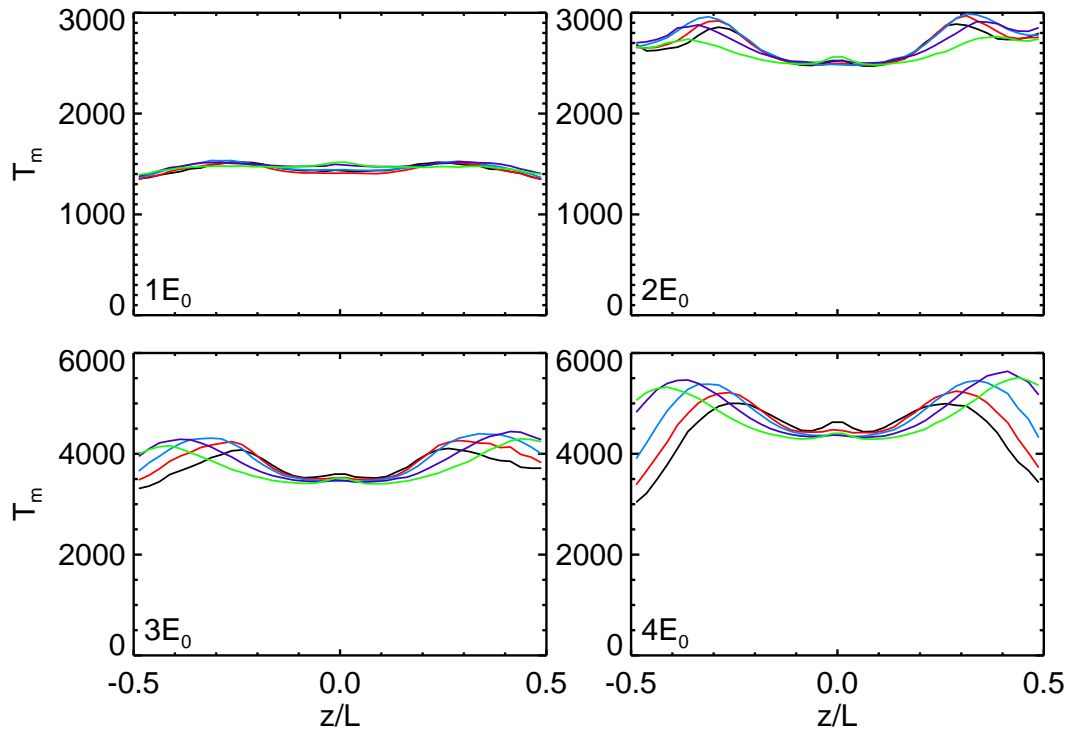


**Figure 1.8:** Blow up of  $O^+$  ions (black line) and protons (red line) trajectories for  $b_n = 0.1$ ,  $E_y = 1E_0$  and  $\delta b = 0.2$ .

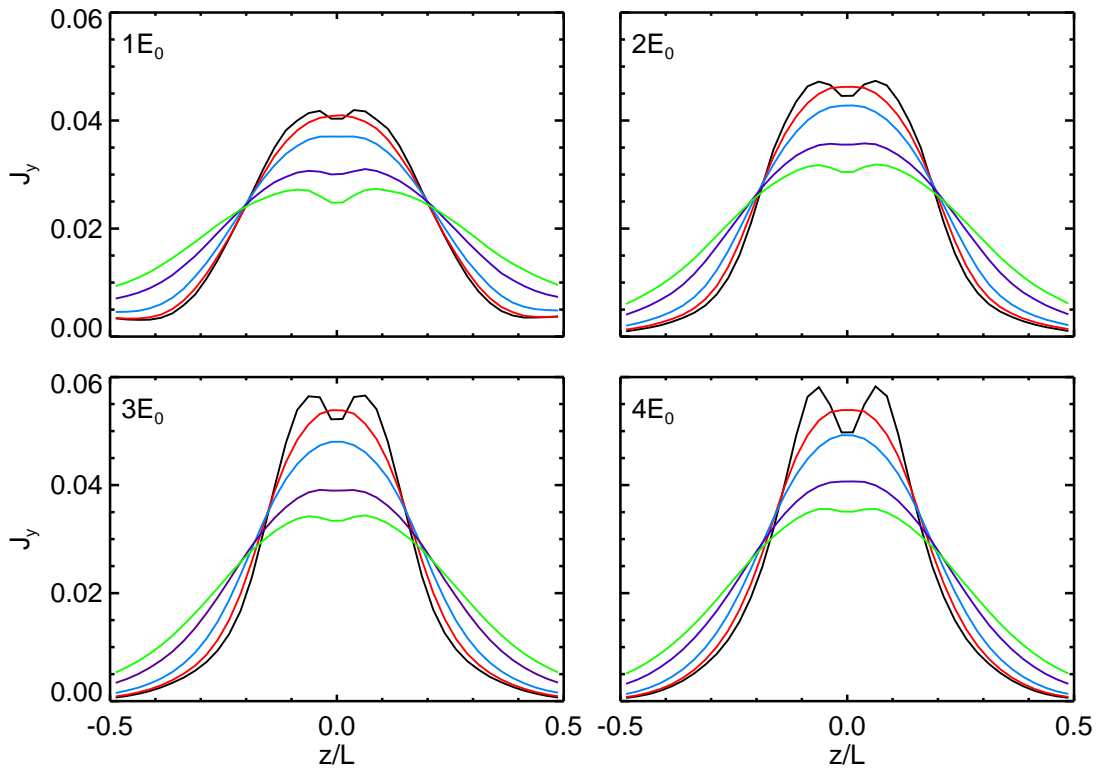
In order to gain understanding in the ion dynamics, we inject many particles in the simulation box and numerically integrate their equation of motion. Then, we compute the distribution function moments as density,  $n$ , current density,  $\mathbf{j}$  and temperature,  $T$ , on a three-dimensional grid with 1 grid point in  $x$  (many grid points in  $x$  could be used; however for the present runs we set this to 1, since  $x$  is a statistically ignorable coordinate in our model), 601 in  $y$  and 40 in  $z$ . Then, the distribution function moments have been averaged over  $y$ , the dependence on which is usually weak, to show the characteristic dependence on the  $z$  coordinate. In a test particle simulation the normalization for the number density is, to good extent, arbitrary. Here, it is based on the consideration that the ion current,  $I_y$ , has to be strong enough to reproduce the unperturbed magnetic field,  $B_{0x}(z)$ , introduced in our model. Indeed, Ampere's law leads to  $2B_0L_x = 4\pi I_y/c$ , with  $I_y = \int j_y dx dz$  the total current across a section of the current sheet of length  $L_x$ . On the other hand, velocity is expressed in units of  $V_E$ , so that the normalization for density is obtained an  $n^* = I_y/[e \int V_y dx dz]$ , with  $I_y$  constant for all the runs (this implies that, when the average value of  $V_y$  is large, the density is low).

In Figures 1.9(a) and 1.9(b), we report the vertical profiles of oxygen temperature,  $T$ , and current density,  $J_y$ , for different values of electric field,  $E_y = (1, 2, 3, 4)E_0$  (*Cattell and Mozer, 1982*), magnetic fluctuations,  $\delta b = 0.0$  (black line), 0.1 (red line), 0.2 (blue line), 0.4 (purple line), 0.6 (green line) and for  $b_n = 0.1$ , which corresponds to a variety of observations in the near-Earth's magnetotail. In Figures 1.10(a) and 1.10(b), we show the vertical profiles of proton temperature,  $T$ , and current density,  $J_y$ , for  $E_y = (1, 2, 3, 4)E_0$ ,  $b_n = 0.1$  and only for two values of the magnetic fluctuations,  $\delta b = 0.0$  (black line), 0.6 (green line) (results for more values of  $\delta b$  have been given by *Greco et al., 2002*). Given the abundance of previous work on protons, we restricted to show for this species only runs in which the oxygen shows a bifurcated current sheet, to be able to get the total current. The oxygen temperature in Figure 1.9(a) increases with the electric field, but there is no clear influence of magnetic fluctuations on heating. Indeed, in each panel, different color lines are at same level. A different situation arises with protons. In this case, turbulence succeeds in scrambling the ordered velocity gained because of



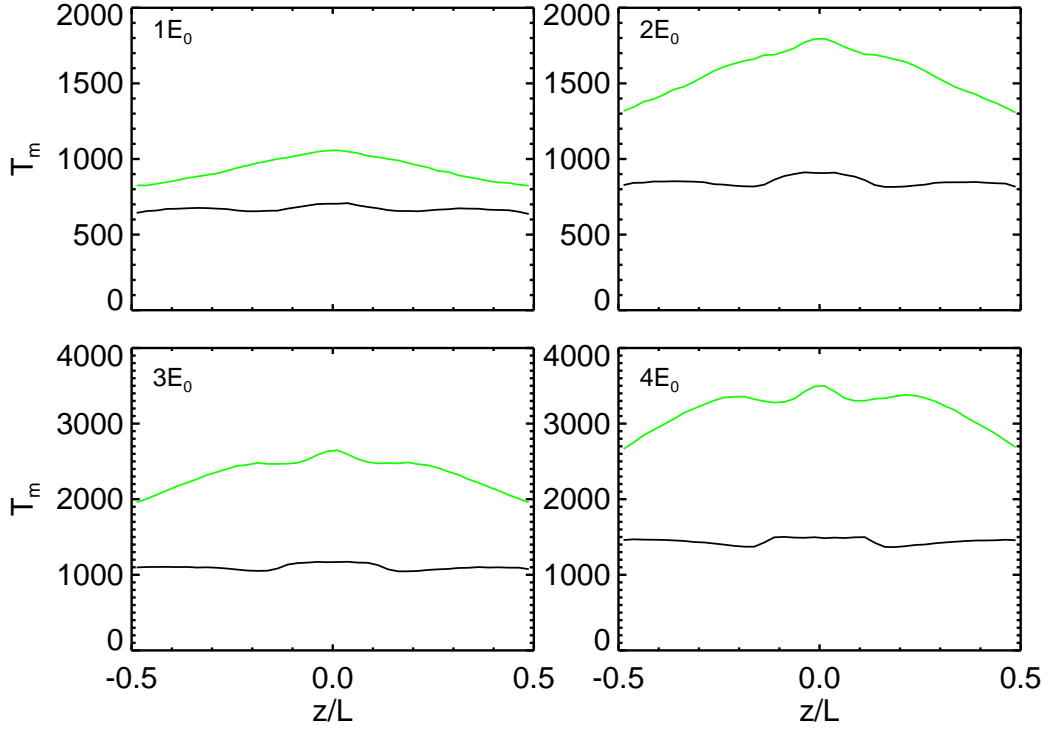
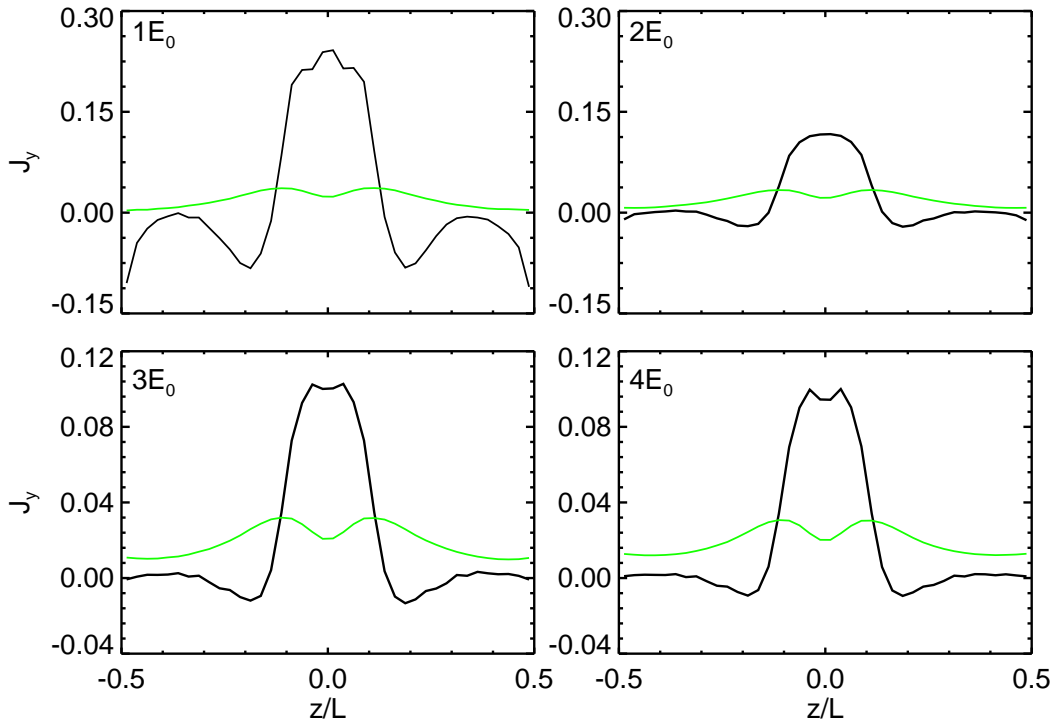


(a) O<sup>+</sup> ion temperature in units of  $m_p V_E^2 / k_B$ .



(b) O<sup>+</sup> ions current density

**Figure 1.9:** Vertical profiles for O<sup>+</sup> ions temperature, Figure 1.9(a), and current density, Figure 1.9(b), for  $E_y = (1, 2, 3, 4)E_0$  and  $b_n = 0.1$ . Here  $\delta b = 0.0$  (black line),  $\delta b = 0.1$  (red line) e  $\delta b = 0.2$  (blue line),  $\delta b = 0.4$  (purple line),  $\delta b = 0.6$  (green line).

(a)  $H^+$  ion temperature in units of  $m_p V_E^2 / k_B$ .(b)  $H^+$  ions current density

**Figure 1.10:** Vertical profiles for  $H^+$  ion temperature, Figure 1.10(a), and current density, Figure 1.10(b), for  $E_y = (1, 2, 3, 4)E_0$  and  $b_n = 0.1$ . Here  $\delta b = 0.0$  (black line) and  $\delta b = 0.6$  (green line).

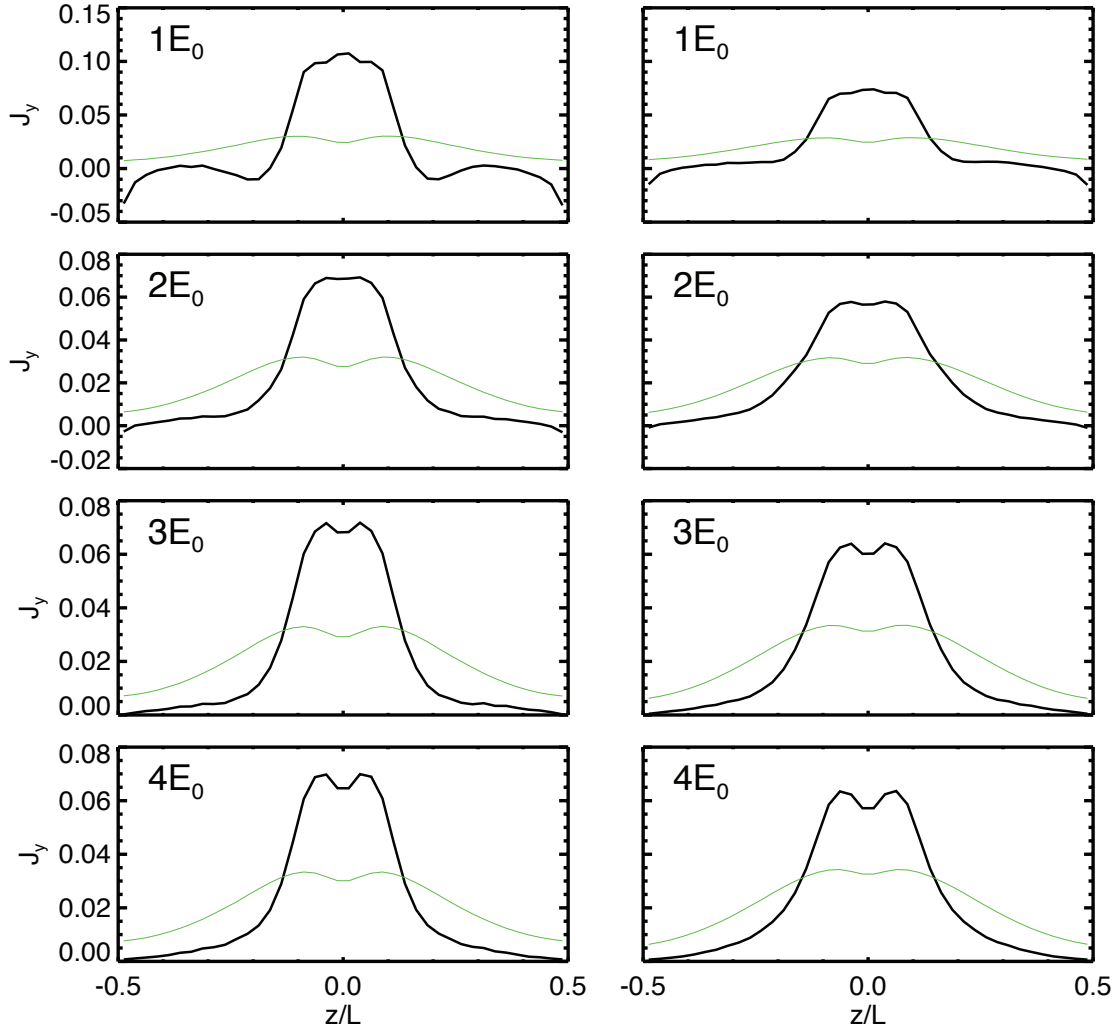


**Figure 1.11:** Total current density profiles for  $E_y = (1, 2, 3, 4)E_0$ ,  $b_n = 0.1$ . Here  $\delta b = 0.0$  (black line) and  $\delta b = 0.6$  (green line). The right column is for  $k = 5$ , the left one is for  $k = 2$  (see text).

$E_y$  into all directions, leading to an effective thermalization of the potential drop (*Greco et al., 2002*). The temperature profiles are larger in the center of the simulation box, where the energization from the electric field is favored and the magnetic fluctuations are stronger. Finally, oxygen and proton temperatures are of the same order ( $\sim 3 - 5$  keV) in the case of  $E_y = 4E_0$  and  $\delta b = 0.6$  (green line), in agreement with observations.

From Figure 1.9(b), it is clear that oxygen current profile is peaked and thin for zero to low fluctuation levels and becomes progressively broader as the fluctuation level is increased, while, at the same time, the maximum current value decreases. Indeed, an obvious effect of magnetic fluctuations is to reduce the bulk velocity (and current density), by inducing random motions, which spread all around single particle velocities. Besides, oxygen current density assumes values which grow with

the electric field. In the absence of magnetic fluctuations (black line), the oxygen ions are able to produce the double current layer, more and more evident when the electric field value grows. We argue that this is due to the velocity increase, caused by the electric field acceleration, so that the oxygen gyroradius and the effect of meandering orbits increases. The double peak disappears for  $\delta b = 0.05$  (not shown), 0.1 (red line), 0.2 (blue line), and appears again for levels  $\delta b \geq 0.4$  (purple and green line). The proton behavior is similar in some aspects and opposite in other ones. We can see from Figure 1.10(b) that the proton current density is larger than that of the oxygen one and, in contrast with the preceding case, it decreases with increasing electric field. This is due to the presence of the negative wings, that are more evident for small values of the electric field. Indeed, since the integral  $I_y$  of the ion current must remain constant, if the contribution of negative wings is big, the positive current must increase. A small hint of a double peak, in absence of magnetic fluctuations (black line), is present only for high values of electric field; instead, in presence of high magnetic fluctuations ( $\delta b = 0.6$  (green line)), protons support the formation of double layer for all  $E_y$  values, the bifurcation being more evident with increasing of the electric field. Moreover, negative values in the current density profiles are observed: they are the so-called diamagnetic currents, due to the magnetization current  $-c\nabla \times (P_\perp \frac{\mathbf{B}}{|\mathbf{B}|})$ , proportional to  $v_\perp^2$  (Zelenyi *et al.*, 2000). If the anisotropy is weak ( $v_\parallel \simeq v_\perp$ ), particles will give a substantial contribution to the formation of the diamagnetic wings; conversely, if there is a strong anisotropy ( $v_\parallel \gg v_\perp$ ), this contribution is small (Greco *et al.*, 2002; Zimbardo *et al.*, 2004).

In order to assess the oxygen contribution in the formation of a bifurcated current sheet in the total current density, we define the density ratio  $k = n(O^+)/n(H^+)$ . Then, we use two different  $k$  values, which are close to the real values observed in the near-Earth's magnetotail, when the oxygen is the most abundant species, to find the total current density. If  $k = 2$ ,  $J_{tot} = (2/3)J_{O^+} + (1/3)J_p$ ; if  $k = 5$ ,  $J_{tot} = (5/6)J_{O^+} + (1/6)J_p$ . As we can see in Figure 1.11, we found that the double peak is present in the total current density profiles, also when it is not present in the proton current density, that is for  $E_y = 2E_0$  and  $\delta b = 0$  (black line).

## 1.6 Discussion and Conclusions

Motivated by the many observations of ionospheric oxygen  $O^+$  in the Earth's magnetotail, we have considered the dynamics of protons and oxygen ions in the magnetotail current sheet, both in the presence and in the absence of magnetic turbulence. The ion motion has been studied by a test particle simulation, where particles are injected in a magnetic quasi-neutral sheet with superimposed magnetic fluctuations. Several runs have been made in order to understand the differences between the proton and the oxygen behavior, with emphasis of the possibility to obtain a bifurcated current sheet.

When protons are injected in the simulation box, a clear bifurcation of the current profile is obtained for turbulence levels  $\delta B/B_0 \geq 0.3$  (see also Greco *et al.*,

2002). Conversely, because of the non-adiabatic meandering motion, oxygen ions are able to support a bifurcated current sheet also in the absence of magnetic fluctuations. One of the most intriguing results concerning the oxygen behavior is the appearance of a double hump in the current profile both for the case of no magnetic turbulence and for relatively high levels of magnetic fluctuations. The explanation for this behavior can be found in the interaction between oxygen ions and the current sheet. Looking at Figure 1.12, which shows a typical oxygen trajectory for  $\delta b = 0$  and  $E_y = 1E_0$ , we can notice that the orbit is very smooth and that oxygen ion probes regions of the current sheet far from the neutral plane (because of its large Larmor radius) during its meandering motion along  $y$ . Therefore, this effect is essentially related to the non-adiabatic motion of oxygen ions. If a great number of this kind of trajectories are statistically added, there will be a concentration of particles with high  $v_y$  at those distances, obtaining a current density,  $J_y$ , which displays two peaks away from the neutral sheet (Delcourt and Belmont, 1998). The distance between the two peaks should be of the same order of the typical excursion in  $z$ , that is  $d \sim \sqrt{\rho_0 \lambda}$ , where  $\rho_0$  is the oxygen Larmor radius in the lobes magnetic field,  $B_0$  (Greco et al., 2002). From Figure 1.9(b), the separation between the two bumps for the case  $\delta b = 0$  (black lines) is  $\sim 0.2L = 800$  km. If we consider that a typical oxygen Larmor radius, in a magnetic field of 20 nT and with a temperature of 0.5 keV, is of the order of 800 km, we obtain for  $d$  a value of the order of 900 km, which is comparable with the distance between the two humps computed in the vertical profile of the current density. The influence of magnetic turbulence on  $J_y$  is twofold: on the one hand,

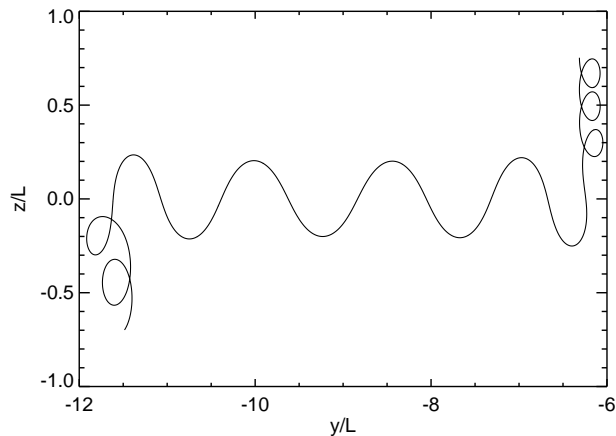


**Figure 1.12:** Projection on the plane of a sample trajectory of  $O^+$  ions for  $b_n = 0.1$ ,  $E_y = 1E_0$  and  $\delta b = 0$ .

relatively low levels of magnetic perturbations,  $\delta b < 0.4$ , cause the two peaks to decrease and smear because fluctuations scatter the oxygen ions around. On the other hand, when the level of magnetic perturbations is high enough, the presence of fluctuations bends the field lines also in  $y$  direction, and allows cross field motion away from the central plane.

Another important difference between the proton and the oxygen behavior is found in the temperature profiles. While the proton temperature grows with the magnetic turbulence level, the oxygen temperature does not. More precisely, the oxygen temperature appears to be uniformly large (that is, independently of  $\delta B/B_0$ ), in the sense that most of the potential drop, due to the electric field, is transformed into heat. This means that, thanks to their larger Larmor radius,  $O^+$  ions are able to

---

gain a large fraction of the potential drop. This is converted into disordered motion by the chaotic dynamics in the quasi-neutral sheet, while the influence of turbulence is evident mostly in the outer part of the simulation box, see Figure 1.9(a). Once again, the comparison of proton and oxygen dynamics shows that the former interact more with turbulence than the latter. To some degree, we can say that the turbulent fluctuations are averaged along the gyroorbit, a behavior which is also found in the studies of plasma transport in the presence of turbulence (e.g., *Zimbardo et al., 2006*; *Pommois et al., 1998*). Finally, when realistic ratios of oxygen to proton are assumed, it is found that a bifurcated current sheets is obtained even in absence of magnetic fluctuations. This suggests that the presence of oxygen ions as the main current carriers can help to explain the observations of bifurcated current sheets in the magnetotail. On the other hand, a complete description of the magnetotail current should take into account the electron contribution (e.g., *Greco et al., 2007*), as we plan to do in a future work.



# Theoretical background

---

## 2.1 Introduction

The present work concerns the study of charged particle magnetic moment conservation in presence of a single or few electromagnetic waves, as well as in presence of turbulent magnetic fields, with direct applications to the solar wind. From the particle orbit theory, for slow temporal and spatial magnetic field variations (i.e., if their characteristic length and time scales are greater than the particle orbit diameter and the time spent by a particle to execute one orbit, respectively), the magnetic moment, defined as  $\mu = v_{\perp}^2/B$ , averaged over the particle gyroperiod, is an adiabatic invariant and remains constant during particle motion. However, in presence of a well-developed magnetic turbulence,  $\mu$  might undergo rapid variations and in any case can no longer be expected to be constant. Of course, this fact could influence particle acceleration and could have a considerable implications in many astrophysical problems, such as coronal heating, cosmic rays transport and temperature anisotropies in the solar wind.

Theoretical attempts to describe the velocity space diffusion of charged particles in electromagnetic plasma turbulence have centered on quasilinear theory, QLT (*Kennel & Petschek, 1966; Hall & Sturrock, 1967; Lerche, 1968*). The basic assumption is that the turbulence level is sufficiently weak that plasma particles trajectories closely resemble those in the mean background magnetic field, i.e., without the addition of turbulence, in the intervals between wave-particle interactions that lead to velocity diffusion. Under these assumptions, it is possible to derive a diffusion equation in velocity space, that describes the temporal evolution of the lowest order velocity distribution. The diffusion coefficients depend on the spectral density and polarizations of the turbulent wave modes. In attempts to better understand the underlying wave-particle interactions for higher levels of turbulence, more dynamical approaches have been undertaken by *Karimabadi et al. (1990)*, *Ginet & Heineman (1990)*, *Karimabadi & Menyuk (1991)*, *Karimabadi et al. (1992)*. These authors explored single particle motion in intermediate amplitude wave fields, employing a perturbation expansion of the single particle Hamiltonian about the resonance point. If the wave electromagnetic field is sufficiently large and it is propagating obliquely to the background magnetic field, particle motion can become stochastic even in the presence of a single wave. Such stochasticity is fundamentally different from quasilinear theory. In the case of a single oblique wave, the source of stochasticity is nonlinear in nature: it is intrinsic to the resonance process and can be traced to the overlapping of adjacent primary resonances (*Karimabadi et al., 1990*). In quasi-



linear theory the phase space structure of the wave-particle resonance interaction is perturbed by extrinsic stochastic forces (*Lichtenberg & Lieberman, 1983*) in the form of randomly phased neighboring (in frequency and wavenumber space) plane waves. The timescales governing the onset of stochasticity in each case are different too. In the quasilinear theory this timescale is the autocorrelation time,  $\tau_{ac}$ , the typical time for an initial distribution of wave phases to phase mix to a uniform phase distribution. Instead, in the single wave case, the nonlinear mixing of orbits occurs on a timescale inversely proportional to the Kolmogorov entropy (whose inverse is deemed very large in quasilinear theory).

In order to reproduce and extend some of the result obtained by *Karimabadi et al. (1992)*, we started to study the interaction between ions and a single or few electromagnetic wave, in order to understand in this very simple case the limit for magnetic moment conservation. The dynamics of charged particles in resonance with parallel propagating electromagnetic waves are investigated numerically and compared with analytical results for the trapping width in velocity space,  $\Delta v_{\parallel}$ , and the bounce frequency,  $\omega_b$ , specialized for this simple case. In addition, we found that the magnetic moment and the pitch angle behaviors are related to each other and we wrote an analogous formula for the magnetic moment trapping width,  $\Delta\mu$ . Then, we studied the behavior of many particles interacting with a broad band slab spectrum. For this case we analyzed the diffusion coefficients and the distribution function of particles pitch angle and magnetic moment.

It is demonstrated how the understanding of the basic resonance phenomenon can lead to a better understanding of the validity regions of the quasilinear theory. It is shown, using analytical results for the bounce frequency,  $\omega_b$ , and trapping width in velocity space,  $\Delta v_{\parallel}$ , that the quasilinear diffusion coefficient can be written in a physically illuminating form. The concept of an effective trapping width in velocity space for the turbulence modified resonance structure is introduced. It is shown that this effective resonance width implies a condition on the density of wavemodes in Fourier space, in the vicinity of the resonant wavenumber. The implications of this condition for simulations incorporating discrete fields is discussed in detail and examples of simulations violating this condition are presented too. Other issues pertinent to the simulation of velocity diffusion in turbulent electromagnetic fields are discussed, paying attention to the discretization of the fields in Fourier and configuration space and the temporal discretization of the dynamical equations.

It is worthwhile noting that recent studies of velocity space scattering have frequently concentrated on the large amplitude strong turbulence case, beginning with the assumption that the system resides deeply within this regime, thus invalidating certain features quasilinear theory at the onset (*Matthaeus et al., 2003; Shalchi et al., 2004; Qin et al., 2006; Shalchi, 2009*). The present approach is very different, attempting to develop physical understanding of the breakdown of simple orbit theory in relatively simple models of magnetic fluctuations. Our motivation is again the potential for gaining insight into more realistic and complex cases that will not be explored in this context.

## 2.2 General theory for magnetic moment conservation

As we know from the classical particle motion theory, a particle with charge  $q$ , moving with a velocity  $\mathbf{v} = \mathbf{v}_{\parallel} + \mathbf{v}_{\perp}$  in a uniform magnetic field  $\mathbf{B}_0$ , experiences the Lorentz force,  $\mathbf{F}_L$ , perpendicular to both the particle velocity,  $\mathbf{v}$ , and the magnetic field  $\mathbf{B}_0$  (see Figure 2.1(a)), so that it does no work on the particle,

$$\mathbf{F}_L = \frac{q}{c}(\mathbf{v} \times \mathbf{B})$$

In a uniform magnetic field, the Lorentz force,  $\mathbf{F}_L$ , can change only the direction

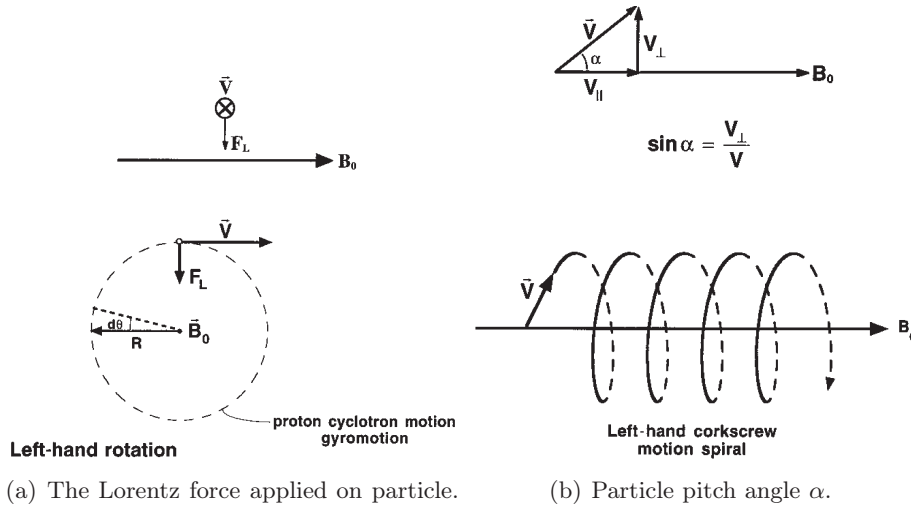


**Figure 2.1:** Motion of a positively charged particle in a uniform magnetic field  $\mathbf{B}_0$

of the particle velocity component,  $v_{\perp}$ , perpendicular to  $\mathbf{B}_0$ : the charged particle moves on a circle around the magnetic field,  $\mathbf{B}_0$ , while the parallel velocity component,  $v_{\parallel}$ , carries the particle along the magnetic field lines, creating an helical trajectory. The gyration radius or Larmor radius, is given by  $r_L = mv_{\perp}/qB_0$  and, for a given gyroradius, the corresponding gyration frequency, the well-known cyclotron frequency, is  $\Omega = qB_0/mc = v_{\perp}/r_L$ . Thus a positively charged particle, moving parallel to the mean magnetic field,  $\mathbf{B}_0$ , as shown in Figure 2.1, moves in a left-hand spiral motion along the magnetic field (see Figure 2.1(a)). This handedness is important for resonant interactions. The central field line around which the particle gyrates in Figure 2.1 is called its guiding center. If the field oscillates slowly, the particle will follow the guiding center accordingly.

The pitch angle  $\theta$  of a particle is defined as the angle between the direction of the magnetic field line and the particle's spiral trajectory (see Figure 2.1(b)). Sometimes is more convenient consider the cosine of pitch angle,  $\alpha$ , directly related

with the particle parallel velocity,

$$\theta = \arctan\left(\frac{v_{\perp}}{v_{\parallel}}\right) \quad \alpha = \cos\theta = \frac{v_{\parallel}}{|v_{tot}|}$$

In a uniform magnetic field, since there are no forces acting in the parallel direction, the particle moves unimpeded with a constant velocity,  $v_{\parallel}$ , along  $\mathbf{B}_0$ ; in addition, although the direction change, the magnitude of  $v_{\perp}$  remains unchanged, i.e., the pitch angle  $\theta$  is constant in a uniform magnetic field. The spiraling motion of the charge  $q$  represents an average current  $I = q/\tau_g$  around the particle orbit, where  $\tau_g$  is the period of one gyration about the line of force,  $\tau_g = 2\pi/\Omega$ . Since the area of the orbit is  $S = \pi r_L^2$ , the gyrotory motion has a magnetic moment,  $\mu$ , given by:

$$\mu = (I/c)S = \pi r_L^2 \frac{q\Omega}{2\pi} = \frac{mv_{\perp}^2}{2|\mathbf{B}|}, \quad (2.1)$$

where  $m$  is the particle mass,  $B$  is the magnetic field and  $v_{\perp}$  is the particle velocity perpendicular to the mean magnetic field. This definition is precise when all the parameters are constant. The magnetic flux through the particle orbit is directly proportional to  $\mu$ , since  $\Omega$  is directly proportional to  $B$ .

If the particle moves in a nonuniform slowly changing magnetic field, the rate of change of  $B$  is sufficiently small so that  $B$  remains practically constant during one gyration period,  $\tau_g$ , i.e., defining a time constant  $T$  by

$$\frac{1}{T} \sim \left| \frac{1}{B} \frac{\partial B}{\partial t} \right| \quad \text{and assuming that} \quad T \gg \tau_g$$

the magnetic moment is an adiabatic invariant of particle motion,

$$\left\langle \frac{d\mu}{dt} \right\rangle_{\tau_g} = 0 \longrightarrow \mu = \text{const}$$

Hereafter, when we refer to magnetic moment conservation, it is understated to mean the gyro-averaged quantity, unless stated otherwise.

### 2.2.1 Demonstration of $\mu$ conservation

Let us consider how  $\mu$  changes when  $\mathbf{B}$  changes with time, but is uniform throughout space. The change of  $\mathbf{B}$  will induce an electromotive force,  $\mathcal{E}$ , around the orbit of the particle. From Faraday's law we have:

$$\mathcal{E} = \oint \mathbf{E} \cdot d\mathbf{s} = - \int \frac{\partial \mathbf{B}}{\partial t} \cdot d\mathbf{S}, \quad (2.2)$$

where  $d\mathbf{s}$  is a line element around the path and  $d\mathbf{S}$  is an element of the surface enclosed by the path. The change of kinetic energy per unit time is the product of  $\mathcal{E}$  and the effective current  $I = q\Omega/2\pi$ . It is readily shown that  $I$  and  $\mathcal{E}$  are in the same direction, if  $B$  is increasing. Hence

$$\frac{d}{dt} \left( \frac{1}{2} m v_{\perp}^2 \right) = \frac{q\Omega}{2\pi} \pi r_L^2 \frac{dB}{dt} = \mu \frac{dB}{dt}. \quad (2.3)$$

The rate of change of  $\mu$  may be found from Eq. 2.1: on multiplication through by  $B$  and differentiation with respect to time we find:

$$\frac{d}{dt}(\mu B) = \frac{d}{dt} \left( \frac{1}{2} m v_{\perp}^2 \right) \quad (2.4)$$

Combination of Eq. 2.3 and Eq. 2.4 shows that  $d\mu/dt$  vanishes, a result valid only for non-relativistic energies. This results would be exact if the charge were distributed uniformly around its circle of gyration. Whether  $\mu$  tends to be constant depends on the rate at which  $B$  changes. It is obvious physically that if all the change in  $B$  occurs while the particle is moving over a small arc of its circle of gyration, the line integral of  $\mathcal{E}$  around the circle in Eq. 2.2 is irrelevant and  $d\mu/dt$  does not vanish. However, if we assume  $dB/dt \propto \omega B$  and solve the equations of motion to first order in  $\omega/\Omega$ , then  $d\mu/dt$  does in fact vanish.

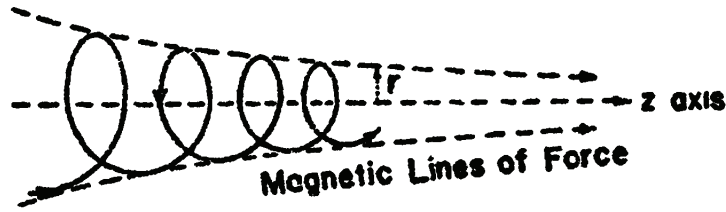


Figure 2.2: Motion of a charged particle in a converging lines of magnetic force.

Next we consider the change of  $\mu$  when  $\mathbf{B}$  varies along the particle path, but is constant with time at each point. Let us suppose that the gyrating particle is moving into a region of greater field. In such case, the lines of force will be convergent and the magnetic field will have a component  $B_r$  directed toward the line of force along which the guiding center is moving (see Figure 2.2). This component produces a retarding force in the direction of particle's motion. Following the original derivation made by Alfvén ([Alfvén, 1950](#)), we shall let the magnetic field in which particle is moving parallel to the  $z$  axis at the guiding center. In cylindrical coordinates  $r, \theta, z$ , the magnetic field is independent of  $\theta$ ; the condition  $\nabla \cdot \mathbf{B} = 0$  gives:

$$\frac{1}{r} \frac{\partial}{\partial r}(r B_r) + \frac{\partial B_z}{\partial z} = 0 \quad (2.5)$$

If we assume that  $\partial B_z / \partial z$  is constant over the cross section of particle's orbit and essentially equal to  $\partial B / \partial z$ , we may integrate Eq. 2.5 to find  $B_r = -r \partial B / 2 \partial z$ . Setting  $r$  equal to the radius of gyration  $r_L$  and taking the  $z$  component of the particle equation of motion, ( $m d\mathbf{v} / dt = \mathbf{v} \times \mathbf{B} / c$ ), we obtain with use of Eq. 2.1:

$$m \frac{dv_{\parallel}}{dt} = -\mu \nabla_{\parallel} B \quad (2.6)$$

where the symbol  $\nabla_{\parallel}$  denotes the component of the gradient in the direction of  $\mathbf{B}$ . Eq. 2.6 is exactly what one would anticipate for a diamagnetic particle. From

Eq. 2.6 and the conservation of the kinetic energy, we can deduce the variation of  $\mu$  with position. On multiplication of Eq. 2.6 by  $v_{\parallel}$ , we obtain:

$$\frac{d}{dt} \left( \frac{1}{2} m v_{\parallel}^2 \right) = -\mu \frac{dB}{dt} \quad (2.7)$$

where  $d/dt$  represents the time derivative take along the path of the particle. By the conservation of energy and Eq. 2.1, we have

$$\frac{d}{dt} \left( \frac{1}{2} m v_{\parallel}^2 \right) = -\frac{d}{dt} \left( \frac{1}{2} m v_{\perp}^2 \right) = -\frac{d}{dt} (\mu B) \quad (2.8)$$

From Eq. 2.7 and Eq. 2.8 it follows again that  $\mu$  is a constant of the motion, a conclusion valid here for particles of relativistic energies too. Again, this result is approximate and does not hold if  $B$  changes markedly over a distance equal to the radius of gyration.

### 2.2.2 Cosequences of $\mu$ invariance

The adiabatic invariance of the magnetic moment requires that, as a particle moves into a stronger field region,  $m v_{\perp}^2/2$  must increase linearly with  $|B|$ . Since the magnetic force that acts on the charged particle does no work, particle's kinetic energy is exactly conserved in the absence of laboratory frame electric fields,  $\mathbf{E}$ . This means that as  $m v_{\perp}^2/2$  increases,  $m v_{\parallel}^2/2$  must decrease such that the sum of the two is a constant. We can also express magnetic moment in terms of particle's pitch angle:

$$\mu = \frac{v^2 \sin^2 \theta}{2B}$$

The magnetic moment invariance implies that the pitch angle,  $\theta$ , increases as the particle moves toward regions of higher magnetic fields and decreases as it moves toward regions of weaker field. If a strong magnetic field gradient exists, the particle can be "mirrored" or reversed in direction by the Lorentz force. The so-called *magnetic mirror* is the effect exhibited by charged particles spiraling into a converging magnetic field. Because of the magnetic moment conservation, higher magnetic field requires larger perpendicular velocities and, consequently, because of the energy conservation, smaller parallel velocities. If in a certain region of space the magnetic field lines are converging, the particle will move in a region of higher magnetic field and his parallel velocity can go to zero, causing the particle reflection or "mirroring". However, depending on the initial pitch angle, the parallel velocities at the highest magnetic field region could be also different from zero and this allows particle to exit the mirror. A particle in correspondence of the minimum  $B_0$  has a velocity  $v_0 = (v_{\parallel 0}, v_{\perp 0})$ ; in contrast, at the maximum,  $B_m$ , where the reflection occurs,  $v_m = (0, v_{m\perp})$ . Because of the energy and magnetic moment conservation, we have  $v_{m\perp}^2 = v_0^2$  and  $v_{\perp 0}^2/B_0 = v_{\perp m}^2/B_m = v_0^2/B_m$ . After some simple algebra and with the pitch angle definition, we can define the *loss-cone angle*,

$$\theta_c = \arcsin \left[ \left( \frac{B_0}{B_m} \right)^{1/2} \right]$$

The exact location at which this mirroring occurs depends only upon the initial pitch angle describing its helical path. Particles with  $\theta > \theta_c$  are trapped in the magnetic mirror; contrary, particles with  $\theta < \theta_c$  are in the loss cone. In this case particle can undergo pitch angle scattering not because of resonant processes but because of mirroring.

### 2.2.3 Poincaré invariant and adiabatic invariant

The constancy of magnetic moment comes from an exact invariant for Hamiltonian motion, the Poincaré invariant. However, it is important to say that Poincaré invariant involves many particles rather than single one. The point is that, because an ion hardly moves in phase space during one cycle, it can be simulated by a ring of ions arranged around the gyration orbit and the Poincaré constant associated with them leads to the magnetic moment conservation of a single ion.

The Poincaré invariant is defined following [Goldstein \(1980\)](#). Consider a closed circle of gyration about the guiding center of the ion and place a collection of ion, labelled by a parameter  $\lambda$ , about this circle. Each of these ions has the same  $v_\perp$  and  $v_\parallel$  as the ion they are simulating, but they differ from it in gyration angle. As these ions move, the integral over  $\lambda$ ,

$$P = \oint \mathbf{p} \cdot \frac{dq}{d\lambda} d\lambda \quad (2.9)$$

is invariant. In fact, if we differentiate this integral with respect to time making use of the Hamiltonian equations

$$\begin{aligned} \frac{dp}{dt} &= -\frac{dH}{dq} \\ \frac{dq}{dt} &= \frac{dH}{dp} \end{aligned}$$

for each particle of fixed  $\lambda$ , we find that the time derivative of the quantity  $P$ , based on this class of ion orbits, is zero.  $H$  is the Hamiltonian describing ion motion in presence of an electromagnetic field:

$$H = \frac{1}{2m} \left( \mathbf{p} - \frac{e\mathbf{A}}{c} \right)^2 + e\Phi, \quad (2.10)$$

where  $\mathbf{A}$  and  $\Phi$  are the vector potential and the electrostatic potential, respectively, and  $\mathbf{p} = m(v - eA/mc)$  is the canonical momentum of the particle. Let us evaluate  $P$ :

$$\begin{aligned} P &= \int p \frac{dq}{d\lambda} d\lambda = \int m v_\perp dq_\perp - \frac{e}{c} \int A dq_\perp \\ &= 2\pi m v_\perp r_L - \frac{e}{c} B (\pi r_L^2) = \left( 2\pi \frac{mc}{e} \right) \mu \end{aligned}$$

where the Stoke's theorem is used to reduce the second integral to the magnetic flux. Because the Poincaré invariant is the product between  $\mu$  and a constant term,  $\mu$  is a constant.

By assumption, the nonuniform magnetic field is always nearly constant over a gyroorbit. The ions representing  $P$  can be chosen to be in the same place as the ion would be if it were slightly delayed in its orbit and the resultant position projected onto the circle perpendicular to  $\mathbf{B}$ . There is no guarantee that the ring of ions will form an exact circle, as the slight inhomogeneity of the field will produce a slight distortion of the circle, so, in this case, there will be a first-order difference between  $P$  and  $(2\pi mc/e)$  times  $mv_{\perp}^2/2B$ . The point is that this description is valid only if the distortion is small, so  $\mu$  always differs by less than a first-order quantity from a constant.

### 2.3 From the guiding center approximation to the quasi-linear theory

Division of particle motion into the motion of the guiding center and the gyromotion around it, is called guiding center approximation (*Rossi & Olbert, 1970*). When analyzing charged particle motion in nonuniform electromagnetic fields, we may neglect the rapid and, relatively, uninteresting gyromotion and focus, instead, on the far slower motion of the guiding centre. Clearly, what we need to do in order to achieve this goal is to somehow average the equation of motion over gyrophase, so as to obtain a reduced equation of motion for the guiding centre. This means that one is not interested in the actual trajectory of the particle, but rather on the trajectory of its guiding center,  $r_{GC}(t)$ . This approximation is valid if the lowest scale lengths of the electromagnetic fields are much larger than the Larmor radius of the particles, i.e., when particle magnetic moment is a constant of motion. This kind of description for particle motion in nonuniform magnetic field is also useful from the point of view of numerical simulations. Indeed, direct simulations of kinetic equations (Vlasov, Boltzmann) with large magnetic field require the numerical resolution of small position and time scales induced by the gyration along the magnetic field. The guiding center approximation, as well as the gyrokinetic approximation, are approximate models, well describing particle motion in presence of strong magnetic field, i.e.,  $r_L \rightarrow 0$ .

The guiding center motion can be broken into the components parallel and perpendicular to the local magnetic field. In the non-relativistic case, the equation of motion parallel to the magnetic field reads

$$\frac{dp_{\parallel}}{dt} = -\mu\nabla_{\parallel}B + qE_{\parallel}, \quad (2.11)$$

where  $\mu$  is the particle magnetic moment and  $\nabla_{\parallel} = (\mathbf{B}/B)\cdot\nabla$  is the spatial derivative in the field direction.

In the perpendicular direction, the guiding center is drifting with a velocity

$$v_D = \frac{\mathbf{F} \times \mathbf{B}}{qB^2}, \quad (2.12)$$

where  $\mathbf{F} = q\mathbf{E} - \mu\nabla B - (mv_{\parallel}^2)\nabla_{\parallel}\mathbf{B}$  is the total force acting on the guiding center, averaged over a gyroperiod, in the (non-inertial) frame co-moving with the guiding center.

We can now easily understand the motion of a charged particle as it moves through slowly varying electric and magnetic fields. The guiding centre behaves exactly like a particle with a conserved magnetic moment,  $\mu$ , which is always aligned with the magnetic field.

To arrive at the guiding center approximation, we made the assumption that the scale length of the fields is much larger than the Larmor radius of the particle. Apart from some localized regions, which can be treated separately in a simulation, this assumption is typically valid in an astrophysical plasma, apart from one component of the electromagnetic field: the turbulence. According to observations, turbulent magnetic fluctuations,  $\delta\mathbf{B}$ , at all scales, from global to kinetic, permeate the space plasmas in practically all environments. Thus, it would seem invalid to resort to guiding center theory. However, it can be shown rather easily that, if the amplitude of the magnetic fluctuations at a given time scale is clearly lower than the mean magnetic field (averaged over the time scale of the fluctuation), a perturbation approach called the quasilinear approximation is applicable (*Jokipii, 1966; Urch, 1977; Jones et al., 1998*). Then, the guiding center reaction to the fluctuations turns out to be a resonant one, so that only fluctuations fulfilling certain resonance conditions contribute to the motion of the particle. Thus, the random turbulent fluctuations of the electromagnetic field cause scattering of the charged particle, which can be modeled with an additional, stochastic term in the particle equation motion. Solving such stochastic differential equations of guiding center motion is then the final task of the modeler of particle acceleration in an astrophysical plasma.

## 2.4 Overview on wave-particle interaction

In space plasma the collision time between charged particles is generally very long in comparison with the characteristic time scale of the system, namely, the inverse of the plasma frequency or cyclotron frequencies and, therefore, plasma can be treated as collisionless. MHD time scales are typically much longer than this, but the collision time in the solar wind is usually much longer still. This would imply that there is virtually no dissipation in space plasmas, as particle-particle collisions are infrequent. This statement is correct provided that there are no wave-particle interactions. The presence of waves in collisionless plasma can introduce finite dissipation in the system: charged particles are scattered by the wave fields, changing their momenta and energies through this process.

Charged particles interacting with weak plasma turbulence, viewed as a field of waves, diffuse in velocity space, i.e., the variance  $\langle(\Delta\alpha)^2\rangle(t)$  increases, in the case of normal diffusion, linearly in time for times exceeding the autocorrelation time,  $\tau_{ac}$ , of the fields. In the expression the angle brackets  $\langle\cdots\rangle$  denote the ensemble average. The autocorrelation time is defined in (e.g. *Karimabadi et al., 1992*), as



$\tau_{ac} = 1/|\Delta(\omega - k_{\parallel}v_{\parallel})|$ . From the particle's point of view, it is the time for any initially smooth initial distribution of wave phases to relax to a uniform phase distribution through dispersion. Alternatively, it can be interpreted as the reciprocal of the spread in Doppler shifted wave frequencies in a frame moving with velocity,  $v_{\parallel}$ , parallel to  $\mathbf{B}_0$ .

The systematic treatment of the transport of charged particles in disordered magnetic fields has been the subject of an extensive amount of work (*Jokipii, 1966; Hall & Sturrock, 1967; Urch, 1977; Schlickeiser, 1989; Jones et al., 1998; Giacalone & Jokipii, 1999; Minnie et al., 2009*). Typically one derives a Fokker-Planck equation for the time evolution of the particle distribution function by a method that is commonly referred to as the *quasilinear theory* (QLT). One of the primary assumptions of this theory is that between the velocity increments, arising from wave-particle resonant interactions, particle dynamics are adequately modelled by their helical trajectories in the mean or zeroth order field, i.e., their unperturbed trajectories. This assumption can only hold on timescales (in the periods between such nonlinear interactions) during which nonlinear effects may be considered to be relatively unimportant. Thus, the typical quasilinear timescale,  $\tau_{ac}$ , and the timescale for the onset of nonlinear orbit effects,  $\tau_{nl}$ , must be well-separated (cf. *Weinstock, 1969; Davidson, 1972*):

$$\tau_{ac} \ll \tau_{nl} \sim \frac{1}{\omega_b}, \quad (2.13)$$

where  $\omega_b$  is the bounce frequency. This means that the turbulent spectrum should be broad enough that the typical timescale for a charged particle to interact with a resonant wave-packet must be much less than its typical bounce time,  $\tau_b = 2\pi/\omega_b$ , in a monochromatic wave at the characteristic wavenumber and frequency of the wave-packet. The bounce time,  $\omega_b$ , for a particle in resonance with an electromagnetic wave is proportional to its oscillation period in the pseudo potential well governing the resonant wave-particle interaction. Frequently this interaction can be approximated by an Hamiltonian pendulum in the vicinity of the resonance point (e.g., *Karimabadi et al., 1990*).

Under these assumptions energy exchange between waves and particles occurs only at discrete resonances:

$$\omega - k_{\parallel}v_{\parallel} = n\Omega, \quad (2.14)$$

where  $\omega$  is the wave frequency,  $k_{\parallel}$  and  $v_{\parallel}$  are the wavevector and the particle velocity along the mean magnetic field,  $B_0$ , respectively, and  $\Omega = qB/mc$  is the particle gyrofrequency.

Depending on the value that the integer  $n$  assumes, we can distinguish between two different kind of resonances: the  $n = 0$  is the so-called Landau resonance (see Section 2.4.1); the  $n = \pm 1, \pm 2, \dots$  are the cyclotron resonances (see Section 2.4.2). If  $n = 0$ , resonance occurs when  $\omega = k_{\parallel}v_{\parallel}$ , so particles *surf* along the wave. *Landau, (1946)* showed that plasma waves in unmagnetized collisionless plasma suffer damping due to wave-particle interactions, or *Landau damping*. Instead, if a particle

is moving in a perpendicular wave field in presence of a strong magnetic field,  $\mathbf{B}_0 = B_0 \mathbf{e}_z$ , it will interact strongly with the wave when its streaming velocity is such that the particle senses the Doppler-shifted wave at its cyclotron frequency or its harmonics, under the assumed steady conditions. The particle response to the perturbation is always periodic, except if the Doppler-shifted frequency in the frame moving with the particle parallel velocity is exactly equal to the cyclotron frequency:  $\omega - k_{\parallel} v_{\parallel} = \Omega$ . In this case the perpendicular electric force due to a wave remains in phase with the rotating particle cyclotron motion and particle response is *secular* and, over short times, non-oscillatory.

In linear theory these resonances are represented by delta functions; of course, in presence of a well-developed magnetic turbulence, at least we expect the discrete resonances to be significantly broadened, due to the rapid decorrelation of the waves phases in strong turbulence. During resonant wave-particle interaction, the secular force acting on a given particle, due to the waves effects, is constant over a particle gyroperiod; thus the magnetic moment conservation is broken. Then interacting particles undergo pitch angle diffusion in the presence of time varying wave fields.

### 2.4.1 Landau Resonance

If  $n = 0$ , resonance occurs when  $\omega = k_{\parallel} v_{\parallel}$ , so particles *surf* along the wave. Let us consider the simple case of a particle interacting with a single plasma wave. We have to solve the particle's equation of motion:

$$m \frac{dv}{dt} = qE \cos(kx - \omega t)$$

$$\frac{dx}{dt} = v$$

where  $m$  and  $q$  are the particle's mass and charge,  $x$  and  $v$  are its position and velocity,  $E$  is the electric field amplitude and  $k$  and  $\omega$  are the wavevector and angular frequency of the wave. If the wave's amplitude is small,  $|E| \ll 1$ , the trajectory of particle will remain close to where it was in absence of the wave (the subscript 0 indicates unperturbed motion, the subscript  $i$  indicates an initial value):

$$m \frac{dv_0}{dt} = 0; \quad v_0 = v_i; \quad x_0 = x_i + v_i t$$

This allows computing the first-order perturbation of the velocity, replacing  $x$  by  $x_0$  in the right-hand side of the equation of motion:

$$m \frac{dv_1}{dt} = qE \cos[(kv_i - \omega)t + kx_i]$$

The first-order velocity perturbation is then obtained by a simple quadrature:

$$v_1 = \frac{qE}{m} \frac{\sin[(kv_i - \omega)t + kx_i] - \sin[kx_i]}{(kv_i - \omega)}$$

This particle's response is always oscillatory except if the particle's velocity is exactly equal to the wave's phase velocity. In that case, the particle is constantly accelerated and

$$v_1 = \frac{qE}{m} \cos(kx_i)t$$

This monotonic particle response to the perturbation is called *secular*, as opposed to the periodic one. It is important to notice that, instead of an electrostatic wave, one can consider a magnetic wave, modulating a large straight magnetic field and propagating along its direction. This interaction is completely similar to the Landau one and is called *transit time magnetic pumping* (Stix, 1992).

### 2.4.1.1 QL diffusion in the Landau case

It is also possible to approach the resonance problem from a statistical point of view, using Vlasov's equation for the same 1D problem:

$$\frac{\partial f}{\partial t} + v \frac{\partial f}{\partial z} + \frac{qE_1}{m} \frac{\partial f}{\partial v} = 0 \quad (2.15)$$

Linearizing this equation, assuming that the field  $E_1$  is a first-order perturbation and that  $f = f_0 + f_1 + \dots$ , averaging over the fast time scale  $\langle \rangle_f$  of Eq. 2.15, we obtain an equation for the slowly varying  $f_0$ :

$$\frac{\partial f_0}{\partial t} + \frac{q}{m} \left\langle E_1 \frac{\partial f_1}{\partial v} \right\rangle_f = 0 \quad (2.16)$$

Extraction of the first-order terms from Eq. 2.15, followed by Fourier transform in space and Laplace transform in time, gives the spectrum of the perturbed distribution function:

$$f_1 = \frac{iqE_1}{m(\omega - kv)} \frac{\partial f_0}{\partial v} \quad (2.17)$$

Inserting this expression in Eq. 2.16 and taking into account that the average value of two real oscillating quantities,  $u$  and  $w$ , is expressed in terms of their Fourier transforms,  $\hat{u}$  and  $\hat{w}$  is given by  $\langle uw \rangle = \text{Re}(\hat{u}\hat{w}^*)/2$ , we obtain:

$$\frac{\partial f_0}{\partial t} = -\frac{q}{m} \frac{1}{2} \text{Re} \left[ E_1^* \frac{\partial}{\partial v} \frac{-iqE_1}{m(\omega - kv)} \frac{\partial f_0}{\partial v} \right] = -\frac{q^2 |E_1|^2}{2m^2} \frac{\partial}{\partial v} \text{Im} \left[ \frac{1}{\omega + i\epsilon - kv} \right] \frac{\partial f_0}{\partial v} \quad (2.18)$$

where the small imaginary part  $+i\epsilon$  ( $\epsilon > 0$ ) comes from the inverse Laplace transformation rules (causality). It is possible to rewrite Eq. 2.18 as:

$$\frac{\partial f_0}{\partial t} = \frac{\partial}{\partial v} \left( D \frac{\partial f_0}{\partial v} \right); \quad D = \frac{q^2 |E_1|^2}{2m^2 |k|} \pi \delta \left( v - \frac{\omega}{k} \right) \quad (2.19)$$

Eq. 2.19 has a form similar to the Fourier heat transfer equation or, more general speaking, a diffusion equation, except that in this case diffusion takes place in velocity space. This is called the *quasilinear diffusion equation*, where  $D$  is the quasilinear diffusion coefficient. The  $\delta$ -function appearing in this coefficient implying that only resonant particles participate in the diffusion process.

### 2.4.2 The cyclotron interaction

In the same way as for the Landau case, we can look at the linearized motion of a particle in a perpendicular wave field in presence of a strong magnetic field,  $\mathbf{B}_0 = B_0 \mathbf{e}_z$  (in this case non-subscripted quantities are first order in the field perturbation):

$$\frac{dv}{dt} = \frac{q}{m} (\mathbf{E} + \mathbf{v} \times \mathbf{B}_0 + \mathbf{v}_0 \times \mathbf{B})$$

Because  $i\omega B \approx kE$ , the last term in the right parenthesis is smaller than the first one,  $\mathbf{E}$ , by the ratio  $v_0/(\omega/k)$ ; so, it can be neglected. In the  $z$  direction, parallel to the mean magnetic field,  $v_z = v_{\parallel} = \text{const}$  and  $z = v_{\parallel}t + z_0$ . Instead, in the perpendicular direction the equations of motion are given by:

$$\frac{d}{dt} \begin{pmatrix} v_x \\ v_y \end{pmatrix} = \Omega \begin{pmatrix} v_y \\ -v_x \end{pmatrix} + \frac{q}{m} \begin{pmatrix} E_x \\ E_y \end{pmatrix}$$

Defining the complex velocity  $u = v_x + iv_y$  and separating the electric field into its left-hand polarized component (rotating in the same sense of ions) of amplitude  $E_+$  and the right-hand one  $E_-$ , we obtain the complex equation of motion:

$$\frac{du}{dt} = -i\Omega u + \frac{q}{m} [E_+ e^{i(k_{\parallel}z - \omega t)} + E_- e^{-i(k_{\parallel}z - \omega t)}]$$

In order to simplify the discussion, we look just at the ion motion, expected to be in resonance with the left-hand polarized component,  $E_+$ . The particle unperturbed motion can be written as:

$$u = v_{\perp} e^{-i\Omega t}; \quad \rho = x + iy = \rho_0 + i \frac{v_{\perp}}{\Omega} e^{-i\Omega t} = \rho_0 + ir_L e^{-i\Omega t},$$

where  $v_{\perp}$  is the constant,  $0^{\text{th}}$  order, perpendicular velocity,  $\rho_0$  is the (complex) guiding center position and  $r_L = v_{\perp}/\Omega$  is the particle gyroradius. In general the electric field amplitude depends on the transverse coordinates:  $E_+ = E_+(x, y) = E_+(\rho, \rho^*)$ . If in a first step we assume that  $E_+ = \text{const}$ , the particle response to the left-hand component is:

$$u = u_0 e^{-i\Omega t} + \frac{q}{m} \frac{e^{-i\Omega t} E_+ [e^{i(k_{\parallel}v_{\parallel} - \omega - \Omega)t + ik_{\parallel}z_0} - e^{ik_{\parallel}z_0}]}{i(k_{\parallel}v_{\parallel} - \omega + \Omega)}$$

Again this response is always periodic, except if the Doppler-shifted frequency in the frame moving with the particle's parallel velocity is exactly equal to the cyclotron frequency:  $\omega - k_{\parallel}v_{\parallel} = \Omega$ . In this case, the perpendicular velocity grows linearly with times:

$$u = u_0 e^{-i\Omega t} + \frac{qE_+}{m} e^{(-i\Omega t + ik_{\parallel}z_0)} t$$

The perpendicular electric force due to a wave remains in phase with the rotating particle cyclotron motion and particle response is *secular*.

### 2.4.2.1 QL diffusion in uniform magnetized plasmas

The derivation of the quasilinear equation for the general case of a uniform plasma immersed in a constant and uniform magnetic field,  $\mathbf{B}_0$ , follows exactly the same steps of the previous case. Starting from the full Vlasov's equation with collisions:

$$\frac{\partial f_s}{\partial t} + v \cdot \nabla f_s + \frac{q_s}{m_s} (\mathbf{E} + \mathbf{v} \times \mathbf{B}) \cdot \frac{\partial f_s}{\partial \mathbf{v}} = \sum_{s'} C(f_s, f_{s'}) \quad (2.20)$$

linearizing  $f \rightarrow f_0 + f_1$  and  $\mathbf{B} \rightarrow \mathbf{B}_0 + \mathbf{B}_1$ , solving for the first-order distribution function and inserting the latter in the averaged Eq. 2.20, one obtains the quasilinear diffusion equation:

$$\frac{\partial f_{s0}}{\partial t} = \left( \frac{1}{v_\perp} \frac{\partial}{\partial v_\perp} v_\perp, \frac{\partial}{\partial v_\parallel} \right) \bar{\mathbf{D}}_s \left( \frac{\partial}{\partial v_\perp}, \frac{\partial}{\partial v_\parallel} \right) f_{s0} + \sum_{s'} C(f_{s0}, f_{s'0}) + S_s + L_s \quad (2.21)$$

where

$$\bar{\mathbf{D}}_s = \frac{q_s^2 k_\parallel^2}{2m_s^2 \omega^2 v_\perp^2} \sum_{p=-\infty}^{\infty} \pi \delta(\omega - k_\parallel v_\parallel - n\Omega_s) \left| \tilde{\mathbf{E}}^* \mathbf{w}_{sn} \tilde{\mathbf{w}}_{sn}^* \mathbf{E} \right| \mathbf{u} \tilde{\mathbf{u}}$$

$$\tilde{\mathbf{u}} = \left( \frac{\omega}{k_\parallel} - v_\parallel, v_\perp \right); \quad \tilde{\mathbf{w}}_{sn}^* = \left( \frac{\Omega_s}{k_\perp} n J_n, i v_\perp J'_n, v_\parallel J_n \right); \quad J = J \left( \frac{k_\perp v_\perp}{\Omega_s} \right)$$

Here  $n$  is the cyclotron harmonic number.

Although more complicated and acting in the  $2D$  velocity space, this equation exhibits the same characteristics as in the Landau case, in particular the fact that only resonant particles participate in the diffusion process. In this equation collisions are incorporated, as well as source term  $S$  (beam-injected particles, alpha particles, etc) and loss term  $L$  (finite confinement, fusion reactions, etc). The  $\mathbf{u}$  vector determines the directions in velocity-space along which diffusion is taken place. One also notices the presence of the Bessel functions  $J_n$ , which argument is the ratio of the Larmor radius to the perpendicular wavelength.

## 2.5 What is Diffusion?

Diffusion usually occurs if there is a spatial difference in concentration (particles, heat, etc...) and it usually acts to reduce these spatial inhomogeneities. The time dependence of the statistical distribution in space is given by the diffusion equation. The motion of a particle undergoing diffusion is sometimes described as a random walk, a discrete process, that has a striking connection to Brownian motion, governed in the continuous limit by the diffusion equation. The mathematics of random walks is often studied using simple models. In the simplest model the random walker takes steps of equal size in any direction. Before each step, he chooses a new random direction and takes a step. Imagine a large number of random walkers all starting out from the same place at the same time. As time proceeds, the initial high concentration of random walkers spreads out, invading regions of lower concentration.

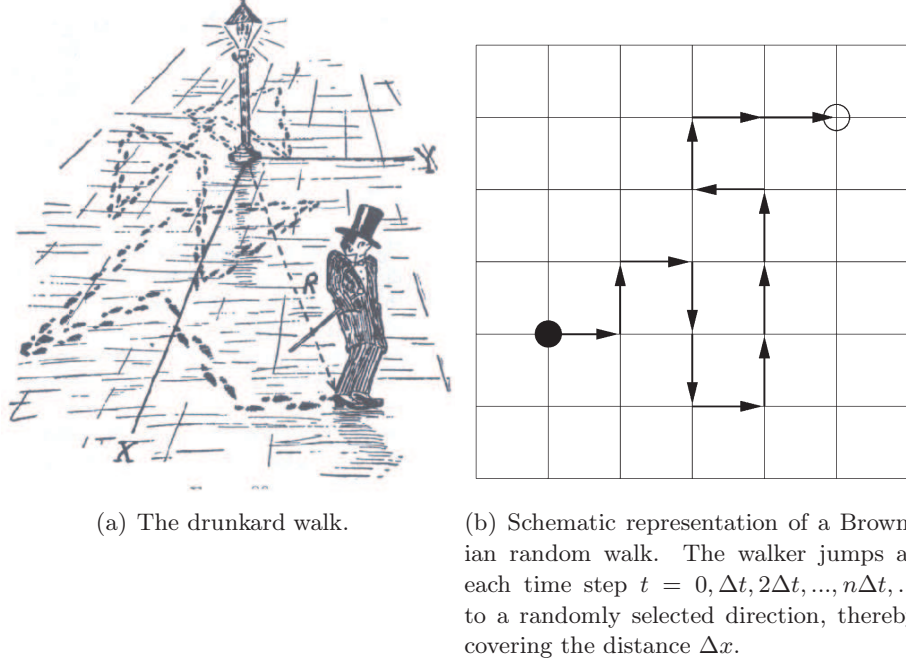
There are two important questions concerning this process: What is the distribution of random walkers as function of time? What is the average distance that a single walker is expected to go in a given time?

### 2.5.1 Historical remarks

The stochastic formulation of transport phenomena in terms of a random walk process as well as the description through the deterministic diffusion equation are the two fundamental concepts in the theory of both normal and anomalous diffusion. Indeed, the history of this dual description basing on erratic motion and on a differential equation for the probability density function is quite interesting and much worth a short digression.

Small flickering of coal dust particles on the surface of alcohol was observed by the Dutch physician Jan Ingenhousz as early as in 1785. In 1827, the Scottish botanist Robert Brown ([Brown, 1828](#)) observed similar irregular movement of small pollen grain under a microscope. At about the same time, in 1822, Joseph Fourier ([Fourier, 1822](#)) came up with the heat conduction equation, on the basis of which A. Fick set up the diffusion equation in 1855 ([Fick, 1955a,b](#)). Subsequently, the detailed experiments by Gouy proved the kinetic theory explanation given by C. Weiner in 1863. After attempts of finding a stochastic footing like the collision model by von Nagéli and John William Strutt, Lord Rayleigh's results, it was Albert Einstein ([Einstein., 1905](#)) who, in 1905, unified the two approaches in his treatises on the Brownian motion, a name coined by Einstein although he reportedly did not have access to Brown's original work. Note that a similar description of diffusion was presented by the French mathematician Louis Bachelier in his 1900 thesis ([Bachelier, 1900](#)), in terms of stock values instead of physical quantities. An important application of Einstein's results was the independent measurement of the Avogadro number by Jean Baptiste Perrin (Nobel Prize in 1926) ([Perrin, 1908, 1909](#)), A. Westgren and Eugen Kappler ([Kappler, 1931](#)), to a rather high accuracy. The random walk, which can be experimentally observed, represents therefore a link between the microscopic dynamics of small atoms, bombarding a larger particle in suspension, and macroscopic observables like the diffusion coefficient, or the Avogadro number. Einstein's ideas also set the scene for Langevin's treatment of Brownian motion with the assumption of an external erratic force, and the Fokker Planck ([Fokker, 1914](#); [Planck, 1917](#)), Smoluchowski ([Smoluchowski, 1915](#)) and Klein-Kramers theories ([Klein, 1922](#); [Kramers, 1940](#)), which culminated in the treatises of Ornstein and Uhlenbeck, Chandrasekhar ([Selected Papers on Noise and Stochastic Processes, 1954](#)) and others, and later in the works of Elliott Montroll and collaborators ([Montroll, 1956](#); [Montroll et al., 1969, 1973](#)). The mathematical treatment of Brownian motion is mainly due to Norbert Wiener ([Wiener, 1923, 1924, 1930, 1938](#)), who proved that the trajectory of a Brownian particle is (almost) everywhere continuous but nowhere differentiable. This observation is related to the self-affine nature of the diffusion process whose resulting spatial trajectory is self-similar.

## 2.5.2 Random walk



(a) The drunkard walk.

(b) Schematic representation of a Brownian random walk. The walker jumps at each time step  $t = 0, \Delta t, 2\Delta t, \dots, n\Delta t, \dots$  to a randomly selected direction, thereby covering the distance  $\Delta x$ .**Figure 2.3:** Random walk representation

We consider a random walk in one dimension and assume that the particles' steps,  $\Delta z$ , are random and equally likely to either side, left or right, and of constant length  $l$  (see Figure 2.3(b)). The position,  $z_N$ , of a particle starting at  $z_0$  after  $N$  steps is:

$$z_N = \Delta z_N + \Delta z_{N-1} + \dots + \Delta z_1 = \sum_{i=1}^N \Delta z_i,$$

so that the squared length of the path equals

$$z_n^2 = \left( \sum_{j=1}^N \Delta z_j \right) \left( \sum_{k=1}^N \Delta z_k \right) = \sum_{j=1, k=j}^N \Delta z_j^2 + \sum_{j, k=1, k \neq j}^N \Delta z_j \Delta z_k = Nl^2 + \sum_{j, k=1, k \neq j}^N \Delta z_j \Delta z_k.$$

When averaging over a large number of particles, we find the mean squared path length as

$$\langle z_N^2 \rangle = Nl^2 + \left\langle \sum_{j, k=1, k \neq j}^N \Delta z_j \Delta z_k \right\rangle.$$

Each step of the walk is equally likely to the left or to the right, so that the displacements,  $\Delta z_i$ , are random variables with zero mean. The products  $\Delta z_j \Delta z_k$  are also random variables, and, since we assume that  $\Delta z_j$  and  $\Delta z_k$  are independent of

each other, the mean value of the products is zero, so that the expectation value of the mixed term is zero. Thus, we obtain:

$$\langle z^2 \rangle = Nl^2. \quad (2.22)$$

The root-mean square displacement after  $N$  steps of constant length  $l$  (mean free path) is:

$$\sqrt{\langle z_N^2 \rangle} = l\sqrt{N}.$$

The mean free path,  $l$ , can be estimated with a simple model. Assuming that a particle is moving inside a gas with a mean speed  $\langle v \rangle$ , the distance traveled between two successive collisions is  $l = \langle v \rangle \tau$ , where  $\tau$  is called collision time. We may thus conclude that the number of steps a particle executes inside a gas during a time  $t$  is  $N = t/\tau$ , and, with Eq. 2.22 and the above relation for  $l$ , the mean squared distances it travels is:

$$\langle z^2 \rangle = Nl^2 = (t/\tau)(\langle v \rangle \tau)l = (\langle v \rangle l)t.$$

Assuming that the random walk takes place in 3D and that the gas is in equilibrium and isotropic, we expect that  $\langle x^2 \rangle = \langle y^2 \rangle = \langle z^2 \rangle = \langle r^2 \rangle/3$ , and the mean square path length in 3D is:

$$\langle r^2 \rangle = 3\langle v \rangle lt = Dt$$

where  $D = 3\langle v \rangle l$  is called the diffusion coefficient, which is a useful parameter to characterize particle diffusion in the normal case. Important, here, is to note the linear scaling relation between  $\langle r^2 \rangle$  and time  $t$ , typical of *normal diffusion*.

To see the connection between random walks and the macroscopic diffusion equation, consider the probability,  $p(m, n)$ , that a walker is at position  $m$  after  $n$  steps. To get to position,  $m$ , the walker must be at position  $m - 1$  or position  $m + 1$  at the previous step. In either case, the probability that it moves to position  $m$  is 0.5. Hence,

$$p(m, n) = \frac{1}{2} [p(m + 1, n - 1) + p(m - 1, n - 1)].$$

Subtracting  $p(m, n - 1)$  from both sides gives:

$$p(m, n) - p(m, n - 1) = \frac{1}{2} [p(m + 1, n - 1) - 2p(m, n - 1) + p(m - 1, n - 1)].$$

The left hand side is the change in  $p$  over one time step and the right hand side has the form of a second derivative with respect to the position (the step size is unity). Letting the time step and the spatial step become infinitesimally small leads to a diffusion equation:

$$\frac{\partial p}{\partial t} = D \frac{\partial^2 p}{\partial x^2},$$

where  $D$  is the diffusion coefficient.



### 2.5.3 Modeling Diffusion with Fick's Law

Let us consider particle diffusion along the  $z$  direction in 3D space and let us assume that two elementary areas perpendicular to the flow (in the  $xy$  plane) are a distance  $\Delta z$  apart. Particle conservation implies that the time variation of the density,  $n(z, t)$ , inside the elementary volume,  $\Delta x \Delta y \Delta z$ , equals the inflow minus the outflow of particles, so that, if  $J(z, t)$  denotes the particle flux,

$$\frac{\partial n(z, t)}{\partial t} \Delta x \Delta y \Delta z = J(z) \Delta x \Delta y - J(z + \Delta z) \Delta x \Delta y = \frac{\partial J}{\partial z} \Delta x \Delta y \Delta z,$$

which leads to the diffusion equation in its general form:

$$\frac{\partial n(z, t)}{\partial t} = \frac{\partial J(z, t)}{\partial z}. \quad (2.23)$$

The problem that remains is to determine the particle flux,  $J$ . From its physical meaning, it obviously holds that  $J(z, t) = n(z, t)v(z, t)$ , where  $v(z, t)$  is an average particle flow velocity. Using this expression in Eq. 2.23 leads to a closure problem, we would need to find ways to determine  $v(z, t)$ . It is well documented experimentally that the flux of particles,  $J$ , crossing a certain area (again, say in the  $xy$  plain), is proportional to the density gradient along the  $z$  axis (Fick's Law):

$$J_z = -D(z) \frac{\partial n}{\partial z}, \quad (2.24)$$

where  $D$  is the diffusion coefficient discussed already in the previous sections and which generally may also depend on  $z$ . With Eq. 2.24, the diffusion equation takes the classical form:

$$\frac{\partial n(z, t)}{\partial t} = -\frac{\partial}{\partial z} D(z) \frac{\partial n(z, t)}{\partial z} \quad \text{or} \quad (2.25)$$

$$\frac{\partial n(z, t)}{\partial t} = -D \frac{\partial^2 n(z, t)}{\partial z^2} \quad \text{for } D = \text{const} \quad (2.26)$$

In infinite space, if all particles start initially from  $z = 0$ , the solution of Eq. ?? is:

$$n(z, t) = \frac{N_0}{\sqrt{4\pi Dt}} e^{-z^2/4Dt}, \quad (2.27)$$

where  $N_0$  is the total number of particles inside the volume under consideration. The solution obviously is identical to a Gaussian distribution with zero mean and variance  $2Dt$ . The variance is defined as:

$$\sigma^2 = \langle z^2(t) \rangle = \int z^2 n(z, t) dz = 2Dt, \quad (2.28)$$

which is just identical to the mean square displacement, so that the results obtained earlier, using the simple version of the random walk in Section 2.5.2, is again confirmed. Diffusion obeying Eq. 2.28 is called normal diffusion and is characteristic for the diffusion processes in systems that are in equilibrium or very close to equilibrium.

### 2.5.4 The Fokker-Planck Equation

The Fokker-Planck (FP) equation is a more general diffusion equation than the simpler equations introduced in Section 2.5.2 and Section 2.5.3. The basic difference between the FP equation and the simple diffusion equation in Eq. 2.26 is the appearance of a drift term and that both the drift velocity and the diffusion coefficient are allowed to be spatially dependent (Fick's law also allows a spatially dependent diffusion coefficient, see Eq. 2.26). These differences allow the FP equation to model more complex diffusive behavior. We can write the FP equation as:

$$\partial_t n(z, t) = -\partial_z [V(z)n(z, t)] + \partial_z^2 [D(z)n(z, t)], \quad (2.29)$$

where  $V(z) = \mu_{\Delta z}(z)/\Delta t$  is a drift velocity and  $D(z) = \langle \Delta z^2 \rangle(z)/2\Delta t$  is the diffusion coefficient. The FP equation is also applied to velocity space, e.g., in plasma physics in order to treat collisional effects or to position and velocity space together.

### 2.5.5 Anomalous diffusion

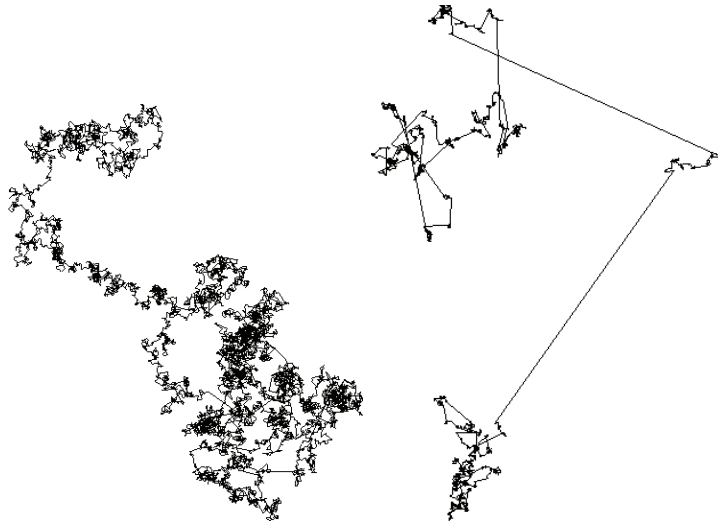


**Figure 2.4:** Random walk in dynamical systems close to equilibrium (normal diffusion: trajectory on the left); random walk in dynamical systems far from equilibrium (anomalous diffusion: trajectory on the right).

Normal diffusion has as basic characteristic the linear scaling of the mean square displacement of the particles with time,  $\langle r^2 \rangle \propto Dt$ . However, many different experiments reveal deviations from normal diffusion, in that diffusion is either faster or slower and which is termed anomalous diffusion. A useful characterization of the diffusion process is again through the scaling of the mean square displacement with time, where now we are looking for a more general scaling of the form

$$\langle r^2 \rangle \propto t^\gamma \quad (2.30)$$

Diffusion is then classified through the scaling index,  $\gamma$ .

1.  $\gamma = 1$  particles follow a Gaussian distribution: this is the *normal or brownian diffusion*.
2.  $\gamma \neq 1$  particles perform Levy flights. This is the case of *anomalous diffusion*
  - If  $\gamma > 1$  we have the family of *superdiffusive processes*
  - If  $\gamma < 1$  we have the family of *subdiffusive processes*

The case  $\gamma = 2$ , which is called ballistic motion or "free streaming", is a particular case of superdiffusive process: let us consider a particle that is moving with constant velocity,  $v$ , and undergoes no collisions and experiences no friction forces. It then obviously holds that  $r = vt$ , so that  $\langle r^2 \rangle \propto t^2$ . Free particles are thus superdiffusive in the terminology used here. The difference between normal and anomalous diffusion is also illustrated in Figure 2.4, where in the case of anomalous diffusion (trajectory on the right) long "flights" are followed by efficient "trapping" of particles in localized spatial regions, in contrast to the more homogeneous picture of normal diffusion (trajectory on the left).

## 2.6 Quasilinear Theory and Diffusion Coefficients

The elementary notion of particles following field lines emerges in single particle orbit theory (e.g., *Rossi & Olbert, 1970*), where the gyrocenter of charged particle motion remains on a certain magnetic field line, when that field is uniform and constant and the electric field is negligible. When constant (or slowly varying) magnetic field gradients and constant electric fields are present, (gyroperiod-averaged) drift velocities provide a correction to the simplest picture and, in the same limit, adiabatic invariants (e.g., magnetic moment) provide useful constraints on possible particle motions. Even in these idealized circumstances, gyrocenter trajectories can become undefined when the field lines themselves become ambiguous, for example when neutral points or separatrices of the magnetic field are present. Moreover, when symmetries of the magnetic field are imposed (*Jokipii et al., 1993; Jones et al., 1998*) the idea that "particles remain on a specific field line" can be replaced by "particles remain on a flux surface", that is, somewhere on a set of equivalent field lines. The situation becomes more complicated when classical (hard sphere or Coulomb) scattering is introduced and conditions for the drifting gyrocenter picture can be strongly violated. It is in the midst of this already complex landscape that one seeks to develop transport theories for charged particles in a low-collisionality turbulent medium.

The wave-particle interaction formalism has been developed in the last years in numerous theoretical papers concerned with weak turbulence in plasma. The special problem of charged particles diffusion in interplanetary space through weak interactions with random electromagnetic fields has been considered by *Jokipii (1966, 1967); Hasselmann & Wibberenz (1968); Klimas & Sandri (1971); Fisk et al. (1974); Jones et al. (1973); Bieber & Matthaeus (1997); Zank (1998); Giacalone & Jokipii*

(1999). These theories are derived by using both the quasilinear and the adiabatic approximations. In the adiabatic approximation the particles distribution function is assumed to vary on a time scale longer than and distinct from the time scale over which a particle experiences a significant interaction with the random magnetic field.

Quasilinear (QL) or Fokker-Planck (FP) approaches (*Jokipii, 1966; Jokipii & Parker, 1968, 1969; Forman et al., 1974; Schlickeiser, 1989*) develop perturbation schemes in which random forces on particles are computed along unperturbed trajectories. Here, one begins to see how problems interpreting the beads-on-a-string picture arise: pitch angle scattering changes the particle magnetic moment and, in fully three dimensional cases, changes the bundle of field lines encircled by the gyro-orbit. For stronger scattering (*Lingenfelter et al., 1971; Urch, 1977; Rechester & Rosenbluth, 1978*), the parallel and perpendicular scattering processes are no longer independent. Scattering parallel to the mean magnetic field can cause a reversal of the particle velocity along the magnetic field, a subsequent reduction of perpendicular random displacement and the possibility of subdiffusion. This process is observed in simulations (*Qin et al., 2002b*). Also seen in some cases is the restoration of diffusive transport (*Qin et al., 2002a*), when the particles effectively change which field line they are following and the magnetic turbulence exhibits sufficient spatial complexity. In such cases a diffusive limit can also be established, once the displacements become uncorrelated, although the reasons for the decorrelation are different from the case of particles simply following field lines. This phenomenon of second diffusion, which replaces perpendicular subdiffusion at longer time intervals for spatially complex turbulence, is reasonably well described by the Nonlinear Guiding Center Theory (NLGC; *Matthaeus et al., 2003; Bieber et al., 2004*) and its offspring (e.g., *Shalchi et al., 2004*). In this picture one can say that the particle guiding centers locally follow field lines over a distance determined by the mean free paths of parallel scattering and the field line random walk. After that, the particle switches to a different field line. The guiding center motion is taken to be randomized, with no "backtracking" along the same field line.

### 2.6.1 Description of particle motion in a random magnetic field

As explained in the original derivation of *Jokipii (1966)*, the goal is not to obtain a complete description of the trajectory of each particle, but instead to find a statistical equation governing the evolution of the particle distribution function. Thus, the behavior of a large number of particles will be assumed to follow the probability distribution of a single particle. This approach is very similar to the ordinary random walk problem, except that here we are tracing the random walk of a particle trajectory under the influence of an irregularly fluctuating magnetic field. If the magnetic field were uniform, the particle would travel in a helical orbit along the field. The irregularities perturb this orbit and cause, among other things, a scattering in pitch angle. If the irregularities were all of a given shape,  $\delta B(x)$ , but occurred, say, with random sign, one could compute an "elementary" scattering,  $\Delta\theta \ll 1$ , and then compute the net change after  $N$  scatterings ( $\Delta\theta_N \simeq N^{-1/2}|\Delta\theta|$ ), because of the

random sign. This then leads to a relaxation of the angular distribution toward isotropy in a characteristic time,  $\tau_c$ , which can be computed from  $\Delta\theta$ . Hence, the diffusion coefficient  $k \simeq \omega^2\tau_c/3$  can be obtained. But, in actuality, the irregularities do not all have the same shape and a more general treatment is necessary.

Suppose a particle of velocity  $v$  and mass  $\gamma m_0$  propagates in the magnetic field  $\mathbf{B}(r)$ , where  $\gamma_m = (1 - v^2/c^2)$ . The equation of motion is:

$$\frac{d\mathbf{v}}{dt} = \frac{q\mathbf{v} \times \mathbf{B}}{\gamma_m m_0 c} = \mathbf{v} \times \boldsymbol{\omega}(\mathbf{r}), \quad (2.31)$$

with  $\boldsymbol{\omega} = q\mathbf{B}/\gamma_m m_0 c$ . The goal is to find a differential equation governing the distribution of particles subject to Eq. 2.31, in terms of the correlation functions of the magnetic field defined as follow:

$$R_{ij\dots k}(\mathbf{r}_1, t_1, \mathbf{r}_2, t_2, \dots, \mathbf{r}_n, t_n) = \langle B_i(\mathbf{r}_1, t_1) B_j(\mathbf{r}_2, t_2) \dots B_k(\mathbf{r}_n, t_n) \rangle, \quad (2.32)$$

where  $\langle B_i(\mathbf{r}, t) \rangle$  is the magnetic vector. In this approach the magnetic field is described statistically, in the sense of random function theory (*Yaglom, 1962*): specification of a hierarchy of correlation functions constitutes a complete statistical description of the field. For example, for  $n = 1$  in Eq. 2.32, one has simply  $\langle B_i(\mathbf{r}, t) \rangle$ , the average magnetic vector, and so on. One can easily see that the general description would involve the entire infinite family of correlations and is thus impractical. To avoid this difficulty, one approach is to define

$$\omega_0 \hat{e}_z = \langle \boldsymbol{\omega} \rangle \quad \text{and} \quad \boldsymbol{\omega}_1(\mathbf{r}) = \boldsymbol{\omega}(\mathbf{r}) - \omega_0 \hat{e}_z \quad (2.33)$$

and to assume  $\langle \omega_1^2 \rangle / \omega_0^2 \ll 1$ , so that the orbit is only slightly perturbed in a coherence length of the field. Then, only the lowest-order correlations of  $\boldsymbol{\omega}_1$  need be retained to obtain a reasonable approximation to the particle motion.

At this point one may proceed in one of two distinct directions to find the equation for the particle distribution. The original approach (*Jokipii, 1966*; *Hasselmann & Wibberenz, 1968*) proceeds by means of Fokker-Planck coefficients in a manner first used by *Sturrock (1965)* in a different problem. After that *Hall & Sturrock (1967)*; *Dolginov et al. (1968)*; *Roelof (1968)*, pointed out that the same equations could be obtained from a more general approach by means of Liouville's equation. In this context, the Fokker-Planck approach of *Jokipii (1966)* will be followed because of its comparative algebraic simplicity. The unperturbed particle trajectory in the uniform field  $\omega_0 \hat{e}_z$  is the usual helix determined by its instantaneous position and velocity. It is assumed that the average cyclotron frequency,  $\omega_0$ , is large compared with any other frequencies, so that all quantities may be averaged over the phase of gyration. Hence, the orbit is completely characterized by the pitch angle,  $\theta = \cos^{-1} v_z/v$ , and position at a given velocity  $v$ . It proves convenient to define the complex variables:

$$\begin{aligned} x_+ &= x + iy \\ v_+ &= v_x + iv_y \\ \omega_+ &= \omega_{1x} + i\omega_{1y} \end{aligned}$$

in the plane normal to the average magnetic field. The unperturbed or zero-order orbit ( $u$  subscript) is then given by:

$$z_u = z_0 + v_{z0}t \quad (2.34)$$

$$x_{+u} = x_{+0} + i(v_{+0} + e^{-i\omega_0 t}/\omega_0) \quad (2.35)$$

with  $|v_{+0}|^2 + v_{z0}^2 = v^2 = \text{const}$ . The fluctuating field,  $\omega_1$ , causes perturbations in this zero-order orbit: the orbit parameters  $x$ ,  $y$ ,  $z$ ,  $v_{z0}$ , execute a random walk under its influence. Define the cosine of pitch angle  $\alpha = v_z/v$ . Then, let

$$n(\mathbf{r}, \alpha, t) d\mathbf{r} d\alpha \quad (2.36)$$

be the probability of finding a particle in  $\mathbf{r}$  to  $\mathbf{r} + d\mathbf{r}$ ,  $\alpha$  to  $\alpha + d\alpha$  at time  $t$ . Hence,  $n$  is a probability density that may be identified with the measured density in position and pitch angle. If the orbit changes caused by the random field,  $\omega_1$ , are small in a correlation time of the fluctuations as seen by a particle, then the evolution of  $n$  is governed by a Fokker-Planck equation, as outlined by [Chandrasekhar \(1943\)](#). That is, the evolution of  $n$  is caused by a succession of small, random, increments and the particles may be regarded as random-walking, or diffusing, in pitch angle and position. The process is a straightforward generalization to more variables of the ordinary particle diffusion due to a spatial random walk, as given in Eq 2.26. If  $\mathbf{r}$  and  $\alpha$  are replaced by the four parameters  $X_i$ , then the Fokker-Planck equation reads formally:

$$\begin{aligned} \frac{\partial n}{\partial t} = & - \sum_{i=1}^4 \frac{\partial}{\partial X_i} \left[ \frac{\langle \Delta X_i \rangle}{\Delta t} n \right] + \frac{1}{2} \sum_{i=1}^4 \frac{\partial^2}{\partial X_i^2} \left[ \frac{\langle \Delta X_i^2 \rangle}{\Delta t} n \right] + \\ & + \sum_{i < j} \frac{\partial^2}{\partial X_i \partial X_j} \left[ \frac{\langle \Delta X_i \Delta X_j \rangle}{\Delta t} n \right] \end{aligned} \quad (2.37)$$

The problem is to evaluate the various FP coefficients,  $\langle \Delta X_i^2 \rangle / \Delta t$ , etc., appearing in Eq. 2.37. To calculate these coefficients, one considers the perturbations about the unperturbed orbit given in Eq. 2.34 and Eq. 2.35. Setting

$$z(t) = z_u(t) + z_1(t) + z_2(t) + \dots \quad (2.38)$$

$$x_{+}(t) = x_{+u}(t) + x_{+1}(t) + x_{+2}(t) + \dots \quad (2.39)$$

where  $z_1(t)$  and  $x_{+1}(t)$  are linear in  $\omega_1$  and  $z_2$  and  $x_{+2}(t)$  are of the second order, substituting Eq. 2.38 and Eq. 2.39 into the equation of motion, Eq. 2.31, one obtains, to first order in  $\omega_1$ :

$$\ddot{z}_1 = -\frac{i}{2} [\omega_{+}(z_u, x_{+u}) v_{+0}^* e^{i\omega_0 t} - \omega_{+}^*(z_u, x_{+u}) v_{+0} e^{-i\omega_0 t}] \quad (2.40)$$

$$\ddot{x}_{+1} + i\omega_0 x_{+1} = i v_{z0} \omega_{+}(z_u, x_{+u}) - i v_{+0} e^{-i\omega_0 t} \omega_{1z}(z_u, x_{+u}) \quad (2.41)$$

and so on, where the superscript \* indicates complex conjugate.

Consider first the scattering in pitch angle. From the definition of  $\alpha$  and the Eq. 2.40,

$$\begin{aligned} \langle (\Delta\alpha)^2 \rangle &= \left\langle \frac{1}{v^2} \dot{z}_1^2 \right\rangle = -\frac{1}{4v^2} \left\langle \int_0^{\Delta\tau} d\tau \int_0^{\Delta\tau} d\tau' \times \right. \\ &\quad \times \left[ \omega_+(z_u, x_{+u}) v_{+0}^* e^{i\omega_0 t} - \omega_+^*(z_u, x_{+u}) v_{+0} e^{-i\omega_0 t} \right] \times \\ &\quad \left. \times \left[ \omega_+(z_u, x_{+u}) v_{+0}^* e^{i\omega_0 t'} - \omega_+^*(z_u, x_{+u}) v_{+0} e^{-i\omega_0 t'} \right] \right\rangle \end{aligned} \quad (2.42)$$

correct to second order in  $\omega_1$ . Define

$$\begin{aligned} \zeta &= v_{z0}(\tau' - \tau) \\ \rho_{+1} &= x_{+u}(\tau') - x_{+u}(\tau) = i \frac{v_{+0}}{\omega_0} e^{-i\omega_0 t} \left( e^{-i\omega_0 \zeta / \alpha v} - 1 \right) \end{aligned}$$

Then, because of the symmetry:

$$\begin{aligned} \langle \omega_+[z_u(\tau), x_{+u}(\tau)] \omega_+^*[z_u(\tau'), x_{+u}(\tau')] \rangle &= 2b(\zeta, \rho_1) + \rho_1^2 a(\zeta, \rho_1) \\ \langle \omega_+[z_u(\tau), x_{+u}(\tau)] \omega_+[z_u(\tau'), x_{+u}(\tau')] \rangle &= a(\zeta, \rho_1) \rho_{+1}^2 \end{aligned}$$

where

$$\rho_1(\zeta) = |\rho_{+1}| = \left[ 2 \frac{(1 - \alpha^2 v^2)}{\omega_0^2} \left( 1 - \cos \frac{\omega_0 \zeta}{\alpha v} \right) \right]^{1/2}. \quad (2.43)$$

Substituting these relations into Eq. 2.42 and remembering that  $\langle \omega_1 \rangle = 0$ , one eventually obtains:

$$\begin{aligned} \langle (\Delta\alpha)^2 \rangle &= \frac{1 - \alpha^2}{|\alpha|v} \int_0^{\Delta t} d\tau \int_{-v_{z0}\tau}^{v_{z0}(\Delta t - \tau)} d\zeta \times \\ &\quad \times \left\{ b[\zeta, \rho_1(\zeta)] e^{-i\omega_0 \zeta / \alpha v} + \frac{(1 - \alpha^2)v^2}{2\omega_0^2} a[\zeta, \rho_1(\zeta)] \left( 1 - e^{-2i\omega_0 \zeta / \alpha v} \right) \right\}. \end{aligned} \quad (2.44)$$

If we further make the usual assumption that  $v_{z0}\Delta t$  is much greater than the correlation length along  $z$ , the  $\zeta$ -integration can be taken from  $-\infty$  to  $+\infty$  and the integrand with respect to  $\tau$  becomes independent of  $\tau$ . Thus,

$$\begin{aligned} \frac{\langle (\Delta\alpha)^2 \rangle}{\Delta t} &= \frac{1 - \alpha^2}{|\alpha|v} \int_{-\infty}^{+\infty} \times \\ &\quad \times d\zeta \left\{ b[\zeta, \rho_1(\zeta)] e^{-i\omega_0 \zeta / \alpha v} + \frac{(1 - \alpha^2)v^2}{2\omega_0^2} a[\zeta, \rho_1(\zeta)] \left( 1 - e^{-2i\omega_0 \zeta / \alpha v} \right) \right\}. \end{aligned} \quad (2.45)$$

Eq. 2.45 is the general expression for the Fokker-Planck coefficient, if the fluctuations are statistically axially symmetric. It gives the rate of relaxation toward isotropy.

By following this same general procedure, one may compute the remaining FP coefficients. However, this may be circumvented noting that scattering in pitch angle must lead to isotropy ( $n$  is independent of  $\alpha$ ); that is, scattering must cause simple diffusion in pitch angle. If scattering did not tend toward isotropy, a spatially

uniform, isotropic distribution would relax toward anisotropy, in violation of Liouville's theorem (the steady-state configuration is isotropic). Hence,  $\langle(\Delta\alpha)\rangle/\Delta t$  and  $\langle(\Delta\alpha)^2\rangle/\Delta t$  must be related by (Jokipii, 1966):

$$\frac{1}{2} \frac{\partial^2}{\partial \alpha^2} \left[ \frac{\langle(\Delta\alpha)^2\rangle}{\Delta t} n \right] - \frac{\partial}{\partial \alpha} \left[ \frac{\langle\Delta\alpha\rangle}{\Delta t} n \right] = \frac{1}{2} \frac{\partial}{\partial \alpha} \left[ \frac{\langle(\Delta\alpha)^2\rangle}{\Delta t} \frac{\partial n}{\partial \alpha} \right], \quad (2.46)$$

which is zero for an isotropic distribution. This result also arises in the alternate approach using Liouville's theorem. Similarly, the symmetry about the  $z$  axis leads to:

$$\langle\Delta x\rangle/\Delta t = \langle\Delta y\rangle/\Delta t = 0 \quad (2.47)$$

$$\langle\Delta x\Delta y\rangle/\Delta t = 0 \quad (2.48)$$

$$\langle\Delta x\Delta\alpha\rangle/\Delta t = \langle\Delta y\Delta\alpha\rangle/\Delta t = 0 \quad (2.49)$$

The equation for  $x_{+1}(t)$  may be integrated, precisely as was done for  $z_1(t)$  to obtain:

$$\begin{aligned} \frac{\langle(\Delta x)^2\rangle}{\Delta t} &= \frac{\langle(\Delta y)^2\rangle}{\Delta t} \\ &= \frac{1}{2\omega_0^2|\alpha|v} \int_{-\infty}^{\infty} d\zeta \{ \alpha^2 v^2 \{ 2b[\zeta, \rho_1(\zeta)] + \rho_1^2 a[\zeta, \rho_1(\zeta)] \} + \\ &\quad + (1 - \alpha^2) v^2 R_{zz}[\zeta, \rho_1(\zeta)] e^{-i\omega_0\zeta/\alpha v} + \\ &\quad + \frac{2i\alpha(1 - \alpha^2)v^3}{\omega_0} \{ a[\zeta, \rho_1(\zeta)]\zeta + d[\zeta, \rho_1(\zeta)] \} e^{-i\omega_0\zeta/\alpha v} \}. \end{aligned} \quad (2.50)$$

The motion in the  $xy$  plane is a simple random walk. Note that, in addition to the resonant terms ( $\propto R_{zz}$ ), the guiding center motion normal to the field depends on simple integrals of  $a$  and  $b$ : the guiding center follows the random walk of a given field line in the  $xy$  plane, as the particle moves in the  $z$  direction.

Finally, consider the motion along the  $z$  axis. This is qualitatively different from the motion normal to the field, because  $\alpha$  is assumed to change only a small amount in a correlation length. Thus, the particle simply moves along the  $z$  axis at a rate  $\alpha v$  and only gradually does this rate change. So, considering  $\langle(\Delta z)\rangle/\Delta t$  and  $\langle(\Delta z)^2\rangle/\Delta t$  one finds further that

$$\langle(\Delta z)\rangle/\Delta t = \alpha v \quad (2.51)$$

$$\langle(\Delta z)^2\rangle/\Delta t = 0(\Delta t) \quad (2.52)$$

Here,  $0(\Delta t)$  means that the right side of Eq. 2.52 goes to 0 as  $\Delta t \rightarrow 0$ . Thus, the full Fokker-Planck equation in this approximation becomes:

$$\frac{\partial n}{\partial t} = -\alpha v \frac{\partial n}{\partial t} + \frac{1}{2} \frac{\partial}{\partial \alpha} \left[ \frac{\langle(\Delta\alpha)^2\rangle}{\Delta t} \frac{\partial n}{\partial \alpha} \right] + \frac{1}{2} \frac{\partial}{\partial x} \left[ \frac{\langle(\Delta x)^2\rangle}{\Delta t} \frac{\partial n}{\partial x} \right] + \frac{1}{2} \frac{\partial}{\partial y} \left[ \frac{\langle(\Delta y)^2\rangle}{\Delta t} \frac{\partial n}{\partial y} \right] \quad (2.53)$$

with the FP coefficients given by Eq. 2.45 and Eq. 2.50.



### 2.6.2 The diffusion limit

Eq. 2.53 contains a great deal of information concerning the particle distribution, including the pitch angle distribution and its evolution. Quite often the scattering in pitch angle is rapid compared to other rates of change, so that the pitch angle distribution may be taken to be isotropic and we may approximate the  $z$  motion as diffusion, with a mean free path,  $\lambda_z$ , of the order of this scattering distance. Since the motion in the  $xy$  plane is already simple diffusion, one may approximate Eq. 2.53 by a diffusion equation.  $n(\mathbf{r}, \alpha, t)$  may be expanded in Legendre polynomials:

$$n(\mathbf{r}, \alpha, t) = \frac{1}{2} \left[ U(\mathbf{r}, t) + \sum_{l=1}^{\infty} n_l(\mathbf{r}, t) P_l(\alpha) \right], \quad (2.54)$$

where  $U$  is the particle density (or probability density) averaged over pitch angle at a given energy,  $T$ . At this point it is necessary to assume that the scattering is such that  $n_{l+1}$  decays faster than  $n_l$  (the  $n_l$  must all decay due to the scattering). Then, to lowest order for slow variations,

$$n(\mathbf{r}, \alpha, t) \simeq \frac{1}{2} [U + n_1 \alpha], \quad (2.55)$$

where  $n_1 \ll U$ . Substituting Eq. 2.55 into the FP Eq. 2.53 and integrating over  $\alpha$  from  $\alpha = -1$  and  $\alpha = 1$  yields

$$\frac{\partial U}{\partial t} + \frac{v}{3} \frac{\partial n_1}{\partial z} = \frac{1}{2} \left[ \frac{\partial^2 U}{\partial x^2} + \frac{\partial^2 U}{\partial y^2} \right] \int_0^{+1} \frac{\langle (\Delta x)^2 \rangle}{\Delta t} d\alpha. \quad (2.56)$$

Substituting again, multiplying by  $\alpha$  and integrating again yields:

$$\frac{v}{3} \frac{\partial U}{\partial z} = -\frac{n_1}{2} \int_0^{+1} \frac{\langle (\Delta \alpha)^2 \rangle}{\Delta t} d\alpha. \quad (2.57)$$

Finally, combining Eq. 2.56 and Eq. 2.57 yields the diffusion equation for  $U$ :

$$\frac{\partial U}{\partial t} = k_{\parallel} \frac{\partial^2 U}{\partial z^2} + k_{\perp} \left[ \frac{\partial^2 U}{\partial x^2} + \frac{\partial^2 U}{\partial y^2} \right], \quad (2.58)$$

where

$$k_{\parallel} = \frac{2v^2}{9} \left[ \int_0^{+1} \frac{\langle (\Delta \alpha)^2 \rangle}{\Delta t} d\alpha \right]^{-1} \quad (2.59)$$

$$k_{\perp} = \frac{1}{2} \int_0^{+1} \frac{\langle (\Delta x)^2 \rangle}{\Delta t} d\alpha \quad (2.60)$$

are the parallel and the perpendicular diffusion coefficient, respectively.

A different derivation of the parallel diffusion coefficient in terms of  $\langle (\Delta \alpha)^2 \rangle / \Delta t$  was first put forth by *Jokipii (1966)* and subsequently emphasized

by *Hasselmann & Wibberenz (1968)*. In this derivation the Legendre expansion is not used. Instead, it is assumed that  $\partial n/\partial t \ll \alpha v(\partial n/\partial z)$  in Eq. 2.53. By carrying through appropriate manipulations while still regarding the anisotropy to be small, one arrives at:

$$k_{\parallel} = v^2 \int_{-1}^1 \alpha' \left[ \int_0^{\alpha'} \frac{(1 - \alpha^2)}{\langle (\Delta\alpha)^2 \rangle / \Delta t} d\alpha \right] d\alpha'. \quad (2.61)$$

This is the same of Eq. 2.59 only in certain case (*Earl, 1974*).

If the fluctuating field  $\omega_1$  depends only on  $z$ , as shown by *Jokipii (1971)*, its possible to obtain an approximate expression of Eq. 2.45 and Eq. 2.50:

$$\frac{\langle (\Delta\alpha)^2 \rangle}{\Delta t} = \frac{\omega_0^2}{vB_0^2} \frac{(1 - \alpha^2)}{|\alpha|} P_{xx} \left( k = \frac{\omega_0}{\alpha v} \right) \quad (2.62)$$

$$\frac{\langle (\Delta x)^2 \rangle}{\Delta t} = \frac{\langle (\Delta y)^2 \rangle}{\Delta t} = \frac{|\alpha|v}{B_0^2} \left[ P_{xx}(k=0) + \frac{1 - \alpha^2}{2\alpha^2} P_{zz} \left( k = \frac{\omega_0}{\alpha v} \right) \right] \quad (2.63)$$

At low energies the resonant term is very small compared with the nonresonant one, since the power spectrum falls off as a power law toward high energies. Thus, defined the *particle rigidity*  $\epsilon = z_L/\lambda_c$ , for  $\epsilon < 1$

$$k_{\perp} = \frac{\langle (\Delta x)^2 \rangle}{2\Delta t} = \frac{\langle (\Delta y)^2 \rangle}{2\Delta t} \simeq \frac{1}{2} \frac{|\alpha|v}{B_0^2} P_{xx}(k=0) \simeq \frac{1}{4} \frac{v}{B_0^2} P_{xx}(k=0), \quad (2.64)$$

which is called *field line random walk limit* (FLRW) limit of perpendicular diffusion, where the perpendicular spread of particles occurs at a rate proportional to the spatial rate of spreading of field lines themselves.

## 2.7 Trapping width and resonance overlapping

Generally, wave-particle interaction problems involve multiple resonances. Particle motion is qualitatively different depending on whether these resonances overlap and can become very complicated. Numerical simulations of the motion of such systems show a complexity, which clearly cannot be described analytically, for example it is not possible to write an equation describing the evolution of the particles distribution when two resonances overlap (*Smith & Kaufman, 1978*). The term which has come into use to describe motion in the presence of overlapping resonances is *stochastic*. It is important at this point to distinguish between two different kind of stochasticity. The problem of wave-particle interaction in presence of perturbations in the form of uncorrelated small amplitude electromagnetic waves ("plasma turbulence") is termed extrinsically diffusive. In this case, the regular phase space structure for a charged particle interacting resonantly with an electromagnetic wave is perturbed by neighboring uncorrelated waves (or generically, external noise), which leads to extrinsic stochasticity and extrinsically diffusive behavior. This contrasts

with nonlinear systems, such as particle interacting resonantly with a large amplitude obliquely propagating (with respect to  $\mathbf{B}_0$ ) electromagnetic plasma wave, which can exhibit intrinsic stochasticity. Once the nonlinear bounce frequency,  $\omega_b$ , exceeds the stochasticity threshold given by approximately  $\Omega/4$ , where  $\Omega = |q|B_0/\gamma mc$  is the relativistic gyrofrequency of the particle, the resonances at the harmonics of the gyrofrequency are sufficiently broadened that they can overlap with adjacent primary resonances and hence particles, interacting even with a single monochromatic wave, exhibit intrinsically stochastic and diffusive behavior (*Karimabadi & Menyuk, 1991*). This is the regime of nonlinear diffusion and irreversible chaotic mixing of orbits.

The trapping half width and bounce frequency for a nonrelativistic particle interacting resonantly with an electromagnetic wave are given by *Karimabadi et al. (1992)* as,

$$\Delta p_{\parallel}^{(n)} = 2|M Z_n|^{1/2} \quad \text{and} \quad \omega_b^{(n)} = k_{\parallel} \left| \frac{Z_n}{M} \right|^{1/2}, \quad (2.65)$$

where  $M = m/(1 - 1/N_{\parallel}^2)$ , the parallel refractive index is  $N_{\parallel} = k_{\parallel} c/\omega$  and

$$\begin{aligned} Z_n = & mc^2 \left\{ \frac{v_{\perp}}{2c} \left[ \left( \epsilon_2 - \frac{k_{\parallel}}{k} \sigma \epsilon_1 \right) J_{n-1}(k_{\perp} \rho) - \left( \epsilon_2 + \frac{k_{\parallel}}{k} \sigma \epsilon_1 \right) J_{n+1}(k_{\perp} \rho) \right] \right. \\ & \left. + \sigma \left( \frac{v_{\parallel}}{c} \frac{k_{\perp}}{k} \epsilon_1 + \epsilon_3 \right) J_n(k_{\perp} \rho) \right\}. \end{aligned} \quad (2.66)$$

The charge sign is  $\sigma = q/|q|$ , the normalized components of the wave polarization vector are  $\epsilon_1 = |q|A_1/mc^2 = |q|E_1/mc\omega$ ,  $\epsilon_2 = |q|A_2/mc^2 = |q|E_2/mc\omega$ ,  $\epsilon_3 = |q|\phi_0/mc^2 = -|q|E_3/mc^2 k$  and the particle gyroradius is given by  $\rho = v_{\perp}/\Omega$ . The  $E_i$  are the components of the electric field polarization vector and the  $A_i$  refer to the components of the polarization vector for the magnetic vector potential:

$$\begin{aligned} \mathbf{A} = & A_1 \frac{k_{\parallel}}{k} \sin \psi \mathbf{e}_x + A_2 \cos \psi \mathbf{e}_y + \\ & - A_1 \frac{k_{\perp}}{k} \sin \psi \mathbf{e}_z + x B_0 \mathbf{e}_y = \mathbf{A}_{em} + x B_0 \mathbf{e}_y \end{aligned} \quad (2.67)$$

in which  $\psi = k_{\perp} x + k_{\parallel} z - \omega t$ . The subscripts 1, 2 and 3 refer to vector components relative to a Cartesian coordinate system with basis vectors defined by:

$$\mathbf{e}_1 = \frac{\mathbf{k} \times (\mathbf{k} \times \mathbf{B})}{|\mathbf{k} \times (\mathbf{k} \times \mathbf{B})|}; \quad \mathbf{e}_2 = -\frac{\mathbf{k} \times \mathbf{B}}{|\mathbf{k} \times \mathbf{B}|}; \quad \mathbf{e}_3 = \frac{\mathbf{k}}{|\mathbf{k}|}, \quad (2.68)$$

hence, the  $\mathbf{e}_i$  form a natural basis for the specification of the polarization relative to  $\mathbf{k}$ .

Particles in resonance with a single finite amplitude fluctuation undergo a finite amplitude nonlinear oscillation, given by half peak-to-peak difference in the particle velocity parallel component,  $v_{\parallel}$ . The trapping associated with each resonance is proportional to  $\delta b^{1/2}$ , where  $\delta b$  is the normalized wave amplitude,  $\delta B/B_0 = \delta b$ .

We can distinguish between two different cases:

- $\delta b \ll 1$ : neighboring resonances are well separated and the particle motion is periodic.
- $\delta b \sim 1$ : adjacent resonances overlap and the motion becomes random or chaotic. The particle can then sample several resonances and gain large energies in the process.

In the derivation of Eq. 2.65 and Eq. 2.66, it is also assumed that each resonance,  $n$ , is well separated from adjacent resonances, which is not always the case when relativistic effects and oblique wave propagation are taken into account. Furthermore, the trapping width is independent of wave phase, which is also an approximation. The full trapping width, including wave phase, can only be obtained by numerical simulation (*Ginet & Heineman, 1990*). Nevertheless, as discussed by *Karimabadi et al. (1992)*, the trapping half width and the bounce frequency as given by Eq.(2.65) with Eq.(2.66) are useful estimates even when these conditions are not rigorously satisfied. For example, when used in conjunction with the quasilinear diffusion coefficient, they yield considerable physical insight into the diffusion process.



# Model and Basic Equations

The aim of this work is to study the behavior of charged particles in presence of one or more resonant waves, as well as of a broad band slab spectrum, in order to understand the conditions for magnetic moment conservation and the nature of its change, when it is not conserved. We assume that there are no electric fields and that

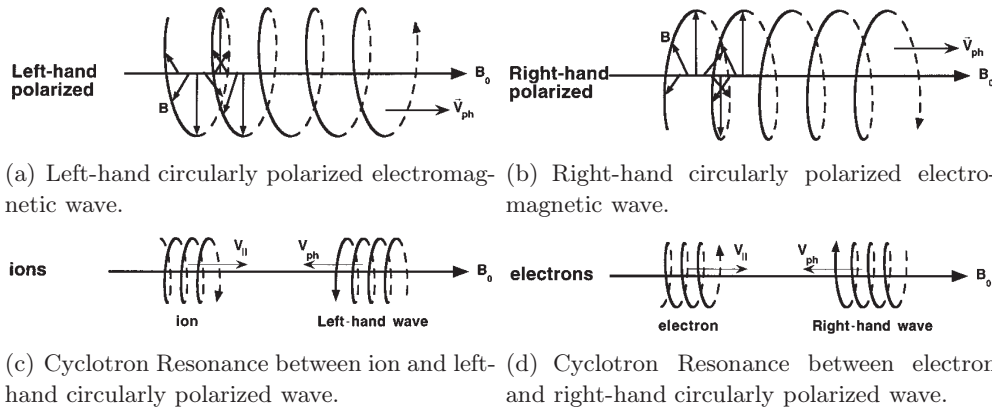


**Figure 3.1:** Schematic representation of wave polarizations (Fig. 3.1(a) and Fig. 3.1(b)) and their interaction with ion (Fig. 3.1(c)) and electron (Fig. 3.1(d)).

our test particles are in resonance with a single or more circularly polarized Alfvén waves, propagating in the direction parallel to a steady background magnetic field,  $\mathbf{B}_0 = B_0 \mathbf{e}_z$ . Figure 3.1(a) and Figure 3.1(b) illustrate the spatial variation of the wave (perturbation) magnetic vector as a function of distance along the magnetic field. Here, we illustrate circularly polarized, parallel-propagating, electromagnetic waves. There are two basic types of polarization, left-handed (Figure 3.1(a)) and right-handed (Figure 3.1(b)). Elliptical or linear polarizations are combinations of these two fundamental polarizations. The wave polarization is defined by the sense of rotation of the wave field with time at a fixed location. The sense is with respect to the ambient magnetic field and is independent of the direction of propagation. Figure 3.1(c) and Figure 3.1(d) schematize the normal cyclotron resonance between waves and charged particles. Left-hand positive ions, Figure 3.1(c), interact with left-handed waves, while right-hand negative electrons, Figure 3.1(d), interact with right-handed waves. Since waves and particles approach each other,  $\mathbf{k} \cdot \mathbf{v}$  has a negative sign. Thus, the Doppler shift term,  $-\mathbf{k} \cdot \mathbf{v}$ , in Eq. 2.14 is a positive one.

Because we are looking at the proton motion ( $\Omega = qB/m > 1$ ) and because resonance occurs for the wave component rotating in the same sense as ions, we use

the left-hand polarized component of the field (see also discussion in Section 2.2). To give an example, when only a single wave is present, the resulting magnetic field is given by:

$$\mathbf{B} = \mathbf{B}_\perp + \mathbf{B}_0 = \delta\mathbf{B}_x \cos(k_0 z) - \delta\mathbf{B}_y \sin(k_0 z) + B_0 \mathbf{e}_z, \quad (3.1)$$

where the mean magnetic field,  $B_0$ , is chosen in the  $z$ -direction,  $\delta B_x$  and  $\delta B_y$  are the amplitudes of the wave in the  $x$  and  $y$  directions, respectively, and  $k_0$  is the wave number. Because in a circularly polarized wave the  $x$  and  $y$  component of the field must have the same amplitude, we also assume  $\delta B_x = \delta B_y = \delta B$ .

First, the fields are assumed to be magnetostatic (see for more details Section 3.1.1). This amounts to the auxiliary assumption that the average particle speed is well in excess of the phase speed of the underlying linear wave mode. We ignore nonlinear wave-wave couplings in the spirit of quasilinear theory (see e.g., *Kennel & Petschek, 1966*; *Swanson, 1989*; *Stix, 1992*), which, for our purposes, shall be assumed to be magnetohydrodynamic (MHD) Alfvén waves, propagating with  $\omega/k = \omega/k_\parallel \simeq \pm v_a$ . With this assumption the magnetostatic approximation can be translated as  $|\mathbf{v}| \gg v_A$  (strictly  $|v_\parallel| \gg v_A$ ). Since particle energy is conserved in a frame moving at the parallel component of the phase velocity of the wave,  $\omega/k_\parallel$ , through (*Kennel & Petschek, 1966*):

$$(v_\parallel - \omega/k_\parallel)^2 + v_\perp^2 = \text{const},$$

this assumption, which sets  $\omega/k_\parallel = 0$ , guarantees particle energy conservation, i.e., it prohibits diffusion in energy and limits the resonant interaction in velocity space to diffusion in pitch angle and gyrophase only. Finally, we ignore all interparticle correlations that might come about through mutual interaction through their microfields (essentially Coulomb collisions, Debye shielding, and polarization) and, moreover, the contribution to the overall macroscopic fields from the charged particles is ignored. That is, we consider only test particles in prescribed macroscopic magnetostatic fields.

The behavior of a test particle is described by its time dependent position  $\mathbf{r}(t)$  and three dimensional velocity  $\mathbf{v}(t)$ , that are advanced according to  $d\mathbf{r}/dt = \mathbf{v}$  and the Lorentz force equation:

$$m \frac{d\mathbf{v}}{dt} = q \left[ \mathbf{E} + \frac{1}{c} (\mathbf{v} \times \mathbf{B}) \right] \quad (3.2)$$

The essence of test particle simulations is that the electric  $\mathbf{E}$  and the magnetic  $\mathbf{B}$  field are not influenced by the particle motion.

Normalization quantities used in this case are listed in Table (3.1). The quantity  $\tau_A$  is called the Alfvén crossing time and, if the particle is interacting with a turbulent wave spectrum, is defined as  $\tau_A = \lambda/v_A$ , where  $v_A$  is the linear speed in the Alfvén background plasma and  $\lambda$  is of the order of the turbulence correlation length,  $\lambda_c$ . In other words,  $\tau_A$  is the time it takes for an Alfvén wave to travel approximately one turbulence correlation length. This is an important time, especially when there

**Table 3.1:** Normalization quantities.

|                             |   |
|-----------------------------|---|
| Arbitrary length scale      | $\hat{L} = \lambda$                                   |
| Characteristic Alfvén speed | $\hat{v} = v_A$                                       |
| Unit transit time           | $\hat{t} = \tau_A = \lambda/V_A$                      |
| Magnetic field              | $\hat{B} = \sqrt{4\pi\rho}v_A$                        |
| Electric field              | $\hat{E} = (V_A/c)\hat{B} = V_A^2/(c\sqrt{4\pi\rho})$ |

is time dependence and dynamics of the turbulence. For the static case, one could as well normalize to another speed, e.g., the light speed ([Minnie \*et al.\*, 2005](#)). If a diffusive random walk has to occur, this could be a critical timescale in determining this behavior. Instead, if we consider a particle interacting with a single or few Alfvén waves, of course it is not possible to define a turbulence correlation length and our typical length scale is totally arbitrary.

At first sight, the introduction of an Alfvén speed into our test particle model, when the waves are treated as magnetostatic, seems somewhat artificial. However, the magnetostatic assumption is valid here provided that  $|v_{\parallel}| \gg v_A$  and this mere fact warrants the introduction of the Alfvén speed as a base unit of velocity. The background plasma plays a passive role in that it is the background plasma, which determines  $v_A$ . Thus, a particular turbulent plasma state is specified, in our abstract model, by the two quantities  $\delta B/B_0$  and  $v_A$ . In addition, we introduce  $v_A$  here in anticipation of future work, where we will drop the magnetostatic assumption. With our choice of normalization quantities, Table (3.1), the dimensionless equations of motion of our charged test particles become:

$$\frac{d\mathbf{r}}{dt} = \mathbf{v} \quad (3.3)$$

$$\frac{d\mathbf{v}}{dt} = \beta(\mathbf{E} + \mathbf{v} \times \mathbf{B}) \quad (3.4)$$

The parameter  $\beta = \Omega\tau_A$ , which arises in Eq.(3.3) as a consequence of our choice of normalizations ( $\alpha$  parameter in [Ambrosiano \*et al.\*, 1988](#)), has a number of important physical interpretations. Indeed, it couples particle and field relative spatial as well as temporal scales and provides a particularly useful means to relate our abstract numerical experiment to real space and astrophysical plasma situations. For example:

$$\beta = \Omega\tau_A = 2\pi\frac{\tau_A}{\tau_g} = \frac{\omega_{pi}\lambda}{c} = \omega_{pi}\tau_c \quad (3.5)$$

where  $\tau_g = 2\pi/\Omega$  is the test particle gyroperiod;  $\omega_{pi} = (4\pi_0q_i^2/m_i)^{1/2}$  is the ion plasma frequency in the background plasma, where  $q_i$  and  $m_i$  are, respectively, the charge and mass of a background ion;  $\tau_c = \lambda/c$ , where  $c$  is the speed of light. Other important test particle parameters can be expressed in terms of  $\beta$  in a easy way. For example, the test particle gyroradius  $\rho_L$  and maximal gyroradius  $r_L$  (or Larmor



radius) are, respectively, given by

$$\rho_L = \frac{v_\perp}{\Omega} = \frac{v_\perp/v_A}{\beta} \lambda, \quad r_L = \frac{v}{\Omega} = \frac{v/v_A}{\beta} \lambda.$$

We can also express the resonant condition for the static case,  $\omega = 0$ , in terms of the  $\beta$  parameters as follow,

$$k_{res} \lambda = \frac{n\beta}{\alpha(v/v_A)} = \frac{n\beta}{(v_\parallel/v_A)} \quad (3.6)$$

In general, in a turbulent collisionless plasma, the bandwidth of the inertial range fluctuations may extend from large fluctuations near the correlation scale,  $\lambda_c$ , to small fluctuations near the ion inertial scale. In this case one expects that  $\beta \gg 1$ . This also means that the turbulent time scales are much slower than the typical particle gyroradius (*Goldstein et al., 1986*).

The particles are moved using a Runge-Kutta fourth-order time integration method, with an adaptive time step calculation (pp. 708-716, *Press et al., 1992*). The entire simulation run was broken down into a number of substeps, each with time interval  $\delta t \ll T_{max}$ , where  $T_{max}$  is the total length of the run. The routine stepped each particle in turn through the time interval,  $dt$ , while maintaining a local relative accuracy of  $racc = 10^{-9}$  at each step. This process was repeated until the run ended and all particles had been stepped through the time interval for the entire run,  $T_{max}$ .

The numerical code that we use was developed by the group of Prof. William H. Matthaeus at Bartol Research Institute, University of Delaware. This code is a parallel implementation of a versatile algorithm for computation of streamlines, magnetic field lines, or charged particle trajectories, based on the Portable MPI (Message Passing Interface) standard. The code works by programming the master node to pass out jobs to the worker nodes. Each job includes the initial data and some parameters. Load balancing is achieved in a standard way: when a node has finished a job, it asks the master if there is another job to do. The results of each job are written to disk. Test of the code are shown in Appendix B.2. The same Appendix contains some of the results obtained in the study of particle interaction with one circularly polarize waves as well as a flat wave spectrum, that can be considered ad additional test for the code (Dalena et al 2, in prep).

### 3.1 The slab model

A particularly simple model of plasma turbulence is the so-called *slab model* (*Jokipii, 1966; Bieber et al., 1994*). Turbulence is assumed to be a sum of right and left hand circularly polarized, parallel propagating, nondispersive plane Alfvén waves. In this model the wave vector is parallel to the direction of the mean field and the magnetic field fluctuations in this component are perpendicular to both the parallel wave vector and the mean field, as shown in Figure 3.2(a). This is motivated by Alfvénic

or slab-like waves in the solar wind propagating along the mean field. From the definition of the slab field, the fluctuation depends only on  $z$  component, not on  $x$ - or  $y$ -components, as evident in Figure 3.2(b), where trajectories of two different field lines in a pure slab turbulence are shown. Therefore, if we consider the slab fluctuation in the  $x - y$  plane at each  $z$ ,  $\mathbf{b}_{slab}$  is the same along that plane but different from the field on other planes, as shown in Figure 3.2(a). For this study it is assumed that the turbulence is static in time for all practical purposes. This yields a turbulence spectrum that has finite width in  $k$  but zero width in  $\omega$ .

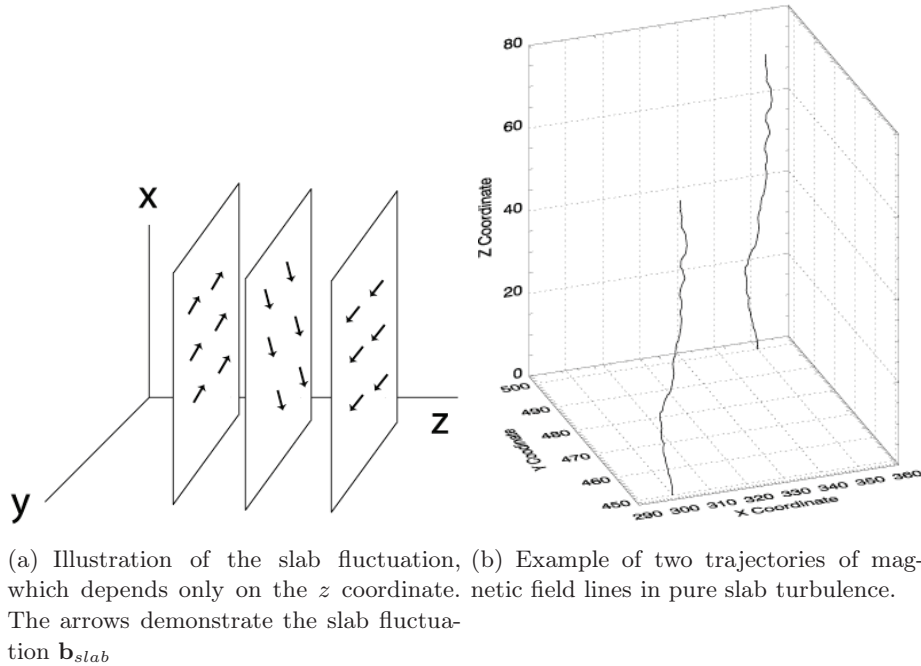


**Figure 3.2:** Illustration of the slab model

### 3.1.1 The magnetostatic assumption

If the Alfvén waves are all propagating in the same direction, the magnetostatic assumption is uniformly valid. Indeed, since all the waves have the same phase velocity, it is possible to transform to the wave frame moving with  $\omega/k_{\parallel} = v_A$ , for all  $k_{\parallel}$ . Turbulence is static in this frame, independently of the transformed particle velocity. This approach has been used mainly in studies of the pitch angle diffusion of cometary newborn ions, where the upstream MHD waves are assumed to be propagating in one direction only (Ziebell, 1990). It is important to mention that, for large wavenumbers, Alfvén and magnetosonic waves become dispersive and the rigorous application of this model must impose some upper cutoff on the allowable wavenumber.

However, in some problem, for example cosmic ray studies, the waves are as-

sumed to be propagating both parallel and antiparallel to the background magnetic field,  $\mathbf{B}_0$ . In this case, the assumption that permits to treat the turbulence as static is  $|v_{\parallel}| \gg v_A$ . This condition is not uniformly valid for all particle velocities and, when a particle moves with  $|v_{\parallel}| < v_A$ , no matter how relativistic it might be, the assumption of magnetostatic fields breaks down. Such particles are characterized by pitch angles  $\theta \simeq \pi/2$ , relative to the mean field,  $\mathbf{B}_0$ . Coincidentally, this is the regime where the quasilinear theory of pitch angle diffusion in magnetostatic fields breaks down (*Jones et al., 1973; Voelk, 1975; Jones et al., 1978*).

It is our point of view that the slab model, applied to particles diffusion, is fundamentally flawed at  $v_{\parallel} \simeq 0$ . Instead of trying to fix the vanishing of the diffusion coefficient,  $D_{\alpha\alpha}$ , as  $\theta \rightarrow \pi/2$ , it is our opinion that the actual underlying model must be changed in this regime. The magnetostatic assumption must be relaxed because there will always be particles with  $|v_{\parallel}| < v_A$  in the vicinity of  $\theta \simeq \pi/2$ . To add further support to this view, it is to be noted that particles with  $v_{\parallel}/v \simeq 0$  resonate with higher wavenumbers. In high beta plasmas, as the solar wind, Alfvén waves exhibit significant dispersion at larger wavenumbers,  $kc/\omega_{pi} \sim 1$ , as we have already mentioned. There is, therefore, no frame of reference where all wave parallel phase velocities vanish simultaneously. Thus, the magnetostatic assumption is violated not only from the particle perspective, but also from the wave perspective.

Notwithstanding these comments, the slab model, applied in the first sense mentioned above, is useful from the point of view of numerical simulations. It is limited to wavenumbers  $|k_{\parallel}| < \Omega/v_A = \omega_{pi}/c$ , that rules out particles with pitch angles close to  $\pi/2$ . Alternatively, one may adopt a model that sets the wave power to zero above  $k_{\parallel} = \Omega/v_A = \omega_{pi}/c$ , whence the diffusion coefficient becomes rigorously zero for  $|\alpha| < v_A/v$ , obviating the discussion of resonance gap effects due to the breakdown of quasilinear orderings (*Ziebell, 1990*). Hereinafter, we shall be concerned primarily with the slab model in the first interpretation.

Since the turbulence is viewed as static in the Alfvén frame, the electric field vanishes. The dispersionless assumption rules out phase mixing and, hence, phase decorrelation due to this process. Consequently, the only way for a particle to see a “wavepacket” decorrelate in phase is to transit an autocorrelation length of the turbulent spectrum (*Kaiser et al., 1978*). The autocorrelation time in this case reduces to

$$\tau_{ac} = \frac{1}{|\Delta(\omega - k_{\parallel}v_{\parallel})|} = \frac{1}{|v_{\parallel}\Delta k_{\parallel}|} \simeq \frac{\lambda_c}{|v_{\parallel}|}, \quad (3.7)$$

where  $\lambda_c$  is the turbulence correlation length. One immediately notices a problem at  $v_{\parallel} \simeq 0$ , because the autocorrelation time tends to infinity. In this limit, the slow transit of a stationary wavepacket leads to behavior that can violate the quasilinear assumption, Eq. 2.13, as we noted above. Dispersive effects cure this pathological behavior of  $\tau_{ac}$ , so they really should be included when modelling diffusion at  $v_{\parallel} \simeq 0$ . Dynamical turbulence models have a similar effect (see also, *Bieber et al., 1994*).

### 3.1.2 Correlation function and power spectrum

The MHD turbulence spectrum is important because it is a characteristic property of turbulent fluid. In MHD turbulence each component ( $x, y, z$ ) of the magnetic field can be written as the sum of a mean term plus a fluctuating part with zero mean:

$$B_i = \langle B_i \rangle + b_i \quad \text{for } i = x, y, z. \quad (3.8)$$

An important statistical quantity, that give us important information about the spatial structure of the turbulent magnetic field, is the *two-point correlation or function*, defined as:

$$R_{i,j}(\mathbf{x}, \mathbf{r}) = \langle b_i(\mathbf{x})b_j(\mathbf{x} + \mathbf{r}) \rangle, \quad (3.9)$$

where  $i$  and  $j$  represents the  $x, y$  and  $z$  components. For homogeneous turbulence, the correlation function is independent of  $\mathbf{x}$ , so we can write:

$$R_{i,j}(\mathbf{r}) = \langle b_i(0)b_j(\mathbf{r}) \rangle, \quad (3.10)$$

The correlation function  $R_{i,j}$  tell us how the magnetic field at two different points is correlated. Because the magnetic field at a given point,  $\mathbf{x}$ , should correlate more highly with itself than with that at other points, if we consider the correlation function of the  $x$  component, the highest value is:

$$R_{x,x}(0) = \langle b_x^2(0) \rangle, \quad (3.11)$$

The Fourier transform of the correlation function,  $R_{i,j}(\mathbf{r})$ , is called the *power spectrum*,  $P_{i,j}(\mathbf{k})$ :

$$P_{i,j}(\mathbf{k}) = \frac{1}{(2\pi)^3} \int_{-\infty}^{\infty} R_{i,j}(\mathbf{r}) e^{i\mathbf{k}\cdot\mathbf{r}} d^3\mathbf{r}, \quad (3.12)$$

where  $\mathbf{k}$  is the wave vector. The correlation function can be written as the inverse Fourier transform:

$$R_{i,j}(\mathbf{r}) = \frac{1}{(2\pi)^3} \int_{-\infty}^{\infty} P_{i,j}(\mathbf{k}) e^{-i\mathbf{k}\cdot\mathbf{r}} d^3\mathbf{k}. \quad (3.13)$$

We can define the correlation function for the slab fluctuations as:

$$R_{i,j}^{slab}(z) = \langle b_i^{slab}(0)\delta b_j^{slab}(z) \rangle. \quad (3.14)$$

Other important quantities, related to the correlation function and the power spectrum, are the correlation length,  $\lambda_c$ , for the slab turbulence and the parallel coherence length,  $l_z$ . The slab correlation length is defined as:

$$\lambda_c = \frac{\int_0^{\infty} R_{xx}^{slab} dz}{R_{xx}^{slab}(z=0)} = \quad (\text{from Eq. 3.11}) \quad = \frac{\int_0^{\infty} R_{xx}^{slab} dz}{\langle b_{x,slab}^2 \rangle} = \frac{\int_0^{\infty} R_{xx}^{slab} dz}{\delta b_{x,slab}^2}, \quad (3.15)$$

where  $\delta b_{x,slab}^2$  is the mean square fluctuation. One interpretation of Eq. 3.15 is that the area of the rectangle  $\lambda_c \times R_{xx}^{slab}(0)$  equals the area under the  $\lambda_c \times R_{xx}^{slab}(z)$  plot, as shown in Figure 3.3.

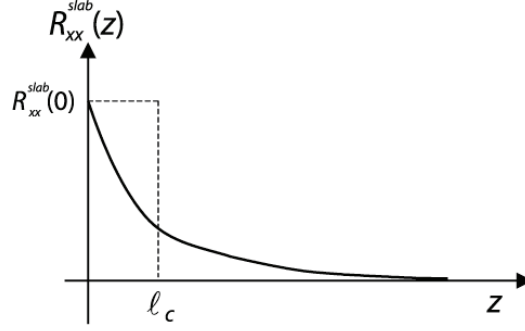


**Figure 3.3:** The correlation function  $R_{xx}^{slab}$  and its relationship with the correlation length  $\lambda_c$ .

The power spectrum for the slab model and the correlation function can be written as:

$$P_{xx}^{slab}(k_z) = \frac{1}{2\pi} \int_{-\infty}^{\infty} R_{xx}^{slab}(z) e^{ik_z z} dz \quad (3.16)$$

$$R_{xx}^{slab}(k_z) = \frac{1}{2\pi} \int_{-\infty}^{\infty} P_{xx}^{slab}(k_z) e^{-ik_z z} dk_z \quad (3.17)$$

The function we use for the slab power spectrum in numerical simulation is:

$$P_{xx}^{slab} = \frac{C_{slab}}{[1 + (k_z l_z)^2]^\nu}, \quad (3.18)$$

where  $\nu$  is the spectral index;  $l_z$  is the coherence length associated with  $k_{l_z} = 1/l_z$ , where the spectrum bends over to the inertial range;  $C_{slab}$  is a normalization constant, chosen to ensure that  $\langle \delta B^2 \rangle / B_0$  took on the desired value, e.g., 0.01, 0.1, etc, and can be determined by the turbulence energy. From Eq. 3.15, rewriting the correlation function in terms of the power spectrum, we have:

$$\lambda_c = \frac{1}{2\pi} \frac{\int_0^\infty \int_{-\infty}^\infty P_{xx}^{slab}(z) e^{-ik_z z} dk_z dz}{\delta b_{x,slab}^2}$$

Integrating over  $z$  (using  $\delta(k) = (\int_{-\infty}^\infty \exp -ikx dx) / 2\pi$ ), we get:

$$\begin{aligned} \lambda_c &= \frac{1}{2} \frac{\int_{-\infty}^\infty P_{xx}^{slab}(k_z) \delta(k_z) dk_z}{\delta b_{x,slab}^2} = \\ &= \frac{P_{xx}^{slab}(0)}{2\delta b_{x,slab}^2} \end{aligned} \quad (3.19)$$

Now, we can set  $P_{xx}^{slab}(0) = C_{slab}$  in Eq. 3.18. In order to find the relation between  $\lambda_c$  and  $l_z$  and write the constant  $C_{slab}$  in terms of  $l_z$ , let substitute the function  $P_{xx}^{slab}$ , as in Eq. 3.18, in  $R_{xx}^{slab}(0)$  :

$$R_{xx}^{slab}(0) = \delta b_{x,slab}^2 = \int_{-\infty}^\infty P_{xx}^{slab}(k_z) dk_z = \frac{1}{2\pi} \int_{-\infty}^\infty \frac{C_{slab}}{[1 + (k_z l_z)^2]^\nu} dk_z$$

From this equation we obtain:

$$C_{slab} = \frac{2\pi\delta b_{x,slab}^2}{\int_{-\infty}^{\infty} [1 + (k_z l_z)^2]^{-\nu} dk_z}. \quad (3.20)$$

From *Gradshteyn & Ryzhik* (1980, pag. 341),

$$\int_0^{\infty} \frac{x^{\mu-1}}{(p+qx^\gamma)^{n+1}} dx = \frac{1}{\gamma p^{n+1}} \left(\frac{p}{q}\right)^{\frac{\mu}{\gamma}} \frac{\Gamma\left(\frac{\mu}{\gamma}\right) \Gamma\left(1+n-\frac{\mu}{\gamma}\right)}{\Gamma(1+n)},$$

where  $0 < \mu/\gamma < n+1$ ,  $p \neq 0$ ,  $q \neq 0$ . Using  $\mu = \gamma = 2$ ,  $n+1 = \nu$  (the spectral index),  $p = 1$  and  $q = l_z^2$ , the integral in Eq. 3.20 becomes:

$$\int_{-\infty}^{\infty} \frac{1}{[1 + (k_z l_z)^2]^\nu} dk_z = \frac{1}{l_z} \frac{\Gamma\left(\frac{1}{2}\right) \Gamma\left(\nu - \frac{1}{2}\right)}{\Gamma(\nu)}.$$

Then, using the fact that  $\Gamma(1/2) = \sqrt{\pi}$ , we obtain:

$$C_{slab} = 2\sqrt{\pi} \frac{\Gamma(\nu)}{\Gamma(\nu - 1/2)} \delta b_{x,slab}^2 l_z \quad (3.21)$$

Finally, substituting  $P_{xx}^{slab} = C_{slab}$  in Eq. 3.15 we find:

$$\lambda_c = \frac{\sqrt{\pi}\Gamma(\nu)}{\Gamma(\nu - 1/2)} l_z \quad (3.22)$$

Set  $\nu = 5/6$  provides  $P_{xx}^{slab} \propto k^{-5/3}$  Kolmogorov inertial range, for  $|k| \gg 1/l_z$ , consistent with the solar wind observations. For this case we obtain

$$\lambda_c = 0.747l_z. \quad (3.23)$$

## 3.2 Slab magnetostatic turbulent fields generation

The test particle simulations are carried out in a unidimensional box of length  $L = 10000l_z$ . The magnetic field,  $\mathbf{B}(z)$ , is stored on a grid of spacing  $\Delta z = L/N_z$ , where  $N_z$  is an even integer which we fixed at  $N_z = 2^{28} = 268,435,456$ . The magnetic field configuration is generated through a spectrum  $P(k)$  in  $k$  space. The field grids in real space are then produced via inverse fast Fourier transform (FFT).

For our one-dimensional field configuration, the turbulent magnetic field satisfied  $\delta B_x(z)\hat{e}_x + \delta B_y(z)\hat{e}_y$ , with the full magnetic field given by:

$$\mathbf{B}(z) = B_0\hat{e}_z + \delta\mathbf{B}(z), \quad (3.24)$$

and clearly  $\nabla \cdot \mathbf{B}(z) = 0$ , identically.

The vectors denoting the FFT of  $\delta\mathbf{B}(z_m)$  ( $m = 1, 2, 3, \dots, N_z$ ) are generated through

$$\begin{aligned} \delta B_x(k_n) &= [P(k_n)]^{1/2} e^{i\Phi_n} \\ \delta B_y(k_n) &= [P(k_n)]^{1/2} e^{i\Psi_n} \end{aligned}$$

**Table 3.2:** Characteristic scales in the spectrum.

| Number of grid points            | Wave vector value               |
|----------------------------------|---------------------------------|
| $N_{kmin} = 1$                   | $k_{min} = 6.28 \times 10^{-4}$ |
| $N_{kl_z} = 1600$                | $k_{l_z} = 1$                   |
| $N_{k_{diss}} = 1.6 \times 10^6$ | $k_{diss} = 10^3$               |
| $N_{k_{MAX}} = 6.7 \times 10^7$  | $k_{MAX} = 4.2 \times 10^4$     |
| $N_{k_{MAX1}} = 1.3 \times 10^8$ | $k_{MAX1} = 8.4 \times 10^4$    |

where  $k_n = 2\pi n/L$  is the discrete wavenumber with spacing  $\Delta k = 2\pi/L$ ;  $\Phi_n$  and  $\Psi_n$  are randomly selected phases;  $P(k)$  is the spectral shape function given by:

$$P(k_n) = \begin{cases} P^{slab}(k_n) = C_{slab}[1 + (k_n l_z)^2]^{-5/6}, & \text{for } k_n < k_{diss} \\ P^{diss}(k_n) = C_{diss} \left( \frac{k_n}{k_{diss}} \right)^{-7/3}, & \text{for } k_n \geq k_{diss} \end{cases} \quad (3.25)$$

where  $C_{slab}$  is the constant for the slab model given by Eq. 3.21;  $k_{diss}$  is the wavenumber at the beginning of the dissipation range;  $C_{diss}$  is the constant for the part of the spectrum corresponding to the dissipation range, determined by the fact that the spectrum must not have discontinuities in  $k$ -space:

$$P^{slab}(k_{diss}) = P^{diss}(k_{diss}) \quad \longrightarrow \quad C_{diss} = C_{slab}[1 + (k_{diss} l_z)^2]^{-5/6}.$$

The vectors of Fourier coefficients are zero-padded from  $N_{max} + 1$  to  $N_z$ , providing an extra level of smoothness to the fields by an effective trigonometric interpolation. In all the simulations, we set  $N_{max} = 6.7 \times 10^7$ . With this high level of smoothness in the fields, we used simple linear interpolation to evaluate the fields at the test particle position. The actual  $\delta B_x(z_m)$  and  $\delta B_y(z_m)$  are generated from the above discrete Fourier transforms through use of the inverse one-dimensional FFT.

### 3.2.1 Importance of scale separation

The spectrum generated by our numerical simulation is shown in Figure 3.4. As evident from the figure, there are several scales of importance, characterized by different wavenumber, labeled in Figure 3.4 as:  $k_{min}$ ,  $k_{l_z}$ ,  $k_{diss}$ ,  $k_{max}$ ,  $k_{N_z}$ . As we showed in the previous section, in the model the discrete wavenumber are given by  $k_n = 2\pi n/L$ , where  $L = 10000l_z$  is the boxlength,  $l_z = 1$  is the coherence length for the slab spectrum, used as the characteristic length of the system,  $n = N_k$  are the number of points for the considered  $k_n$ . We have:

$$k_n = \frac{2\pi n}{L} = (6.28 \times 10^{-4})n \quad \text{and} \quad n = N_k = \frac{L}{2\pi}k = 1600k \quad (3.26)$$

From the above relations, in Table 3.2 are summarized the values for  $k$  and  $N_k$  used in our simulations.

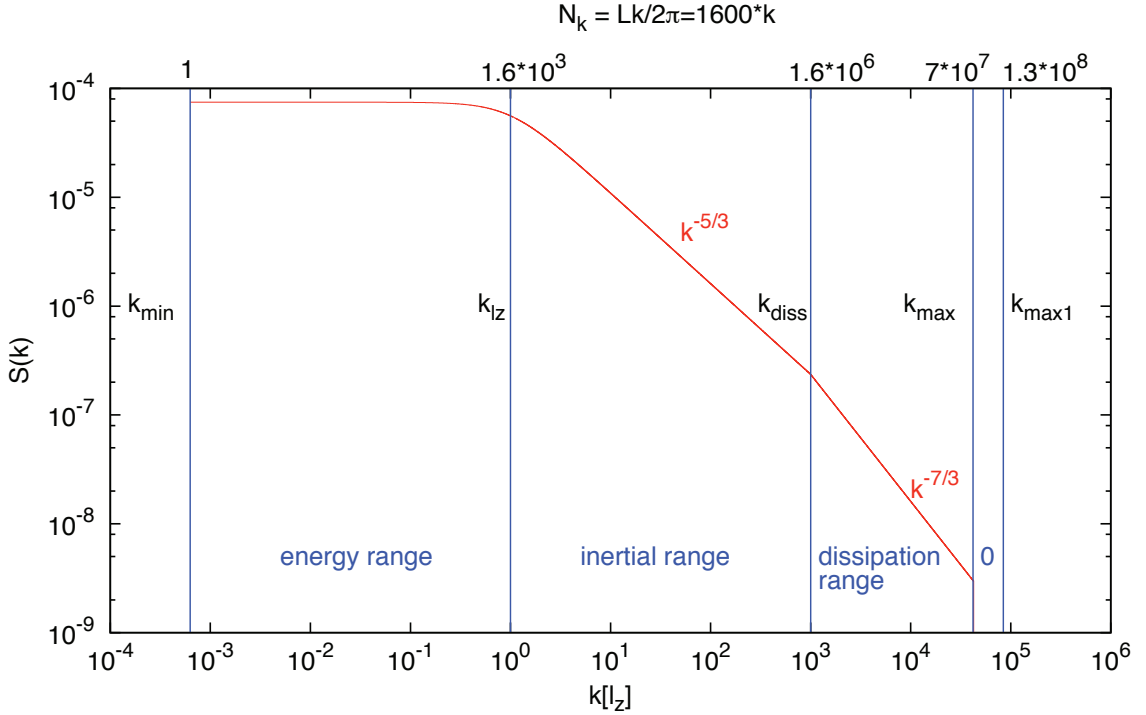


**Figure 3.4:** Power spectrum from numerical simulation of our magnetic field turbulent mode.  $k$  is normalized to the coherence length,  $l_z$ .

- $k_{min} = 2\pi/L$  is the minimum wave vector of the spectrum, corresponding with  $N_k = N_{kmin} = 1$ .
- $k_{l_z} = 1/l_z = 1$  is the threshold wave vector of the spectrum, corresponding with  $l_z$ , that mark the beginning of the *inertial range*. Three decades of the *energy containing scale*, from  $k_{min}$  to  $k_{l_z}$ , ensure turbulence homogeneity.  $l_z$  (or  $\lambda_c = 0.747l_z$ ) is also the typical scale for pitch angle diffusion. It is really important that there is power before  $\lambda_c$ , that means  $\lambda_c$  must be not at the beginnings of the spectrum. This condition, for example, rules out flat-like spectrum, where the same amount of energy is distributed for each wavevector, for a good descriptions of diffusion. Indeed, because  $\lambda_c \propto P(0)/R(0)$ , if  $P(0) = 0$   $\lambda_c = 0$ , too, and there can not be  $\alpha$ -diffusion. Three decades of the inertial range, characterized by  $P(k) \propto k^{-5/3}$ , well represent the solar wind case.
- $k_{diss}$  is the wavevector corresponding to the beginning of the *dissipation range*. After  $k_{diss}$  we could set  $P(k) = 0$ , but the problem in this case is that  $k_{diss}$  is strictly related with the *resonance gap* of pitch angle diffusion coefficient,  $D_{\alpha\alpha}$ , predicted by QLT ( $\delta b \ll 1$ ) for  $\alpha_{min} = 0$ . Indeed,  $\alpha_{min} = 1/(rLk_{diss})$  and, if there is a sharp cut-off of the spectrum at a scale corresponding to  $k_{diss}$ , there will be a sharp cut-off in  $D_{\alpha\alpha}$ , too. There are different ways to cross the  $\alpha_{min}$  barrier and to allow that particles fill both the  $\alpha$ -hemispheres. One



way is to use time dependent model for the magnetic field, so that the barrier is crossed thanks to  $\Delta\alpha$  time-variation. Another possibility is to overtake the QL approximation and use large  $\delta b$  values; in this way the barrier is crossed thanks to the resonance broadening effects. The last possible solution, that we used in our model, is to extent the spectrum after  $k_{diss}$  with  $P(k) \propto k^{-7/3}$ . Because  $k_{diss} = 1/\lambda_{ii} = \omega_{pi}/c$  (where  $\lambda_{ii}$  is the ion inertial length,  $\omega_{pi}$  is the ion plasma frequency and  $c$  is the speed of light) and because typically in the solar wind at 1A.U.  $\lambda_{ii} \simeq 1000\text{km}$  and  $\lambda_c \simeq 10^6\text{km}$ ,  $k_{diss}l_z \sim \lambda_z/\lambda_{ii} \simeq 10^3$ .

- After other two decades,  $k_{MAX}$  determines the end of the dissipation range:  $k_{MAX} = \sqrt{m_i/m_e}k_{diss}$ .
- After that there are almost other two decades, from  $k_{MAX} = 4.2 \times 10^4$  to  $k_{MAX1} = 8.4 \times 10^4$ , of zero-padding, important for the trigonometric interpolations and for the smoothness of the field.
- In addition, another important scale in the model (not labeled in Figure 3.4 because depends on test-particle velocity) is the wavevector corresponding to  $z_{max} = vT_{tot}$ , the maximum trajectory of a test charged particle, moving at a speed  $v$ , in the simulation running time  $T_{tot}$ . It is really important that the boxlength,  $L$ , is large enough so that each particle trajectory is limited to a small fraction of the full length, in order to avoid periodicity effects. That means  $L \gg z_{max}$  or  $k_{min} \ll z_{max}$ . Indeed, one of the most important characteristic of 1D field lines is periodicity. In slab-like field, periodicity could have some bad repercussion on field lines diffusion, that means it is possible to find 'fake' diffusion due to periodicity of the field.

### 3.3 Velocity space diffusion coefficient $D_{\alpha\alpha}$ for slab model

For static slab turbulence the spectral density is zero unless the frequency  $\omega$  is zero, so all frequencies are set to zero through the term  $\delta(\omega)$ . Because there are no perpendicular (oblique) waves, the terms  $\delta(k_x)$  and  $\delta(k_y)$  are included. Thus, the spectral density is given by:

$$\lim_{V,T \rightarrow +\infty} \langle b_x(k, \omega) b_x^*(k, \omega) \rangle = 2\pi\delta(k_x)2\pi\delta(k_y)2\pi S(k_z)2\pi\delta(\omega) \quad (3.27)$$

where  $S(k_z) = P_{xx}(k_z)/2\pi$ ,  $V$  and  $T$  are the total volume and time, respectively, where there is turbulence  $\langle b^2 \rangle = \langle b_x^2 \rangle + \langle b_y^2 \rangle$ . Because of the symmetry in  $x$  and  $y$  directions, we furthermore assume

$$\lim_{V,T \rightarrow +\infty} \langle b_y(k, \omega) b_y^*(k, \omega) \rangle = \lim_{V,T \rightarrow +\infty} \langle b_x(k, \omega) b_x^*(k, \omega) \rangle = (2\pi)^4 \delta(k_x) \delta(k_y) \delta(\omega) \quad (3.28)$$

We have normalized so that

$$\lim_{V,T \rightarrow +\infty} \frac{1}{VT} \int \frac{d^3k}{(2\pi)^3} \int \frac{d\omega}{2\pi} \langle b_x(k, \omega) b_x^*(k, \omega) \rangle = \frac{1}{2} \langle \delta b^2 \rangle. \quad (3.29)$$

It is not difficult to show, starting for example from Eq. (1) of [Lee & Voelk \(1975\)](#), which is valid in the resonant limit ( $\text{Im}\omega \rightarrow 0$ ) that in the magnetostatic limit, setting  $k_{\perp} \rightarrow 0$ , one obtains

$$\begin{aligned} \left(\frac{\partial}{\partial t} + v_{\parallel} \frac{\partial}{\partial t}\right) f(x, \mathbf{p}, t) = & \lim_{V, T \rightarrow +\infty} \frac{\pi}{4} \left(\frac{q}{\gamma mc}\right)^2 \frac{1}{VT} \int \frac{d^3k}{(2\pi)^3} \int \frac{d\omega}{2\pi} \frac{\partial}{\partial \alpha} [\langle b_{-}(\mathbf{k}, \omega) b_{-}^{*}(\mathbf{k}, \omega) \rangle \delta(-k_{\parallel} v_{\parallel} + \Omega) \\ & + \langle b_{+}(\mathbf{k}, \omega) b_{+}^{*}(\mathbf{k}, \omega) \rangle] (1 - \alpha^2) \frac{\partial}{\partial \alpha} f(x, \mathbf{p}, t), \end{aligned}$$

where  $b_{-}(\mathbf{k}, \omega) = b_x(\mathbf{k}, \omega) - ib_y(\mathbf{k}, \omega)$  and  $b_{+}(\mathbf{k}, \omega) = b_x(\mathbf{k}, \omega) + ib_y(\mathbf{k}, \omega)$ . Assuming zero helicity,  $\langle b_x(k, \omega) b_y^{*}(k, \omega) \rangle = \langle b_x^{*}(k, \omega) b_y(k, \omega) \rangle = 0$ , we obtain the equation for the velocity diffusion coefficient  $D_{\alpha\alpha}$ :

$$\begin{aligned} D_{\alpha\alpha} = & \frac{\pi}{4} \left(\frac{q}{\gamma mc}\right)^2 \lim_{V, T \rightarrow +\infty} \int \frac{d^3k}{(2\pi)^3} \int \frac{d\omega}{2\pi} [\langle b_x(\mathbf{k}, \omega) b_x^{*}(\mathbf{k}, \omega) \rangle + \langle b_y(\mathbf{k}, \omega) b_y^{*}(\mathbf{k}, \omega) \rangle] \frac{1}{|v_{\parallel}|} \delta\left(k_{\parallel} - \frac{\Omega}{v_{\parallel}}\right) + \\ & + [\langle b_x(\mathbf{k}, \omega) b_x^{*}(\mathbf{k}, \omega) \rangle + \langle b_y(\mathbf{k}, \omega) b_y^{*}(\mathbf{k}, \omega) \rangle] \frac{1}{|v_{\parallel}|} \delta\left(k_{\parallel} + \frac{\Omega}{v_{\parallel}}\right)]. \end{aligned}$$

Finally, using Eq. 3.27 and Eq. 3.28, we arrive at:

$$D_{\alpha\alpha} = \pi \left(\frac{q}{\gamma mc}\right)^2 \frac{(1 - \alpha^2)}{v_{\parallel}} S(k_z)|_{k_z = k_{res} = \Omega/v_{\parallel}}. \quad (3.30)$$

Using our expression for the turbulent spectrum, we have:

$$D_{\alpha\alpha} = \begin{cases} \frac{\sqrt{\pi}}{2} \frac{\Gamma(\nu)}{\Gamma(\nu-1/2)} \Omega^2 \frac{l_z}{v_T} \frac{(1-\alpha^2)}{|\alpha|} \frac{\langle b^2 \rangle}{B_0^2} (1 + k_{res}^2 l_z^2)^{-\nu}, & \text{for } k < k_{diss} \\ \frac{\sqrt{\pi}}{2} \frac{\Gamma(\nu)}{\Gamma(\nu-1/2)} \Omega^2 \frac{l_z}{v_T} \frac{(1-\alpha^2)}{|\alpha|} \frac{\langle b^2 \rangle}{B_0^2} (1 + k_{diss}^2 l_z^2)^{-\nu} \left(\frac{k_{res}}{k_{diss}}\right)^{-\xi}, & \text{for } k_n \geq k_{diss} \end{cases}, \quad (3.31)$$

with  $\nu = 5/6$  and  $\xi = 7/3$ . Putting  $\nu = 1$  reduces  $D_{\alpha\alpha}$  for  $k < k_{diss}$  to Eq. (13) of [Kaiser et al. \(1978\)](#).



# Analytical and numerical results for magnetic moment conservation

---

## 4.1 Interaction between particles and a single wave

In order to understand the basic features of the non-conservation of particles magnetic moment, we start to study the ions motion in presence of a constant magnetic field,  $\mathbf{B}_0$ , plus a perpendicular circularly polarized wave. We use the left-hand polarized component of the field, rotating in the same sense as ions. In this case the resulting magnetic field is given by:

$$\mathbf{B} = \mathbf{B}_\perp + \mathbf{B}_0 = \delta\mathbf{B}_x \cos(k_0 z) - \delta\mathbf{B}_y \sin(k_0 z) + B_0 \mathbf{e}_z, \quad (4.1)$$

where the mean magnetic field,  $B_0$ , is chosen in the  $z$  direction,  $\delta B_x$  and  $\delta B_y$  are the amplitudes of the wave in the  $x$  and  $y$  directions and  $k_0$  is the wavevector assumed to lie only in the  $z$ -direction. We also assume  $\delta B_x = \delta B_y = \delta B$  for the r.m.s. average values.

### 4.1.1 Expected behavior at resonance

In the quasilinear approximation particle motion is well described by the unperturbed motion. Thus, particle velocity is given by:

$$\mathbf{v} = \mathbf{v}_\perp + \mathbf{v}_\parallel = (v_\perp \sin(\Omega t) \mathbf{e}_x, v_\perp \cos(\Omega t) \mathbf{e}_y, v_\parallel \mathbf{e}_z) \quad (4.2)$$

If the particle is in resonance with the wave:

- $v_x$  should be in phase with  $-B_y$
- $v_y$  should be in phase with  $B_x$

We are looking at the changes in the cosine of pitch angle  $\alpha$ :

$$\frac{d\alpha}{dt} \simeq \frac{dv_\parallel}{dt} = \frac{q}{m} E_\parallel = \frac{q}{m} E_z, \quad (4.3)$$

where  $E_\parallel$  is the induced electric field parallel component to the mean field. Let us calculate this component. First of all we have to insert the expression of the particle velocity, Eq. 4.2, in the expression of our magnetic field, Eq. B.8, in order to obtain the magnetic field seen by the particle,  $\mathbf{H}(t)$ :

$$\mathbf{H}(t) = \{ \delta B \cos [(k_0 v_\parallel - \omega_0)t + k_0 z_0] \mathbf{e}_x, -\delta B \sin [(k_0 v_\parallel - \omega_0)t + k_0 z_0] \mathbf{e}_y, B_0 \mathbf{e}_z \} \quad (4.4)$$

Using Eq. 4.2 and Eq. 4.4 for particle velocities and for the magnetic field, respectively, we obtain the parallel component of the induced electric field:

$$\begin{aligned} E_z &= (\mathbf{v} \times \mathbf{H})_z = v_x B_y - v_y B_x = \\ &= -v_\perp \delta B \cos \{ \Omega t - [(k_0 v_\parallel - \omega_0)t + k_0 z_0] \} \end{aligned} \quad (4.5)$$

Of course, in absence of perturbations  $\delta B = 0$ , this electric field is zero. The argument of the cosine in Eq. 4.5 is exactly the resonance condition plus a constant term,  $k_0 z_0$ . Thus, resonant particles should also have  $E_z \sim (v_\perp \delta B) \sim \text{const}$ . At resonance, i.e. during the intervals in which  $E_z \sim \text{const}$ , particle cosine of pitch angle,  $\alpha$ , and magnetic moment,  $\mu$ , must show secular changes. Of course, for particles out of resonance, the cosine of pitch angle,  $\alpha$ , the magnetic moment,  $\mu$ , and the parallel component of the induced electric field,  $E_z$ , exhibit an oscillating behavior.

#### 4.1.2 Trapping width derivation for a single circularly polarized wave

Starting from Eq. 2.65 and Eq. 2.66, we were able to derive a simplified expression for the trapping half width and the bounce frequency in the case of an Alfvén static wave. Thus, in our case,  $k_\perp = 0$  and  $\phi = 0$ . We can rewrite Eq. 2.66 as,

$$\begin{aligned} Z_n &= mc^2 \left\{ \frac{v_\perp}{2c} [(\epsilon_2 - \sigma \epsilon_1 \cos \alpha) J_{n-1}(k_\perp \rho) - (\epsilon_2 + \sigma \epsilon_1 \cos \alpha) J_{n+1}(k_\perp \rho)] \right. \\ &\quad \left. + \sigma \left( \frac{v_\parallel}{c} \epsilon_1 \sin \alpha + \epsilon_3 \right) J_n(k_\perp \rho) \right\}, \end{aligned} \quad (4.6)$$

with  $\cos \alpha = 1$  and  $\sin \alpha = 0$ . Because  $\mathbf{k} \parallel \mathbf{B}_0$ , we can choose  $\mathbf{e}_3 = \mathbf{B}_0/|\mathbf{B}_0|$ ,  $\mathbf{e}_2$  is any arbitrary direction perpendicular to  $\mathbf{e}_3$  and  $\mathbf{e}_1 = \mathbf{e}_2 \times \mathbf{e}_3$ . The vector potential could be obtained from the magnetic field,  $\nabla \times \mathbf{B}_\perp = B_x \mathbf{e}_x + B_y \mathbf{e}_y$ . In the Fourier space  $\nabla \rightarrow (ik_z \mathbf{e}_z)$  so we obtain:

$$\begin{aligned} A_x &= -\frac{i}{k_\parallel} B_y \\ A_y &= \frac{i}{k_\parallel} B_x \end{aligned} \quad (4.7)$$

Now, we assume that there is a single circularly polarized wave in space, considering separately the two different possible helicities:

$$\begin{aligned} \mathbf{B}_\pm &= (B_\pm \mathbf{e}_\pm) \exp [i(k_\parallel z)] \quad \text{where} \\ B_\pm &= \frac{1}{\sqrt{2}} (B_x \mp i B_y) \quad \text{are the complex amplitudes and} \\ \mathbf{e}_\pm &= \frac{1}{\sqrt{2}} (\mathbf{e}_x \mp i \mathbf{e}_y) \quad \text{are the orthogonal polarization unit vectors} \end{aligned}$$

The  $+$ ( $-$ ) polarization state is the positive (negative) helicity, i.e. the vector  $\mathbf{B}$  is rotating counter-clockwise (clockwise). At first, let's consider only the left-handed

Table 4.1: Wave polarization and resonance contribution to trapping width.

| Polarization       | $\eta$           | resonance $n$ |
|--------------------|------------------|---------------|
| $B_+$ left-handed  | 1 parallel       | -1            |
| $B_-$ right-handed | -1 anti-parallel | 1             |
| $B_+$ left-handed  | -1 parallel      | 1             |
| $B_-$ right-handed | 1 parallel       | -1            |

polarized wave,  $\mathbf{B}_+$ . Assuming  $B_+ = \sqrt{2}\delta B e^{-i\pi/2}$ , we can write the  $x$  and  $y$  component of the wave magnetic field as,

$$\begin{aligned} B_x &= \delta B \exp [i(k_{\parallel}z - \pi/2)] \\ B_y &= \delta B \exp (ik_{\parallel}z) \end{aligned} \quad (4.8)$$

Inserting this two expressions into Eq. 4.7, we find:

$$\begin{aligned} A_x &= \frac{\delta B}{k_{\parallel}} \exp [i(k_{\parallel}z - \pi/2)] \\ A_y &= \frac{\delta B}{k_{\parallel}} \exp (ik_{\parallel}z) \end{aligned}$$

Comparing the real parts of these equations with Eq. 2.67, we obtain an expression for the coefficients  $A_1$  and  $A_2$  and for the normalized components of the wave polarization vector,  $\epsilon_1$ ,  $\epsilon_2$  and  $\epsilon_3$ :

$$\begin{aligned} A_1 &= \eta \frac{\delta B}{k_{\parallel}} \quad A_2 = \frac{\delta B}{k_{\parallel}} \quad \text{where} \quad \eta = \frac{k_{\parallel}}{|k_{\parallel}|} \\ \epsilon_1 &= \frac{|q|\eta\delta B}{mc^2k_{\parallel}} \quad \epsilon_2 = \frac{|q|\delta B}{mc^2k_{\parallel}} \quad \epsilon_3 = 0 \end{aligned} \quad (4.9)$$

Similarly, for a right-handed circularly polarized wave,  $\mathbf{B}_-$ , we have:

$$\begin{aligned} A_1 &= -\eta \frac{\delta B}{k_{\parallel}} \quad A_2 = \frac{\delta B}{k_{\parallel}} \quad \text{where} \quad \eta = \frac{k_{\parallel}}{|k_{\parallel}|} \\ \epsilon_1 &= -\frac{|q|\eta\delta B}{mc^2k_{\parallel}} \quad \epsilon_2 = \frac{|q|\delta B}{mc^2k_{\parallel}} \quad \epsilon_3 = 0 \end{aligned} \quad (4.10)$$

In case of a single circularly polarized wave propagating parallel (or antiparallel) to the magnetic field, there is only one resonance present and particle motion is integrable *Karimabadi et al. (1992)*: indeed,  $J_n(0) = 0$ , unless  $n = 0$ . So, depending on the sense of polarization and of the wave and on its direction of propagation,  $\eta$ , only  $l = 1$  or  $l = -1$  resonances contribute to the trapping width, as shown in Table 4.1. Thus, considering Eq. 2.65, Eq. 4.6 and Eq. 4.9, with knowledge  $J_0(0) = 1$ , we find a specialized formula for the trapping half width and bounce

frequency applied to the case of a circularly polarized wave propagating parallel,  $k_{\parallel} > 0$  and  $n = -1$ , or antiparallel,  $k_{\parallel} > 0$  and  $n = 1$  to  $\mathbf{B}_0$ :

$$\begin{aligned}\Delta v_{\parallel}^{(-1)} &= 2v \left[ (1 - \alpha^2)^{1/2} |\alpha| \frac{\delta B}{B_0} \right]^{1/2} \\ \omega_b^{(-1)} &= \Omega_0 \left[ \frac{(1 - \alpha^2)^{1/2} \delta B}{|\alpha| B_0} \right]^{1/2}\end{aligned}\quad (4.11)$$

if  $k_{\parallel} v_{\parallel} > 0$  and zero otherwise, in which  $\alpha = \cos \theta$  is the cosine of pitch angle. Exactly the same set of equations hold for  $\Delta v_{\parallel}^{(+1)}$  and  $\omega_b^{(+1)}$  by using Eq. 2.65, Eq. 4.6 and Eq. 4.10, but the condition for their being nonzero is reversed, i.e.,  $k_{\parallel} v_{\parallel} > 0$ . Below we shall omit the superscripts  $(\pm 1)$  because of this degeneracy.

The pitch angle trapping half width can be obtained from these equations as:

$$\Delta \alpha = \frac{\Delta v_{\parallel}}{v} = 2 \left[ (1 - \alpha^2)^{1/2} |\alpha| \frac{\delta B}{B_0} \right]^{1/2} \quad (4.12)$$

Recall that the particle magnetic moment,  $\mu$ , is related to the particle pitch angle by the relation:

$$\mu \simeq \frac{v_{\perp}^2}{|B|} = \frac{v^2}{|B|} (1 - \alpha^2) \quad (4.13)$$

For this reason it is clear that the behavior of magnetic moment may be strongly related to the pitch angle behavior, i.e., when particle is in resonance with a single finite amplitude fluctuation its magnetic moment should undergo a finite amplitude nonlinear oscillation. Considering Eq. 4.13, we can relate the trapping width expected for the magnetic moment with that predicted for pitch angle as follows,

$$\Delta \mu = 2\alpha \Delta \alpha \quad (4.14)$$

This formula is correct for a circularly polarized wave. Constant magnetic moment requires a lack of resonance or else interaction with extremely small wave amplitude. If we consider the static case, that is  $\omega = 0$ , the resonance condition takes the form:

$$k_r = \frac{n}{\alpha r_L} = \frac{n\Omega}{v\alpha} = \frac{n\Omega}{v_{\parallel}} \quad (4.15)$$

The minimum value of the wavevector,  $k_{min}$ , required to have resonance, is obtained for  $\alpha = 1$  or, equivalently, for  $\theta = 0$ .

#### 4.1.2.1 The quasilinear diffusion coefficient

Making use of Equations 4.28, the quasilinear diffusion coefficient derived for our particular spectrum, Eq. 3.30, can be cast in a particularly physically illuminating form. First, let us write

$$\delta B_{res}^2 = \frac{1}{4} \langle \delta B^2 \rangle (1 + k_{\parallel}^2 \lambda^2)^{-\nu}_{|k_{\parallel}=k_{res}}, \quad (4.16)$$

that corresponds roughly to the power density in the Fourier resonant wave mode, with the particle characterized by  $v_{\parallel} = \alpha v$ . Using this expression to define  $\delta B$ , i.e., setting  $\delta B = \delta B_{res}$  in Equations 4.28, we obtain

$$\omega_b^2 (\Delta v_{\parallel})^2 = 4v_{\perp}^2 \Omega^2 \frac{\delta B_{res}^2}{B_0^2} = 4v^2 \Omega^2 (1 - \alpha^2) \frac{\delta B_{res}^2}{B_0^2}. \quad (4.17)$$

Introducing Eq. 4.16 and Eq. 4.17 in Eq. 3.30, it is simple to show that  $D_{\alpha\alpha}$  can be expressed as:

$$D_{\alpha\alpha} = \frac{\omega_b^2 \tau_{ac}^2 (\Delta\alpha)^2}{2\tau_{ac}} \equiv \frac{(\Delta\alpha_{\text{eff}})^2}{2\tau_{ac}}, \quad (4.18)$$

where we have defined the trapping width in  $\alpha$ -space as  $\Delta\alpha \equiv (\Delta v_{\parallel})/v$ , with  $\Delta v_{\parallel}$  given by Eq. 4.28, and the effective trapping width as  $\Delta\alpha_{\text{eff}} \equiv \omega_b \tau_{ac} \Delta\alpha$ . To the best of our knowledge the pitch angle diffusion coefficient in magnetostatic slab turbulence has not previously been cast in these forms.

Eq. 4.18 has an obvious Fokker-Planck form and provides a physical interpretation of the process of pitch angle diffusion, that builds on ideas already presented in the previous sections. The numerator defines an effective trapping width in  $\alpha$  due to the resonance with a finite length wave packet. The length of this wavepacket is determined by the spectral characteristics of the turbulence. This effective trapping, or interaction, half width is given by  $\omega_b \tau_{ac} \Delta\alpha$ , where  $\Delta\alpha$  is the (nonlinear) trapping width for interaction with a single wave mode. Thus, the nonlinear trapping width, reduced by the factor  $\omega_b \tau_{ac} \ll 1$ , accounts for the rapid decorrelation of the particle with the resonant wavepacket, on timescales of the order of  $\tau_{ac} = \lambda_c / |v_{\parallel}|$ . Because  $\omega_b \tau_{ac} \ll 1$ , the particle typically completes only a small part of its regular resonant bounce motion, i.e., unperturbed by the noise induced by neighboring wavemodes, in the time it takes to transit a wavepacket,  $\tau_{ac}$ , and consequently it undergoes only a small “kick” in  $v_{\parallel}$  (or  $\alpha$ ). The magnitude of this kick is of the order of the interaction width in parallel velocity,  $\Delta v_{\parallel}^{\text{eff}} = v \Delta\alpha_{\text{eff}}$ . Conversely, when  $\omega_b \tau_{ac} \simeq 1$  the particle will on average have time to complete its regular bounce motion without the disturbance of noise, during its transit of a resonant wavepacket. That is, it will behave largely as if trapped by a resonant wave mode and the diffusion picture begins to break down. Indeed, the parameter regime  $\omega_b \tau_{ac} > 1$  violates the quasilinear assumption. As has been pointed out previously, this is most likely to occur at small  $v_{\parallel} \simeq 0$  or  $\mu \simeq 0$ , where the condition  $\omega_b \tau_{ac} \ll 1$  is difficult to satisfy. Oscillatory behavior without the decay of parallel velocity correlations has been observed in simulations of pitch angle diffusion in the vicinity of  $\alpha \simeq 0$  (*Kaiser et al., 1978*).

### 4.1.3 Resonant vs non resonant particles

Particles are loaded randomly in space at  $t = 0$  throughout a one-dimensional simulation box of length  $L$ , where the fields are as described in Chapter 3. Their initial velocities are generated through the standard spherical coordinate transformations, where the pole of the spherical coordinate system corresponds with the Cartesian



basis vector  $\mathbf{e}_z$ ,

$$\begin{aligned} v_x &= v \sin \theta \cos \phi \\ v_y &= v \sin \theta \sin \phi \end{aligned} \quad (4.19)$$

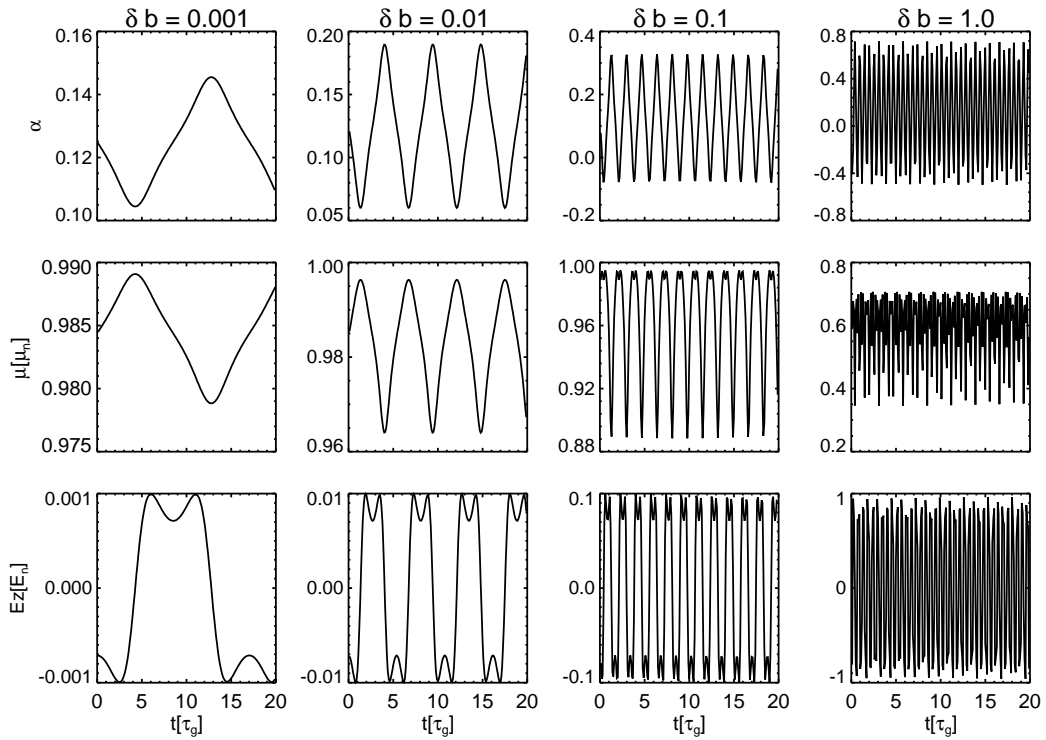
$$v_z = v \cos \theta = \alpha v \quad (4.20)$$

where  $\phi$  is the gyrophase randomly distributed between  $[0 : 2\pi]$ ; the velocity magnitude  $v$  and the cosine of pitch angle  $\alpha = \cos \theta$  are determined by the particular type of experiment designed.

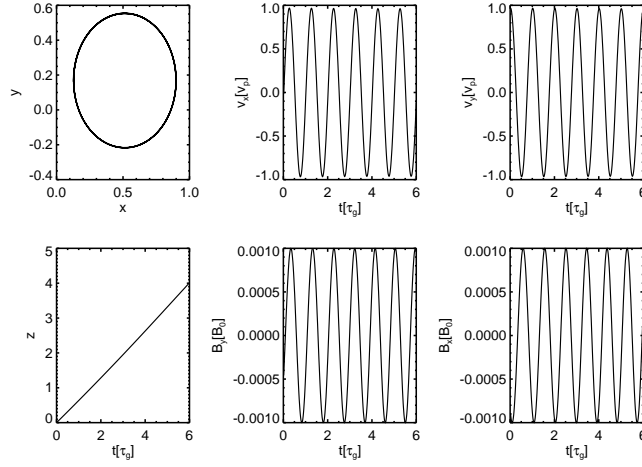
In our simulations  $\beta = 10^3$ , according to the solar wind parameters at 1A.U. Because of the magnetostatic approximation, we use typical velocities of  $v = 100v_A$ . In each simulations all particles are injected with the same cosine of pitch angle,  $\alpha = 1/8$ , that corresponds to an initial pitch angle  $\theta \simeq 82^\circ$ . In order to have these particles in resonance with the wave, following the resonance condition, Eq. 3.6, we fixed the wavevector  $k_0 = 80/\lambda$ . Obviously, particles at different pitch angle will not be in resonance with this wave and they will show a different behavior. To make a comparison between resonant and non resonant particles, we also performed some simulations in which particles, interacting with the same wave, have an initial cosine of pitch angle  $\alpha = 1/2$  ( $\theta = 60^\circ$ ), so they are non-resonant. We follow the test-particles until they complete a total number of gyroperiods equal to  $N_{\tau_g} = 100$ . We also define  $\delta b = \delta B/B_0$ .

Figure 4.1 shows the cosine of pitch angle,  $\alpha$ , particle magnetic moment,  $\mu$ , and the parallel component of the induced electric field,  $E_z$ , for a resonant particle with  $v = 100v_A$  and  $\alpha_0 = 1/8$ . Different columns corresponds to different values of the wave amplitude:  $\delta b = 0.001$  (first column),  $\delta b = 0.01$  (second column),  $\delta b = 0.1$  (third column) and  $\delta b = 1.0$  (fourth column). Magnetic moment and electric field are expressed in units of  $\mu_n = v^2/B_0$  and  $E_n = vB_0$ , respectively. Magnetic moment results are averaged on a particle gyroperiod. During periods in which the parallel component of the induced electric field is almost constant and equal to  $E_z \sim -v_\perp \delta b$ , it is immediately apparent that  $\mu$  and  $\alpha$  show *secular* variations. Of course, this is more evident for small wave amplitudes, i.e.,  $\delta b = 0.001$  and  $\delta b = 0.01$ . The resonant interaction produces a complicated periodic variations in both  $\alpha$  and  $\mu$ . The period of these variations is termed the bounce period,  $\tau_b = 2\pi/\omega_b$ , where  $\omega_b$  is the bounce frequency discussed above. The bounce period  $\tau_b = 2\pi/\omega_b$  is the typical timescale over which the velocity, and hence particle trajectory, exhibits significant deviations from its linear  $v_\parallel = \text{const}$  and  $v_\perp = \text{const}$  counterparts.

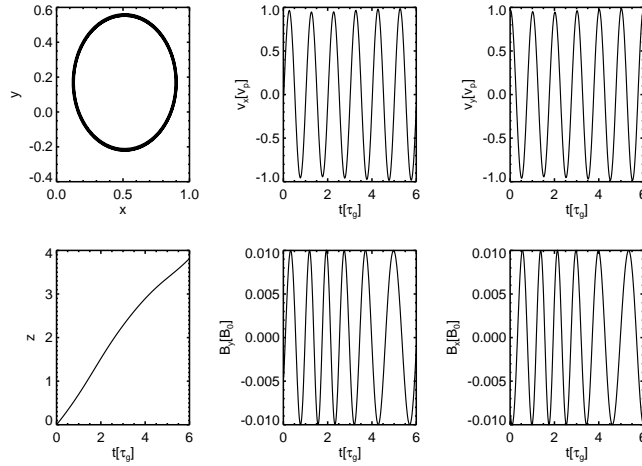
In Figure 4.2, particle trajectory in the  $x - y$  plane, particle  $v_x$  and  $v_y$  velocities, the  $z$ -coordinate,  $x$  and  $y$  component of the magnetic field seen by the particle versus  $t$ , are shown. For  $\delta b = 0.001$  (Figure 4.2(a)), as predicted by QLT, particle motion is the same of that we should observe without the wave. Indeed, particle trajectory form a circle in the  $x - y$  plane and the  $z$ -coordinate grows linearly with time. Particle and wave are perfectly in resonance:  $v_x$  ( $v_y$ ) component of the particle velocity is in phase with  $-B_y$  ( $B_x$ ) component of the magnetic field seen by the particle. Increasing the wave amplitude,  $\delta b = 0.01$  (Figure 4.2(b)), particle starts



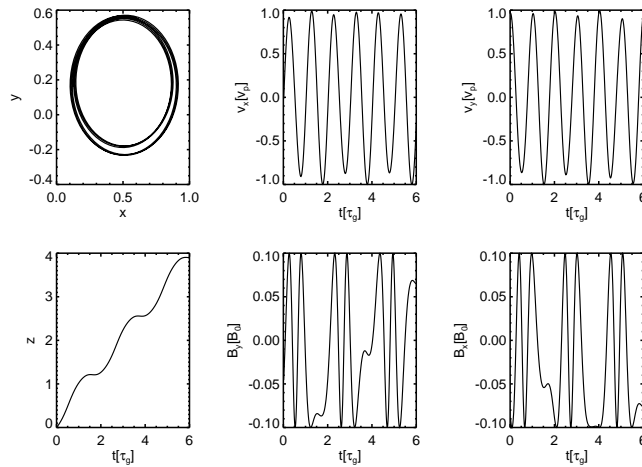
**Figure 4.1:** Gyroresonant interaction between a circularly polarized wave and a particle with  $v = 100v_A$  and  $\alpha = 1/8$ : cosine of pitch angle  $\alpha$  on the top, particle magnetic moment  $\mu$  in the middle, parallel component of the induced electric field on the bottom. Four different values of wave amplitude are used:  $\delta b = 0.001$  (first column),  $\delta b = 0.01$  (second column),  $\delta b = 0.1$  (third column) and  $\delta b = 1.0$  (fourth column).



(a)  $v_p = 100v_A$  and  $\delta b = 0.001$ .



(b)  $v_p = 100v_A$  and  $\delta b = 0.01$ .



(c)  $v_p = 100v_A$  and  $\delta b = 0.1$ .

**Figure 4.2:** Top row (from left to right): particle trajectory in  $x - y$  plane,  $x$  component of particle velocity  $v_x$ , versus time;  $y$  component of particle velocity,  $v_y$  versus time. Bottom row (from left to right):  $z$  particle position versus time;  $x$  component of magnetic field seen by the particle,  $B_x$ , versus time;  $y$  component of magnetic field seen by the particle,  $B_y$ , versus time.

**Table 4.2:**  $\alpha$  and  $\mu$  trapping width values: comparison between theory and numerical simulations.

| $\delta b$ | $\Delta\alpha_{th}$ | $\Delta\alpha_{sim}$ | $\Delta\mu_{th}$ | $\Delta\mu_{sim}$ |
|------------|---------------------|----------------------|------------------|-------------------|
| 0.001      | 0.022               | 0.02                 | 0.0056           | 0.0055            |
| 0.01       | 0.07                | 0.075                | 0.0176           | 0.02              |
| 0.1        | 0.2227              | 0.2                  | 0.0556           | 0.055             |
| 1.0        | 0.704               | 0.6                  | 0.176            | 0.175             |

to spread in  $x - y$  plane and, after 2 or 3 gyroperiods, the  $z$  coordinate shows some irregular changes, that we encounter at the same times in the  $x$  and  $y$  component of the magnetic field. For  $\delta b = 0.1$  (Figure 4.2(c)), we are moving away from the quasilinear approximation: the particle spread in  $x - y$  plane is more and more evident and a lot of irregular changes in the  $z$  coordinate are observed. The same irregularities are encountered at the same times in the  $x$  and  $y$  component of the magnetic field. Looking at the behavior of the parallel component of the induced electric field,  $E_z$ , particle magnetic moment,  $\mu$ , and cosine of pitch angle,  $\alpha$ , (Figure 4.1), these are the time intervals during which  $\mu$  and  $\alpha$  show secular changes and the parallel component of the induced electric field is almost constant. We derived previously, in Section 4.1.2, the analytical expression for the half trapping width of magnetic moment for a particle interacting with a left or right hand circularly polarized wave. Explicitly:

$$\Delta\mu = 4\alpha \left[ (1 - \alpha^2)^{1/2} |\alpha| \frac{\delta B}{B_0} \right]^{1/2} \quad (4.21)$$

For each of the cases analyzed, we calculated the values of the half peak-to-peak difference in  $\alpha$  and  $\mu$ ,  $\Delta\alpha = (\alpha_{max} - \alpha_{min})/2$  and  $\Delta\mu = (\mu_{max} - \mu_{min})/2$ , for the resonant interaction. These values, compared with the theoretical ones obtained by Eq. 4.12 and Eq. 4.29, are listed in Table 4.2. The excellent agreement between theory and simulations confirms the formula 4.12 for the trapping width, specialized for the case of a single circular polarized wave and our guess that magnetic moment behavior is strictly related to the pitch angle one.

In order to have a direct comparison between resonant and non-resonant behaviors, Figure 4.3 shows the cosine of pitch angle,  $\alpha$  (first row), magnetic moment,  $\mu$  (third row), and their distribution function,  $f(\alpha)$  (second row) and  $f(\mu)$  (fourth row), for a resonant particle,  $\alpha = \alpha_{res} = 1/8$  (left column), and a non-resonant one,  $\alpha = \alpha_{non-res} = 1/2$  (right column). Again magnetic moment values are averaged over a particle gyroperiod. In contrast with the resonant case, in which  $\alpha$  and  $\mu$  exhibit the well-known secular variations with typical period equal to  $\tau_b$ , the cosine of pitch angle and magnetic moment for a non-resonant particle show a regular oscillating behavior, a distinctive signature of regular particle motion characterized by linear  $v_{\parallel} = const$  and  $v_{\perp} = const$ . The values of the half peak-to-peak difference in  $\alpha$  and  $\mu$  from the simulation,  $\Delta\alpha_{sim} = 0.0025$  and  $\Delta\mu_{sim} = 0.003$ , are also smaller and smaller in comparison to the theoretical values expected from Eq. 4.12

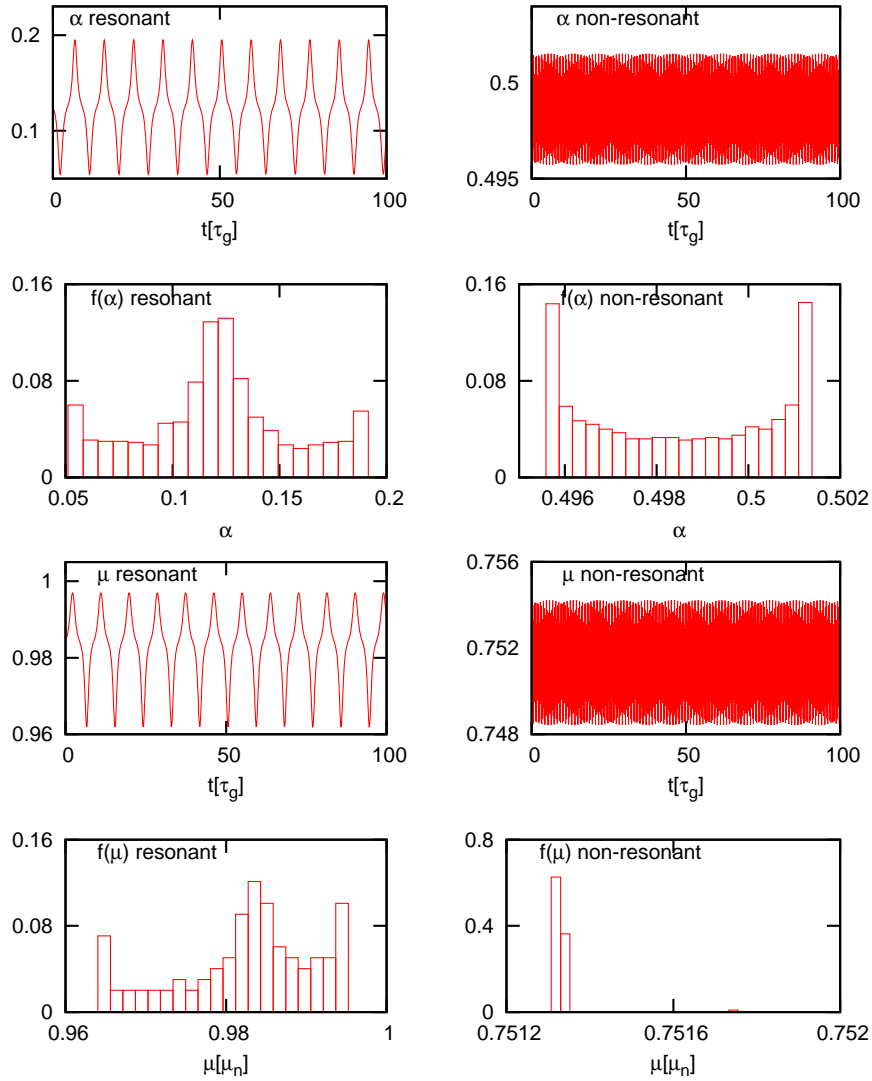


**Figure 4.3:** Resonant vs non resonant behavior: two particles with  $v = 100v_A$ ,  $\alpha_{res} = 1/8$  (left column) and  $\alpha_{non-res} = 1/2$  (right column), in the field of a circularly polarized wave with  $\delta b = 0.01$ . Cosine of pitch angle  $\alpha$  (first line) and its distribution function  $f(\alpha)$  (second line), magnetic moment  $\mu$  (third line) and its distribution function  $f(\mu)$  (fourth line) are shown for both particles.

and Eq. 4.14 for  $\delta b = 0.01$  and  $\alpha = 1/2$ ,  $\Delta\alpha_{th} = 0.1316$  and  $\Delta\mu_{th} = 0.1316$ . Also the distribution functions  $f(\alpha)$  and  $f(\mu)$  for a single particle are really different in the two considered cases. For a resonant particle,  $f(\alpha)$  and  $f(\mu)$  start to have a Gaussian shape, typical of normal diffusion, around the initial values,  $\alpha_0 = 1/8$  and  $\mu_0/\mu_n = 0.98$ . In the non-resonant case  $f(\mu)$  is peaked at the initial value, that means the magnetic moment remains constant during particle motion and the variations in  $\alpha$  are of the order of 10%, that is a small variation considering that, in the other case, variations of the order of 40% are observed.

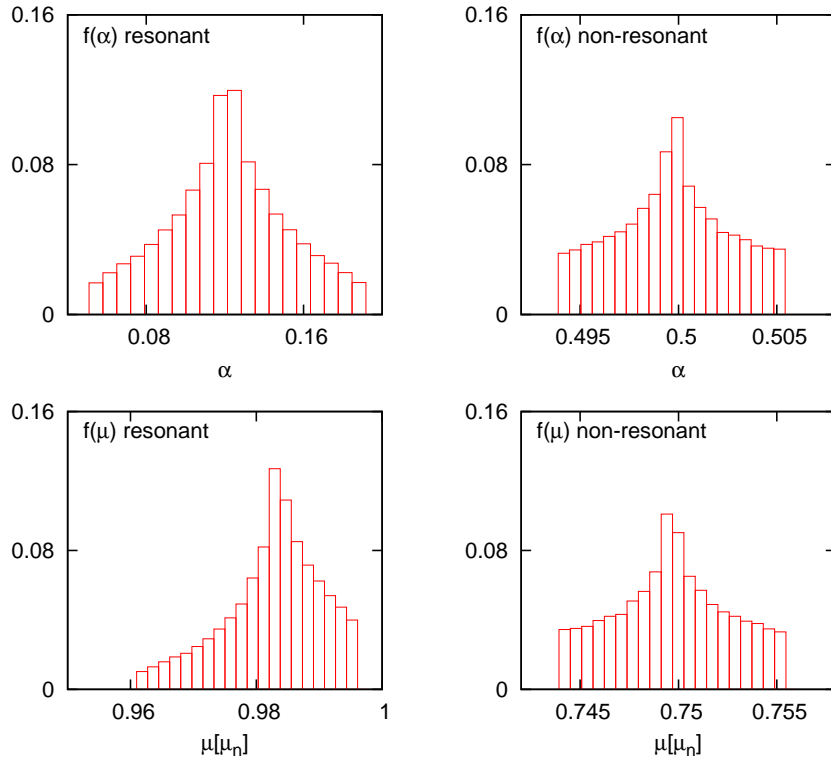


**Figure 4.4:** Resonant vs non resonant behavior:  $f(\alpha)$  (first line)  $f(\mu)$  (second line), for an initial distribution of 1000 resonant (left column) and non-resonant (right column) particles randomly loaded in the simulation box.  $\delta b = 0.01$ .

To make an additional comparison between resonant and non-resonant particle dynamics, in Figure 4.4 the distributions functions,  $f(\alpha)$  and  $f(\mu)$ , of 1000 resonant and non-resonant particles, injected with random position and random phase in the simulation box, are shown. For an initial distribution of non-resonant particles,  $f(\alpha)$  and  $f(\mu)$  have the same tendency to remain peaked around their initial values,  $\alpha_0 = 1/2$  and  $\mu_0/\mu_n = 0.75$ , and have high tails at their side. For the resonant distribution,  $f(\alpha)$  exhibits a Gaussian shape centered around the initial value,  $\alpha_0 = 1/8$ . In addition, the spread in the distribution function,  $\sim 0.1$ , is equal to the total value of the trapping width for the single particle, shown in Figure 4.3,

$2\Delta\alpha = 0.014$ . The magnetic moment distribution for the resonant distribution has a shape that we found characteristic for  $\mu$  in the range in which pitch angle exhibits a Gaussian behavior and the density distribution function is still isotropic (particle free-streaming regime). Instead, increasing  $\delta b$ ,  $f(\alpha)$  becomes isotropic and the density distribution function exhibits a Gaussian shape, signature of spatial parallel diffusion. In this regime  $f(\mu)$  has a Gaussian shape too. As in the pitch angle case, the spread in the distribution function,  $\sim 0.03$ , is equal to the total value of the trapping width for the single particle, shown in Figure 4.3,  $2\Delta\mu = 0.00352$  (see Eq. 4.21).

#### 4.1.4 Resonance overlap

In order to study the effect of resonances overlap, we designed a particular experiment in which four different particles are loaded in the simulation box with random initial position. All particles have the same initial velocity,  $v_{0tot} = 100v_A$ , but different values of cosine of pitch angle,  $\alpha$ , at the injections and, consequently, different parallel velocity:  $\alpha_1 = 1/2, \alpha_2 = 1/2, \alpha_3 = 1/4, \alpha_4 = 1/32$ . Setting again  $\beta = 10^3$  and following the resonance condition for the static case in dimensionless units, Eq. 3.6, these particles will be in cyclotron resonance  $n = 1$  with four different waves, that means same amplitude,  $\delta B/B_0$ , but different wave numbers  $k$ :  $k_1 = 201/\lambda, k_2 = 401/\lambda, k_3 = 801/\lambda, k_4 = 3201/\lambda$ . If we now allow resonance broadening effects, then all particles in the velocity distribution with parallel velocities in the range

$$v_{\parallel} - \Delta v_{\parallel} < v_{\parallel} < v_{\parallel} + \Delta v_{\parallel} \quad (4.22)$$

can potentially resonate with a wave, whose wave number is  $k_{\parallel} = \Omega/v_{\parallel}$ . As found by [Chirikov \(1978\)](#), the direct evidence of resonances overlapping is the disappearance of constants of motion, i.e., the onset of stochasticity, in the Hamiltonian formalism. In order to study the resonance overlap effects, the magnetic field is given by,

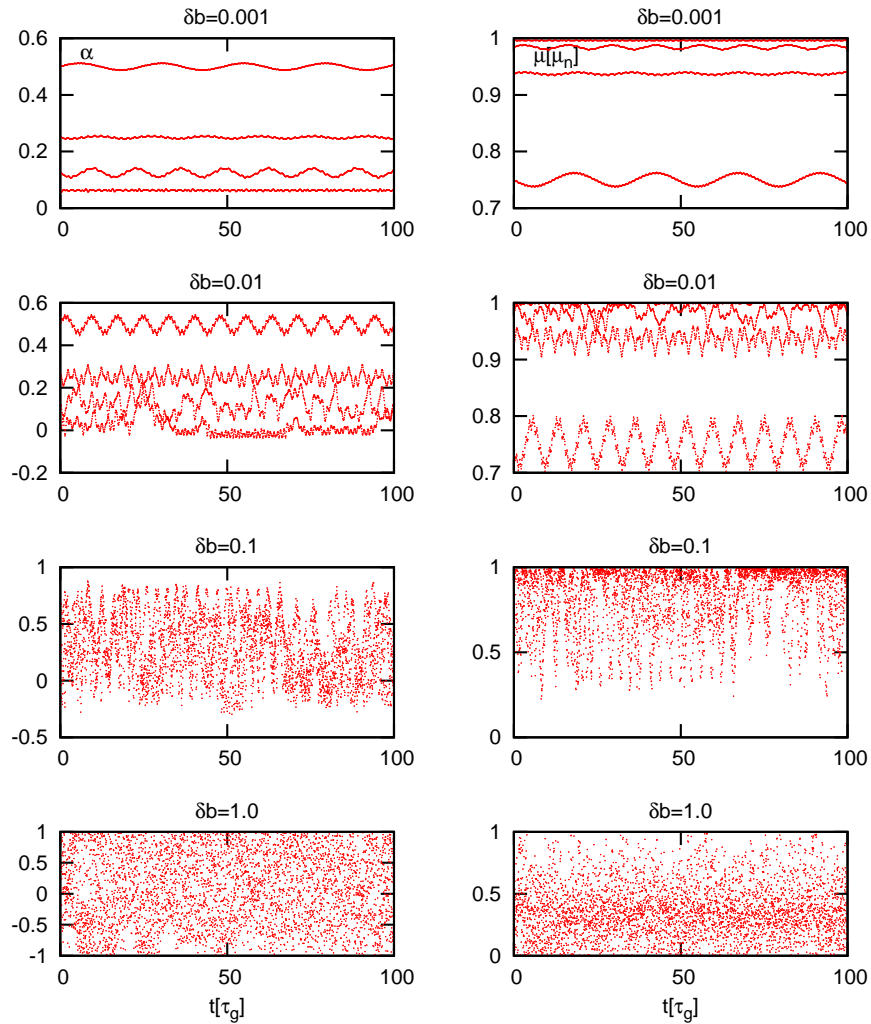
$$\mathbf{B} = B_0\mathbf{e}_z + \sum_{i=1}^4 \delta b \cos[k(i)z]\mathbf{e}_x - \sum_{i=1}^4 \delta b \sin[k(i)z]\mathbf{e}_y. \quad (4.23)$$

We make simulations for four different waves amplitudes,  $\delta b = (0.001, 0.01, 0.1, 1.0)$ . As in the previous case, test-particles are followed until they complete a total number of gyroperiods equals to  $N_{\tau_g} = 100$ . The values of the trapping half-widths,  $\Delta v_{\parallel}$ , calculated using our specialized formula, Eq. 4.28, for  $\alpha_1 = 1/2, \alpha_2 = 1/2, \alpha_3 = 1/4, \alpha_4 = 1/32$  are listed in Table 4.3 for all the  $\delta b$  values used in the experiment.

In Figure 4.5,  $\alpha$  (left column) and  $\mu$  (right column) profiles varying the waves amplitude,  $\delta b = 0.001$  (first row),  $\delta b = 0.01$  (second row),  $\delta b = 0.1$  (third row),  $\delta b = 0.001$  (fourth row), are shown. At a first sight, it is again visible the similar behavior of particles pitch angle and magnetic moment that focus of our study. When the wave amplitude is small,  $\delta b = 0.001$ , the four different resonances are well-recognized both in pitch angle and magnetic moment profiles and there are not overlapping resonances, since they are well separated. Increasing the wave

**Table 4.3:** Values of  $\Delta v_{\parallel}$  for the  $\alpha = (1/2, 1/4, 1/8, 1/32)$  resonances at different  $\delta b$ .

| $\delta b$ | $\alpha = 1/2$ | $\alpha = 1/4$ | $\alpha = 1/8$ | $\alpha = 1/32$ |
|------------|----------------|----------------|----------------|-----------------|
| 0.001      | 4.16           | 3.1            | 2.227          | 1.3             |
| 0.01       | 13.1           | 9.85           | 7.042          | 3.583           |
| 0.1        | 41             | 31.1           | 22.27          | 11.33           |
| 1.0        | 131            | 98.3           | 70.42          | 35.83           |

**Figure 4.5:** Transition from non-overlapping to overlapping resonances:  $\alpha$  (left column) and  $\mu$  (right column) profiles varying the waves amplitude:  $\delta b = 0.001$  (first row),  $\delta b = 0.01$  (second row),  $\delta b = 0.1$  (third row),  $\delta b = 1.0$  (fourth row).



amplitude,  $\delta b = 0.01$ , we start to observe the overlap of the resonances for  $\alpha_3 = 1/8$  and  $\alpha_4 = 1/32$ ; indeed, in this case, the initial parallel velocity of the particle injected at the smallest pitch angle,  $v_{\parallel,4} = 3.125v_A$ , lies in the range of velocities (see Eq. 4.22) in possible resonance with  $k_{\parallel} = k_3$ , because of the broadening effects. For the other two cases considered,  $\delta b = 0.1$  and  $\delta b = 1.0$ , the condition (4.22) is satisfied by all particles velocities. Indeed, it is not possible to distinguish anymore the different resonances in both pitch angle and magnetic moment profiles, because the stochasticity arises.

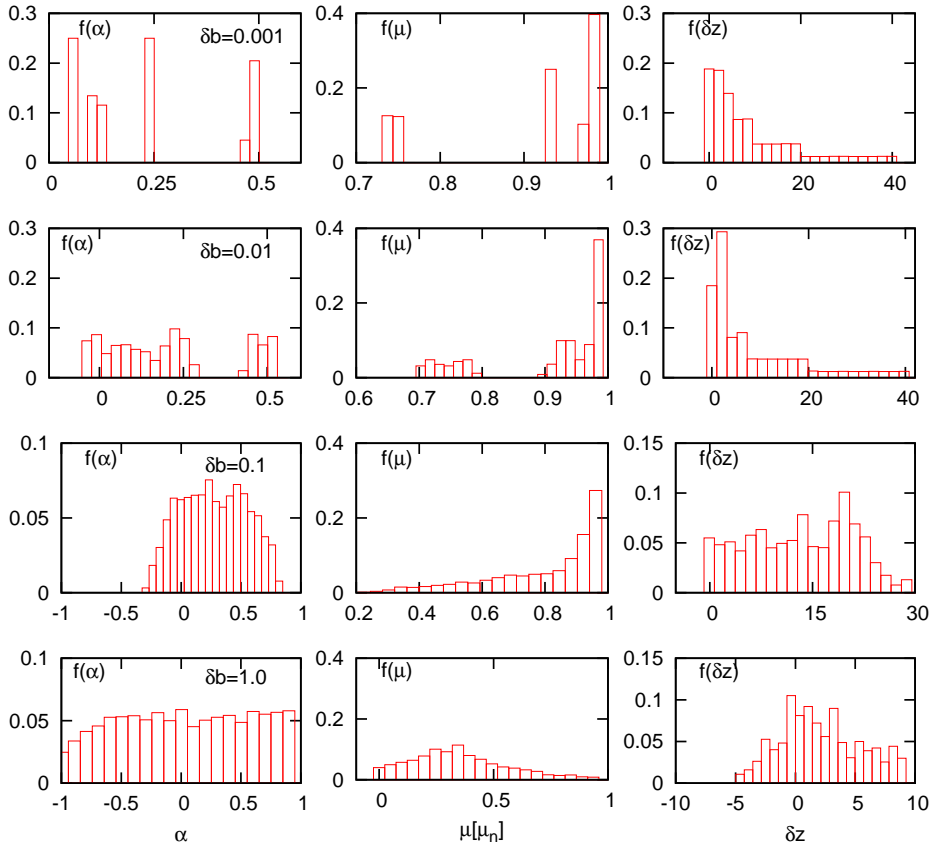


**Figure 4.6:** Demonstration of transition from non-overlapping to overlapping resonances: distribution functions  $f(\alpha)$  (left column),  $f(\mu)$  (central column) and  $f(\delta z)$  (right column) varying the waves amplitude:  $\delta b = 0.001$  (first row),  $\delta b = 0.01$  (second row),  $\delta b = 0.1$  (third row),  $\delta b = 1.0$  (fourth row).

For this experiment, we also analyzed the distribution functions of pitch angle,  $f(\alpha)$ , magnetic moment,  $f(\mu)$  and relative position  $f(\delta z)$ , where  $\delta z = z - z_0$ . They are shown in Figure 4.6 at various  $\delta b$ :  $\delta b = 0.001$  (first row),  $\delta b = 0.01$  (second row),  $\delta b = 0.1$  (third row),  $\delta b = 1.0$  (fourth row). Also from the distribution functions, it is clear when the resonances are well separated and when the particles motion starts to become stochastic. Indeed, for  $\delta b = 0.001$  (first line), pitch angle and magnetic moment distributions exhibit four different peaks, in correspondence

of their initial values, as consequence of the good separation between the different resonances. Looking at  $f(\delta z)$ , it is also evident that particles free-streaming in the parallel direction and, depending on their initial parallel velocity, they cover shorter or longer distances in  $z$ . For  $\delta b = 0.01$ , the pitch angle distribution function is not peaked anymore around the four initial values but, in correspondence of them, the distribution spreads, because particles are resonant interacting with a wave of bigger amplitude. In addition, the effect of the overlapping resonances,  $n = 1$  and  $n = 4$ , discussed previously, for  $\alpha < 1/4$  appears too. The same effects are also present in  $f(\mu)$ , confirming the fact that for small  $\delta b$  the resonant interaction affects magnetic moment and pitch angle in an analogous way. Particles continue to free-stream in the direction parallel to  $B_0$ . Larger changes start to appear for  $\delta b = 0.1$ , with the arising of stochasticity. Pitch angle distribution starts to isotropize and magnetic moment exhibits a one-sided long tail distribution in the direction of smaller  $\mu$ , in what appears to be a signature of magnetic moment behavior in the regime of overlapping resonances. This is the regime discussed previously in the single wave experiment: when  $f(\alpha)$  is nearly isotropic but particles do not diffuse in the parallel direction ( $f(\delta z)$  is still typical of free-streaming), the magnetic moment distribution displays this characteristic shape. This transient regime for intermediate levels of wave amplitude will be present also when particles move in a large turbulent spectrum, so it is a typical magnetic moment feature. For  $\delta b = 1.0$ ,  $f(\alpha)$  is completely isotropic, but  $f(\delta z)$  starts to become more Gaussian, as spatial diffusion begins to set in. In this regime  $f(\mu)$  loses its long-tail and exhibits a more Gaussian behavior as well.

In conclusion we can say that the behavior of magnetic moment is strictly related to pitch angle behavior for a low level of magnetic fluctuation, i.e.,  $\delta b = 0.001, 0.01$ . It undergoes the same finite amplitude nonlinear oscillation during the interaction with a single finite amplitude fluctuation and its distribution half-width is directly related to pitch angle distribution. When stochasticity arises, as a consequence of overlapping resonances, its effect on pitch angle is the isotropization of the distribution function. This is a transient regime during which magnetic moment exhibits a one-sided long-tail distribution and starts to be influenced by the onset of spatial parallel diffusion. When  $f(\alpha)$  completely isotropizes, spatial diffusion sets in and  $f(\mu)$  behavior is closely related to the sampling of spatially varying magnetic field strength associated with that spatial diffusion. Thus, we have identified, depending on particle properties, that there are three distinct regimes of magnetic moment statistical behavior with increasing turbulence level (Dalena et al 1, in prep).

## 4.2 Interaction with the slab spectrum

In this section, the results concerning the interaction of a particles distribution with a broad band slab spectrum (see Eq. 3.25 and Figure 4.7) are shown. In order to gain some insight of magnetic moment conservation, different simulations are performed varying both particles velocity,  $v_p$ , and the amplitude of magnetic field fluctuations,

$\delta b$ . We fixed the value of the  $\beta$  parameter (see Eq. 3.5) equal to  $10^4$ , in agreement

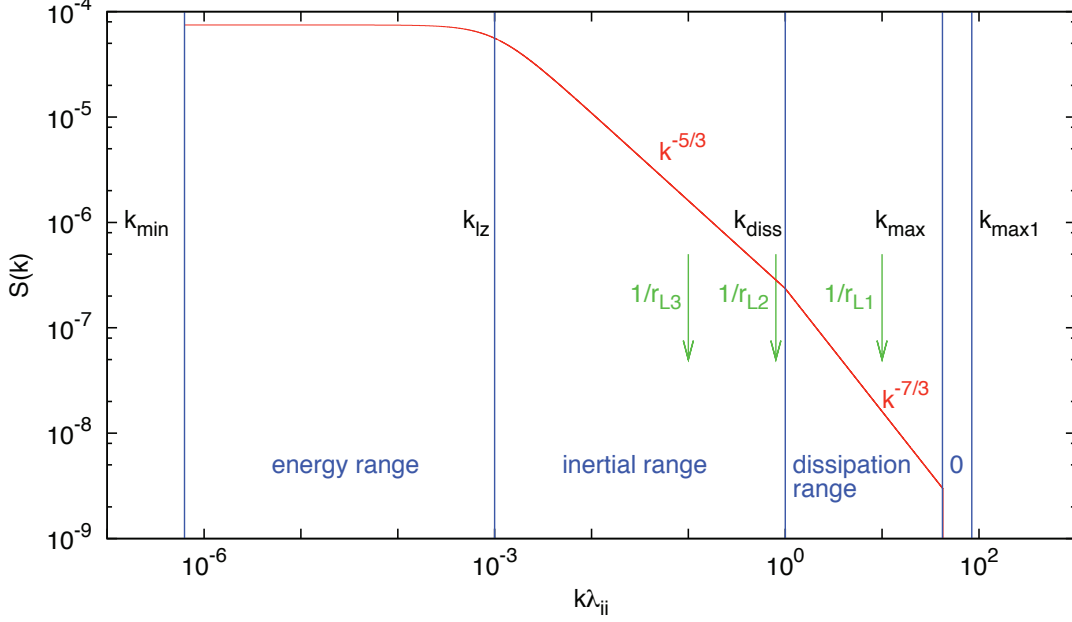


**Figure 4.7:** Power spectrum in numerical simulations.  $k$  is normalized to the ion inertial length,  $\lambda_{ii}$ .

with the solar wind observations at 1A.U. Indeed, from Eq. 3.5, it is possible to write:

$$\beta = \frac{\lambda_c}{\lambda_{ii}}, \quad (4.24)$$

where  $\lambda_c$  is the turbulence correlation length and  $\lambda_{ii} = c/\omega_{pi} = (c^2 m_p / 4\pi n_p e^2)^{1/2}$  is the ion inertial length. If  $n_i = n_e$ ,  $\lambda_{ii} = (m_p/m_e)^{1/2} \rho_{ie}$ . Because the solar wind density at 1AU is, approximately,  $n \sim (1 - 10)$  particles  $\text{cm}^{-3}$ , on average  $\lambda_{ii}(1\text{A.U.}) \sim 1000\text{km}$ . At the same distance, the turbulence correlation length,  $\lambda_c$ , measures approximately  $10^6\text{km}$  (Matthaeus *et al.*, 1986); thus,  $\beta \simeq 10^4$ . Typically 1000 particles are injected in the simulation with initial random positions; their initial velocities are given by Eq. 4.20. Particles are loaded from a cold ring beam distribution (see discussion in Section 2.2.3) wherein the velocity magnitude is held constant,  $\sin \theta$  is set equal to  $(1 - \alpha_0^2)^{1/2}$ , where  $\alpha_0$  is the initial pitch angle cosine with respect to the background field,  $B_0$ , identical for each particle; the initial gyrophase,  $\phi$ , is chosen randomly. For all the simulations we set  $\alpha_0 = 0.125$ . From the previous section, we know that the behavior of magnetic moment is strictly related to pitch angle behavior for a low level of magnetic fluctuation. Pitch angle and magnetic moment are characterized by Gaussian distribution functions, typical of normal diffusion process. Increasing the turbulence level, pitch angle distribution approaches isotropization and a transient regime is observed for magnetic moment, that starts to be influenced by the onset of spatial parallel diffusion. When  $f(\alpha)$

Table 4.4: Typical values used in the simulations.

| $V_p[v_A]$ | $r_L[l_z]$ | $k_{res}$       | $\epsilon$            | $t_c[\tau_A]$ |
|------------|------------|-----------------|-----------------------|---------------|
| 1          | $10^{-4}$  | $8 \times 10^4$ | $1.33 \times 10^{-4}$ | 0.747         |
| 10         | $10^{-3}$  | $8 \times 10^3$ | $1.33 \times 10^{-3}$ | 0.0747        |
| 100        | $10^{-2}$  | $8 \times 10^2$ | $1.33 \times 10^{-2}$ | 0.00747       |

completely isotropizes, spatial diffusion sets in and  $f(\mu)$  behavior is closely related to the sampling of varying magnetic field strength associated with that spatial diffusion. From quasilinear theory we know that velocity and real space diffusion occur at two different time scale. Typically, velocity space diffusion takes place at a time scale,  $\tau_c = \lambda_c/v_p$ , shorter than the typical time scale at which parallel diffusion occurs,  $t_{\parallel} = \lambda_{\parallel}/v$ , where  $\lambda_{parallel} = 3D_{\parallel}/v$  is the parallel mean free path. For this reason we follow test particles in the simulation box for a time  $T$  greater than the velocity space diffusion time scale,  $\tau_c$ , in order to investigate the effect of spatial diffusion on the magnetic moment distribution too. Usually,  $T = 20\tau_c$ . Typical particles parameters used in the simulations are listed in Table 4.4.

An important parameter for particles description is  $\epsilon = r_L/\lambda_c$ , that is related with the bend over scale of the spectrum,  $k_{bo}$ , and with the minimum resonant wavenumber,  $k_{res}^{min}$ . Indeed, because  $k_{res}^{min} = 1/r_L$  and  $k_{bo} = 1/\lambda_c$ ,  $(k_{res}^{min})/k_{bo} = \epsilon^{-1}$ ; for example, if  $r_L \gg \lambda_c$ , in few gyroperiods particles experience all the possible  $k$  mode, starting to resonate from the energy containing scale ( $k_{res}^{min} \ll k_{bo}$ ). Considering our turbulent spectrum, Figure 4.7, depending on their initial energy, our test particles will start to resonate at different positions: in the dissipation range,  $v_p = 1v_A$  ( $r_{L1}$ ), at the end of the inertial range,  $v_p = 10v_A$  ( $r_{L2}$ ) and in the middle of the inertial range,  $v_p = 100v_A$  ( $r_{L3}$ ). In addition, as explained in Section 3.2.1, the condition  $k_{min} \ll z_{max}$ , necessary to avoid 'fake' diffusion behavior (including possibly subdiffusive behavior) related with the periodicity of the field, is satisfied for all the cases considered.

From the classical definition, the statistic analysis of particle magnetic moment must be done averaging on a particle gyroperiod,  $\tau_g = 2\pi/\Omega$ . If the wave amplitude is small, ( $0.1 < \delta b \leq 0.001$ ), particle cyclotron frequency is given by:  $\Omega \simeq \Omega_0 = eB_0/mc$ . On the contrary, if the wave amplitude is great,  $\delta b \geq 0.1$ , the wave contribute at the strength of the total magnetic field is not negligible and  $\Omega = \Omega(t) = eB(t)/mc$  and  $\tau_g = 2\pi/\Omega(t)$ . Because in the performed simulations  $\delta b$  values in the range  $[0.001 \div 1.0]$  are used, it becomes important for  $\delta b \geq 0.1$  to calculate the effective number of gyroperiod,  $N_{\tau_g}$ , that particles performed in a given magnetic field configuration, in order to well-average magnetic moment values. A given time  $t$  in the simulation can be written as  $t = N_{\tau_g}\tau_g(N_{\tau_g})$ ; so,  $dN_{\tau_g} = dt/\tau_g(t) = dt\Omega(t)/2\pi$ . In this way we obtain the correct value of the total number of gyroperiods that particle performs in the simulation when  $\delta b \geq 0.1$ :

$$N_{\tau_g} = \int_0^t \frac{dt}{2\pi} \frac{eB(t)}{mc}. \quad (4.25)$$

Figure 4.8 shows pitch angle  $f(\alpha)$  (left column), magnetic moment  $f(\mu)$  (central

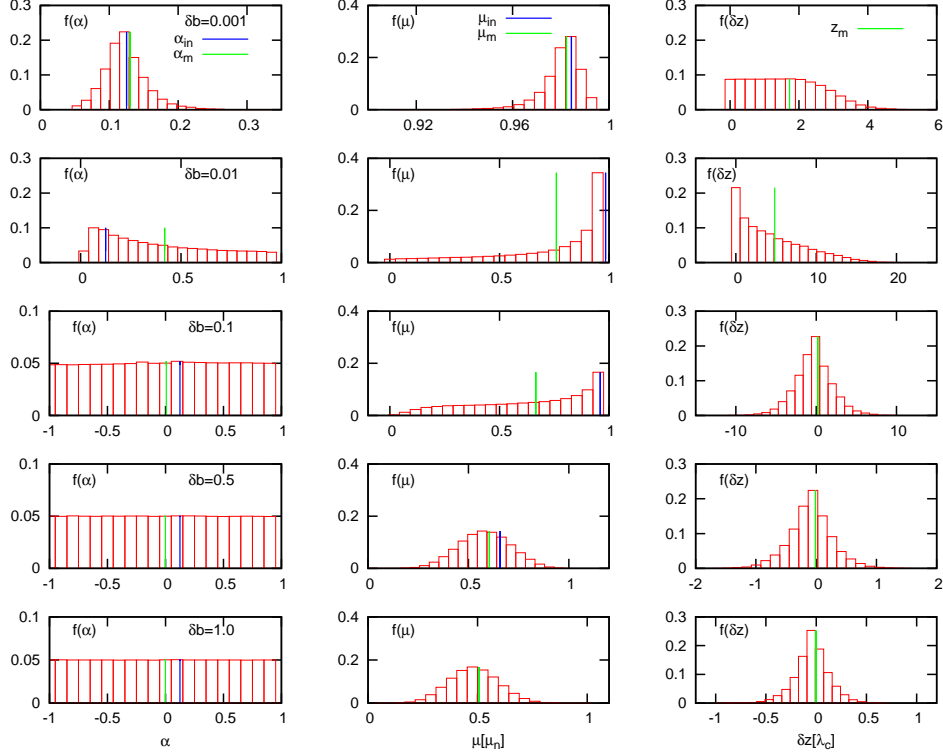


**Figure 4.8:** Distribution functions  $f(\alpha)$  (left column),  $f(\mu)$  (central column) and  $f(\delta z)$  (right column) varying the waves amplitude:  $\delta b = 0.001$  (first row),  $\delta b = 0.01$  (second row),  $\delta b = 0.1$  (third row),  $\delta b = 0.5$  (fourth row),  $\delta b = 1.0$  (fifth row). Particle parameters at injection:  $v_{tot} = 10v_A$  and  $\alpha_0 = 0.125$ .

column) and particle position  $f(\delta z)$  (right column) distribution function, for a distribution of particles, moving with an initial velocity  $v_p = 10v_A$ , interacting with a slab turbulent spectrum. Because particles are injected at different positions, it is convenient to define the quantity  $\delta z = z(j) - z(0)$ , where  $j$  is a temporal index. In this way it is possible to take out from the distribution function  $f(\delta z)$  both the drift effect,  $v_D t$ , and particle diffusion relative to their own positions,  $\Delta z_i$ . Indeed, the general expression for the  $z$  position of the  $i$ -th particle is given by

$$z_i = z_i(0) + v_D t + \Delta z_i = z_i(0) + \delta z_i. \quad (4.26)$$

In Figure 4.9(a) the same distribution functions are shown, with the corresponding variances, Figure 4.11(b),  $\langle (\Delta \alpha)^2 \rangle$  (first row),  $\langle (\Delta \mu)^2 \rangle$  (second row) and  $\langle (\Delta z)^2 \rangle$  (third row). In Figure 4.8 blue line and green line indicate the initial value and the mean value (at the end of the simulation) of each distribution. As in the previous section, magnetic moment values are expressed in units of  $\mu_n = v^2/B_0$ . For  $\delta b = 0.001$ , pitch angle distribution  $f(\alpha)$  has the usual Gaussian shape, typical of

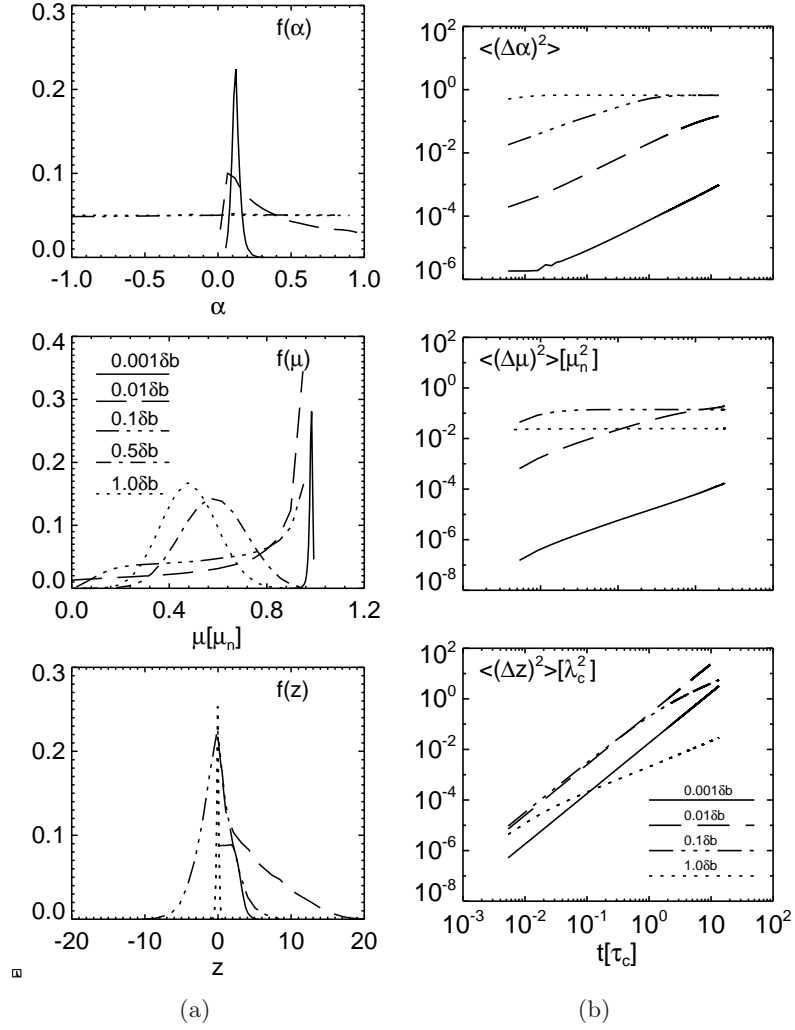


**Figure 4.9:** Statistics for  $v_p = 10v_A$ . Distribution functions in Figure 4.9(a) and variances in Figure 4.11(b) for  $\alpha$  (first row),  $\mu$  (second row) and  $\delta z$  (third row), for different  $\delta b$  level:  $\delta b = 0.001$ , solid line,  $\delta b = 0.01$ , dashed line,  $\delta b = 0.1$ , three dot-dashed line,  $\delta b = 1.0$ , dotted line

**Table 4.5:** Statistic for particles with  $v_p = 10v_A$  and  $\alpha = 0.125$ , interacting with a broad band slab spectrum. Magnetic moment data are averaged on particle gyroperiod.

| $\delta b$ | $\bar{\alpha}$        | $\bar{\mu}$ | $\bar{\delta z}$ | $\tau_\alpha$ | $\tau_\mu$ | $\tau_z$ | $\sigma(\alpha)$ | $\sigma(\mu)$ | $\sigma(z)$ | $N_{\tau_g}$ |
|------------|-----------------------|-------------|------------------|---------------|------------|----------|------------------|---------------|-------------|--------------|
| 0.001      | 0.130                 | 0.982       | 1.725            | 22.78         | 18.33      | 2.055    | 0.031            | 0.008         | 1.063       | 3182         |
| 0.01       | 0.418                 | 0.760       | 4.845            | 5.07          | 5.61       | 5.145    | 0.273            | 0.263         | 4.111       | 3182         |
| 0.1        | 0.007                 | 0.665       | 0.202            | 0.63          | 0.109      | 25.99    | 0.574            | 0.265         | 2.361       | 3195         |
| 0.5        | $-9.6 \times 10^{-4}$ | 0.604       | -0.012           | 0.013         | 0.035      | 24.15    | 0.576            | 0.129         | 0.360       | 3449         |
| 1.0        | $-4.4 \times 10^{-4}$ | 0.506       | -0.001           | 0.003         | 0.029      | 25.17    | 0.576            | 0.112         | 0.173       | 4055         |

normal diffusion. An analogous behavior is observed for magnetic moment distribution,  $f(\mu)$ , while particles free-stream in the  $z$ -direction. However, from  $f(\delta z)$  is obvious that there are few particles that cover greater distance in  $z$  and that are more scattered in pitch angle and, consequently, in  $\mu$ . It is important to notice that in this case  $f(\alpha)$  and  $f(\mu)$  are centered around their initial values. If we consider the variances in Figure 4.11(b) for  $\delta b = 0.001$ , solid line, our discussion regarding the distribution function are confirmed. Indeed, it is evident the super-diffusive behavior of particles that typically free-stream along  $z$  and the scaling  $\propto t$  in  $\langle(\Delta\alpha)^2\rangle$  and  $\langle(\Delta\mu)^2\rangle$ , characteristic of normal diffusion. For  $\delta b = 0.01$  particles cover one side of the  $\alpha$  hemisphere, continuing to free-stream along  $z$ , as evident in Figure 4.11(b) (dashed line). This is the transient regime, already observed in Figure 4.6, during which  $f(\mu)$  exhibits a one-sided long tail distribution in the direction of smaller  $\mu$ . For  $\delta b = 0.1$  pitch angle distribution is completely isotropic and spatial diffusion starts to set in, as evident from the change of the slope of  $\langle(\Delta z)^2\rangle$  in Figure 4.11(b) (three dot-dashed line). At the same time,  $f(\mu)$  shows the same long-tail distribution, but the influence of spatial diffusion starts to appear. Indeed, the well-pronounced peak observed in  $f(\mu)$  for  $\delta b = 0.01$  is substantially reduced and the mean value of magnetic moment distribution is moving towards the center of the  $\mu$ -space ( $\mu[\mu_n]$  can assume values in the range  $[0 \div 1]$ ). Magnetic moment behavior is diffusive, however the Gaussian shape is not reached yet, probably because the spatial diffusion is just at the beginning. For  $\delta b = 0.5$  and  $\delta b = 1.0$ ,  $f(\alpha)$  is isotropic, particle motion is completely diffusive in the real space (as the different slope in  $\langle(\Delta z)^2\rangle$  in Figure 4.11(b) (dotted line) shows) and  $f(\mu)$  behavior is closely related to the sampling of varying magnetic field strength associated with that spatial diffusion, displaying a Gaussian distribution centered at the middle of  $\mu$ -space.

Figure 4.10 shows the distribution functions, Figure 4.10(a), and the variances, Figure 4.10(b), for pitch angle (first row), magnetic moment (second row) and particle position (third row) for a distribution of particles, moving with an initial velocity  $v_p = 1v_A$ , and, as in the previous case, for many  $\delta b$  levels. For  $\delta b = 0.001$ , both  $\langle(\Delta\alpha)^2\rangle$  and  $\langle(\Delta\mu)^2\rangle$  exhibit initial transient oscillations similar to those seen by [Kaiser et al. \(1978\)](#) before it settles at  $t = 1\tau_c$ . [Kaiser et al. \(1978\)](#) offered no explanation for these initial transient oscillations. However, in a detailed analysis of the resonance integrals appearing in magnetostatic quasilinear theory, [Jones et al. \(1973\)](#) showed that  $D_{\alpha\alpha}$  actually possesses an oscillatory part (with frequency  $\Omega$ ) that damps away exponentially on the timescale  $\lambda_c/v_{\parallel}$ . [Mace et al. \(2000\)](#), noticing that the observed oscillations have a period almost equal to the particle gyroperiod, offered the following explanation. Since particles are loaded with an initial pitch angle,  $\theta_0$ , relative to the average field,  $B_0$ , the actual pitch angle measured relative to the true field at the particle position can be expected to be  $\theta \sim \theta_0 \pm \delta$ , where  $\delta$  is the mean angle of deflection of the actual field about  $B_0$ . Since  $\tan \delta \simeq \langle\delta B^2\rangle^{1/2}/B_0$  and  $\delta \ll 1$ , we have  $\delta \simeq \langle\delta B^2\rangle^{1/2}/B_0$ . This means that, on the average, the helical orbit about the local magnetic field is inclined at an angle  $\sim \delta$  with respect to a helical

**Table 4.6:** Statistic for particles with  $v_p = 1v_A$  and  $\alpha = 0.125$ , interacting with a broad band slab spectrum. Magnetic moment data are averaged on particle gyroperiod.

| $\delta b$ | $\bar{\alpha}$        | $\bar{\mu}$ | $\bar{\delta}z$      | $\tau_\alpha$ | $\tau_\mu$ | $\tau_z$ | $\sigma(\alpha)$ | $\sigma(\mu)$      | $\sigma(z)$ | $N_{\tau_g}$ |
|------------|-----------------------|-------------|----------------------|---------------|------------|----------|------------------|--------------------|-------------|--------------|
| 0.001      | 0.125                 | 0.985       | 1.670                | 19.22         | 12.84      | 2.56     | 0.004            | $7 \times 10^{-4}$ | 0.964       | 31824        |
| 0.01       | 0.126                 | 0.984       | 1.681                | 4.11          | 3.12       | 2.60     | 0.012            | 0.003              | 0.978       | 31826        |
| 0.1        | 0.019                 | 0.956       | 0.381                | 5.19          | 4.46       | 25.8     | 0.194            | 0.038              | 1.638       | 31842        |
| 0.5        | $-6.6 \times 10^{-4}$ | 0.624       | 0.008                | 0.072         | 0.094      | 22.24    | 0.564            | 0.277              | 0.780       | 31938        |
| 1.0        | $4.2 \times 10^{-4}$  | 0.514       | $3.4 \times 10^{-4}$ | 0.002         | 0.002      | 24.27    | 0.572            | 0.255              | 0.255       | 31955        |

orbit about the mean field  $B_0$ . This gives rise to an oscillating pitch angle, relative to the mean field, whose period of oscillation is equal to the gyroperiod. As time progresses, the particle distribution evolves by pitch-angle diffusion toward a partial shell distribution and ultimately, given sufficient wave power at large wavenumbers, a complete shell distribution forms. When the pitch angle distribution is broadened sufficiently by this relaxation, so that  $\langle(\theta - \langle\theta\rangle)^2\rangle$  exceeds  $\langle\delta B^2\rangle^{1/2}/B_0$ , then the effect of these oscillations is diminished and eventually quenched. This can be seen in Figure 4.10(b) for  $\delta b = 0.001$  (solid line), where the oscillations are rapidly diminishing for  $t = \tau_c$ , the autocorrelation time of the field as seen by the particles. Furthermore, taking the typical amplitude of the pitch angle oscillation about the initial  $\theta_0$  to be  $\sim \delta$  and defining  $\alpha = \cos(\theta \pm \delta)$ ,  $\alpha_0 = \langle\alpha\rangle = 0.125$  and  $\delta = \delta b = 0.001$ , the quantity  $\langle(\Delta\alpha)^2\rangle = (\alpha - \langle\alpha\rangle)^2 \sim 10^{-6}$ , which agrees very well with the initial oscillation amplitude seen in Figure 4.10(b). The oscillations will persist longer when the initial pitch angle is near  $\pi/2$ . Indeed, the diffusion coefficient,  $D_{\alpha\alpha}$  is small and, consequently, the timescale for the formation of a shell distribution is longer. Indeed, although  $f(\alpha)$  and  $f(\mu)$  have a typical gaussian distribution for both  $\delta b = 0.001$  and  $\delta b = 0.1$ , their standard deviation  $\sigma(\alpha)$  and  $\sigma(\mu)$ , see Table 4.6, are smaller in comparison with that obtained for  $v_p = 10v_A$ , see Table 4.5. In this range, particles simply free-stream in  $z$ , as clear from both the distribution functions and the mean square displacement. Increasing  $\delta b$ , spatial diffusion start to set in (three-dott-dashed line), but  $f(\alpha)$  is not still completely isotropic and  $f(\mu)$  is in the transient regime of long tail one-side distribution. For  $\delta b = 1.0$ ,  $f(\alpha)$  is isotropic, spatial diffusion occurs and  $f(\mu)$  starts to recovery a Gaussian shape.

The results obtained for  $v_p = 100v_A$ , Figure 4.9, confirm the tendency of particles magnetic moment to follow pitch angle behavior, as long as  $f(\alpha)$  becomes isotropic. Until the total isotropization in pitch angle is not reached, also if particles start to diffuse in real space,  $f(\mu)$  is in the transient regime of long tail distribution. When particles cover uniformly both sides of the  $\alpha$  hemisphere and spatial diffusion occurs,  $f(\mu)$  recover a Gaussian shape, as evident in this case for  $\delta b = 1.0$ . In this specific case, the persistent tail in the distribution are a possible effect of the average on particle gyroperiod. Indeed, increasing particle speed, the total number



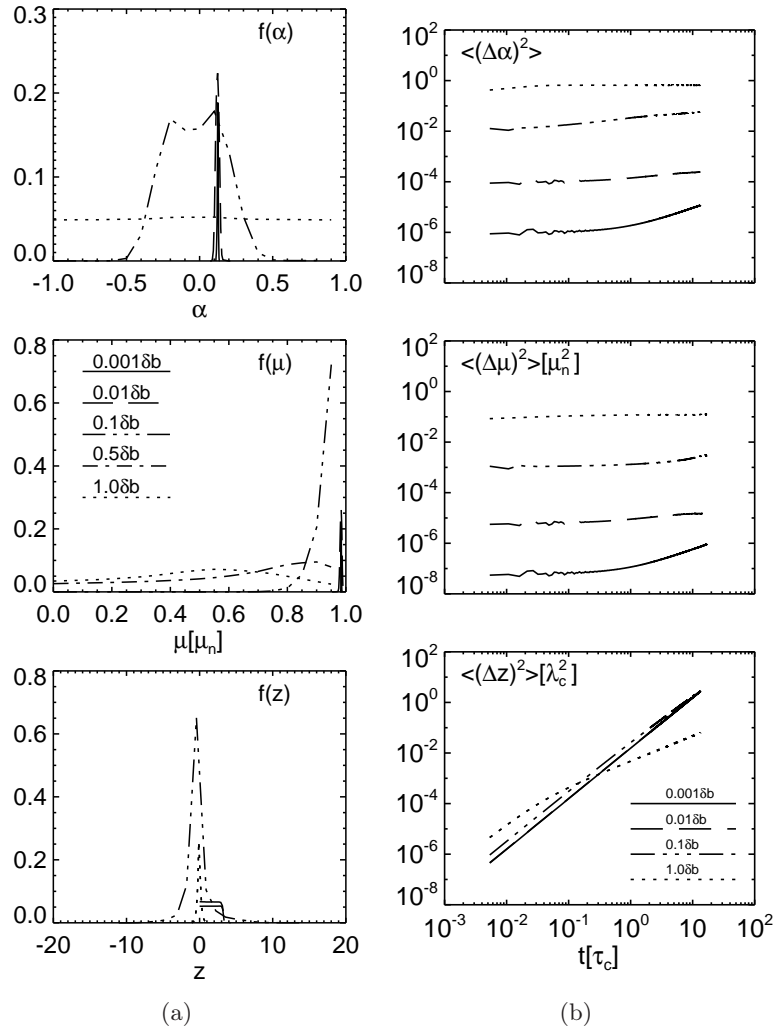


**Figure 4.10:** Statistics for  $v_p = 1v_A$ . Distribution functions in Figure 4.9(a) and mean square displacement in Figure 4.11(b) for  $\alpha$  (first row),  $\mu$  (second row) and  $\delta z$  (third row), at different  $\delta b$  level:  $\delta b = 0.001$ , solid line,  $\delta b = 0.01$ , dashed line,  $\delta b = 0.1$ , three dot-dashed line,  $\delta b = 1.0$ , dotted line

of gyroperiods,  $N_{\tau_g}$ , that particle performs decreases, so slower particles sample more variation in magnetic field strength, that successfully scrambles particle orbits leading to a faster diffusion.

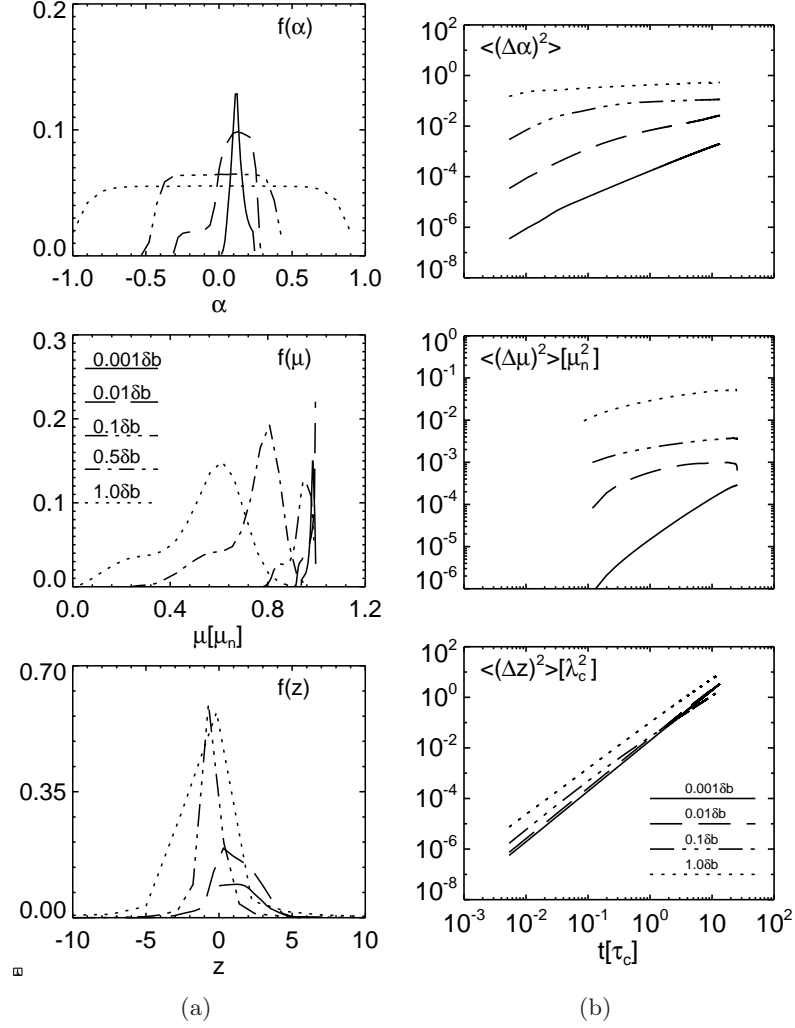


**Figure 4.11:** Statistics for  $v_p = 100v_A$ . Distribution functions in Figure 4.9(a) and mean square displacement in Figure 4.11(b) for  $\alpha$  (first row),  $\mu$  (second row) and  $\delta z$  (third row), at different  $\delta b$  level:  $\delta b = 0.001$ , solid line,  $\delta b = 0.01$ , dashed line,  $\delta b = 0.1$ , three dot-dashed line,  $\delta b = 1.0$ , dotted line

In Figure 4.12 variance for pitch angle,  $\langle(\Delta\alpha)^2\rangle$ , and magnetic moment,  $\langle(\Delta\mu)^2\rangle$ , are compared for  $\delta b = 0.1$ , varying particle velocity:  $v_p = 1v_A$  (solid line),  $v_p = 10v_A$  (dashed line),  $v_p = 100v_A$  (dotted line). More than the relation widely discussed between  $\alpha$  and  $\mu$ , from these plots it is possible to notice the different behavior of particles distribution moving at different velocities and, consequently, resonating in different part of the spectrum. The oscillating behavior, already dis-

**Table 4.7:** Statistic for particles with  $v_p = 100v_A$  and  $\alpha = 0.125$ , interacting with a broad band slab spectrum. Magnetic moment data are averaged on particle gyroperiod.

| $\delta b$ | $\bar{\alpha}$ | $\bar{\mu}$ | $\bar{\delta z}$ | $\tau_\alpha$ | $\tau_\mu$ | $\tau_z$ | $\sigma(\alpha)$ | $\sigma(\mu)$ | $\sigma(z)$ | $N_{\tau_g}$ |
|------------|----------------|-------------|------------------|---------------|------------|----------|------------------|---------------|-------------|--------------|
| 0.001      | 0.132          | 0.981       | 1.744            | 21.95         | 18.65      | 2.97     | 0.043            | 0.012         | 1.133       | 318          |
| 0.01       | 0.092          | 0.974       | 1.461            | 8.77          | 1.36       | 11.21    | 0.132            | 0.022         | 1.453       | 318          |
| 0.1        | 0.006          | 0.936       | 0.050            | 0.35          | 1.84       | 24.11    | 0.244            | 0.045         | 1.262       | 319          |
| 0.5        | 0.003          | 0.747       | 0.168            | 0.36          | 4.05       | 23.85    | 0.421            | 0.126         | 2.260       | 344          |
| 1.0        | 0.004          | 0.549       | 0.306            | 0.2           | 2.18       | 22.95    | 0.529            | 0.168         | 2.772       | 419          |

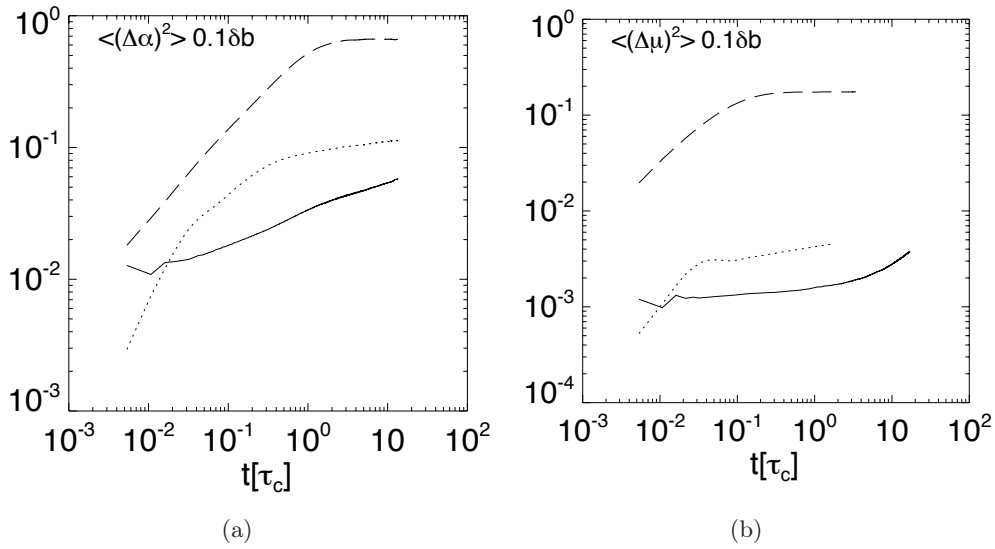


**Figure 4.12:** Variance of pitch angle, Figure 4.12(a), and magnetic moment, Figure 4.12(b), for  $\delta b = 0.1$  and  $v_p = 1v_A$  (solid line),  $v_p = 10v_A$  (dashed line),  $v_p = 100v_A$  (dotted line).

cussed for  $v_p = 1v_A$ , persists, but is less pronounced, for  $v_p = 10v_A$  and completely disappears for  $v_p = 100v_A$ , an effect probably related again with the different sampling of magnetic field irregularities of particle moving at different speed. Because of this oscillations, pitch angle and magnetic moment diffusion, takes place after longer time. As predicted from QLT (see Eq. 3.31),  $D_{\alpha\alpha}$  is inversely proportional to  $v_p$ , for particle resonating at the same part of the spectrum, i.e.,  $10v_A$  and  $100v_A$  (both in the inertial range).

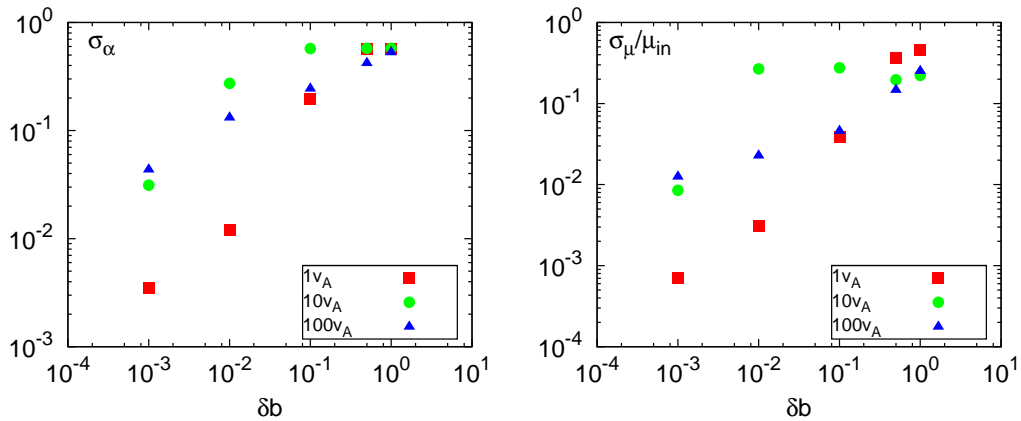


**Figure 4.13:** Standard deviation of pitch angle  $\sigma_\alpha$  and magnetic moment  $\sigma_\mu/\mu_{in}$  versus  $\delta b$ , for  $v_p = 1v_A$  (red squares),  $v_p = 10v_A$  (green circles) and  $v_p = 100v_A$  (blue triangles)

Figure 4.13 shows the standard deviations (listed in Table 4.6, Table 4.5, Table 4.7), relative to the distributions already shown,  $\sigma_\alpha$  (left panel) and  $\sigma_\mu/\mu_{in}$  (right panel), versus the turbulence level  $\delta b$  for  $v_p = 1v_A$ , red squares,  $v_p = 10v_A$ , green circles, and  $v_p = 100v_A$ , blue triangles. These quantities represent the spread of the distribution relative to the mean values and are closely related with the diffusion coefficients. As for the variance, for particles resonating in the same range of the spectrum, these quantities are inversely proportional to the particles velocity. In addition, they increase with increasing  $\delta b$ , as one expects from QLT, for  $\delta b \leq 0.1$ . Both of them converges at a single value, when  $\delta b \geq 0.5$ , i.e., when  $f(\alpha)$  reaches the isotropization and  $f(\mu)$  loses the characteristic one-side long tail form and recovers the original Gaussian shape.

In Table 4.6, Table 4.5, Table 4.7 the typical correlation time,  $\tau_\alpha$ ,  $\tau_\mu$ ,  $\tau_z$ , are listed. In order to calculate these values, first the autocorrelation functions ( $C_{\alpha\alpha}$ ,  $C_{\mu\mu}$ ,  $C_{zz}$ ) relative to each quantities are computed, then the corresponding correlation time are calculated using two different methods, depending on when the functions  $C$  reach the value  $1/e$  or not. The correlation function measures how the value of the order parameter at one point is correlated to its value at some other point, so it is a measure of the order of the system. It decreases very fast with distance, then far away points are relatively uncorrelated and the system is dominated by its microscopic structure and short-ranged forces. Given a generic quantity  $A$ , it

can be written as the sum of a mean value,  $\bar{A}$ , plus a fluctuating part  $\delta A$  with zero mean ( $\langle \delta A \rangle = 0$  by definition).

$$C_{\delta A \delta A} \equiv C_{AA} = \langle \delta A \delta A \rangle = \langle (A - \bar{A})(A' - \bar{A}) \rangle = \langle [A(t_0) - \bar{A}][A(t_0 + \tau) - \bar{A}] \rangle = \langle AA' - A\bar{A} - \bar{A}A' + \bar{A}^2 \rangle \simeq \langle AA' \rangle - \langle A \rangle^2$$

which just measures the fluctuations in the quantity  $A$ . From the above definition, we can define the correlation function for pitch angle and magnetic moment, respectively, as:

$$C_{\alpha\alpha}(\tau) = \langle \delta\alpha\delta\alpha \rangle = \langle (\alpha - \bar{\alpha})(\alpha' - \bar{\alpha}) \rangle$$

$$C_{\mu\mu}(\tau) = \langle \delta\mu\delta\mu \rangle = \langle (\mu - \bar{\mu})(\mu' - \bar{\mu}) \rangle$$

with the property

$$C_{\alpha\alpha}(0) = \langle \alpha^2 \rangle - \langle \alpha \rangle^2 = \langle \delta\alpha^2 \rangle$$

and

$$C_{\mu\mu}(0) = \langle \mu^2 \rangle - \langle \mu \rangle^2 = \langle \delta\mu^2 \rangle$$

In Figure 4.14 an example of the correlation functions,  $C_{\alpha\alpha}$  (left panel) and  $C_{\mu\mu}$

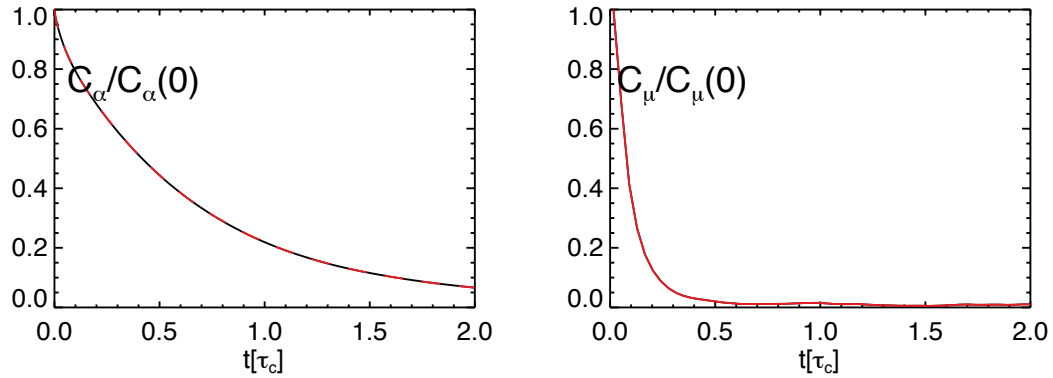


**Figure 4.14:** Correlation functions  $C_{\alpha\alpha}$  (left panel) and  $C_{\mu\mu}$  (right panel) for  $v_p = 10v_A$  and  $\delta b = 0.1$ .

(right panel), is given, for  $v_p = 10v_A$  and  $\delta b = 0.1$ . For a generic quantity  $A$  the correlation time is defined as:

$$\tau_c^A = \int_0^\infty \left[ \frac{C_{AA}(t')}{C_{AA}(0)} \right] dt' \quad (4.27)$$

Let suppose  $C_{AA}(t) = \langle \delta A^2 \rangle e^{-t/\tau_c}$ , then

$$\frac{C_{AA}(t)}{C_{AA}(0)} = e^{t/\tau_c} = \frac{1}{e} \iff t = \tau_c$$

However, it could happen that the function  $C_{AA}(t)$  does not reach the value  $1/e$ . To have a good estimation of the correlation time, the best fit method is used, that

consists to fit the data points with the best line that minimizes the mean square error relative to the data sample. This method is based on the assumption that, if data points follow  $C \sim \exp -t/\tau_c$ , plotting  $\ln C = -t/\tau_c$ , a straight line with slope  $-1/\tau_c$  will result. Considering the data series :  $\{C_j, t_j | j = 1, N\}$  :  $(t_j, C_j)$ , where  $C_j = \ln C_j$ . The best line  $\hat{C} = mt + b$  is the one who minimizes the mean square error relative to the data sample, defined as:

$$\mathcal{E} = \sum_{j=1}^N (C_j - \hat{C}_j)^2 = \sum_{j=1}^N (R_j - mt_j - b)^2$$

From  $\partial \mathcal{E} / \partial m = 0$  we obtain  $m = \sum_{j=1}^N (t_j R_j / \sum_{j=1}^N t_j^2)$  and  $\tau_c = -1/m$ . In Fig-

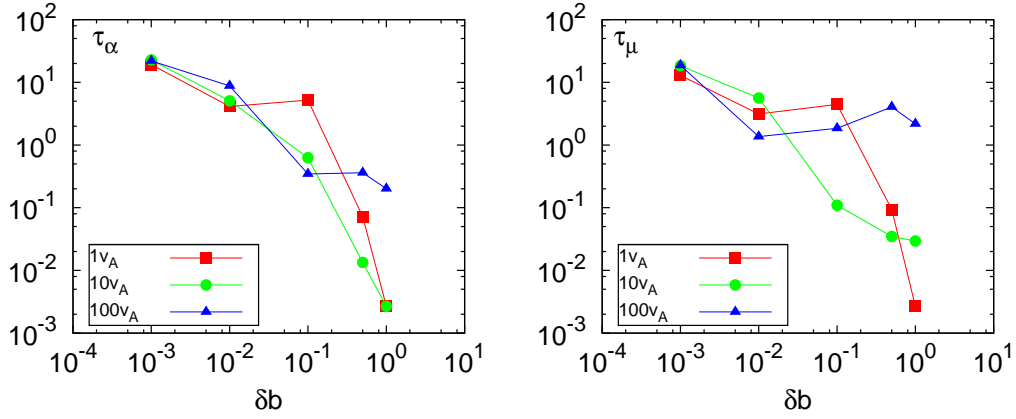


**Figure 4.15:** Correlation times  $\tau_c^\alpha$  (left panel) and  $\tau_c^\mu$  (right panel) versus  $\delta b$  for  $v_p = 1v_A$  (red square),  $v_p = 10v_A$  (green circle) and  $v_p = 100v_A$  (blue triangle).

ure 4.15 the correlation times,  $\tau_c^\alpha$  (left panel) and  $\tau_c^\mu$  (right panel), versus  $\delta b$  are shown for  $v_p = 1v_A$ , red square,  $v_p = 10v_A$ , green circle, and  $v_p = 100v_A$ , blue triangle. For a good understanding of the figure it is necessary to consider the corresponding distribution function. For  $v_p = 1v_A$  (red square, distribution function in Figure 4.10),  $\tau_{alpha}$  and  $\tau_\mu$  decrease with increasing  $\delta b$  for  $\delta b \leq 0.01$ , when  $f(\alpha)$  and  $f(\mu)$  follow a Gaussian distribution and for  $\delta b > 0.1$ , when  $f(\alpha)$  completely isotropizes and  $f(\mu)$  is influenced by spatial diffusion and starts to recover the Gaussian shape. For  $\delta b = 0.1$ ,  $\tau_\alpha$  and  $\tau_\mu$  increase: this is the  $\delta b$  value for which  $f(\alpha)$  is almost isotropic, covering uniformly the  $\alpha$ -space from  $0.5\alpha$  to  $-0.5\alpha$  and  $f(\mu)$  shows a well-pronounced long-tail distribution. For  $v_p = 10v_A$  (green circle, distribution function in Figure 4.9), one can immediately notice that  $\tau_\alpha$  is always decreasing; indeed, in contrast with the previous case, there are not  $\delta b$  value for which  $f(\alpha)$  is almost isotropic, but it is localized in one-side of the  $\alpha$  hemisphere, for  $\delta b = 0.001 - 0.01$  and it is completely isotropic for  $\delta b = 0.1 - 0.5 - 1.0$ . If we consider  $\tau_\mu$ , one immediately notice the same trend until the value  $\delta b = 0.1$  is reached. Looking at the distribution functions  $f(\mu)$ , we would expect an increases

in  $\tau_\mu$ , passing from  $\delta b = 0.001$  to  $\delta b = 0.01$ , as for  $v_p = 1v_A$  when the distribution takes the long-tail shape. However, in contrast with this case for  $\delta b = 0.001$ ,  $f(\mu)$  as a Gaussian-like form, but already shows a tail longer in the side of smaller  $\mu$ . The successive change evident for  $\delta b = 0.5$  corresponds to the recover of Gaussianity in  $f(\mu)$ . For  $v_p = 100v_A$  (blue triangle, distribution function in Figure 4.11),  $\tau_\alpha$  decreases till  $\delta b = 0.1$ . For this value and for  $\delta b = 0.5$ ,  $f(\alpha)$  is almost isotropic, as in the  $1v_A$  case for  $\delta b = 0.1$ . For  $\delta b = 1.0$   $f(\alpha)$  reaches the isotropization, that corresponds to the final decreasing trend in  $\tau_\alpha$ . For  $\delta b = 0.001 - 0.1$ ,  $f(\mu)$  is a Gaussian-like distribution and  $\tau_\mu$  is a decreasing function of  $\delta b$ . For  $\delta b = 0.1 - 0.5$   $f(\mu)$  shows long tail at which corresponds an increase in  $\tau_\mu$ . Notice that greater  $\tau_\mu$  corresponds to longer tail in  $\mu$ -space. Finally, for  $\delta b = 1.0$  magnetic moment behavior is influenced by spatial diffusion and  $\tau_\mu$  returns to decreasing behavior.

# Conclusions

In this thesis work, we studied the effects related to non-adiabatic particle motion in two different physical contexts: the near-Earth's magnetotail and the solar wind. Final discussion and conclusions regarding the first part of this study, *Non-adiabatic particle motion in the near-Earth magnetotail*, have already been given in Section 1.6.

In a more general context, we start to investigate the conservation of charged particle magnetic moment in presence of turbulent magnetic fields. Generally, for slow spatial and temporal changing magnetic field, the magnetic moment,  $\mu$ , is an adiabatic invariant of particle motion. But in the presence of well developed magnetic turbulence,  $\mu$  might undergo rapid variations and in any case can no longer be expected to be constant. Of course, this fact could influence particle acceleration and could have a considerable implications in many astrophysical problems, such as coronal heating, cosmic rays transport or temperature anisotropies in the solar wind.

We have re-analyzed the problem of charged particle diffusion in static turbulent one-dimensional magnetic fields from a semi-dynamical point of view, using the analytical results of *Karimabadi et al. (1992)* for the trapping width in velocity space,  $\Delta v_{\parallel}$  and the bounce frequency,  $\omega_b$ , of a particle in resonance with an electromagnetic wave. In order to reproduce and to extend some of the result obtained by *Karimabadi et al. (1992)*, we started to study the resonant interaction between ions and a single parallel propagating electromagnetic wave, to understand in this very simple case the limit for magnetic moment conservation. During the interaction with a single finite amplitude fluctuation, a resonant particle undergoes a finite amplitude nonlinear oscillation, given by half peak-to-peak difference in the particle parallel velocity component, the so-called trapping width,  $\Delta v_{\parallel}$ . The period of this oscillation is given by  $\tau_b = 1/\omega_b$ , where  $\omega_b$  is the bounce or trapped frequency. We specialized the expressions for  $\Delta v_{\parallel}$  and  $\omega_b$ , given by *Karimabadi et al. (1992)*, in the case of a single circularly polarized wave:

$$\begin{aligned}\Delta v_{\parallel}^{(-1)} &= 2v \left[ (1 - \alpha^2)^{1/2} |\alpha| \frac{\delta B}{B_0} \right] \\ \omega_b^{(-1)} &= \Omega_0 \left[ \frac{(1 - \alpha^2)^{1/2} \delta B}{|\alpha| B_0} \right]\end{aligned}\tag{4.28}$$

and we wrote a similar expression for the magnetic moment trapping width,  $\Delta\mu$  (*Dalena et al.*, in prep).

$$\Delta\mu = 4\alpha \left[ (1 - \alpha^2)^{1/2} |\alpha| \frac{\delta B}{B_0} \right]\tag{4.29}$$

Results from different simulations are shown, varying both particle velocity and the amplitude of the wave. For each of them we compared the values of  $\Delta\mu$  and  $\Delta v_{\parallel}$



resulting from numerical simulations, with the value obtained using our specialized expression. A good agreement between theory and simulations is obtained. Moreover, analyzing the distribution functions of particles pitch angle,  $f(\alpha)$ , magnetic moment,  $f(\mu)$  and  $z$ -position  $f(z)$  in a particular experiment designed to study the effects of resonances overlapping, three regimes of behavior of the magnetic moment distribution. First, for a low level of magnetic fluctuation, i.e.,  $\delta b = 0.001, 0.01$ , the magnetic moment distribution half-width is directly related to pitch angle distribution. Second, when stochasticity arises as a consequence of overlapping resonances, its effect on pitch angle is the isotropization of the distribution function. This is a transient regime during which magnetic moment exhibits a one-sided long-tail distribution, in what appears to be a signature of magnetic moment behavior in the regime of overlapping resonances, and starts to be influenced by the onset of spatial parallel diffusion. Finally, when  $f(\alpha)$  completely isotropizes, spatial diffusion sets in and  $f(\mu)$  behavior is closely related to the sampling of varying magnetic field strength associated with that spatial diffusion.

Other studies, regarding particles interaction with two electromagnetic waves as well as a flat turbulent spectrum, are also conducted and they confirmed this general view.

Motivated by these preliminary results, we studied the behavior of many particles interacting with a broad band slab spectrum. One of the goal of our simulations is the direct applicability of the results obtained here to the solar wind physical system. Indeed, our slab spectrum is generated in order to reproduce some of the major features of the solar wind (see Figure 3.4), considering three decades of *energy containing scale*, to ensure turbulence homogeneity, three decades of the inertial range, characterized by:

$$P(k_n) = P^{slab}(k_n) = C_{slab}[1 + (k_n l_z)^2]^{-5/6}, \text{ for } k_n < k_{diss}$$

that well represent the solar wind case, other two decades of the *dissipation range*, characterized by:

$$P(k_n) = P^{diss}(k_n) = C_{diss} \left( \frac{k_n}{k_{diss}} \right)^{-7/3}, \text{ for } k_n \geq k_{diss}$$

in order to cross the  $\alpha_{min}$  barrier, related with the problem of the *resonance gap* predicted by quasilinear theory. After that there are almost other two decades of zero-padding, important for the trigonometric interpolations and for the smoothness of the field. The resulting magnetic field is stored on a grid of spacing  $\Delta z = L/N_z$ , where  $N_z$  is an even integer fixed at  $N_z = 2^{28} = 268, 435, 456$ .

In order to gain some insight of magnetic moment conservation, different simulations are performed varying both particles velocity,  $v_p$ , and the amplitude of magnetic field fluctuations,  $\delta B/B_0 = (0.001 - 0.01 - 0.1 - 0.5 - 1.0)$ . Particles injected at different velocities,  $v_p = (1 - 10 - 100)v_A$ , start to resonate at different points of the spectrum (see Figure 4.7); thus, the related effects are also analyzed. For this case we analyzed the variance and the distribution function of particles pitch angle  $\alpha$ ,

magnetic moment  $\mu$  and parallel position  $z$ , the corresponding standard deviation  $\sigma$  and the correlation time  $\tau_c$ . From the experiment of resonances overlapping, we understood that magnetic moment behavior is related to pitch angle for low level of magnetic fluctuations or for shorter time. On the contrary, increasing  $\delta b$  or the integration time, spatial diffusion sets in, pitch angle distribution isotropizes and magnetic moment is influenced by diffusion that takes place in real space. Because velocity and real space diffusion occur at different time scale, in order to investigate the effects of both processes on magnetic moment distribution, we followed test-particles in the simulation box for time  $T$  greater than the velocity space diffusion time scale. We found that, for low level of magnetic fluctuations, pitch angle distribution,  $f(\alpha)$ , assumes a Gaussian shape, usual of normal diffusion. An analogous behavior is observed for magnetic moment distribution,  $f(\mu)$ , while particles free-stream in the  $z$ -direction. In this case  $f(\alpha)$  and  $f(\mu)$  are centered around their initial values. Generally, for  $\delta B/B_0 = 0.01$  particles start to cover completely one side of the  $\alpha$  hemisphere, continuing to free-stream along  $z$ . This is the transient regime, during which  $f(\mu)$  exhibits a one-sided long tail distribution in the direction of smaller  $\mu$ , that appears to be a typical feature of magnetic moment distribution, during which the distribution of particles nearly conserves its magnetic moment. Increasing the  $\delta B/B_0$  value, as spatial diffusion starts to take place,  $f(\mu)$  recovers the typical Gaussian shape, centered in the middle of  $\mu$ -space, related to the sampling of varying magnetic field strength associated with that spatial diffusion. This general view is also confirmed from the analysis of the magnetic moment correlation times,  $\tau_c^\mu$ , versus  $\delta B/B_0$ , that are decreasing when a Gaussian shape in  $f(\mu)$  is observed and tend to assume greater values when  $f(\mu)$  shows the one-side long tail distribution, that means that  $\mu$  values at different times are more correlated and  $\mu$  is more conserved. Of course, we suppose that these transitions in magnetic moment behavior are related not just with the variation of the turbulence level,  $\delta B/B_0$ , but also with the different time scale at which magnetic moment conservation is studied, in the sense that if we performed longer simulation for  $\delta B/B_0 = 0.1$ , we should find an initial regime characterized by normal diffusion, as a consequence of pitch angle diffusion, a transient regime in which  $f(\alpha)$  starts to isotropize and  $f(\mu)$  shows is typical long-tail distribution, and a third regime during which spatial diffusion sets in, causing the recovering of the Gaussian shape in  $f(\mu)$ .

Finally, making use of the for  $\Delta v_{\parallel}$  and  $\omega_b$ , it was shown that the diffusion coefficient for velocity space diffusion in  $v_{\parallel}$  can be written in the physically intuitive forms

$$D_{\alpha\alpha} = \frac{\omega_b^2 \tau_{ac}^2 (\Delta\alpha)^2}{2\tau_{ac}} = \frac{(\Delta\alpha_{\text{eff}})^2}{2\tau_{ac}},$$

where the effective trapping width  $\Delta\alpha_{\text{eff}} = \Delta v_{\parallel}^{\text{eff}}/v$  characterizes the trapping width of the potential well in the extrinsically stochastic system of the resonant wave plus the perturbations induced by randomly phased neighboring wavemodes in the resonant wave packet. The trapping width is also of the order of the magnitude of the kick in pitch angle cosine that the particle experiences during this resonant interaction. The timescale for the particle to interact resonantly with the wavepacket

is given by the autocorrelation time of the fields as seen by the particle, which, in the simplified magnetostatic model considered here, is simply the transit time for the wavepacket in the particle frame of reference,  $\tau_{ac} = \lambda_c/|v_{\parallel}|$ . To the best of the author knowledge, it is the first time that the diffusion coefficient for pitch angle diffusion in magnetostatic turbulence has been written in this physically appealing form. It is shown how this effective resonance width implies a condition on the density of wavemodes in Fourier space, in the vicinity of the resonant wavenumber. The implications of this condition for simulations incorporating discrete fields is discussed in detail and examples of simulations violating this condition are presented too.

# Acknowledgments

As usual, at the end of a chapter, it must be remembered that nothing would have been possible without the support and the help of all the people around me. Indeed, this was a long way, sometimes difficult and some other times amusing, but in any case, nothing would have been the same without all the people I met during these years and, of course, without the old friends and my family that have always been close to me, also when an ocean was between us.

First of all, I am heartily thankful to my supervisor, Dr. Antonella Greco, for her encouragement, guidance and support from the initial level of my studies until to this final point.

I would like to show my gratitude to Prof. Gaetano Zimbardo for always giving me supervision and the helpful suggestions during my graduate study.

I wish to sincerely express my gratitude to my co-advisors, Prof. William H. Matthaeus. He provided encouragement, good teaching, good company and lots of good ideas. Without his guidance, I could not finish this work.

I would like to thank, of course, all the people from my research group both at the University of Calabria and at the University of Delaware. In particular Silvia P. and Luca S. V. for helping me to learn the real Calabrese language, Sergio S. and Franco V., that did not steal my research topics, Antonio V. for providing the necessary portion of sugar every twelve months, Franco R. for his support and encouragement when the job got me almost crazy, Penny W. and Tulasi N. P. for their sincere friendship.

I am indebted to my Ph.D. colleagues, Denise P., Giuseppe N., Sandro D. and Vincenzo C., for providing a stimulating and fun environment in which to learn and grow together.

Beyond Physics, that sometimes seems almost an unrealistic world, I am deeply indebted to all the people that I met abroad during the last two years and who have made the distance from my home in Italy less hard to bear. A special thank is for Susan E. and Niki R. C., Lucia V., Ilaria M., Federica A., Damiano Z., my US family.

I would like to thank all the people closest to me, rigorously in alphabetic order: Aldo B., Alessandra A. (a.k.a. Beecella), Alessandra A. (a.k.a. Bellezza), Armando A., Ileana F., Francesco T., Margherita M. (a.k.a. Sequoia), Melissa I.. You have been in my life every day since I met you for the first time and of course, with my family, you are the people I love. I know we will be always together, despite the large distances that sometimes are between us.

Finally, never enough thanks and all my love is for all my family, always behind me during all these years. I have to specify some names here too: my mom Annamaria, my dad Piero, my brother Matteo, my aunt Giuliana, my uncle *Zu* Nando, my cousins Giorgia (a.k.a. Georgette), Federica (a.k.a. Titta), Mirko (a.k.a. Mimí) and Lorenza (a.k.a. Luana), and finally my wonderful grandmother, *signora* Maria.



# Details of the model used in Chapter 1

---

## A.1 Parity of Magnetic Perturbations

As usual, reality of  $\delta\mathbf{B}(\mathbf{r})$  implies  $\delta B_\sigma(\mathbf{k}) = \delta B_\sigma(-\mathbf{k})$  and  $\phi_{\mathbf{k}}^\sigma = -\phi_{-\mathbf{k}}^\sigma$ . Since the assumed amplitude  $\delta B_\sigma(\mathbf{k})$  is independent of the sign of  $\mathbf{k}$  and of the polarization, that is  $\delta B_\sigma(\mathbf{k}) = \delta B(\mathbf{k})$ , for the components of perturbed magnetic field  $\delta\mathbf{B}_i(\mathbf{r})$  we get:

$$\delta B_x(\mathbf{r}) = \sum_{k_x, k_y, k_z \geq 0} 2\delta B(\mathbf{k}) \left[ \frac{k_\perp}{k} g_{\mathbf{k}}(\mathbf{r}) \right] \quad (\text{A.1})$$

$$\delta B_y(\mathbf{r}) = \sum_{k_x, k_y, k_z \geq 0} 2\delta B(\mathbf{k}) \left[ \frac{k_y k_x}{k_\perp k} g_{\mathbf{k}}(\mathbf{r}) + \frac{k_z}{k_\perp} h_{\mathbf{k}}(\mathbf{r}) \right] \quad (\text{A.2})$$

$$\delta B_z(\mathbf{r}) = \sum_{k_x, k_y, k_z \geq 0} 2\delta B(\mathbf{k}) \left[ \frac{-k_x k_z}{k_\perp k} g_{\mathbf{k}}(\mathbf{r}) + \frac{k_y}{k_\perp} h_{\mathbf{k}}(\mathbf{r}) \right] \quad (\text{A.3})$$

where

$$g_{\mathbf{k}}(\mathbf{r}) = \cos(\mathbf{k} \cdot \mathbf{r} + \phi_{\mathbf{k}}^2), \quad h_{\mathbf{k}}(\mathbf{r}) = \sin(\mathbf{k} \cdot \mathbf{r} + \phi_{\mathbf{k}}^1)$$

and  $k_\perp = \sqrt{k_x^2 + k_y^2}$ ,  $k = \sqrt{k_x^2 + k_y^2 + k_z^2}$ .

In order to describe the formation of magnetic islands in the vicinity of the neutral sheet during the tearing mode development, in addition to reality, we have to impose further restrictions in the random phases. Such restrictions impose parity rules for the perturbed magnetic field of a given tearing mode with wave vector  $\mathbf{k}$ . In particular, the  $x$  component of the perturbed magnetic field has to have odd parity with respect to the  $z = 0$  plane, i.e.,

$$\delta B_x(x, y, z) = -\delta B_x(x, y, -z) \quad (\text{A.4})$$

and the  $z$  component of  $\delta B$  has to have even parity:

$$\delta B_z(x, y, z) = \delta B_z(x, y, -z). \quad (\text{A.5})$$

Taking the sum of the perturbed  $x$  and  $z$  components with the same  $k_x$  and  $k_y$  but opposite  $k_z$  in Eq. (A.2) - (A.3) and imposing the above parity relations, we obtain the following conditions that random phases have to satisfy:

$$\phi_{k_x, k_y, k_z}^1 = \phi_{k_x, k_y, -k_z}^1 \quad (\text{A.6})$$

$$\phi_{k_x, k_y, k_z}^2 = \phi_{k_x, k_y, -k_z}^2 + \pi \quad (\text{A.7})$$

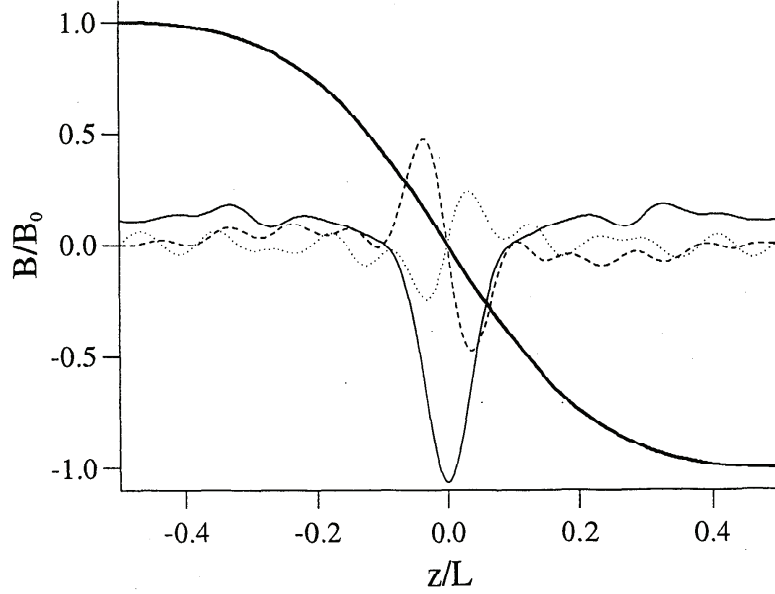


**Figure A.1:** The  $z$  dependence of the perturbed components of the magnetic field at a sample position  $x, y$  inside the simulation box for  $\delta B/B_0 = 0.5$ :  $\delta B_x$ , dotted line,  $\delta B_y$ , dashed line and  $\delta B_z$ , thin solid line. Also plotted is the unperturbed component,  $B_{0x}(z)$ , thick solid line.

The  $\delta B_y$  component has automatically odd parity from these conditions, as evident in Figure A.1. At the same time, to represent the concentration of the perturbations in the vicinity of the plane  $z = 0$ , as the tearing mode turbulence requires (*White et al., 1977*), we will take phases  $\phi^1$  and  $\phi^2$  as randomly chosen for the different  $k_x$  and  $k_y$  but independent of  $|k_z|$ .

Figure A.1 shows a vertical profile of the three  $\delta \mathbf{B}$  components. The dotted line represents  $\delta B_x$ , the dashed line corresponds to  $\delta B_y$ , and the thin solid line to  $\delta B_z$ . Also plotted, using a thick solid line, is the unperturbed component,  $B_{0x}(z)$ . The requested parity of  $\delta \mathbf{B}$  and the typical spatial variations are evident in the figure.

## A.2 Velocity Space Injection

Particles are injected at the boundaries of the simulation box,  $z = \pm 0.5L$ , with a distribution corresponding, in velocity space, to the flux of a shifted Maxwellian, see Eq. 1.9. Since the particles are entering the simulation box by moving along  $z$ , this yields  $F(v_x, v_y, v_z) \propto v_z f(v_{\parallel}, v_{\perp})$ . We express  $v_{\parallel}$  and  $v_{\perp}$  through  $v_x, v_y$  and  $v_z$  to have:

$$v_{\parallel} = \frac{\mathbf{v} \cdot \mathbf{B}}{|\mathbf{B}|} = \frac{v_x B_x + v_y B_y + v_z B_z}{\sqrt{B_x^2 + B_y^2 + B_z^2}} \quad (\text{A.8})$$

$$v_{\perp} = v^2 - v_{\parallel}^2 = v_x^2 + v_y^2 + v_z^2 \quad (\text{A.9})$$

The unperturbed magnetic field components at the  $z = \pm 0.5L$  surfaces are equal to  $|B_x| = B_0$ ,  $B_y = 0$ ,  $B_z = B_n$ . We introduce the components of the unit vector along  $B$  at  $z = \pm 0.5L$ :

$$\hat{b}_x = \frac{B_0}{\sqrt{B_0^2 + B_n^2}} \equiv \frac{1}{\sqrt{1 + b_n^2}} \quad (\text{A.10})$$

$$\hat{b}_z = \frac{B_n}{\sqrt{B_0^2 + B_n^2}} \equiv \frac{b_n}{\sqrt{1 + b_n^2}} \quad (\text{A.11})$$

As far as injection is concerned, only the nonfluctuating magnetic field is considered. Inserting these expressions into Eq. 1.9, we finally come to the equation that has to be solved for the variables  $v_x$ ,  $v_y$  and  $v_z$ , distributed according to a shifted Maxwellian:

$$\begin{aligned} & \frac{\exp(-u^2/2v_{th}^2)}{(\sqrt{2\pi}v_{th}^3)} \exp\left(-\frac{v_x^2 - 2u\hat{b}_x v_x}{2v_{th}^2}\right) \exp\left(-\frac{v_y^2}{2v_{th}^2}\right) \\ & \times v_z \exp\left(-\frac{v_z^2 - 2u\hat{b}_z v_z}{2v_{th}^2}\right) dv_x dv_y dv_z = C d\xi d\eta d\zeta, \end{aligned}$$

where  $\xi$ ,  $\eta$  and  $\zeta$  are random numbers evenly distributed in the interval  $[0, 1]$ , and  $C$  is a constant calculated from the conditions specified below. The coefficient  $(\sqrt{2\pi}v_{th}^3)^{-1} \exp(-u^2/2v_{th}^2)$  depends only on the constant parameters  $u$  and  $v_{th}$  and hereinafter can be included in the constant  $C$ . We will also assume for this Appendix that all velocities are normalized to thermal velocity  $v_{th}$  and drop  $v_{th}$  in what follows. As it is clear from Eq. A.12, the dependence on each of the velocity components is factorized, and we can solve independently three different equations, namely:

$$\exp\left[-\left(v_x^2 - 2u\hat{b}_x v_x\right)/2\right] dv_x = C_\xi d\xi \quad (\text{A.12})$$

$$\exp\left[-v_y^2/2\right] dv_y = C_\eta d\eta \quad (\text{A.13})$$

$$v_z \exp\left[-\left(v_z^2 - 2u\hat{b}_z v_z\right)/2\right] dv_z = C_\zeta d\zeta \quad (\text{A.14})$$

Clearly,  $v_y$  is distributed according to a Maxwellian and we can use the Central Limit Theorem for  $v_y$  (Veltri *et al.*, 1998).

For  $v_x$  and  $v_z$  we have to take into account the asymmetry introduced by the streaming velocity  $u$ . Assuming that  $x$  varies in the interval  $0 < x < 1$  with uniform probability, and integrating Eq. A.13 from  $-\infty$  to  $v_x$  on the l.h.s. and from 0 to  $\xi$  on the r.h.s., we easily obtain the equation to be solved for  $v_x$ :

$$1 + erf\left[\left(v_x - u\hat{b}_x\right)/\sqrt{2}\right] = C_\xi \xi \quad (\text{A.15})$$

where the coefficient  $(\sqrt{\pi}/2) \exp u^2 \hat{b}_x^2 / 2$  can again be assumed to be included in  $C_\xi$  and  $erf(x)$  is the well known Error function:  $erf(x) = (2/\sqrt{\pi}) \int_0^x \exp(-t^2) dt$ . It is evident that, for  $\xi = 0$ ,  $v_x = -\infty$  ( $erf(-\infty) = -1$ ). The coefficient  $C_\xi$  is fixed



by the condition that  $v_x = +\infty$  for  $\xi = 1$ . Thus for  $C_\xi$  we obtain from Eq. A.15:  $C_\xi = 1 + \text{erf}(+\infty)$ . Finally, to get the distribution of  $v_x$  corresponding to function given by Eq. A.13, we have to solve for each random number  $\xi$  ( $0 < \xi < 1$ ) the equation:  $1 + \text{erf} \left[ (v_x - u\hat{b}_x)/\sqrt{2} \right] = 2\xi$ .

The integral in Eq. A.13 for  $v_x$  is positively defined over all the interval of integration. This is not the case for  $v_z$  component (see Eq. A.14), where we have to consider separately positive and negative  $v_z$  for particles entering into the current sheet from the lower ( $z = -0.5L$ ) and upper ( $z = 0.5L$ ) boundaries, respectively, of the simulation box. Integrating Eq. A.14 for  $z > 0$  in the interval  $-\infty < v_z < 0$  we obtain:

$$I^-(v_z, u) = -\exp \left[ (v_z^2 - u^2\hat{b}_z^2)/2 \right] + \alpha \text{erf} \left[ (v_z - u\hat{b}_z)/\sqrt{2} \right] \quad (\text{A.16})$$

where  $\alpha = \sqrt{\pi/2} u \hat{b}_z \exp \left( u^2 \hat{b}_z^2 / 2 \right)$ . For  $v_z = 0$  we will have

$$I^-(v_z, u) = -1 + \alpha(1 - \Psi) \equiv C^- \quad (\text{A.17})$$

where  $\Psi = \text{erf} \left( u\hat{b}_z/\sqrt{2} \right)$ . Here we have used the antisymmetric property of the Error function,  $\text{erf}(-x) = -\text{erf}(x)$ .  $C^-$  defines the weight of negative velocities  $v_z$  in the distribution. Now, integrating equation for  $v_z$  in Eq. A.14 for  $z < 0$ , in the interval  $0 < v_z < \infty$ , it is easy to show that the corresponding integral on the left side is equal to  $I^+(v_z, u) = -I^-(-v_z, -u)$ . Introducing the coefficient  $C^+$  as the weight of positive  $v_z$  in the distribution, we will obtain:

$$C^+ \equiv I^+(0, u) = 1 + \alpha(1 + \Psi). \quad (\text{A.18})$$

Now, the interval  $[0, 1]$  for the random number  $z$  has to be divided, according to the corresponding weights, in two intervals:  $0 < \zeta < \zeta_1$  for negative  $v_z$  and  $\zeta_1 < \zeta < 1$  for positive  $v_z$ , where  $\zeta_1$  is equal to:

$$\zeta_1 = \frac{|C^-|}{|C^+| + |C^-|} = \frac{1 - \alpha(1 - \Psi)}{2(1 + \alpha\Psi)}. \quad (\text{A.19})$$

Here we have used the fact, that  $C^-$  is negative and  $C^+$  positive for any positive  $u$ . Integrating now Eq. A.14 for the proper intervals, we will have for negative and positive  $v_z$  the following relations:  $I^-(v_z, u) = C_\zeta^- \zeta$  and  $I^+(v_z, u) = C_\zeta^+(1 - \zeta)$ , respectively, where the coefficients  $C_\zeta^-$  and  $C_\zeta^+$  have to satisfy the following conditions:

$$C_\zeta^- \zeta_1 = I^-(0, u) \equiv C^-, \quad C_\zeta^+(1 - \zeta_1) = I^+(0, u) \equiv C^+. \quad (\text{A.20})$$

From this system of equations and the expressions for  $C^-$  and  $C^+$ , given by Eq. A.17 and Eq. A.18 we will obtain for the coefficients  $C_\zeta^-$  and  $C_\zeta^+$ :

$$C_\zeta^- = -2(1 + \alpha\Psi), \quad C_\zeta^+ = 2(1 + \alpha\Psi). \quad (\text{A.21})$$

When  $u = 0$ ,  $\zeta_1$  is equal to 0.5 and we recover the results obtained by citeVeltriEA98 for a Maxwellian distribution of the inflowing particles. Solving Eq. A.20 and Eq. A.21 for each random number  $\zeta$  in the corresponding interval we will obtain the required particle distribution.

# Details of the model for $\mu$ conservation and additional results.

---

## B.1 About test particle simulations & Streamline code

Plasma consists of positive charged ions and negative charged electrons. Since  $m_i \gg m_e$ , there are many intrinsic spatial and time scales in a plasma system, even if a uniform background environment is considered. For time scale smaller than the intrinsic time scales, it is hard for the system to reach a thermal dynamic equilibrium state and kinetic effect might become important. These also means that the typical length scale of the system  $L$  is comparable to the characteristic length scale of a given species (ions and/or electrons), i.e. the Larmor radius,  $r_L = v_{th}/\Omega$ , in which  $v_{th}$  is the particle thermal velocity and  $\Omega = mv/qB$  is the particle gyrofrequency.

Generally, two different numerical approaches may be considered in order to study plasma evolution: kinetic approach and fluid approach. Kinetic simulations are used to study the non-linear evolutions of wave-particle interactions in the phase-space on spatial and time scale on which kinetic effects are not negligible. On the other hand, a fluid simulation code can provide reasonable and relatively quick results, when the kinetic effects become unimportant. Depending on their resolutions in phase-space, we can classify the most common plasma simulations as follows:

- Fluid Simulations
  - MHD code:  $L \geq 10^3 r_{Li}$
  - Two-Fluid code:  $10^3 r_{Li} \geq L \geq 10 r_{Li}$
- Kinetic Simulations
  - Hybrid code (fluid electrons & kinetic ions):  $10 r_{Li} \geq L \geq r_{Li}$
  - Full particle code:  $r_{Li} \geq L \geq r_{Le}$
  - Test particle code: when a strong magnetic field is present
  - Vlasov code:  $r_{Li} \geq L \geq r_{Le}$

where  $L$  is the typical length scale of the system and  $r_{Li,e}$  are the typical ion/electron gyroradius. When  $L$  approaches the ion thermal gyroradius, ions become demagnetized and the plasma can no longer behave as a simple fluid. As a consequence, the

usual MHD description breaks down in favor of a more complex (kinetic) plasma description.

In this paper we concentrate our discussion on the test-particle methods, that means the electromagnetic fields are treated as prescribed and particles can be treated fully independently from each other in the simulation. In the absence of iterations and feedback from calculated particle trajectories, the results are generally not self-consistent. Test-particle calculations can be used to study a broad class of problems in space physics and astronomy, such as particle transport, energization and dynamics in complex systems, for which a fully consistent kinetic calculation is not practical. Indeed test-particle simulations represent a complementary approach between fluid and fully kinetic models. Fluid models are powerful tools for modelling complex systems while accounting for realistic geometry together with multiple physical processes. However, they are limited to the description of macroscopic properties of plasmas in terms of the local distribution functions momenta. On the other hand, kinetic models provide detailed information on particle dynamics but, because of their complexity, they are limited to relatively simple geometries in the range of physical processes that they can account for. In that context test-particles provide a useful bridge between the two approaches. Using approximate fields obtained from macroscopic models or analytical field expressions, they can be applied to assess kinetic effects in complex systems under realistic conditions.

This latest version of Streamline is part of a succession of programs developed at the University of Delaware within Dr. Matthaeus's group in the Department of Physics and Astronomy and Bartol Research Institute. Replacement of working and tested code is generally frowned upon, but the main ordinary differential equations (ODE) integration (in all versions) relied on modified code from Numerical Recipes. Thus, the ODE integration is performed using published routines that are operationally unchanged from their documented source code. Streamline has the ability calculate static field-lines, particle trajectories, or more generally solve the first order ODE:

$$\frac{d\mathbf{x}}{ds} = \mathbf{f}(\mathbf{x}), \quad (\text{B.1})$$

where  $\mathbf{x} = (x_1, x_2, \dots, x_N)$  is an  $N$ -dimensional generalized position,  $s$  is a generalized arc length parameterization, and  $\mathbf{f}(\mathbf{x}) = (f_1(\mathbf{x}), f_2(\mathbf{x}), \dots, f_N(\mathbf{x}))$  is vector field determinable at every generalized position  $\mathbf{x}$ . As an illustration, consider a particle with mass  $m$  moving under the time-dependent force  $\mathbf{F}(\mathbf{x}, t)$ . In this case,  $s \equiv t$ , and we have:

$$\mathbf{x} = (x, y, z, v_x, v_y, v_z), \quad (\text{B.2})$$

$$\mathbf{f} = (v_x, v_y, v_z, a_x, a_y, a_z) \quad (\text{B.3})$$

where  $a = \mathbf{F}/m$  and  $N \equiv 6$ . This system is usually written as two coupled ODE's:

$$\frac{d\mathbf{x}}{dt} = \mathbf{v}(\mathbf{x}, t), \quad (\text{B.4})$$

$$\frac{d\mathbf{v}}{dt} = \mathbf{a}(\mathbf{x}, t). \quad (\text{B.5})$$

This code is a MPI parallel implementation of a versatile algorithm for computation of streamlines, magnetic field lines or charged particle trajectories. Each of these has in common that a set of generalized "trajectories" is generated, beginning from a set of specified initial conditions. The trajectories are generated by integrating a set of ODE's, either three (for streamlines and field lines) or six (for charged particle orbits). In each case one or more vector fields, appearing as coefficients in the ODE's, must be specified. Physically what is required for each different case is:

- Streamlines: specify a velocity field and an initial position;
- Magnetic Field Lines: specify a magnetic field and an initial position;
- Charged Particle Orbits: specify a magnetic field, and electric field, and an initial position and velocity.

The ODE's are integrated using an adaptive step fourth order Runge-Kutta method with a fifth order error estimate (*Press et al.*, 1992, pp. 708-716). The entire simulation run is broken down into a number of substeps, each with time interval  $\delta t \ll T_{max}$ , where  $T_{max}$  is the total length of the run. The routine steps each particle in turn through the time interval  $dt$ , while maintaining a local relative accuracy of  $racc = 10^{-9}$  at each step. This process is repeated until the run ends and all particles are stepped through the time interval for the entire run,  $T_{max}$ . Several standard cases are built in at present, choicing of ODE's (field line or charged particle orbit equations) and the magnetic field input model (slab, slab plus 2D, data read from file). Several test cases are also installed in the code. Provisions are made for user-supplied ODE's (routine DERIVS) and user-supplied electromagnetic fields (routine EMFIELDS) that are externally linked and communicate with the internal routines through standard data structures. Streamline version 4 is capable of handling analytic fields, tabulated fields read and interpolated from file, or no fields at all, so long as Eq. B.1 is fully defined. These fields are expected to be electromagnetic fields, but this is not assumed.

This piece of software is a very versatile field generation code, with lot of features that gives the advanced users all the power through the various input files. This also has the provision for extending e/o adding new programs and algorithms. The whole MPI part could be used as wrapper around different versions of electromagnetic fields and various derivatives. This is done by considering the whole setup as a black-box and writing customized "emflds" and "derivs" subroutines by following the interfaces provided in this program. The code works programming the master node to pass out "jobs" to the worker nodes. Each job includes the initial data and some other parameters. Load balancing is achieved in a standard way: when a node is done a job, it asks the master if there is another job to do. Results of each job are written to disk.

## B.2 Test of Accuracy of Streamline Code

In order to substantiate the accuracy of numerical results coming from more complex electromagnetic field configurations, we test the streamline code for different and simpler cases:

- Particles moving in a constant magnetic field  $\mathbf{B} = B_0 \mathbf{e}_z$
- Particles moving in a constant magnetic field  $\mathbf{B} = B_0 \mathbf{e}_z$  plus a constant electric field  $\mathbf{E} = E_0 \mathbf{e}_x$ .
- Particles moving in a circularly polarized wave field
- Particles moving in two circularly polarized waves field

For the first two cases, the exact solution of the problem is known. Thus, it is possible to compare directly the analytical solution with the numerical results. For the last two cases the condition that guarantees the accuracy of our simulations is the energy conservation. Indeed, because no electric fields are present in the system the energy of a given particle must be conserved.

### 1. Particles moving in a constant magnetic field $\mathbf{B} = B_0 \mathbf{e}_z$ .

As we know from the classical particle motion theory, a particle with charge  $q$ , moving with a velocity  $\mathbf{v} = \mathbf{v}_{\parallel} + \mathbf{v}_{\perp}$  in a uniform magnetic field  $\mathbf{B}_0$  experiences a force, the so-called Lorentz force  $\mathbf{F}_L$ , perpendicular to both the particle velocity  $\mathbf{v}$  and the magnetic field  $\mathbf{B}_0$ , so that it does no work on the particle. The Lorentz force  $\mathbf{F}_L$  can change only the direction of the particle velocity component  $v_{\perp}$  perpendicular to  $\mathbf{B}_0$ . The analytic solution of this problem is given by:

$$\begin{aligned} v_x(t) &= v_{x0} \cos(\Omega t) + v_{y0} \sin(\Omega t) \\ v_y(t) &= v_{y0} \cos(\Omega t) - v_{x0} \sin(\Omega t) \\ v_z(t) &= v_{z0} = \text{const} \end{aligned} \tag{B.6}$$

where  $\Omega = mv/qB$  and  $v_{x0}$ ,  $v_{y0}$  and  $v_{z0}$  are the initial velocities in  $x$ ,  $y$  and  $z$  respectively. Thus, the charged particle moves on a circle in the  $x - y$  plane around the magnetic field  $\mathbf{B}_0$ , while the parallel velocity component  $v_{\parallel}$  carries the particle along the magnetic field lines, creating an helical trajectory.

### 2. Particles moving in a constant magnetic field $\mathbf{B} = B_0 \mathbf{e}_z$ plus a constant electric field $\mathbf{E} = E_0 \mathbf{e}_x$ .

The analytic solution for this case is:

$$\begin{aligned} v_x(t) &= v_{x0} \cos(\Omega t) + \left( v_{y0} + \frac{E_0}{B_0} \right) \sin(\Omega t) \\ v_y(t) &= \left( v_{y0} + \frac{E_0}{B_0} \right) \cos(\Omega t) - v_{x0} \sin(\Omega t) - \frac{E_0}{B_0} \\ v_z(t) &= v_{z0} \end{aligned} \tag{B.7}$$

Since an electric field is present in the  $x$  direction, particles drift in the  $y$  direction and their trajectories assume a cycloidal shape. In this case the energy is oscillating and not constant, as in the previous case.

We define the relative error as:

$$\text{Relative Error} = \frac{|v_{num}^2 - v_{an}^2|}{v_{an}^2},$$

where  $v_{an}$  and  $v_{num}$  are the magnitude of velocity from analytical solution and from numerical results, respectively. We test 10 particles injected with random initial points and initial velocities given by  $v_{x0} = 10v_A$ ,  $v_{y0} = 0$  and  $v_{z0} = 0$ . Thus,  $v_{num}$  is the average velocity for 10 particles.

For the two cases described above we collect results at various  $racc$  values. When particles move in a uniform magnetic field, the relative error increases linearly with time in a log-log scale with a slope= 1, as shown in Figure B.1(a). For the second case, particles moving in uniform magnetic and electric field, results at various  $racc$  are shown in Figure B.1(b). The accuracy oscillates a bit and, for  $racc = 10^{-16}$ , round-off effects appears. The error grows with the same slope of the previous case.

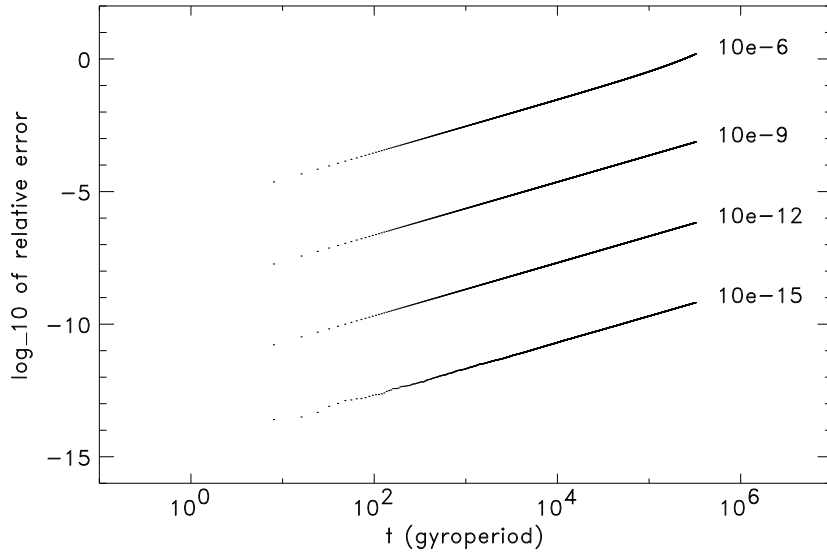
From the accuracy tests, we can see that the relative error depends on the parameter  $racc$  and increases linearly with time at the beginning of the simulation. For the two tested cases, at  $10^5$  gyroperiods, a time longer than all the simulations that we performed to study realistic physical problem, we get a relative error of order  $10^{-4}$  for  $racc = 10^{-9}$ . Thus,  $racc = 10^{-9}$  can be chosen as best value for the accuracy parameter of our numerical simulations.

Once fixed  $racc = 10^{-9}$  for all the simulations, additional test are done in order to verify if the relative error remains of the same order also when some typical parameters, as particles velocity,  $v$ , and  $\beta$  are varied. In Figure B.2 the relative error of particle trajectories in a uniform magnetic field is shown for different values of particle velocities,  $v_p = (1 - 10 - 1000)v_A$  (top row) and for different values of the  $\beta$  parameter,  $\beta = (1 - 10 - 10^4)$  (bottom row). It is evident that after  $10^5$  particle gyroperiods the relative error is always of the order of  $10^{-4}$  for all the cases.

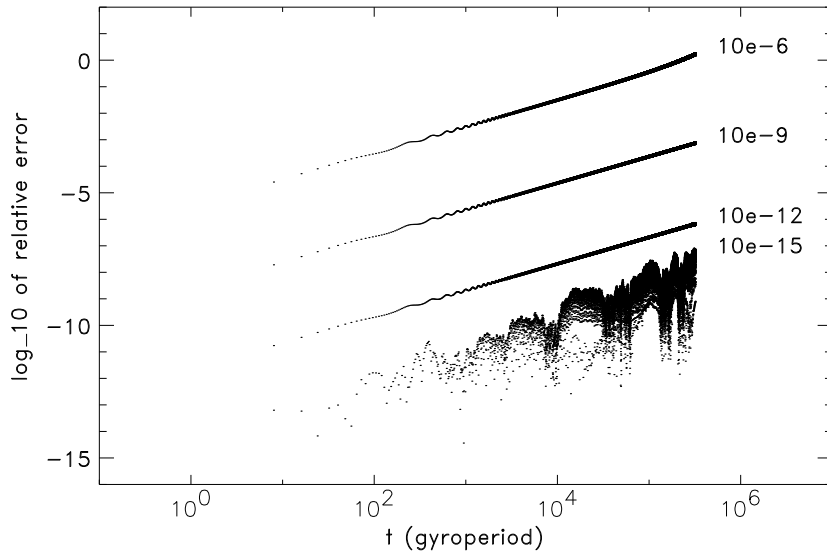
### 3. *Particles moving in a circularly polarized wave field.*

Now we consider the ions motion in presence of a constant magnetic field  $\mathbf{B}_0 = B_0\mathbf{e}_z$  plus a perpendicular circularly polarized wave. We use the left-hand polarized component of the wave field, rotating in the same sense as ions. The handedness is important to properly study the resonance wave-particle interaction. Indeed, left-hand positive ions interact with left-handed waves, while right-hand negative electrons interact with right-handed waves. The resulting magnetic field is given by:

$$\mathbf{B} = \delta\mathbf{B}_x \cos(k_0z) - \delta\mathbf{B}_y \sin(k_0z) + B_0\mathbf{e}_z, \quad (\text{B.8})$$



(a)



(b)

Figure B.1: Accuracy of particle orbits in a uniform magnetic field B.1(a) and in a uniform magnetic and electric field B.1(b) at various  $r_{acc}$ .

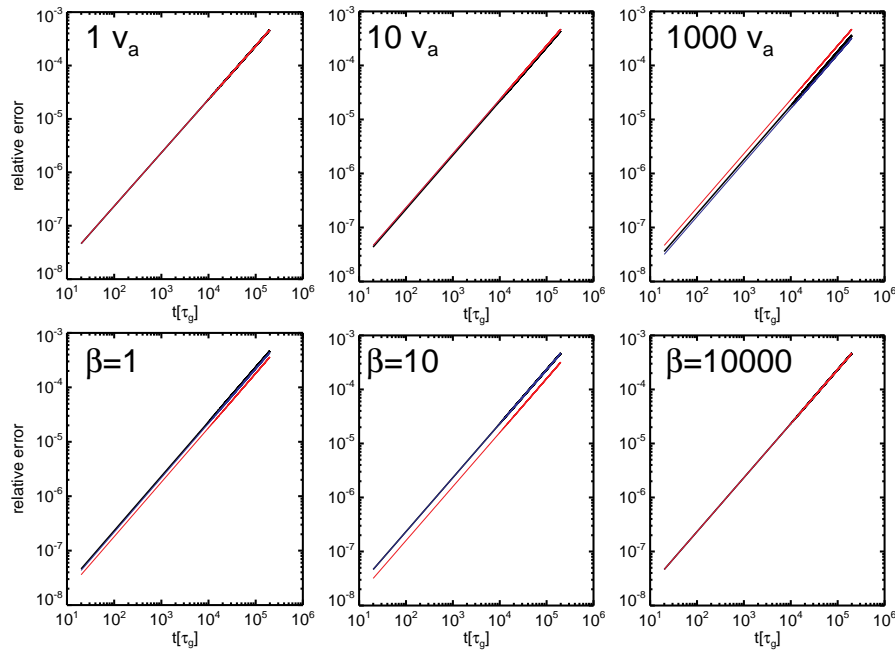


**Figure B.2:** Accuracy of particle orbits in a uniform magnetic field for  $racc = 10^{-9}$  for different values of  $\beta = \Omega/\tau_A$  parameter (on the top in the row:  $\beta = 1$  black line,  $\beta = 10$  blue line,  $\beta = 10^4$  red line) and for different particle velocities (on the bottom in the row:  $v_p = 1v_A$  black line,  $v_p = 10v_A$  blue line,  $v_p = 10^3v_A$  red line,).

where the mean magnetic field  $B_0$  is chosen in the  $z$  direction,  $\delta B_x$  and  $\delta B_y$  are the amplitudes of the wave in the  $x$  and  $y$  directions and  $k_0$  is the wavevector assumed to lie only in the  $z$ -direction. We also assume  $\delta B_x = \delta B_y = \delta B$  for the r.m.s. average values. In this case a different type of analysis is used to test the accuracy of the numerical results. Because a static magnetic field does not work on a charged particle, the energy will be conserved. Therefore, it is possible to compare the magnitude of velocity at each simulation time with its initial value. Thus, in this case the relative error is defined as:

$$\text{Relative Error} = v_{in}^2 - v^2,$$

Both  $v_{in}$  and  $v$  are averaged over 10 particles. The results are shown in Figure B.3 for different values of wave amplitude,  $\delta B/B_0 = 0.001$  (Fig. B.3(a)),  $\delta B/B_0 = 0.01$  (Fig. B.3(b)) and  $\delta B/B_0 = 0.1$  (Fig. B.3(c)), two values of particles velocity,  $v_p = (1 - 10^3)v_A$ , and for  $\beta = (1 - 10^4)$ . When the  $\beta$  value is unchanged and equal to  $10^4$  (top row), tests are performed varying the velocity value:  $v = 1v_A$  is shown with the black line and  $v = 10^3v_A$  with red line. On the other hand, when we fixed  $v = 10^3$  (bottom row), two different  $\beta$  values are used in the test simulation, that are  $\beta = 1$ , black line, and  $\beta = 10^4$ , red line. Although for this cases the simulations last for  $10^3$  particle gyroperiods, the relative error for all the considered cases is of the order of  $2 \times 10^{-6}$ , that



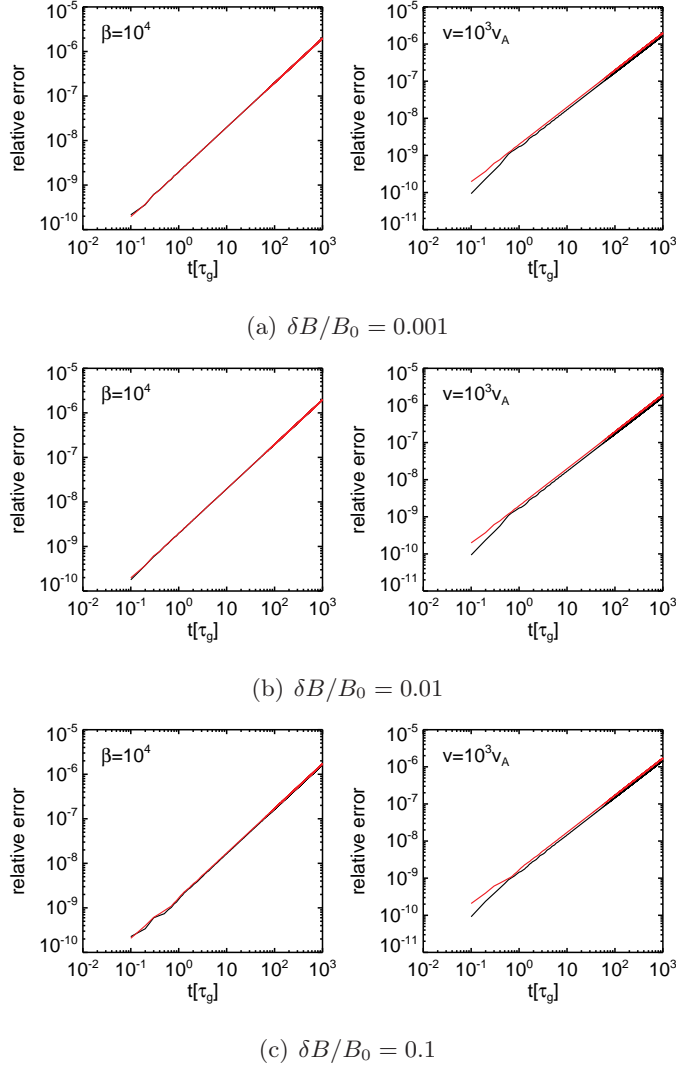


**Figure B.3:** Accuracy of particle orbits in a circularly polarized electromagnetic wave, for  $racc = 10^{-9}$  and for  $\delta B/B_0 = 0.001$  (Fig. B.3(a)),  $\delta B/B_0 = 0.01$  (Fig. B.3(b)),  $\delta B/B_0 = 0.1$  (Fig. B.3(c)). When  $\beta = 10^4$  is fixed,  $v = 1v_A$ , black line, and  $v = 10^3v_A$ , red line. When  $v = 10^3$  is fixed,  $\beta = 1$ , black line, and  $\beta = 10^4$ , red line.

corresponds to the relative error obtained in the previous analysis after only  $10^3$  gyroperiods. These additional tests confirm that our results are valid with an accuracy of  $10^{-9}$ .

### B.3 Particles moving in two circularly polarized waves field

In this section, the resonant interaction between ions and two perpendicular circularly polarized waves is analyzed in details. For this reason, just the left-hand polarized component of the waves, rotating in the same sense of ions, is considered. In addition, the fields are assumed to be static and a constant background magnetic field,  $B_0\mathbf{e}_z$ , is also present. The waves magnetic fields can be written as:

$$\begin{aligned} B_1 &= \delta B_{1x} \cos(k_1 z) - \delta B_{1y} \sin(k_1 z) && \text{for the first wave} \\ B_2 &= \delta B_{2x} \cos(k_2 z) - \delta B_{2y} \sin(k_2 z) && \text{for the second wave} \end{aligned}$$

where  $\delta B_{ix}$  and  $\delta B_{iy}$  ( $i = 1, 2$ ) are waves amplitudes in  $x$  and  $y$  directions,  $\omega_0$  is the wave frequency,  $k_i$  ( $i = 1, 2$ ) are the wavevectors components parallel to the mean field,  $B_0\mathbf{e}_z$ :

$$k_1 = |k_0| \cos \theta_1 \quad \text{and} \quad k_2 = |k_0| \cos \theta_2,$$

in which  $\theta_1$  and  $\theta_2$  are the angles between the wavevector,  $k$ , and the constant magnetic field,  $B_0$ . We also assume  $\delta B_{1x} = \delta B_{1y} = \delta B_1$ ,  $\delta B_{2x} = \delta B_{2y} = \delta B_2$  and  $\delta B_1 = \delta B_2 = \delta B$ . The resulting magnetic field is given by:

$$\begin{aligned} \mathbf{B} &= 2\delta\mathbf{B} \cos\left[\frac{(k_1 + k_2)}{2}z\right] \cos\left[\frac{(k_1 - k_2)}{2}z\right] + \\ &- 2\delta\mathbf{B} \sin\left[\frac{(k_1 + k_2)}{2}z\right] \sin\left[\frac{(k_1 - k_2)}{2}z\right] + B_0\mathbf{e}_z \end{aligned} \quad (\text{B.9})$$

For two waves moving parallel to each other,  $\theta_1 = \theta_2$  so  $k_1 = k_2 = k_0$ , the resulting magnetic field is equal to that associated with a single wave but with a double amplitude:

$$B_x = 2\delta\mathbf{B} \cos(k_0 z) \quad \text{and} \quad B_y = -2\delta\mathbf{B} \sin(k_0 z)$$

As for the single wave case, in order to study the changes in the cosine of pitch angle,  $\alpha$  (see Eq. 4.3), we calculate the parallel component of the induced electric field,  $E_{\parallel} = E_z$ . Inserting the solution obtained for particle velocity, Eq. 4.2, in the expression for the magnetic field, Eq. B.9, the magnetic field seen by the particle,  $\mathbf{H}(t)$ , is:

$$\begin{aligned} \mathbf{H}(t) &= 2\delta B \cos\left[\left(\frac{(k_1 + k_2)}{2}v_{\parallel} - \omega_0\right)t + \frac{(k_1 + k_2)}{2}z_0\right] \cos\left[\frac{(k_1 - k_2)}{2}(v_{\parallel}t + z_0)\right] \mathbf{e}_x, \\ &- 2\delta B \sin\left[\left(\frac{(k_1 + k_2)}{2}v_{\parallel} - \omega_0\right)t + \frac{(k_1 + k_2)}{2}z_0\right] \sin\left[\frac{(k_1 - k_2)}{2}(v_{\parallel}t + z_0)\right] \mathbf{e}_y, \\ &+ B_0\mathbf{e}_z \end{aligned} \quad (\text{B.10})$$

Using Eq. 4.2 and Eq. B.10, the parallel component of the induced electric field for the two waves case is given by:

$$\begin{aligned} E_z &= (\mathbf{v} \times \mathbf{H})_z = v_x B_y - v_y B_x = \\ &= -2v_\perp \delta B \cos \left[ \frac{(k_1 - k_2)}{2} (v_\parallel t + z_0) \right] \cos \left\{ (\Omega t) + \left[ \frac{(k_1 + k_2)}{2} v_\parallel - \omega_0 \right] t + \frac{(k_1 + k_2)}{2} z_0 \right\} \end{aligned}$$

As in the single wave case, the cosine argument in the expression for  $E_z$  is the resonance condition plus a constant term. Here,  $k_\parallel = (k_1 + k_2)/2$  and it replaces  $k_0$  in the constant term,  $k_0 z_0$ , obtained for the single wave case. Of course, considering two parallel propagating waves,  $\theta_1 = \theta_2 \rightarrow k_1 = k_2 = k_0$ , we obtain again  $\omega_0 - k_\parallel v_\parallel = \Omega$  and the induced electric field is exactly that one associated with a single wave but with a double amplitude:

$$E_z = -2v_\perp \delta B \cos [(\Omega t) + (k_0 v_\parallel - \omega_0)t + k_0 z_0]$$

### B.3.1 Results from numerical simulations

In this case, our aim is to study the different particle behavior varying both waves amplitudes,  $\delta B/B_0$ , and orientations,  $\theta_1$  and  $\theta_2$ . Particles are injected in the simulation box with an initial velocity  $v = 4v_A$  and  $\beta = 10$ .

Figure B.4 and Figure B.5 show  $x$  and  $y$  components of particle velocity ( $v_x$ , top left, and  $v_y$ , top right) and  $x$  and  $y$  components of magnetic field seen by the particle ( $B_y$ , bottom left, and  $B_x$ , bottom right), for two different waves amplitudes,  $\delta b = 0.001$  and  $\delta b = 0.1$ , respectively, using four different waves orientations:

1.  $\theta_1 = 0^\circ$  and  $\theta_2 = 0^\circ$ ,
2.  $\theta_1 = 0^\circ$  and  $\theta_2 = 15^\circ$ ,
3.  $\theta_1 = 0^\circ$  and  $\theta_2 = 30^\circ$ ,
4.  $\theta_1 = 0^\circ$  and  $\theta_2 = 180^\circ$ .

The initial value of cosine of pitch angle is  $\alpha = 1/4$ , so the resonance condition, Eq. 3.6, is satisfied. When the waves amplitude is small, Figure B.4, and the waves are moving parallel to each other, Figure B.4(a),  $v_x$  and  $v_y$  are perfectly in phase with the  $x$  and  $y$  components of magnetic field seen by the particle. Instead, considering two antiparallel waves, Figure B.4(d), the  $y$  component of particle velocity is still in phase with  $-B_x$ , but the other two component are not in phase anymore. This behavior is easily understood from  $B_x$  and  $B_y$ :

$$\begin{aligned} B_x &= 2\delta\mathbf{B} \cos(kz) \\ B_y &= -2\delta\mathbf{B} \sin(kz) \end{aligned} \tag{B.11}$$

for two parallel waves,

$$\begin{aligned} B_x &= 2\delta\mathbf{B} \cos(kz) \\ B_y &= 2\delta\mathbf{B} \sin(kz) - \cos(kz) \end{aligned} \tag{B.12}$$

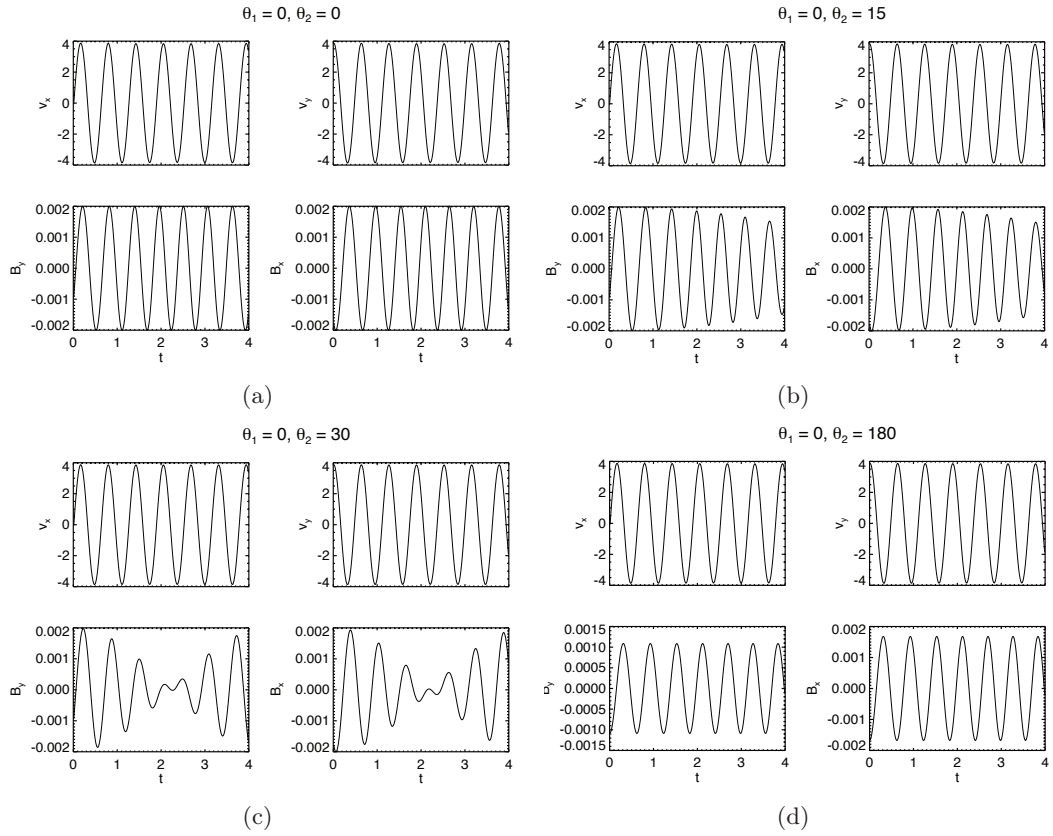


**Figure B.4:** Particle  $v_x$  (top left) and  $v_y$  (top right) velocities and  $B_y$  (bottom left) and  $B_x$  (bottom right) component of magnetic field seen by the particle. Particle initial total velocity and wave amplitude are  $v = 4v_A$  and  $\delta b = 0.001$  respectively. Four different panels correspond to four different waves orientations: [B.4\(a\)](#) for  $\theta_1 = 0^\circ$  and  $\theta_2 = 0^\circ$ , [B.4\(b\)](#) for  $\theta_1 = 0^\circ$  and  $\theta_2 = 15^\circ$ , [B.4\(c\)](#) for  $\theta_1 = 0^\circ$  and  $\theta_2 = 30^\circ$ , [B.4\(d\)](#) for  $\theta_1 = 0^\circ$  and  $\theta_2 = 180^\circ$ .

for two antiparallel waves.

$B_x$  in the parallel case is the same of that one obtained for the antiparallel case. However, this is not true for  $B_y$ : the minus sign disappears for the antiparallel case; indeed, particle and waves are not in resonance anymore.

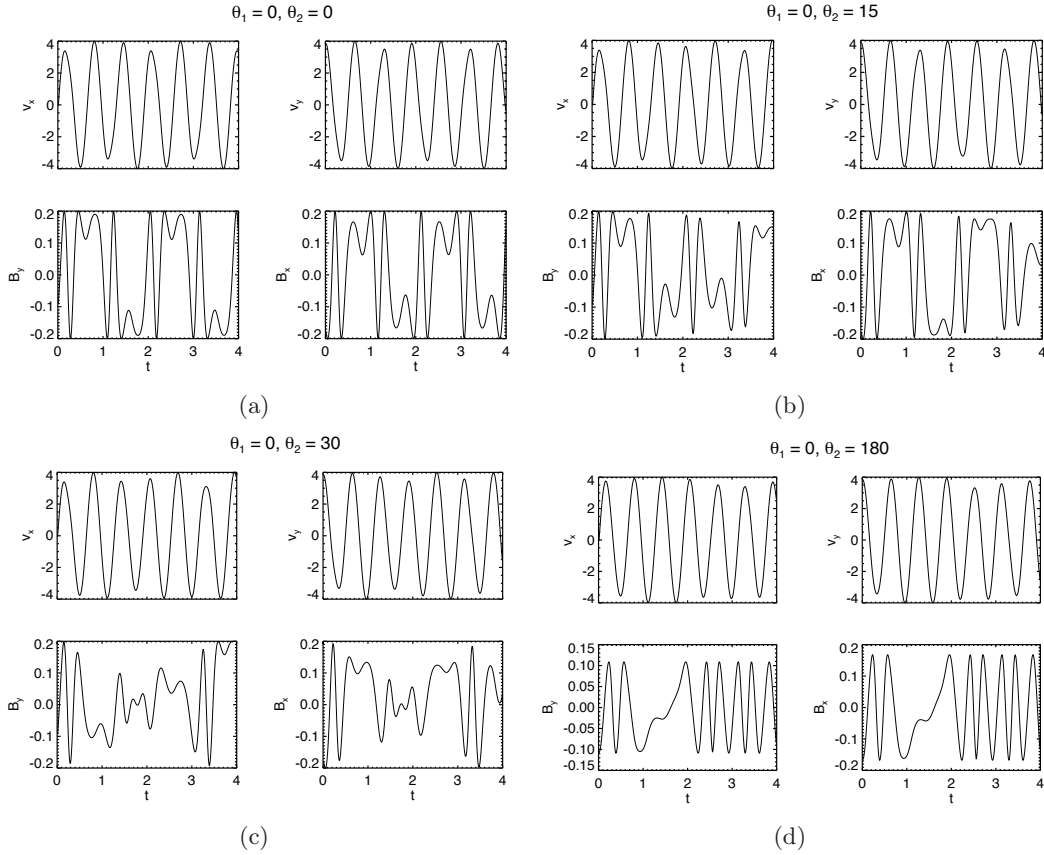


**Figure B.5:** Same of Figure(B.4) but for  $\delta b = 0.1$  .

When the second wave is not parallel or antiparallel to the first one ( $\theta_2 = 15^\circ$ , Figure B.4(b), and  $\theta_2 = 30^\circ$ , Figure B.4(c)), after some particle gyroperiods the magnetic field amplitude is modulated by the presence of the term  $(k_1 \pm k_2)$  in the cosine and sine arguments of Eq. B.9.

Increasing the waves amplitudes,  $\delta b = 0.1$  (Figure B.5), irregular changes are observed in the  $x$  and  $y$  component of the magnetic field. These changes occur at regular intervals only for two parallel waves. Looking at the behavior of the parallel component of the induced electric field,  $E_z$ , particle magnetic moment,  $\mu$ , and cosine of pitch angle,  $\alpha$ , as in the single wave case, during these time intervals  $\mu$  and  $\alpha$  show secular changes and the parallel component of the induced electric field is almost constant. These three quantities are shown in Figure B.6 and Figure B.7, for  $\delta b = 0.001$  (left column),  $\delta b = 0.01$  (central column) and  $\delta b = 0.1$  (right column), and for the different orientations considered:

**Table B.1:**  $v_{\parallel}$  values at resonances for different  $\theta$  values for  $l = \pm 1$  resonances.

| $\theta$    | $k_{\parallel} = k_0 \cos \theta$ | $v_{\parallel} = \mp(\beta/k_{\parallel})$ |
|-------------|-----------------------------------|--|
| $0^\circ$   | $k_0$                             | $\mp 1$                                    |
| $30^\circ$  | $\frac{\sqrt{3}}{2}k_0$           | $\mp 1.154$                                |
| $180^\circ$ | $-k_0$                            | $\pm 1$                                    |
| $210^\circ$ | $-\frac{\sqrt{3}}{2}k_0$          | $\pm 1.154$                                |

- $\theta_1 = 0^\circ$  and  $\theta_2 = 0^\circ$ , Figure B.6(a),
- $\theta_1 = 0^\circ$  and  $\theta_2 = 15^\circ$ , figure B.6(b),
- $\theta_1 = 0^\circ$  and  $\theta_2 = 30^\circ$ , Figure B.7(a),
- $\theta_1 = 0^\circ$  and  $\theta_2 = 180^\circ$ , figure B.7(b).

In the first two cases (Figure B.6(a) and Figure B.6(b))  $E_z$ ,  $\alpha$  and  $\mu$  profiles are really similar, as we observed for  $x$  and  $y$  components of particle velocities and magnetic field. For all  $\delta b$ , periods of constant  $E_z$  are clearly evident and  $\alpha$  and  $\mu$  show secular changes. Increasing the angle of the second wave,  $\theta_2 = 30^\circ$  (Figure B.7(a)),  $E_z$ ,  $\alpha$  and  $\mu$  start to show an oscillating behavior and not a resonant one, that is more evident for  $\theta_2 = 180^\circ$  (Figure B.7(b)): indeed there are not period of constant  $E_z$ , that is oscillating around zero.

To gain some insight into the nature of gyroresonant interaction, we show particles motion in  $v_{\parallel} - v_{\perp}$  space, varying both the initial value of cosine of pitch angle,  $\alpha$ , and waves amplitudes,  $\delta b$ , for different waves orientations. Different resonances are associated with different values of the angle between the wavevector and the mean constant magnetic field,  $B_0 \mathbf{e}_z$ . Following the resonance condition, Eq. 3.6, different resonances are obtained for different values of particle parallel velocity, i.e., different  $\alpha$ , if particles are loaded with the same initial velocity,  $v$ :

$$\begin{aligned} \text{Resonance } l = 0 : & & v_{\parallel} &= \frac{\beta}{k_{\parallel}} \\ \text{Resonances } l = \pm l : & & v_{\parallel} &= \frac{l\Omega}{k_{\parallel}} \end{aligned}$$

The  $l = 0$  resonance corresponds to  $v_{\parallel} = 0$ ; instead, other resonances are obtained for different  $v_{\parallel}$ , depending on  $k_{\parallel}$ . These velocities are listed in Table B.1 for different angles and for  $l = \pm 1$ . In Figure B.8 particles orbits in  $v_{\parallel} - v_{\perp}$ -space are shown, for  $\delta b_1 = \delta b_2 = 0.1$ , Figure B.8(a), and for  $\delta b_1 = 0.1$  and  $\delta b_2 = 0.2$ , Figure B.8(b), using four different values of waves orientations:

- $\theta_1 = 0^\circ$  and  $\theta_2 = 0^\circ$  (top left),
- $\theta_1 = 0^\circ$  and  $\theta_3 = 0^\circ$  (top right),

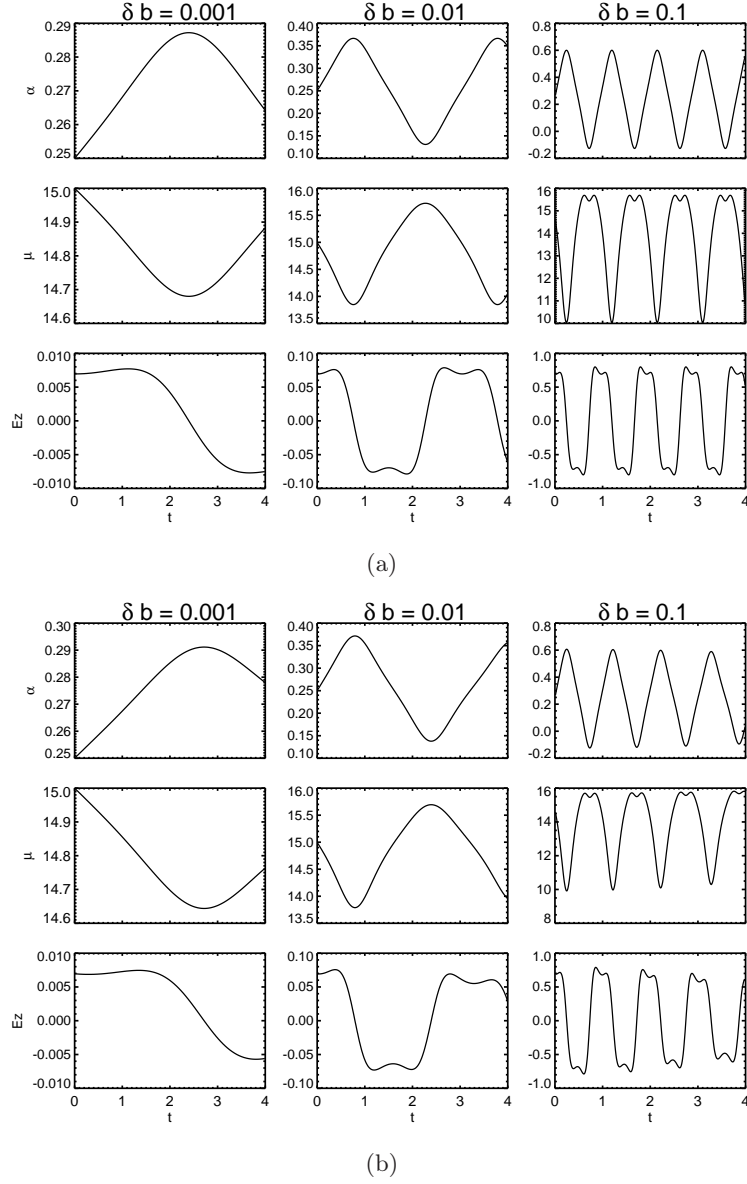
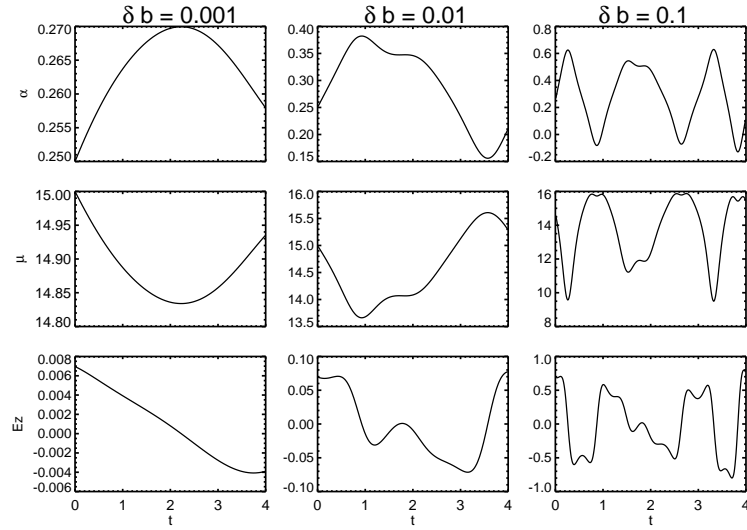
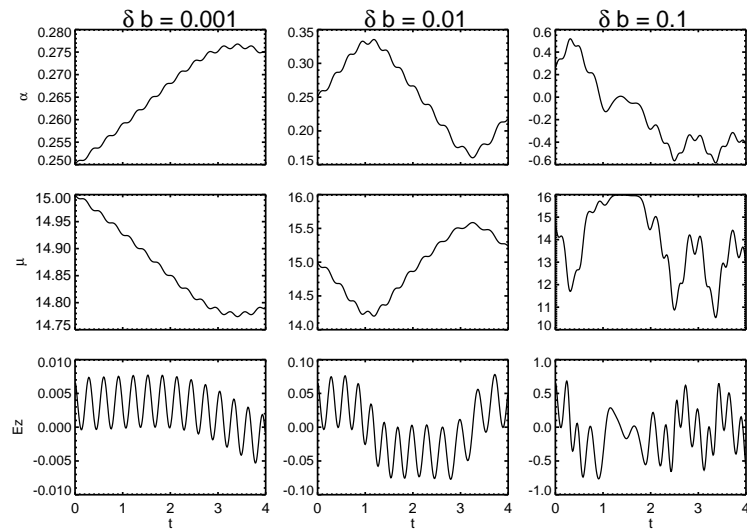


**Figure B.6:** Particle cosine of pitch angle  $\alpha$  on the top, particle magnetic moment  $\mu$  in the middle, parallel component of the induced electric field,  $E_{\parallel}$ , on the bottom. Initial total velocities  $v = 4v_A$  and initial cosine of pitch angle  $\alpha = \alpha_{res} = 1/4$ . Three different values of wave amplitude are used:  $\delta b = 0.001$  (left column),  $\delta b = 0.01$  (central column) and  $\delta b = 0.1$  (right column). Two panels correspond to two different waves orientations: [B.6\(a\)](#) for  $\theta_1 = 0^\circ$  and  $\theta_2 = 0^\circ$ , [B.6\(b\)](#) for  $\theta_1 = 0^\circ$  and  $\theta_2 = 15^\circ$ .



(a)



(b)

**Figure B.7:** Same of Figure B.6, but for different waves orientations: B.7(a) for  $\theta_1 = 0^\circ$  and  $\theta_2 = 30^\circ$ , B.7(b) for  $\theta_1 = 0^\circ$  and  $\theta_2 = 180^\circ$ .



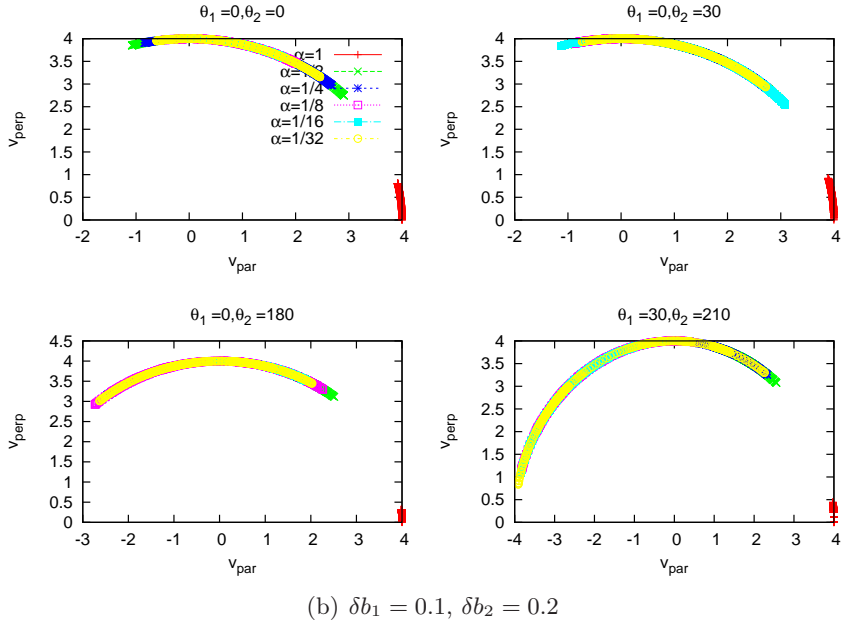
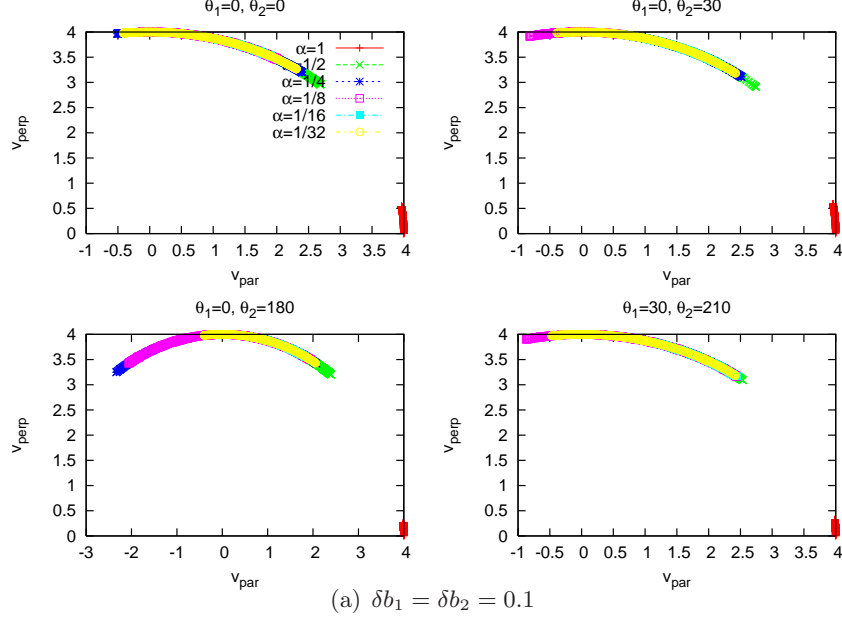


**Figure B.8:** Particle orbits in  $v_{\parallel} - v_{\perp}$  space for  $v = 4v_A$  and  $\delta b = 0.1$ . Different panels correspond to four different values of the waves orientations:  $\theta_1 = 0^\circ, \theta_2 = 0^\circ$  (top left),  $\theta_1 = 0^\circ, \theta_2 = 30^\circ$  (top right),  $\theta_1 = 0^\circ, \theta_2 = 180^\circ$  (bottom left),  $\theta_1 = 30^\circ, \theta_2 = 210^\circ$  (bottom right). Different colors in each panel correspond to particle injected at different cosine of pitch angle:  $\alpha = 1$  (red line),  $\alpha = 1/2$  (green line),  $\alpha = 1/4$  (blue line),  $\alpha = 1/8$  (purple line),  $\alpha = 1/16$  (light blue line) and  $\alpha = 1/32$  (yellow line)

- $\theta_1 = 0^\circ$  and  $\theta_2 = 180^\circ$  (bottom left),
- $\theta_1 = 30^\circ$  and  $\theta_2 = 210^\circ$  (bottom right).

Particles are injected at six different initial cosine of pitch angle,  $\alpha$ , close to the resonant value,  $\alpha_{res} = 1/4$ . Because the amplitude of the wave is big, adjacent resonances overlap and particles with an initial cosine of pitch angle different from  $\alpha_{res} = 1/4$  can also cover a big portion of the  $v_{\parallel} - v_{\perp}$  space, although the most spread is associated with  $\alpha = 1/4$  (blue line). From Figure B.8(a) it is possible to notice that, when these particles interact with two parallel wave (top left), the motion is centered around  $v_{\parallel} = 1v_A$ , the point at which corresponds the  $l = -1$  resonance for both waves. If the particles are moving in the field of two obliquely propagating waves, they can cover a larger portion of  $v_{\parallel} - v_{\perp}$  space, depending on their relative orientation. These behavior is evident in the other three plots of Figure B.8.

- $\theta_1 = 0^\circ$  and  $\theta_2 = 30^\circ$  (top right): particles starts to spread a bit more; moreover, the motion is localized just in the positive side of  $v_{\parallel} - v_{\perp}$  space, because resonances width due to both waves is stronger on one side of the circle.
- $\theta_1 = 0^\circ$  and  $\theta_2 = 180^\circ$  (bottom left): the second wave is moving in the opposite direction with respect to the first one. The second resonance allows particles to go completely around the circle. The motion now is centered at  $v_{\parallel} \sim 0$ , because two opposite resonances and two waves with the same amplitude are considered.
- $\theta_1 = 30^\circ$  and  $\theta_2 = 210^\circ$  (bottom right): this situation is similar to the previous one, expect for the fact that in this case the motion is centered at  $v_{\parallel} \sim 0.57v_A$ , because resonances occur at  $v_{\parallel} = \mp l * 1.154v_A$ .

When waves with different amplitudes are considered, depending on which wave is stronger, the center of particles motion can move to the left or to the right of the circle, as evident in the Figure B.8(b). In this case the second wave has a double amplitude respect to the first one, so the motion moves on the portion of the circle where resonances associated with the second wave are localized.

## B.4 Diffusion in velocity space: nonlinear effects and implications for simulations.

Because this Appendix section is part of a work different from the study of magnetic moment conservation, that is velocity space diffusion of charged particles in slab-like magnetic field, a different notation is used. Indeed, following the quasi-linear theory and other studies of velocity space diffusion of charged particle in random magnetic field, from here until the end of the section  $\mu$  is referred to particle cosine of pitch angle and  $D_{\mu\mu}$  indicates pitch angle diffusion coefficient.

### B.4.1 Finite wavenumber spacing $\Delta k$

The finite effective width in velocity space,  $\Delta v_{\parallel}^{\text{eff}} = v\Delta\mu_{\text{eff}} = \omega_b\tau_{ac}\Delta v_{\parallel}$ , for the gyro-resonance interaction naturally gives rise to a finite spacing in Fourier space. That is, for a particle to resonate with a wave, the wavenumber must lie between  $k$  and  $k + \Delta k$ , where  $\Delta k$  depends on  $\Delta v_{\parallel}$ .

First of all let us consider a single wave mode in the magnetostatic slab model, interacting with a distribution of particles. In the magnetostatic slab model a particle with velocity component  $v_{\parallel}$  can resonate with only two possible wavenumbers,  $k_{\pm 1} = \mp\Omega/v_{\parallel}$ , assuming zero resonance width broadening. If we now allow nonlinear resonance broadening effects, all particles in the velocity distribution, with parallel velocities in the range  $v_{\parallel} - \Delta v_{\parallel} < v_{\parallel} < v_{\parallel} + \Delta v_{\parallel}$  (where  $\Delta v_{\parallel}$  is the effective width of the resonance in  $v_{\parallel}$  the superscript “eff” is omitted for brevity), can potentially resonate with a wave whose wavenumber is  $k_{+1}$ . A similar argument holds for a wave with wavenumber  $k_{-1}$ .

Let us now reverse the situation and consider a broad continuous spectrum of waves and a single particle with velocity  $v_{\parallel}$ . According to the resonance condition, this particle will select from the spectrum a wave with wavenumber either  $k_{+1}$  or  $k_{-1}$ . However, since the spectrum is broad in  $k$  space and the resonance width in velocity space is finite, it could, in fact, resonate with a range of wavenumbers given by  $k_2 - k_1$ , where  $k_1 = \Omega/(v_{\parallel} - \Delta v_{\parallel})$  and  $k_2 = \Omega/(v_{\parallel} + \Delta v_{\parallel})$ . The difference between these two wavenumbers yields the equivalent half width in wavenumber space

$$\Delta k_{\parallel} = \left| \frac{\Omega}{v_{\parallel}^2 - \Delta v_{\parallel}^2} \Delta v_{\parallel} \right| = \left( \frac{\Delta v_{\parallel}/v_{\parallel}}{1 - (\Delta v_{\parallel}/v_{\parallel})^2} \right) k_{res}, \quad (\text{B.13})$$

where we again omit the sub-superscript “eff” for brevity. This equation says that, given a sufficiently broad spectrum, a particle with parallel velocity  $v_{\parallel}$  can resonate with any wavenumber in the range  $k_{\parallel} - \Delta k_{\parallel} < k_{\parallel} < k_{\parallel} + \Delta k_{\parallel}$ .

In the discrete wavenumber space of the numerical experiment, Eq. B.13, governing the finite width of the resonance in wavenumber space, serves as a guide in the choice of a suitable box length. Since the discrete wavenumber is  $k_n = 2\pi n/L$ , with spacing  $\Delta k = 2\pi/L$ , one must choose a box length (or periodicity length) sufficiently large that the effective resonance trapping width is well resolved in  $k_{\parallel}$ -space, so that particles may be successively captured by adjacent resonances and diffuse stochastically. On the other hand, a longer box length means that the resonant wavenumber, and hence  $n$ , increases and can become closer to the Nyquist wavenumber,  $k_{\text{Nyq}} = \pi N/L = \pi/\Delta z$ . This can lead to poorer energy conservation properties, primarily due to field interpolation errors; hence a compromise must be sought.

### B.4.2 Numerical results

In order to show the validity of our numerical model, we give an example of a well-resolved simulations for particle pitch angle diffusion in random slab magnetic

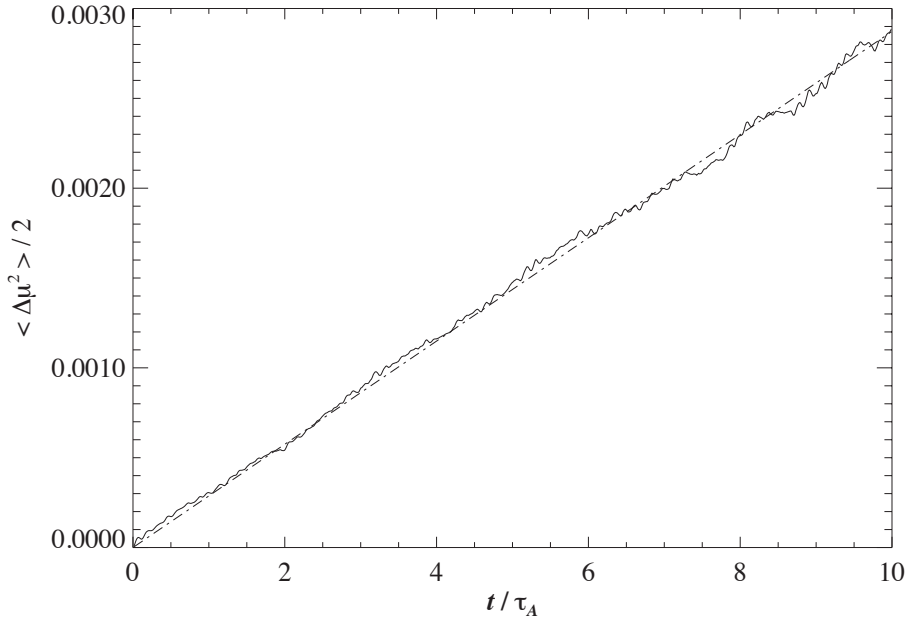


**Figure B.9:** Evolution of  $\langle \Delta\mu^2 \rangle / 2$  as a function of time (solid curve) for  $\beta = 50$ ,  $\mu_0 = 0.6$ ,  $v = 10v_A$ ,  $\delta B/B_0 = 0.01$  and a box length of  $L = 1000\lambda$ . The dot dashed curve is  $D_{\mu\mu}t$  from the quasilinear prediction.

fields. Particles are loaded from a ring beam distribution in velocity space, with an initial cosine of pitch angle  $\mu_0 = 0.6$ . Other parameters used in the simulation are  $v/v_A = 10$ ,  $\delta B/B_0 = 0.01$  and  $\beta = 50$ , so  $\omega_b\tau_{ac} \simeq 0.16$ . Figure B.9 shows the mean square displacement of cosine of pitch angle  $\langle (\Delta\mu)^2 \rangle$  for this simulation. This figure demonstrates very good agreement between our simulations and the quasilinear theory over the full duration of the simulations, about 80 correlation times  $\tau_{ac}$ . Indeed,  $\langle \Delta\mu^2 \rangle$  evolves linearly with time, according to  $\langle \Delta\mu^2 \rangle / 2 = D_{\mu\mu}t$ , plotted in the same figure with a dot-dashed line.

#### B.4.2.1 Effects related to box size

As we already mentioned, one of the most important parameter in the simulation is the box size. It must be chosen so that: (i) the simulated turbulent wave spectrum adequately approximates a continuum; (ii) the extent of the spectrum in wavenumber space is sufficient to have wave power at the resonant wavenumber; (iii) any effects due to periodicity are minimized.

The first condition can be thought as follows. Let us call the typical width of the Fourier spectrum  $k_0 \simeq k_{\text{corr}}$ , where  $k_{\text{corr}}$  is the correlation wavenumber. In our simulations  $k_{\text{corr}} = 1/\lambda$ , where  $\lambda$  is of the order of the turbulence correlation length, that typically defines the length over which a group of waves remains correlated in space, i.e., the length of a wave packet. In order to have the continuum approximation, this group of waves must consist of a large number of Fourier modes. This

implies the following condition

$$\Delta k \ll k_{\text{corr}} \quad \text{or} \quad 2\pi \frac{\lambda}{L} \ll 1. \quad (\text{B.14})$$

These inequalities tell us immediately that, in order to approach the continuum limit, the box length should be many correlation scales. The ratio,  $k_{\text{corr}}/\Delta k$  gives a rough estimate of the number of Fourier modes in a typical wave group. Furthermore, the inequality (B.14) can be thought as a condition on the smoothness of the distribution of phases in a wavepacket: the smaller is  $\Delta k$  relative to  $k_{\text{corr}}$ , the smoother the distribution of wave phases.

However, as discussed in Section B.4.1, there is another potentially more restrictive criterion that limits the choice of the wavenumber spacing:  $\Delta k$  must be less than the effective trapping width translated into wavenumber space through Eq. B.13. So the second condition on  $\Delta k$  is:

$$\Delta k \ll \Delta k_{\text{trap}} \quad \text{or} \quad \frac{2\pi}{L} \ll \Delta k_{\text{trap}}, \quad (\text{B.15})$$

where  $\Delta k_{\text{trap}} = \Delta k_{\parallel}$  of Eq. B.13. This criterion can be interpreted as a necessary condition for the resonance structure of the unperturbed Hamiltonian of a particle resonantly interacting with a wave mode, in order to be sufficiently perturbed by wave noise (extrinsic stochasticity due to neighboring wavemodes with random phases) so that the orbits in phase space lead to stochastic behavior instead of regular elliptic orbits around the resonance point. Thus, it is not simply sufficient that the resonances overlap in  $k$ -space, but there must be a sufficiently large number of neighboring randomly phased wavemodes to guarantee stochastic behavior in the vicinity of the resonance point.

In order to illustrate some effects associated with a short length box, we perform different simulations starting with the same initial conditions but different box lengths:  $L = 50\lambda, 150\lambda, 500\lambda, 1000\lambda$ . As in the previous case, particles are loaded from a ring beam distribution with  $\mu_0 = 0.6$ . Other parameters used in the simulations are:  $v/v_a = 10$ ,  $\delta B/B_0 = 0.001$  and  $\beta = 500$ . The bounce frequency determined from Eq. 4.28 is  $\omega_b = 2.04/\tau_A$  and, since  $\tau_{ac} = 0.124\tau_A$ , this yields  $\omega_b\tau_{ac} = 0.25$ , that satisfies the assumptions of quasilinear theory. The effective trapping half width in  $k$ -space is  $\Delta k_{\text{trap}} = 0.17/\lambda = 0.17k_{\text{corr}}$ , a value smaller than the correlation wavenumber. This guarantees the validity of the condition (B.14) and hence the condition (B.15) is relevant in the simulation. Figure B.10 shows the pitch angle mean square displacement,  $\langle(\Delta\mu)^2\rangle/2$ , as a function of time for the four different cases:  $L = 50\lambda$  is shown with ( $\cdots$ ) line,  $L = 150\lambda$  with ( $- -$ ) line;  $L = 500\lambda$  with ( $- \cdot -$ ) line and  $L = 1000\lambda$  with ( $- \cdots -$ ) line. The numerical results are compared with the quasi-linear theory result,  $\langle(\Delta\mu)^2\rangle/2 \simeq D_{\mu\mu}t$ , plotted in the same figure with the solid line. The curve that shows the best agreement with the quasi-linear theory prediction is the case with largest box length ( $L = 1000\lambda$ , ( $- \cdots -$ ) line), i.e., the highest  $k$ -space density of Fourier modes ( $\Delta k = 0.0063k_{\text{corr}} \ll 0.17k_{\text{corr}}$ ) and consequently the smoothest distribution of wave phases. For all the other cases, the

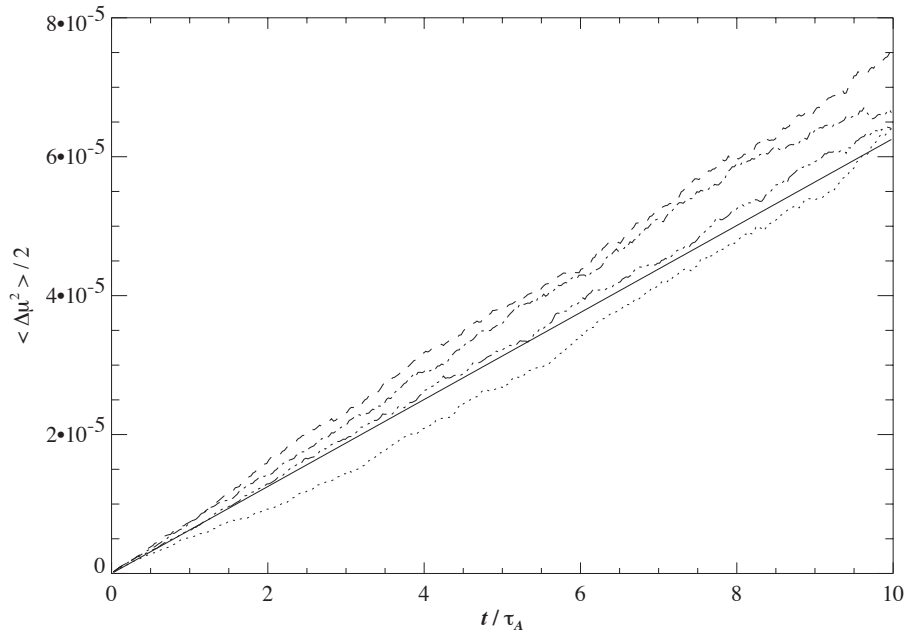


**Figure B.10:** Temporal evolution of  $\langle (\Delta\mu)^2 \rangle$  for  $\delta B/B_0 = 0.001$ , varying the box length:  $L = 50\lambda$  ( $\cdots$ );  $L = 150\lambda$  ( $--$ );  $L = 500\lambda$  ( $- \cdot -$ ) and  $L = 1000\lambda$  ( $- \cdot \cdot \cdot -$ ). The solid line is the quasi-linear prediction,  $D_{\mu\mu}t$ .

agreement of the simulation result with the quasi-linear prediction is relatively poor. We believe that the main source of error for the shorter box lengths comes from the wider spacing of their Fourier components in  $k$ -space. Once the particles begin to spread in  $v_{\parallel}$  and hence decorrelate with their initial resonant wavenumber, they need to encounter other resonant  $k$ -modes, so that their motion become stochastic and leads to diffusion in velocity. In the continuum case, a given particle will always find another wavenumber with which to resonate, provided there is finite power in a neighborhood of its original resonant wavenumber. This is expected to be typical of very large homogenous systems with essentially continuum wavenumber distributions of wave energy. However, in the finite case, decreasing the density of discrete Fourier modes, the likelihood that a particle find a matching  $k$  and increases the importance of nonlinear effects, such as resonance broadening and trapping, decreases. So, when nonlinear trapping widths are sufficiently reduced, the discreteness of the Fourier spectrum of the simulated turbulence is plainly exposed and manifests itself in very poor agreement of the simulation results with the quasi-linear theory, when  $\Delta k \ll \min\{k_{\text{corr}}, \Delta k_{\text{trap}}\}$  is not well satisfied. This disagreement can manifest itself as either a subdiffusive ( $L = 50\lambda$ ) or superdiffusive (e.g.,  $L = 150\lambda, 500\lambda$ ) trend relative to the quasilinear theory. Furthermore, since the case for  $L = 500$  does not agree with the quasilinear diffusion theory and, on average, the distance travelled by a particle down the simulation box is about  $60\lambda \ll 500\lambda$ , this rules out periodicity effects associated with the fields as the possible cause.

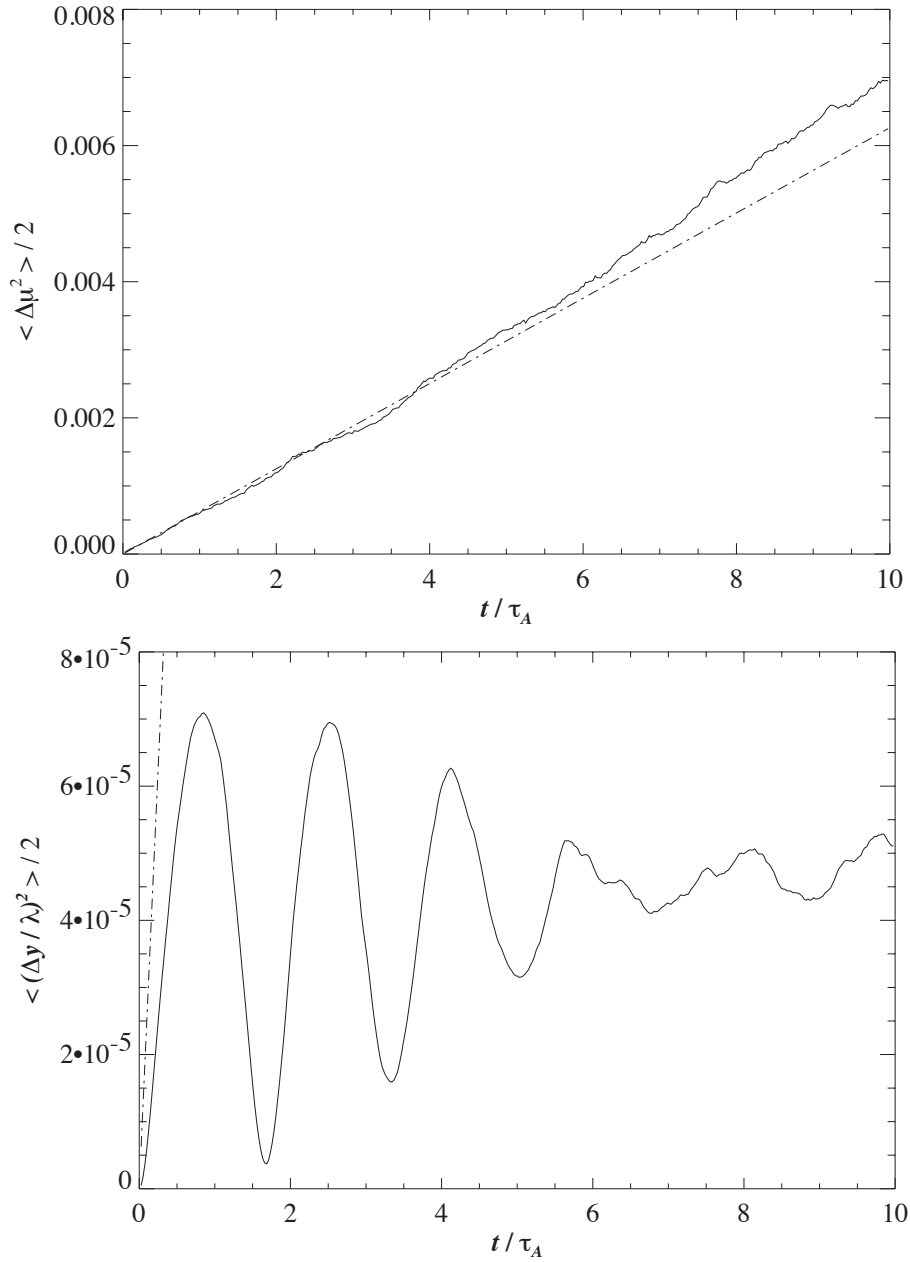


**Figure B.11:** Temporal evolution of the variance of the pitch angle cosine (top panel) and  $\langle (\Delta y)^2 \rangle$  (bottom panel) for a box length of  $L = 10\lambda$ . Other parameters were  $\beta = 500$ ,  $\mu_0 = 0.6$  and  $v = 10v_A$ .

In order to study the effects of box periodicity in velocity space diffusion, i.e., the periodicity of the magnetic field configuration, we consider extremely short box lengths, so that the particles make many box transits during a run. Figure B.11 illustrates the mean square displacement for both pitch angle,  $\langle(\Delta\mu)^2\rangle$  (top panel), and particle position  $\langle(\Delta y)^2\rangle$  (bottom panel), in an extreme case,  $L = 10\lambda$  and  $v_{\parallel} = 6v_A$ , so that particles make more than 5 transits through the simulation box during the total duration of the simulation,  $10\tau_A$ . The numerical curve for  $\langle(\Delta\mu)^2\rangle$  exhibits oscillations with a frequency equal to the box-crossing frequency. Each successive box crossing is depicted by a peak in the curve of  $\langle(\Delta y)^2\rangle$ . At the beginning these peaks are coherent because particle velocity in the parallel direction is strongly peaked around the initial value,  $v_{\parallel} = \mu_0 v = 6$ . As the particles diffuse in pitch angle, the distribution in  $v_{\parallel}$  broadens and the trajectories begin to decorrelate, yielding a lack of coherence evident in the spatial variance after  $t \simeq 5.5\tau_A$ . After  $t = 4\tau_A$ ,  $\langle(\Delta\mu)^2\rangle$  deviates from the theoretical curve: this regime could be termed diffusive too, but the diffusion coefficient is quite different from that one predicted by the quasilinear theory. At the same time the spatial coherence is lost and the spatial oscillations are less pronounced.

There is another subtle, numerically important effect related with the box size: the index of the Fourier component/coefficient corresponding to the resonant wavenumber depends on the normalized box length,  $L/\lambda$ . Indeed

$$|k_{res}| = \frac{\Omega}{|v_{\parallel}|} = \frac{\alpha}{\mu(v/v_A)\lambda} \quad \text{or} \quad n_{res} = \frac{1}{2\pi} \frac{\alpha}{\mu(v/v_A)} \frac{L}{\lambda} \quad (\text{B.16})$$

where  $n_{res}$  is the index of the resonant Fourier coefficient. Thus, varying the box length has the property of proportionally varying  $n_{res}$  and varying the wavenumber spacing  $\Delta k = 2\pi/L$  in inverse proportion. Indeed, a shorter box length is advantageous from the point of view that it lowers the ratio  $n_{res}/n_{\text{Nyq}}$ , where  $n_{\text{Nyq}}$  is the  $n$  corresponding to the Nyquist wavenumber. Consequently it ensures plenty of wave power above the resonant wavenumber and that the sinusoidal Fourier mode corresponding to the resonant wavenumber is well resolved spatially, reducing interpolation errors. The high spatial resolution of the resonant mode gives rise to good energy conservation and consequently high fidelity in the particle orbit dynamics. The 'Hamiltonicity' of the problem is thus very nearly conserved.

Indeed, although the theory of pitch angle diffusion in magnetostatic fields rigorously predicts no diffusion in particle energy, i.e., particles are confined to a particular  $H$ -surface for all time, finite diffusion in energy is difficult to avoid in the discrete model. We illustrate the good energy conservation for low  $L/\lambda$  in Figure B.12: energy is conserved much better in the  $L/\lambda = 25$  case (lower curve) respect to the other case studied,  $L/\lambda = 1000$  (upper curve). Thus a compromise must be sought whereby the resonant wavenumber is placed in a region of  $k$ -space where (i) the Fourier mode corresponding to the resonant wavenumber is sufficiently well resolved spatially that the drift across  $H$  surfaces is minimized, and (ii) the interwavenumber spacing should be small enough so that the resonance condition is easily satisfied, allowing particles to diffuse stochastically along their constant  $H$



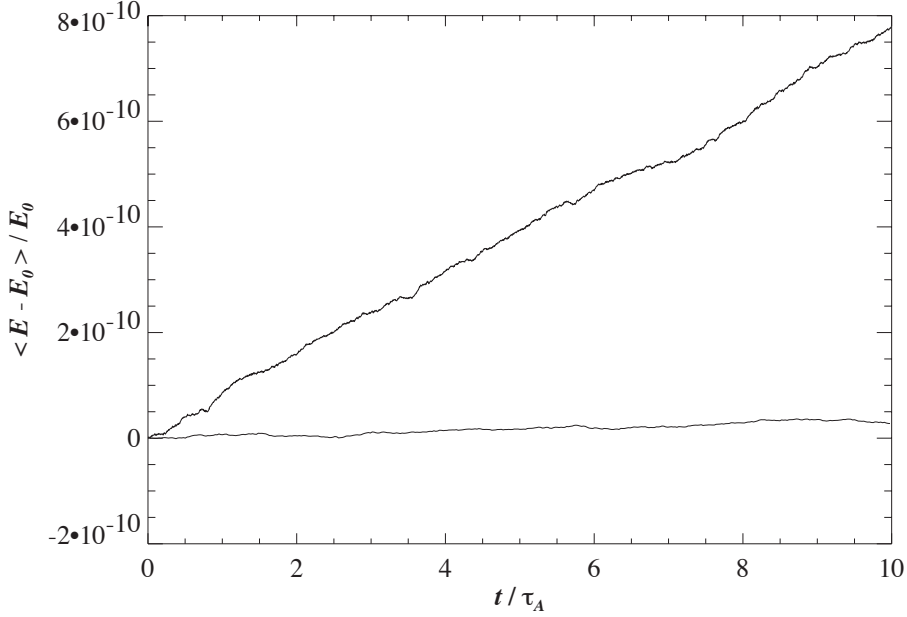


**Figure B.12:**  $\langle E(t) - E_0 \rangle / E_0$  as a function of time for runs with a box length of  $L = 25\lambda$  (lower curve) and  $L = 1000\lambda$  (upper curve).

surface.

#### B.4.2.2 Violation of the quasilinear assumption

We have tried to emphasize the importance of the quasilinear assumption,  $\tau_{ac} \ll \tau_{NL} \simeq \tau_b$ . In practice, even if this inequality is violated, in our simulations the quasilinear prediction appears to be quite accurate. Figure B.9 is an example where the inequality is only marginally satisfied but the agreement between theory and simulation is very good. Figure B.13 illustrates a simulation where  $\delta B / B_0 = 0.001$  and  $\mu_0 = 0.1$ . Hence  $\tau_{ac} = 0.7468\tau_A$  and  $\omega_b = 2.65/\tau_A$ , yielding  $\omega_b\tau_{ac} \simeq 1.98$  in complete violation of the quasilinear ordering of timescales. For reference, we note that the effective trapping width in  $k$  space is very large:  $\Delta k_{\text{trap}} \simeq 10.5k_{\text{corr}}$ . Nevertheless, the agreement between the quasilinear result and the experiment is surprisingly good. It appears that around  $t = 11\tau_A$ ,  $17\tau_A$ ,  $22\tau_A$  and  $30\tau_A$ , the variance differs quasi-periodically from the quasilinear prediction, but during the short intervals (typically one to a few  $\tau_{ac}$ ) between these deviations, the overall trend approaches the expected one. The initial large deviation from the quasilinear trend occurs at  $t \simeq 8\tau_A$ , i.e., about  $11\tau_{ac}$ . Prior to this time the agreement with quasilinear theory is excellent. Subsequent returns to the quasilinear curve occur at intervals of  $\sim 5\tau_{ac}$ . At  $t = 27\tau_A$  there is a large deviation and a slow return after nearly  $20\tau_A \simeq 3\tau_{ac}$ .

A possible interpretation of this behavior is that we are evidencing successive interactions of particles with resonant wavepackets. As the particles traverse each suc-

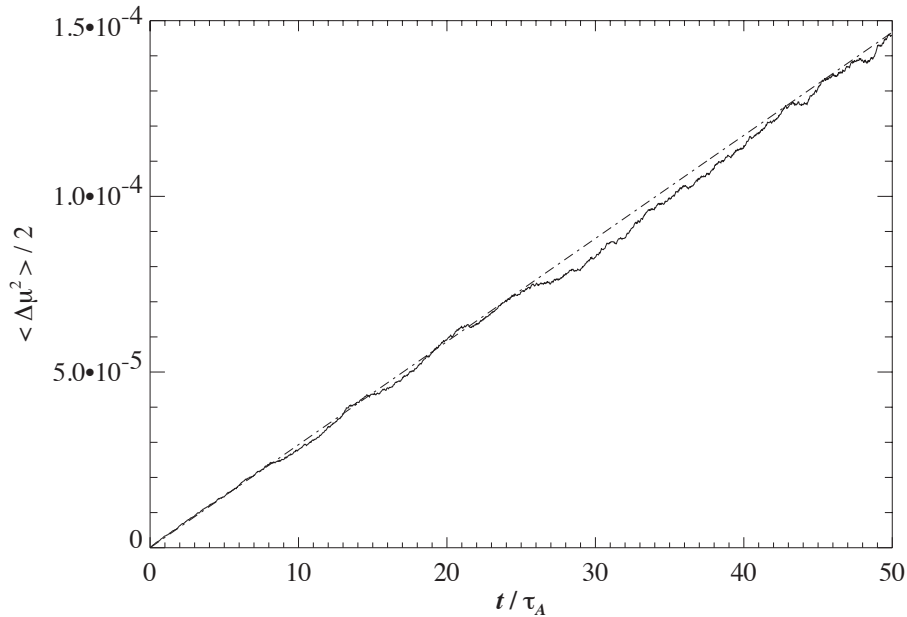


**Figure B.13:** Temporal evolution of  $\langle (\Delta\mu)^2 \rangle / 2$  for a simulation with  $\delta B/B_0 = 0.001$ ,  $\mu_0 = 0.1$ ,  $\beta = 500$ ,  $L = 1000\lambda$  and  $n_s = 1657864$ .

cessive stationary wavepacket, their parallel velocities begin to decorrelate through gyroresonance and  $\langle (\Delta\mu)^2 \rangle$  approaches the behavior expected from quasilinear theory. However, because of the finite spatial extent ( $\sim \lambda_c$ ) of the wavepacket, the resonance is rapidly destroyed within a time of about  $\tau_{ac}$  and particles are once more subjected to enhanced nonlinear effects such as trapping, that tend to destroy diffusive behavior unless primary resonances overlap. So  $\langle (\Delta\mu)^2 \rangle$  rather rapidly decays away from the quasilinear prediction. In effect, this situation is similar to the case in which the experiment is interrupted and re-started again at intervals of the order of several autocorrelation times  $\tau_{ac}$ . Indeed, this is the same behavior observed decreasing the box length, e.g. Figure B.11, so that particles make many box transits during a run (note the striking similarity between Figure B.11 and Figure B.13). The decreased box length increases the importance of nonlinear trapping through a widely spaced Fourier spectrum. As particles cross the box each time, they begin to transit and resonate with the same wavepacket due to field periodicity. After an autocorrelation time, they decorrelate with the wavepacket and their parallel velocities will remain correlated until they encounter another resonant wavepacket and the process begins anew. This oscillatory deviation from quasilinear theory appears in this way to be very similar to that seen in Figure B.13.

#### B.4.2.3 Grid spatial resolution: interpolation errors

In order to illustrate the effect of field grid resolution, we perform two simulations with the same initial conditions ( $\beta = 500$ ,  $L = 1000\lambda$ ,  $v/v_A = 10$  and  $\mu_0 = 0.6$ ),

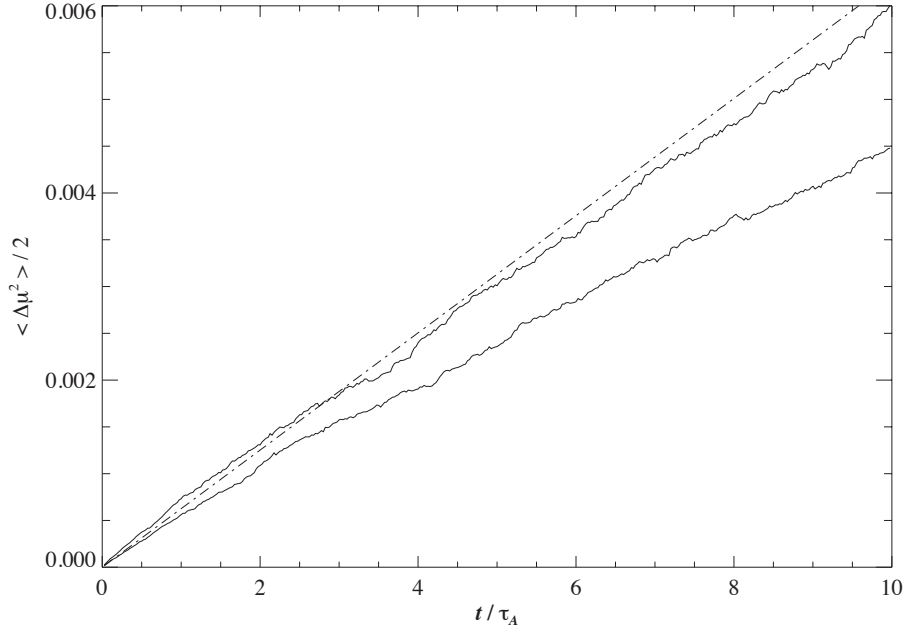


**Figure B.14:** Simulations with the same number, 65535, of nonzero Fourier components, but the curve that shows better agreement with the quasilinear prediction (– · –) has had its Fourier coefficient array padded with zeros up to  $n = 4194304$ .

but using a different number  $N$  of grid points,  $N = N_1 = 2^{16} = 65536$  in the first case and  $N = N_2 = 2^{22} = 4194304$  in the second one. The resonant mode number in each case is  $n_{res} \simeq 13263$  and  $k_{res} = 2\pi n_{res}/L$ . Both simulations have the same number of non-zero Fourier components, that is  $n = N_1 = 2^{16} = 65536$ , but in the second case the Fourier coefficient array is zero-padded up to  $n = N_2 = 2^{22} = 4194304$ . That is, in the second run the vector of Fourier coefficients is of length  $2^{22}$ , but there is nonzero power only in  $2^{16}$  coefficients. Thus, the difference between these two runs is the actual spatial resolution, or smoothness, of the fields. The run with the zero padded coefficient array has effectively a higher degree of 'trigonometric interpolation' and much smoother fields. Results are shown in Figure B.14 with solid line: the upper solid line is for the case of  $N = N_2 = 2^{22}$ , the lower one is for  $N = N_1 = 2^{16}$ . The quasi-linear prediction is also plotted in the figure with the dot-dashed line. It is evident that the run with the poorest spatial resolution of the fields deviates strongly from the theory. Note that the spacing in  $k$ -space between adjacent Fourier modes,  $\Delta k = 2\pi/L$ , is the same for each run. This rules out any effects related to the density of Fourier modes in  $k$ -space. However, by zero padding the Fourier array to a larger  $n$ , we obtain, after the inverse transform, better resolved fields. In effect we can 'restrict' (or bandwidth-limit) the largest wavenumber in the system to be  $k_s = 2\pi n_s/L$ , but the effective sampling rate is increased by increasing the Nyquist wavenumber  $k_{Nyq} \equiv \pi N/L = \pi/\Delta z$ , where  $N/2 \gg n_s$ . Thus, the smallest spatial variations of the fields occur on scale lengths

of the order of  $l_{\min} \sim L/n_s$ , but the fields are resolved down to scale lengths of the order of  $\Delta z = L/N = (n_s/N)l_{\min}$ .

In other words we are using the inverse of the sampling theorem (*Press et al., 1992*): if a function  $h(z)$ , sampled in space at an interval  $\Delta z$ , is known to be bandwidth limited to wavenumbers smaller in magnitude than  $k_s$  and if it turns out that the Fourier coefficients for  $k > k_s$  are all identically zero, then the function is completely determined by its discrete samples  $h_n(n\Delta z)$ . Indeed, in this case we have (*Press et al., 1992*)

$$h(z) = \Delta z \sum_{n=-\infty}^{\infty} h_n \frac{\sin[k_{\text{Nyq}}(z - n\Delta z)]}{\pi(z - n\Delta z)}.$$

At first sight, the idea of bandwidth limit the signal might seem artificial, but has a valid physical reason. Indeed, at least within the context of MHD turbulence, frequencies and wavenumbers are bandwidth limited by the basic assumptions governing the validity of MHD. These are  $\omega < \Omega_i$  and  $k\rho_i < 1$ , where  $\Omega_i$  is the ion gyrofrequency and  $\rho_i = v_{th,i}/\Omega$  is the ion thermal gyroradius. A left hand circularly polarized mode, whose electric field vector has the same sense of gyration about the mean magnetic field as an ion, has a resonance at  $\Omega_i$ , so it is bandwidth limited physically through ion cyclotron damping at  $\omega(k_{\parallel}) = k_{\parallel}v_A \simeq \Omega_i$  (that inverted gives the maximum parallel wavenumber).

The smoother fields, as a result of these extra zero Fourier coefficients, allow us to use safely simple linear interpolation to evaluate the electromagnetic fields at the particle positions. The advantage of the approach, from the point of view of CPU cycles, is the speed. The disadvantage is, of course, the extra computer memory required.

#### B.4.2.4 Increasing the extent of the Fourier spectrum $k_N$

Casting our attention back to Figure B.9 we observe, in comparison with Figure B.14, the effects of increasing both the spatial resolution of the fields and the number of Fourier modes,  $k_n = 2\pi n/L$ . In the run represented by Figure B.9 we set the largest wavenumber to correspond to  $n = 1657864$ . In this case, the agreement with the quasi-linear theory is even more convincing than the better of the two curves in Figure B.14. The likely reason is the broader 'spectral width' and hence the larger degree of stochasticity in the fields. It is to be recalled that one of the basic assumptions of the quasi-linear theory is a broad band turbulence spectrum.



# Bibliography

- Alfveń, H., *Cosmical electrodynamics*, Clarendon Press, Oxford, 1950.
- Alfveń, H., Some properties of magnetospheric neutral surfaces, *J. Geophys. Res.*, 73, 4379, 1968.
- Ambrosiano, J., W. H. Matthaeus, M. L. Goldstein, and D. Plante, Test particle acceleration in turbulent reconnecting magnetic fields, *J. Geophys. Res.*, 93, 14383, 1988.
- Asano Y., T. Mukai, M. Hoshino, Y. Saito and H. Hayakawa, and T. Nagai, Evolution of the thin current sheet in a substorm observed by Geotail., *J. Geophys. Res.*, 108, A5, 1189, 2003.
- Asano Y., T. Mukai, M. Hoshino, Y. Saito and H. Hayakawa, and T. Nagai, Statistical study of thin current sheet evolution around substorm onset., *J. Geophys. Res.*, 109, A0513, 2004.
- Ashour-Abdalla M., L. M. Zelenyi, V. Perroomian, and R. Richard, Consequences of magnetotail ion dynamics., *J. Geophys. Res.*, 93, 383, 1994.
- Bachelier, L., Théorie de la spéculation, *Ann. de l'Ecole Normale Supérieure*, vol. 3, Gauthier-Villars, Paris, 1900. (English translation, in *The Random Character of Stock Market Prices*, edited by P. H. Cootner, pp. 17-78, MIT Press, Cambridge, Mass., 1964.)
- Bauer T. M., W. Baumjohann, R. A. Treumann, N. Sckopke, and H. Luhr, What is cluster telling us about magnetotail dynamics?, *J. Geophys. Res.*, 100, 9605, 1995.
- Bieber, J. W., W. H. Matthaeus, C. W. Smith; W. Wanner; M. B. Kallenrode and G. Wibberenz, Proton and electron mean free paths: The Palmer consensus revisited, *Astrophys. J.*, 420, 294, 1994.
- Bieber, J. W. and W. H. Matthaeus, Perpendicular Diffusion and Drift at Intermediate Cosmic-Ray Energies, *Astrophys. J.*, 485, 655, 1997.
- Bieber, J. W., W. H. Matthaeus, A. Shalchi, and G. Qin, Nonlinear guiding center theory of perpendicular diffusion: General properties and comparison with observation, *Geophys. Res. Lett.*, 31, L10805, 2004.
- Borovsky, J. E., R. C. Elphic, H. O. Funsten and M. F. Thomsen, The Earth's plasma sheet as a laboratory for flow turbulence in high-[beta] MHD, *J. Plasma Physics*, 57, 1, 1997.

- Brown, R., A brief account of microscopical observations made in the months of June, July and August, 1827, on the particles contained in the pollen of plants; and on the general existence of active molecules in organic and inorganic bodies, *Phil. Mag.* 4, 161, 1828.
- Büchner, J, and L. M. Zelenyi, Regular and chaotic charged particle motion in magnetotail-like field reversal 1. Basic theory of trapped motion, *J. Geophys. Res.*, 94, A9, 11821, 1989.
- Cai C. L., I. Dandouras, H. Rème, J. B. Cao, G. C. Zhou and G. K. Parks, Cluster observations on the thin current sheet in the magnetotail., *Ann. Geophys.*, 26, 929, 2008.
- Cattell C. A. and F. S. Mozer, Electric field measured by ISEE-1 within and near the neutral sheet during quiet and active times., *Geophys. Res. Lett.*, 9, 9, 1041-1044, 1982.
- Chandrasekhar, S., Stochastic Problems in Physics and Astronomy, *Rev. Mod. Phys.*, 15, 1, 1943.
- Chirikov, B. V., Motion stability of a charged particle in a magnetic trap, *Fizika Plazmy*, 4, 521, 1978.
- Daglis I. A., E. T. Sarris and G. Kremser, Ionospheric contribution to the cross-tail current enhancement during the substorm growth phase., *J. Atmosph and Terrest. Phys.*, 53:1091-1098, dec 1991.
- Dalena S., A. Greco, G. Zimbardo, P. Veltri, Role of oxygen ions in the formation of a bifurcated current sheet in the magnetotail., *J. Geophys. Res.*, 115, A03213, 2010.
- Davidson, R. C., Methods in a Nonlinear Plasma Theory, *Academic Press, New York*, 356, 1972.
- Delcourt D. C. and G. Belmont, Ion dynamics at the earthward termination of the magnetotail current sheet, *J. Geophys. Res.*, 103, 4605, 1998.
- Delcourt, D. C., R. F. Martin, Jr., and F. Alem, A simple model of magnetic moment scattering in a field reversal., *Geophys. Res. Lett.*, 21, 14, 1543, 1994.
- Delcourt D. C., H. V. Malova, and L.M. Zelenyi, Dynamics of charged particles in bifurcated current sheets: the  $k \simeq 1$  regime., *J. Geophys. Res.*, 109, A01222, 2004.
- Dolginov, A. Z. and I. N. Toptygin, Cosmic rays in the interplanetary magnetic fields, *Icarus*, 8, 54, 1968.
- Earl, J. A., The diffusive idealization of charged-particle transport in random magnetic fields, *Astrophys. J.*, 193, 231, 1974.

- Echer E., A. Korth, Q.-G. Zong, M. Fränz, W. D. Gonzalez, F. L. Guarnieri, S. Y. Fu, and H. Reme, Cluster observations of O<sup>+</sup> escape in the magnetotail due to shock compression effects during the initial phase of the magnetic storm on 17 August 2001., *J. Geophys. Res.*, 113, A05209, 2008.
- Einstein, A., Über die von der molekularkinetischen Flüssigkeiten suspendierten Teilchen, *Ann. Phys.*, 17, 549-560, 1905. (English translation, in *Investigations on the Theory of Brownian Movement* by Albert Einstein, edited with notes by R. Fürth, pp. 1-35, Methuen, London, 1926.)
- Fick, A., Ueber diffusion, *Poggendorffs Ann. Phys. Chem.*, 59 - 86, 1855a.
- Fick, A., On liquid diffusion, *Philos. Mag. J. Sci.*, 10, 31 - 39, 1855b.
- Fisk, L. A., M. L. Goldsteins, A. J. Klimas and G. Sandri, The Fokker-Planck Coefficient for Pitch-Angle Scattering of Cosmic Rays., *Astrophys. J.*, 190, 417, 1974.
- Fok M. C., T. E Moore, P. C. Brandt, D. C. Delcourt, S. P. Slinker, and J. A. Fedder, Impulsive enhancements of oxygen ions during substorms., *J. Geophys. Res.*, 111, A10222, 2006.
- Fokker, A. D., *Ann. Phys. (Leipzig)*, 43, 810, 1914.
- Forman, M. A., J. R. Jokipii and A. J. Owens, Cosmic-Ray Streaming Perpendicular to the Mean Magnetic Field., *Astrophys. J.*, 192, 535, 1974.
- Fourier, J. B. J., Théorie Analytique de la Chaleur, *F. Didot, Paris*, 1822.
- Giacalone, J. and J. R. Jokipii, The Transport of Cosmic Rays across a Turbulent Magnetic Field, *Astrophys. J.*, 520, 204, 1999.
- Ginet, G. P. and M. A. Heineman, Test particle acceleration by small amplitude electromagnetic waves in a uniform magnetic field, *Phys. Fluids B*, 2, 700, 1990.
- Goldstein, H., *Classical Mechanics*, 2nd ed, Addison & Wesley, Reading, MA, 1980.
- Goldstein, M. L., W. H. Matthaeus and J. J. Ambrosiano, Acceleration of charged particles in magnetic reconnection: Solar flares, the magnetosphere and solar wind, *Geophys. Res. Lett.*, 13, 205, 1986.
- Gray, P. C. and L. C. Lee, Particle pitch angle diffusion due to nonadiabatic effects in the plasma sheet., *J. Geophys. Res.*, 87, A9, 7445, 1982.
- Gradshteyn, I. S. and Ryzhik, I. M., *Table of integrals, series and products.*, Academic Press, New York, 1980.
- Greco A., A. L. Taktakishvili, P. Veltri, G. Zimbardo, and L. M. Zelenyi, Ion dynamics in the near earth magnetotail: magnetic turbulence versus normal component of the average magnetic field., *J. Geophys. Res.*, 107, 1267, 2002.



- Greco A., R. De Bartolo, G. Zimbardo, and P. Veltri, A three-dimensional kinetic-fluid numerical code to study the equilibrium structure of the magnetotail: The role of electrons in the formation of the bifurcated current sheet., *J. Geophys. Res.*, 112, A06218, 2007.
- Greco A., S. Perri, G. Zimbardo and L.M. Zelenyi, Particle acceleration by stochastic fluctuations and dawn-dusk electric field in the Earth's magnetotail, *Adv. Space Res.*, 44, 4, 528, 2009.
- Hall, D. E. and P. A. Sturrock, Diffusion, Scattering, and Acceleration of Particles by Stochastic Electromagnetic Fields, *Phys. Fluids*, 10, 2620, 1967
- Harris, E. G., On a plasma sheet separating regions of oppositely directed magnetic fields, *Nuovo Cimento*, 23, 115, 1962.
- Hasselmann, K. and G. Wibberenz, *Zs. f. Geophys.*, 34, 353, 1968.
- Hoshino M., T. Yamamoto, A. Nishida, Y. Saito, and S. Kokubun, Turbulent magnetic field in the distant magnetotail: Bottom-up process of plasmoid formation?, *Geophys. Res. Lett.*, 21, 2935, 1994.
- Hoshino M., T. Yamamoto, T. Mukai, A. Nishida and S. Kokubun, Structure of plasma sheet in magnetotail: double-peaked electric current sheet., *J. Geophys. Res.*, 101, 1996.
- Israelevich, P. L., A. I. Ershkovich and R. Oran, Current carriers in the bifurcated tail current sheet: Ions or electrons?, *J. Geophys. Res.*, 113, A04215, 2008.
- Jokipii, J. R., Cosmic-Ray Propagation. I. Charged Particles in a Random Magnetic Field, *Astrophys. J.*, 149, 405, 1966.
- Jokipii, J. R., Cosmic-Ray Propagation. II. Diffusion in the Interplanetary Magnetic Field, *Astrophys. J.*, 146, 480, 1967.
- Jokipii, J. R. and E. N. Parker, Random Walk of Magnetic Lines of Force in Astrophysics, *Phys. Rev. Lett.*, 21(1), 44, 1968.
- Jokipii, J. R. and E. N. Parker, Stochastic Aspects of Magnetic Lines of Force with Application to Cosmic-Ray Propagation, *Astrophys. J.*, 155, 777, 1969.
- Jokipii, J. R., Propagation of cosmic rays in the solar wind., *Rev. Geophys. Space Phys.*, 9, 27, 1971.
- Jokipii, J. R., J. Kóta, and J. Giacalone, Perpendicular transport in 1- and 2-dimensional shock simulations., *Geophys. Res. Lett.*, 20(17), 1759, 1993.
- Jones, F. C., T. B. Kaiser and T. J. Birmingham, New Approach to Cosmic-Ray Diffusion Theory, *Phys. Rev. Lett.*, 7, 485, 1973.

- Jones, F. C., T. J. Birmingham and T. B. Kaiser, Partially averaged field approach to cosmic ray diffusion, *Phys. Fluids*, 21, 347, 1978.
- Jones, F. C., J. R. Jokipii and M. G. Baring, Charged-particle motion in electromagnetic fields having at least one ignorable spatial coordinate, *Astrophys. J.*, 509(1), 238, 1998.
- Kaiser, T. B., T. J. Birmingham and F. C. Jones, Computer simulation of the velocity diffusion of cosmic rays, *Phys. Fluids*, 21, 361, 1978.
- Karimabadi, H., K. Akimoto, N. Omid and C. R. Menyuk, Particle acceleration by a wave in a strong magnetic field - Regular and stochastic motion, *Phys. Fluids B*, 2, 606, 1990.
- Karimabadi, H. and C. R. Menyuk, A Fast and Accurate Method of Calculating Particle Diffusion: Application to the Ionosphere, *J. Geophys. Res.*, 96, 9669, 1991
- Karimabadi, H., D. Krauss-Varban and T. Terasawa, Physics of pitch angle scattering and velocity diffusion. I - Theory, *J. Geophys. Res.*, 97, A9, 13853, 1992.
- Kappler, E., *Ann. d. Phys.*, (Leipzig), 11, 233, 1931.
- Kistler L. M., C. Mouikis, E. Mobius, B. Klecker, J. A. Sauvaud, H. Rome, A. Korth, M. F. Marcucci, R. Lundin, G. K. Parks, and A. Balogh, Contribution of nonadiabatic cross-tail current in a O<sup>+</sup> dominated thin current sheet., *J. Geophys. Res.*, 11, A06213, 2005.
- Kennel, C. F. and Petschek, H. E., Limit on Stably Trapped Particle Fluxes, *J. Geophys. Res.*, 71, 1, 1966.
- Kennel, C. F. & F. Engelmann, Velocity Space Diffusion from Weak Plasma Turbulence in a Magnetic Field, *Phys. of Fluids*, 9, 2377, 1966.
- Klein, O., *Arkiv Mat. Astr. Fys.*, 16, 5, 1922.
- Klimas, A. J. and G. Sandri, Foundation of the Theory of Cosmic-Ray Transport in Random Magnetic Fields, *Astrophys. J.*, 169, 41, 1971.
- Korth A., R.H.W. Friedel, F. Frutos-Alfaro, C. G. Mouikis, and Q. Zong, Ion composition of substorms during storm-time and non-storm-time periods., *J. Atmosph. Solar-Terrest. Phys.*, 64:561–566, 2002.
- Kramers, H. A., *Physica*, 7, 284, 1940.
- Landau, L. D., *J. Phys. (Moscow)*, 10, 25, 1946.
- Lapenta, G., and J. U. Brackbill, 3D reconnection due to oblique modes: A simulation of Harris current sheets., *Nonlinear Process. Geophys.*, 7, 151, 2000.

- Lee, M. A., and H. J. Voelk, Hydromagnetic waves and cosmic-ray diffusion theory, *Astrophys. J.*, 198, 485, 1975.
- Lerche, I., Quasilinear Theory of Resonant Diffusion in a Magneto-Active, Relativistic Plasma, *Phys. Fluids*, 11, 1720, 1968.
- Lichtenberg, A. J. and M. A. Lieberman, Regular and stochastic motion, *Springer-Verlag, New York*, pp. 24, 300, 1983.
- Lingenfelter, R. E., R. Ramaty and L. A. Fisk, Compound diffusion of cosmic rays, *Astrophys. Lett.*, 8, 93, 1971.
- Mace, R. L., W. H. Matthaeus and J. H. Bieber, Numerical Investigation of Perpendicular Diffusion of Charged Test Particles in Weak Magnetostatic Slab Turbulence, *Astrophys. J.*, 538(1), 192, 2000.
- Matthaeus, W. H., M. L. Goldstein and J. H. King, An interplanetary magnetic field ensemble at 1 AU, *J. Geophys. Res.*, 91, 59, 1986.
- Matthaeus, W. H., P. C. Gray, D. H. Pontius J. W. and Bieber, Spatial Structure and Field-Line Diffusion in Transverse Magnetic Turbulence, *Phys. Rev. Lett.*, 75, 2136, 1995.
- Matthaeus, W. H., G. Qin, J. W. Bieber and G. P. Zank, Nonlinear Collisionless Perpendicular Diffusion of Charged Particles, *Astrophys. J.*, 590, L53, 2003.
- Minnie, J., R. A. Burger, Parhi S., W. H. Matthaeus and J. W. Bieber, Comparison of the effects of two models for perpendicular diffusion on cosmic-ray latitudinal gradients, *Adv. Sp. Res.*, 35(4), 543, 2005.
- Minnie, J., W. H. Matthaeus, J. W. Bieber, D. Ruffolo and R. A. Burger, When do particles follow field lines?, *J. Geophys. Res.*, 114, A1, 2009.
- Montroll, E.W., *J. SIAM*, 4, 241, 1956.
- Montroll, E.W. and G.H. Weiss, *J. Math. Phys.*, 10, 753, 1969.
- Montroll, E.W. and H. Scher, *J. Stat. Phys.*, 9, 101, 1973.
- Nakamura R., W. Baumjohann, A. Runov, T. L. Zhang, and M. Volwerk, Fast flow during current sheet thinning., *J. Geophys. Res.*, 29, 2140, 2002.
- Ness N. F., The earth's magnetic tail., *J. Geophys. Res.*, 70:2989, 1965.
- Perroomian V., M. El-Alaoui, M. Ashour-Abdalla, and L. M. Zelenyi, Dynamics of ionospheric O<sup>+</sup> ions in the magnetosphere during the 24-25 September magnetic storm., *J. Geophys. Res.*, 111, A12203, 2006.
- Perri S., A. Greco and G. Zimbardo, Stochastic and direct acceleration mechanism in the Earth's magnetotail., *Geophys. Res. Lett.*, 36, L04103, 2009.

- Perrin, J., *Comptes Rendus* (Paris) 146, 967, 1908.
- Perrin, J., *Ann. Chim. Phys.*, 18, 5, 1909.
- Planck, M., *Sitzber. Preuß. Akad. Wiss.*, 324, 1917.
- Pommois P., G. Zimbardo and P. Veltri, Anomalous, non-Gaussian transport of charged particles in anisotropic magnetic turbulence., *Phys. Plasmas*, 5, 1998.
- Pommois P., G. Zimbardo and P. Veltri, Magnetic field line transport in three dimensional turbulence: Levy random walk and spectrum models, *Phys. PRev. E.*, 14, 2007.
- Press, W. H., Teukolsky, S. A., Vetterling, W. T. and Flannery, B. P., Numerical recipes in FORTRAN. The art of scientific computing, *Numerical Recipes, 2nd edition*, Cambridge University Press, New York, 1992.
- Qin, G., W. H. Matthaeus and J. W. Bieber, Perpendicular transport of charged particles in composite model turbulence: Recovery of diffusion, *Astrophys. J.*, 578(2), L117, 2002a.
- Qin, G., W. H. Matthaeus, and J. W. Bieber (2002b), Subdiffusive transport of charged particles perpendicular to the large scale magnetic field, *Geophys. Res. Lett.*, 29(4), 1048, 2002b.
- Qin, G., W. H. Matthaeus and J. W. Bieber, Parallel Diffusion of Charged Particles in Strong Two-dimensional Turbulence, *Astrophys. J.*, 640, L103, 2006
- Rechester, A. B. and M. N. Rosenbluth, Electron heat transport in a Tokamak with destroyed magnetic surfaces, *Phys. Rev. Lett.*, 40(1), 38, 1978.
- Ricci P., G.Lapenta, and J. U. Brackbill, Structure of the magnetotail current: Kinetic simulation and comparison with satellite observations., *Geophys. Res. Lett.* 31, 6801, 2004.
- Roelof, E. C., Transport of cosmic rays in the interplanetary medium., *Can. J. Phys.*, 46, S990, 1968.
- Rossi B. and S. Olbert, Introduction to the physics of space., *McGraw-Hill*, 1970.
- Runov A., R. Nakamura, W. Baumjohann, R. A. Treumann, T. L. Zhang, M. Volwerk, Z. Vörös, A. Balogh, K. H. Glaßmeier, B. Klecker, H. Rème and L. Kistler., Current sheet structure near magnetic X-line observed by Cluster., *Geophys. Res. Lett.* 30, 2003.
- Runov A., R. Nakamura, W. Baumjohann, T. L. Zhang, M. Volwerk, H.-U. Eichelberger and A. Balogh., Cluster observation of a bifurcated current sheet., *Geophys. Res. Lett.*, 30, 2003.

Runov A., Sergeev V., Nakamura R., Baumjohann W., Vörös Z., Volwerk M., Asano Y., Klecker B., Rème H. and Balogh A., Properties of a bifurcated current sheet observed on 29 August 2001., *Ann. Geophys.*, 22, 2535, 2004.

Aggiungere

Runov A., Sergeev V. A., Nakamura R., Baumjohann W., Apatenkov S., Asano Y., Takada T., Volwerk M., Vörös Z., Zhang T. L., Sauvaud J.-A., Rème H., and Balogh A., Local structure of the magnetotail current sheet: 2001 Cluster observations., *Ann. Geophys.*, 24, 247, 2006.

Sauvaud J.-A., P. Louarn, G. Fruit, H. Stenuit, C. Vallat, J. Dandouras, H. Rème, M. André, A. Balogh, M. Dunlop, L. Kistler, E. Möbius, C. Mouikis, B. Klecker, G. K. Parks, J. McFadden, C. Carlson, F. Marcucci, G. Pallochia, R. Lundin, A. Korth, and M. McCarthy, Case studies of the dynamics of ionospheric ions in the Earth's magnetotail., *J. Geophys. Res.*, 109, A01212, 2004.

Sergeev V. A., D. G. Mitchell, C. T. Russel and D. J. Williams, Structure of the tail plasma/current sheet at  $\sim 11$  RE and its changes in the course of a substorm., *J. Geophys. Res.*, 98, 17, 345, 1993.

Sergeev V., A. Runov, R. Nakamura, W. Baumjohann, T. L. Zhang, M. Volwerk, J. A. Sauvaud, H. Rème, A. Balogh, and M. André and B. Klecker, Current sheet flapping motion and structure observed by Cluster., *Geophys. Res. Lett.*, 30, 1327, 2003.

Shalchi, A., J. W. Bieber, W. H. Matthaeus and G. Qin, Nonlinear Parallel and Perpendicular Diffusion of Charged Cosmic Rays in Weak Turbulence, *Astrophys. J.*, 616, 617, 2004.

Shalchi, A., 2009, Nonlinear Cosmic Ray Diffusion Theories, *Astrophysics and Space Science Library*, 362 (Springer-Verlag, Berlin Heidelberg), 2009.

Schlickeiser, R., Cosmic-ray transport and acceleration. I - Derivation of the kinetic equation and application to cosmic rays in static cold media. II - Cosmic rays in moving cold media with application to diffusive shock wave acceleration, *Astrophys. J.*, 336, 243, 1989.

Sitnov M. I. and P. N. Gudzar and M. Swisdak, A model of the bifurcated current sheet., *Geophys. Res. Lett.*, 30, 1712, 2003.

Smith, G. R. and Kaufman, A. N., Stochastic acceleration by an obliquely propagating wave - An example of overlapping resonances., *Phys. of Fluids*, 21, 2230, 1978.

Smoluchowski, M. V., *Ann. Phys.*, 48, 1103, 1915.

Sonnerup, B. U. O., Adiabatic particle orbits in a magnetic null sheet., *J. Geophys. Res.*, 76, 8211, 1971.

- Speiser T. W., Particle trajectory in model current sheet., *J. Geophys. Res.*, 70, 4219, 1965.
- Speiser, T. W, On the uncoupling of perpendicular and parallel motion in the neutral sheet., *J. Geophys. Res.*, 73, 1112, 1968.
- Stix, T. H., Waves in plasmas., *American Institute of Physics, New York*, 141(1), 186, 1966.
- Sturrock, P. A., Stochastic Acceleration., *Phys. Rev.*, 1965.
- Swanson, D. G., Plasma waves., *Academic Press, Boston*, 1989.
- Taktakishvili A., G. Zimbardo, E. Amata, S. Savin, A. Greco, P. Veltri and R. E. Lopez, Ion escape from the high latitude magnetopause: analysis of oxygen and proton dynamics in the presence of magnetic turbulence, *Ann. Geophys.*, 25, 1877, 2007.
- Urch, I. H., Charged particle transport in turbulent magnetic fields: The perpendicular diffusion coefficient, *Astrophys. Space Sci.*, 46, 389, 1977.
- Vainshtein, D. L., L. M. Zelenyi and A. I. Neishtadt, Motion of charged particles in the field of monochromatic wave in the Earth's magnetospheric tail., *Plasma Phys. Rep.*, 25, 887, 1999.
- Vaisberg O. L., L. A. Avanov, J. L. Burch and J. H. Waite, Jr, Measurements of plasma in the magnetospheric tail lobes., *Adv. Space. Res.*, 18, 8, 1996.
- Veltri P., G. Zimbardo, A. L. Taktakishvili, and L. M. Zelenyi, Effect of magnetic turbulence on the ion dynamics in the distant magnetotail., *J. Geophys. Res.*, 103, 14897, 1998.
- Voelk, H. J., Cosmic ray propagation in interplanetary space, *Rev. Geophys. Space Phys.*, 13, 547, 1975.
- Wax, N. (Ed.), *Selected Papers on Noise and Stochastic Processes*, Dover, New York, 1954.
- Weinstock, J., Formulation of a Statistical Theory of Strong Plasma Turbulence, *Phys. Fluids*, 12, 1045, 1969
- White, R. B., D. A. Monticello, M. N. Rosenbluth and B. V. Waddell, Saturation of the tearing mode, *J. Geophys. Res.*, 109, A02206, 2004.
- Wiener, N., *J. Math. and Phys.* (MIT), 2, 131, 1923; *Bull. Soc. math.* (France), 52, 569, 1924; *Acta Math.*, 55, 117, 1930; *Amer. J. Math.*, 60, 897, 1938.
- Wilber M., E. Lee, G. K. Parks, K. Meziane, C. W. Carlson, J. P. McFadden, H. Rème, I. Dandouras, J. A. Sauvaud, J. M. Bosqued, L. Kistler, E. Mobius,

- M. McCarthy, A. Korth, B. Klecker, M. B. Bavassano-Cattaneo, R. Lundin, and E. Lucek, Cluster observation of velocity space-restricted ion distribution near the plasma sheet., *Geophys. Res. Lett.*, 31, L24802, 2004.
- Wilson G. R., D. M. Ober, G. A. Germany and E. J. Lund, Nightside auroral zone and polar cap ion outflow as a function of substorm size and phase., *Phys. Fluids*, 20, 800, 1977.
- Wygant J. M., C. A. Cattel, R. Lysak, Y. Song, J. Dombek, J. McFadden, F. S. Mozer, C. W. Carlson, G. Parks, E. A. Lucek, A. Balogh, M. Andre, H. Rème, M. Hesse, and C. Mouikis, Cluster observations of an intense normal component of electric field at a thin reconnecting current sheet in the tail and its role in the shock-like acceleration of the ion fluid into the separatrix region., *J. Geophys. Res.*, 110, A09206, 2005.
- Yau, A. W., P. H. Beckwith, W. K. Peterson and E. G. Shelley, Long-term (solar cycle) and seasonal variations of upflowing ionospheric ion events at DE 1 altitudes, *J. Geophys. Res.*, 90, 8417, 1985.
- Yau, A. M., Some Mathematical Models Generalizing the Model of Homogeneous and Isotropic Turbulence, *J. Geophys. Res.*, 67(3), 3081, 1962.
- Zank, G. P., W. H. Matthaeus, J. W. Bieber and H. Moraal, The Cosmic Ray Diffusion Tensor in the Heliosphere, *Proc. of the 25th International Cosmic Ray Conference*, 2, 9, 1997.
- Zelenyi L. M., A. V. Milovanov and G. Zimbardo New perspectives on the Earth's magnetotail, *Geophys. Mon. Ser.*, 105, 321, 1998.
- Zelenyi L. M., M. I. Sitnov, H. V. Malova, and A. S. Sharma, Thin and superthin ion current sheets. Quasi-adiabatic and nonadiabatic models., *Nonlinear Process. Geophys.*, 7, 127, 2000.
- Zelenyi L. M., D. C. Delcourt, H. V. Malova, and A. S. Sharma, Aging of the magnetotail thin current sheet., *Geophys. Res. Lett.*, 29:1608, 2002.
- Zelenyi L. M., H. V. Malova, and V. Y. Popov, Splitting of thin current sheets in the earth's magnetosphere., *JETP Lett.*, 78, 296, 2003.
- Ziebell, L. F., P. H. Yoon, C. S. Wu and D. Winske, Pitch angle diffusion of newborn ions due to intrinsic turbulence in the solar wind, *J. Geophys. Res.*, 95, 17075, 1990.
- Zimbardo G., P. Veltri, G. Basile and S. Principato, Anomalous diffusion and Lévy random walk of magnetic field lines in three dimensional turbulence, *Phys. Plasma*, 2, 2653, 1995.

- Zimbardo G., A. Greco, A. L. Taktakishvili, P. Veltri, and L. M. Zelenyi, Magnetic turbulence and particle dynamics in the earth's magnetotail., *Ann. Geophys.*, 21, 1947, 2003.
- Zimbardo G., A. Greco, A. L. Taktakishvili, P. Veltri, and L. M. Zelenyi, Double peak structure and diamagnetic wings of the magnetotail current sheet., *Ann. Geophys.*, 22, 2541, 2004.
- Zimbardo, G., P. Pommiois and P. Veltri, Superdiffusive and Subdiffusive Transport of Energetic Particles in Solar Wind Anisotropic Magnetic Turbulence., *Astroph. Journal*, 639, L91, 2006.
- Zimbardo G., A. Greco, L. Sorriso-Valvo, S. Perri, Z. Voros, G. Aburjania, Kh. Chargazia, O. Alexandrova, Magnetic turbulence in the geospace environment, *Space Sci. Rev.*, 156(4), 89, 2010.